The Effect of Design on Endovascular Embolisation Device Performance



Thomas W. Peach

Magdalen College

University of Oxford

Supervised by

Professor Yiannis Ventikos and Professor Zhong You

Hilary Term 2015

This thesis is submitted to the Department of Engineering Science, University of Oxford, in partial fulfilment of the requirements for the degree of Doctor of Philosophy

Abstract

MOTIVATION

Cerebral aneurysms have presented considerable challenges to effective treatment since their first clinical observation. For some 100 years the only clinical solution was dangerous and often debilitating open-surgery in the form of a craniotomy. The safety and efficiency of cerebral aneurysm treatment was greatly improved in the early-1990s with the introduction of minimally invasive procedures such as endovascular coiling. The development in the mid-2000s of low-porosity stents, known as flow-diverters, presented a more sophisticated treatment rationale that focussed on vessel reconstruction, and addressed cases that would otherwise be problematic to treat by other endovascular means.

However, current designs of flow-diverter (and all known designs in development) are limited to near-identical products that risk under-exploiting the potential benefits of the treatment method. These devices are of a cylindrical, woven construction that necessitates a fixed mesh design, which means that any variation in design focusses on device porosity alone. As such, the precise hemodynamic mechanisms, and the resulting quality of aneurysm treatment by flow-diverter, are under-developed and poorly understood. There is also concern in the clinical community that the cylindrical nature of current flow-diverter devices may lead to daughter vessel sacrifice when used to treat bifurcation aneurysms.

This thesis specifically focusses on the effect of flow-diverter mesh topology on the complex hemodynamic environment within the treated aneurysm, and the resulting implications for treatment success.

METHODOLOGY

In this study, a number of both novel and commercially available flow-diverter designs are virtually implanted into idealised and patient-specific aneurysm geometries. These devices are then modelled under realistic blood flow conditions with computational fluid dynamics (CFD) techniques. The devices chosen encapsulate a range of features that allow the effects of device porosity and device mesh design to be controlled for and evaluated independently. Conventional cylindrical devices are also

compared to a novel, non-cylindrical device for the dedicated treatment of bifurcation aneurysms. The aneurysm hemodynamic environment both pre- and post-treatment is quantified with a number of *in-silico* measures, such as flow rate, velocity, pressure, and wall shear stress. Finally, a model of angiographic contrast agent transport is developed *in-silico* to begin to verify the complex flow patterns predicted by CFD simulations with the corresponding *in-vivo* behaviour seen clinically. A number of inaccuracies of previous 'virtual contrast' models, as presented in the literature, are addressed and quantified by comparison to a gold-standard *in-vivo* porcine model.

RESULTS

In a number of aneurysm geometries, novel flow-diverter designs are shown to outperform current commercially available devices. The strong influence of device porosity on aneurysm inflow reduction is confirmed with a 10% decrease in device porosity correlating with around 10-20% reduction in inflow. Variation attributed to device design alone is also seen; in a number of geometries, differences in flow-diverter mesh design, at constant porosity, are shown to introduce approximately 10-30% variation in aneurysm inflow reduction. Such variation is significant and potentially very important to the development of future endovascular treatment devices. The greatest variation in inflow reduction seen across the device designs also corresponds to changes in vorticity and secondary flow effects.

The flow reduction achieved by the novel bifurcation aneurysm device discussed compares favourably to conventional devices in half of the geometries simulated, achieving a flow reduction of approximately 30-70%. Across all bifurcation aneurysms studied, conventional devices produce a relatively uniform flow reduction of 50-70%. Little change in flow rates for vessels jailed by a conventional flow diverter suggest that concerns of daughter vessel sacrifice appear unfounded, at least immediately following device deployment and prior to any neointimal formation.

A number of unusual flow phenomena, which are almost entirely unreported in the literature, are observed in several aneurysm geometries. In particular, the emergence of stable and unstable laminar flow patterns under stationary conditions lead to oscillatory behaviour in one aneurysm geometry. Pseudo-stable behaviour is also observed in another aneurysm geometry whereby steady state and transient simulations conducted under identical conditions converge to solutions with radically different flow patterns.

A good *in-silico* prediction of contrast residence is possible for a pre-treatment aneurysm geometry, where mixing is prominent. Aneurysm flow patterns after de-

vice placement reveal large spatial-variation in contrast infiltration that challenge the validity of quantifying contrast residence with a spatially-averaged decay curve. The most significant source of error between aneurysm contrast decay rate predicted *in-silico* and the *in-vivo* porcine model is found to be the variation in parent vessel flow rate, and not the density and viscosity changes of the contrast-blood mixture.

CONCLUSIONS

In addition to porosity, flow-diverter device design has a substantial effect on aneurysm inflow reduction and aneurysm flow pattern. When coupled with improved knowledge of aneurysm thrombosis mechanisms, appropriate changes in flow-diverter mesh design have the potential to improve the success rate of flow-diverter treatment. However, the clinical implications of these effects are currently unknown due to the lack of design variation in commercially available devices.

In cases of bifurcation aneurysms, conventional flow-diverter devices have been shown to equal or outperform a novel device designed exclusively for bifurcation cases. Although no immediate complications were predicted from daughter vessel occlusion, the long-term integrity of treatment with conventional cylindrical devices is uncertain, and dedicated devices designed to preserve daughter vessel patency may become necessary.

The complexity of the flow environment within a cerebral aneurysm has been reinforced, and a number of effects have been observed that demand further investigation. In particular, the role that the observed flow instabilities and the resulting changes in aneurysm wall shear stress may have in aneurysm rupture mechanisms is an emerging area of the literature.

Verification of CFD simulations with *in-vivo* results remains a significant challenge. The virtual modelling of angiographic contrast residence currently offers the best route to such verification; although contrast transport may be integrated into current CFD simulations with relative ease, washout behaviour appears highly sensitive to parent vessel flow rates. As such, any contrast-based validation requires knowledge of patient-specific flow rates, which begins to challenge how representative flow conditions seen during angiography may be.

Acknowledgements

My thanks go first and foremost to my supervisors, Yiannis Ventikos and Zhong You. Thank you, Yiannis, for your continual enthusiasm and encouragement, for mentoring me as your student, and being an incredible source of academic wisdom. Thank you, Zhong, for fuelling my interest in deployable structures and their biomedical applications and, in doing so, encouraging me to pursue a DPhil at Oxford. Thanks also for the opportunity to be involved in a number of experiments, which led to the imaging that underpins much of this thesis.

Significant parts of this work resulted from a very fruitful collaboration with the Minimally Invasive New Technologies (MINT) Group at Weill-Cornell Medical College, New York. Thanks to Fred Cornhill and the entire MINT team for hosting me as a visiting researcher in 2013, offering a wealth of commercial and clinical expertise, and for financial support throughout this study.

Many thanks to my colleagues in both the Fluidics and Biocomplexity Group and the Centre for Doctoral Training (CDT) in Healthcare Innovation—I have learnt more about research from each of you than I could from any peer-reviewed publication. I would also like to thank the CDT faculty who provided an immensely useful first year of teaching that gave me a research experience with both great depth and breadth.

Within the broader academic community at Oxford, I would also like to thank James Byrne for his clinical insights and for giving me the opportunity to observe endovascular interventions in the clinic, and Paul Watton for a wealth of expertise, data, and clinical imaging. The generous advice and suggestions of Jiayao Ma, Rafik Rizkallah, and Jianhua Zhai were also much appreciated.

My deepest thanks also go to the large number of patients who freely gave their anonymised data for this study and many others. Without such contributions the progression of Medicine and Biomedical Engineering would be much the poorer, and studies such as this would be impossible.

Practically this thesis would not have been possible without the financial support of the Engineering and Physical Sciences Research Council (EPSRC), the Research Councils UK (RCUK) Digital Economy Programme, and the Wellcome Trust. I

would also like to thank Magdalen College and the Department of Engineering Science for a number of travel grants that allowed me to share this work both nationally and internationally.

Thanks also go to my examiners, Robin Cleveland and Alejandro Frangi, whose comments and suggestions have greatly improved this thesis and made my *viva voce* defence a lividly, fascinating, and challenging discussion. I am also indebted to my Transfer of Status and Confirmation of Status examiners Pete Dobson and Alison Noble.

My long DPhil journey was also wonderfully supported by numerous friends in Oxford and further afield who were always quick with encouragement and enthusiasm. The almost five years needed to complete this study would have been impossible without the love and support of my family: thank you Mum, Dad, Benji, and Emily, and latterly, Rosemary, Ed, and Alexa. Each of you has offered great wisdom, unconditional support, and words of encouragement.

Finally my heartfelt thanks must go to Kira Allmann—without your love, energy, and patience this document would never have happened. The tens of thousands of words in a thesis do not come close to the number needed to fully express my thanks at having you at my side, and me at yours.

Contents

1 Introduction and Physiological Background **1**

1.1 The Cardiovascular System, the Structure of the Vasculature, and Vascular Disease 1

1.2 Properties of Blood and Arterial Blood Flow 3

1.3 Intracranial Aneurysms 5

1.3.1 Aneurysm Prevalence and Risks 6

1.3.2 Aneurysm Formation and Growth 7

1.3.3 Aneurysm Types and Locations 8

1.3.4 Factors Affecting Rupture Risk 10

1.4 Aneurysm Treatment Methods 11

1.4.1 Clipping 11

1.4.2 Endovascular Coiling 12

1.4.3 Stent-Assisted Coiling 13

1.4.4 Flow-Diverter 14

1.4.5 Other Treatment Methods 16

1.5 Commercially Available Flow-Diverter Devices 16

1.6 Thrombosis and Hemodynamic Factors 19

1.6.1 Complete and Partial Occlusion 19

1.6.2 Aneurysm Inflow and Turnover Time 20

1.6.3 Flow Residence Time 20

1.6.4 Velocity and Flow Jetting 21

1.6.5 Wall Shear Stress 21

2 Numerical Methods **24**

2.1 Computational Fluid Dynamics and the Finite Volume Method 24

2.1.1 The Navier-Stokes Equations 25

2.1.2 The Scalar Transport Equation and Finite Volume Method 27

2.2 Strategies for Solving the Discretised Equations 29

2.2.1 The Diffusion Term 29

2.2.2 The Convection Term 30

2.2.3 The Temporal Term . . . 32
2.2.4 Pressure-Velocity Coupling and Iterative Methods . . . 33
2.3 Meshing and Mesh Independence . . . 34
2.3.1 Structured Meshes . . . 34
2.3.2 Unstructured Meshes . . . 35
2.3.3 Mesh Quality and Refinement . . . 35
2.4 Comparison to Other Studies in the Field . . . 36
2.5 Flow Regime and Features . . . 37
2.6 Boundary Conditions . . . 39
2.7 Flow-Diverter Device Deployment Methods . . . 41

3 Flow-Diverter Mesh Design and Large-Scale Flow Features 45
3.1 Introduction . . . 45
3.2 Investigating Flow-Diverter Meshes in Idealised Flow Conditions . . . 48
3.2.1 Mesh Designs . . . 49
3.2.2 Methodology . . . 51
3.2.3 Simulation Results . . . 52
3.2.4 Idealised Geometry Conclusions . . . 58
3.3 Anatomically Accurate Aneurysm Simulations . . . 59
3.3.1 Anatomically Accurate Geometries . . . 59
3.3.2 Simulation Methodology . . . 61
3.3.3 Results: Flow Reduction . . . 66
3.3.4 Results: Wall Shear Stress . . . 74
3.3.5 Anatomically Accurate Geometry Conclusions . . . 79
3.4 Conclusions . . . 79

4 Alternative Flow-Diverter Design Concepts: the 'Sphere' Device 81
4.1 Introduction . . . 81
4.2 Idealised Aneurysm Geometry Simulations . . . 83
4.2.1 Aneurysm and Device Geometries . . . 83
4.2.2 Simulation setup . . . 84
4.2.3 Mesh Independence . . . 86
4.2.4 Steady and Transient Results . . . 87
4.2.5 Positioning Study . . . 89
4.2.6 Conclusions: Prototype device and Idealised Aneurysm Geometry . . . 89
4.3 Anatomically Accurate Aneurysm Geometries . . . 90
4.3.1 Aneurysm Geometries and Device Modifications . . . 91
4.3.2 Simulation Methodology . . . 92

4.3.3 Mesh independence . . . 95
4.3.4 Simulation Results . . . 97
4.4 Comparing the 'Sphere' to the Performance of a Conventional Flow-Diverter . . . 110
4.4.1 Simulation Setup . . . 110
4.4.2 Simulation Results . . . 111
4.5 Conclusions . . . 119

5 Flow Instabilities in the Aneurysm Dome 121
5.1 Introduction . . . 121
5.1.1 Aneurysm Flow Instability in the Literature . . . 123
5.2 Lack of Convergence in Steady State . . . 123
5.2.1 Simulation Setup . . . 124
5.2.2 Results and Discussion . . . 125
5.2.2.1 MCA Geometry . . . 125
5.2.2.2 ICA_01 Geometry . . . 127
5.2.3 Conclusions: Lack of Convergence in Steady State . . . 129
5.3 Variation Between Steady State and Transient Solutions . . . 130
5.3.1 Simulation Setup . . . 134
5.3.2 Results and Discussion . . . 134
5.3.3 Conclusions: Steady State and Transient Inconsistencies . . . 137
5.4 Conclusion . . . 137

6 Development of a Virtual Contrast Model 139
6.1 Introduction . . . 139
6.1.1 Motivation: the Need for a Virtual Contrast Model . . . 139
6.1.2 Contrast Transport Models in the Literature . . . 141
6.1.3 Proposed Contrast Model . . . 142
6.2 The Basis of *In-vivo* and *In-silico* Contrast Validation . . . 143
6.3 *In-vivo* Experiment . . . 145
6.3.1 Experimental Methodology . . . 146
6.3.1.1 Experiment . . . 146
6.3.1.2 Postprocessing . . . 147
6.3.2 *In-vivo* Results . . . 148
6.4 *In-silico* Experiment . . . 151
6.4.1 Simulated Geometry . . . 151
6.4.2 Modelling Contrast *in-silico* . . . 152
6.4.3 Simulation Setup . . . 154
6.4.4 *In-silico* Results . . . 156

6.5 Comparing *in-vivo* and *in-silico* Results . . . 159
6.6 Accounting for Contrast Viscosity and Density . . . 160
6.6.1 Simulations Incorporating Contrast Viscosity and Density . . . 160
6.6.2 Simulation Results . . . 163
6.6.3 Summary: The Influence of Contrast Viscosity and Density . . . 169
6.7 Accounting for Parent Vessel Flow Rate . . . 170
6.7.1 The Effect of Placing a Catheter in a Vessel Lumen . . . 171
6.7.2 Simulations Incorporating Variation in Parent Vessel Flow Rates . . . 174
6.7.3 Simulation Results . . . 175
6.7.4 Summary: The Influence of Parent Vessel Flow Rate . . . 180
6.8 Chapter Conclusions: Evaluating the Virtual Contrast Model . . . 182

7 Applying the Virtual Contrast Model to Flow-Diverter Treatment in Animal Models 185
7.1 Introduction . . . 185
7.2 *In-vivo* Flow-Diverter Deployment . . . 186
7.2.1 Experimental Protocol . . . 186
7.2.2 Contrast Decay . . . 187
7.3 *In-silico* Flow-Diverter Deployment and Contrast Modelling . . . 189
7.3.1 Simulation Setup . . . 189
7.3.2 Simulation Results . . . 190
7.4 Accounting for Partial Thrombosis of the Aneurysm . . . 195
7.5 Comparing the Effect of Device Deployment: *in-silico* and *in-vivo* . . . 200
7.5.1 The 'No Device' and 'With Device' Cases . . . 200
7.5.2 The 'With Device' and 'No Device Geometry With Device' Cases . . . 205
7.6 Conclusions . . . 208

8 Conclusions and Future Work 210
8.1 Summary . . . 210
8.2 Specific Contributions to the Field . . . 215
8.3 Future Work . . . 217
List of Software Utilised in this Study . . . 218
List of Publications and Presentations . . . 219
Bibliography . . . 222

List of Figures

1.1 Layers of healthy arterial wall. Adapted from Holzapfel et al. 2
1.2 Flow magnitude and pulsatility from the aorta to the middle cereal artery (average in bold of in-vivo measurements in healthy volunteers). Adapted from Reymond et al. [123] 4
1.3 The arteries of the cerebral circulation located at the base of the brain, which form the Circle of Willis. The cerebral circulation is fed by blood from the Vertebral and Internal Carotid arteries, which originate at the aorta. (Image: WikiCommons) 6
1.4 Typical aneurysm types: Saccular, bifurcation, and fusiform. 8
1.5 Typical aneurysm locations in the cerebral vasculature of the general population (from Brisman et al. [12]) 9
1.6 Aneurysm treatment by clip ligation (clipping) (from Brisman et al. [12]) 11
1.7 Aneurysm treatment by endovascular coiling (from Brisman et al. [12]) 12
1.8 Stent-assisted endovasular coiling of a wide-necked cerebral aneurysm (from Brisman et al. [12]) 13
1.9 Flow-diverter treatment of a sidewall aneurysm 14
1.10 Dominant flow-diverter devices in clinical use: the Silk flow-diverter and Pipeline Embolization Device (Images: Balt Extrusion and EV3 promotional material) . . 16
1.11 WEB II device (Image: Pierot et al. [113]) 18

2.1 A generalised fluid control volume, CV 25
2.2 The physical relationship expressed in equation 2.10 28
2.3 The control volume, CV, indicated with north(n), south(s), east(e), west(w), top(t) and bottom(b) faces and corresponding neighbouring cell centres N, S, E, W, T and B in the directions indicated. (Figure adapted from: Versteeg and Malalasekera [154]) 29
2.4 Generalised pressure correction algorithm methodology 33
2.5 Idealised meshing schemes: (a) structured and (b) unstructured 34

2.6 Flow in 4mm diameter tubes at a constant Reynolds number and variable curvature, which results in different Dean numbers and the emergence of a pair of vortices in the case of a non-zero Dean number. In-plane flow is indicated with flow vectors while longitudinal velocity is colour coded. 38
2.7 Pressure and flow waveforms measured in-vivo (upper of each pair of plots) and the corresponding 1D analytical model prediction (lower of each pair of plots), at salient locations in the cerebral vasculature. Reproduced from Reymond et al. [123] 40
2.8 Cylindrical projection deployment of a flow-diverter with a vessel. Adapted from Appanaboyina et al. [4] 42
2.9 In the FVS method the projected device geometry is given localised stiffness. Adapted from Larrabide et al. [82] 43
2.10 Longtitudinal and torsional spring analogy of the deployment scheme proposed by Spranger et al. Figure adapted from Blom [10] and Farhat et al. [44] 43

3.1 Detail of the method used to laser-cut Nitinol hollow tubing into a flow-diverter device 46
3.2 Four of the almost infinite number of possible mesh designs that may be laser-cut 47
3.3 Mesh designs to be tested for flow-diverting action (not to scale) 49
3.4 Flow diverter testing geometries where the device is positioned between the dashed lines. I: 90 degree bend, II: 60 degree bend and III: 30 degree bend 50
3.5 Rhomboid mesh deployed in the 90 degree bend geometry (cutaway) 50
3.6 Mesh independence tests 52
3.7 Flow reduction by mesh topology type and geometry 53
3.8 Velocity and vorticity plots of the 90 degree bend geometry 54
3.9 Velocity and vorticity plots of the 60 degree bend geometry 55
3.10 Velocity and vorticity plots of the 30 degree bend geometry 56
3.11 Patient specific geometries with inlets and direction of inflow indicated 60
3.12 Flow-diverter designs 60
3.13 All four flow-diverter devices deployed in the ICA_Giant geometry 62
3.14 Mesh independence plots 63
3.15 Parent vessel flow profiles 65
3.16 Changes in both aneurysm inflow reduction and Ophthalmic artery flow due to variation in outlet pressure condition (Stent I) 66
3.17 Reduction in aneurysm inflow due to device deployment in each aneurysm geometry 67
3.18 Streamlines of flow (lines tangential to instantaneous velocity vectors) at mean parent vessel flow rate across all three aneurysm geometries with and without a flow-diverting stent deployed 69

3.19 Aneurysm inlet planes for the MCA geometry. Velocity magnitude and vorticity are indicated for mean and maximum flow rate. Darker areas correspond to the region of inflow. 71
3.20 Aneurysm inlet planes for the ICA_Bifurc and ICA_Giant geometries with velocity magnitude and in-plane direction indicated 72
3.21 Parent vessel velocity magnitude and vorticity profiles at mean flow rate for cross-sections proximal to each aneurysm 73
3.22 WSS at mean flow rate 75
3.23 Spatially-averaged and maximum WSS values for the dome of each aneurysm at mean arterial flow 76

4.1 Conventional flow-diverter design deployed in both a sidewall and bifurcation aneurysm 82
4.2 Prototype device and the idealised bifurcation aneurysm geometry 84
4.3 BA flow profile 85
4.4 Idealised bifurcation aneurysm geometry mesh independence 86
4.5 Mean (and range of) aneurysm inflow reduction due to device deployment for the idealised BA geometry 88
4.6 Idealised BA geometry streamlines, steady state simulation 89
4.7 Idealised BA geometry streamlines, transient simulation 90
4.8 Idealised BA geometry repositioned 91
4.9 Aneurysm geometries with inlets and direction of inflow indicated 92
4.10 Sphere device deployed in a silicone phantom 93
4.11 Sphere device deployed in an aneurysm geometry 94
4.12 ICA flow profile 95
4.13 BA geometry mesh independence 96
4.14 ICA geometry mesh independence 97
4.15 'No Device' aneurysm inflow 98
4.16 'With Device' aneurysm inflow 99
4.17 Aneurysm inflow reduction 100
4.18 Streamlines of flow (lines tangential to instantaneous velocity vectors) at mean parent vessel flow rate both with and without the Sphere device deployed in the BA geometries 101
4.19 Streamlines of flow (lines tangential to instantaneous velocity vectors) at mean parent vessel flow rate both with and without the Sphere device deployed in the ICA geometries 102
4.20 WSS plots of all six aneurysm geometries with and without the Sphere device deployed at peak parent vessel flow rate 105

4.21 Plots of Flow Reduction and Geometry Metrics with Spearman's Rank Correlation Coefficient . . . 106
4.22 BA pressure plots . . . 108
4.23 ICA pressure plots . . . 109
4.24 Approximate vessel centrelines (white dashes) along which the SILK flow-diverter is deployed for each bifurcation geometry . . . 111
4.25 Aneurysm inflow with conventional flow-diverter device (SILK) implanted . . . 112
4.26 Inflow reduction with SILK device . . . 113
4.27 Streamlines of flow (lines tangential to instantaneous velocity vectors) at mean parent vessel flow rate across the BA aneurysm geometries with a Sphere or a SILK device deployed . . . 114
4.28 Streamlines of flow (lines tangential to instantaneous velocity vectors) at mean parent vessel flow rate across the ICA aneurysm geometries with a Sphere or a SILK device deployed . . . 115
4.29 Mean percentage of inflow leaving the dominant daughter vessel (the vessel selected for flow-diverter placement) with no device, the SILK, and the Sphere deployed . . . 116
4.30 Comparing WSS distributions at peak systole (max flow rate) for all geometries implanted with the SPHERE and SILK devices . . . 117
4.31 Plots of Flow Reduction and Geometry Metrics . . . 118
4.32 Aneurysm inflow reduction for both the Sphere and SILK devices . . . 119

5.1 Summary of the results of steady state and transient simulations for the three geometries discussed (aneurysm inflow rate) . . . 122
5.2 Significant oscillations are seen in the velocity magnitude of flow within the aneurysm dome at a constant inflow rate . . . 125
5.3 Fourier decomposition plot for the indicated portion of the oscillating velocity magnitude plot shown in figure 5.2 . . . 126
5.4 Two distinct flow regimes observed in a particle image velocimetry (PIV) study of the MCA geometry at mean flow rate. Image credit: Dr. Jianhua Zhai . . . 127
5.5 No significant oscillations are seen for the ICA_01 geometry . . . 128
5.6 Steady state and transient (stationary boundary conditions) simulations of the ICA_01 geometry with no device deployed, and corresponding aneurysm inflow rates . . . 128
5.7 Steady state simulation of BA_01 with and without a 'Sphere' device . . . 130
5.8 Steady state simulation of BA_01 with and without a 'Sphere' device . . . 131
5.9 Approximate vector directions of the circulation within the aneurysm dome of BA_01 with no device in both steady state and transient simulations . . . 131

5.10 Confirmation of the same flow pattern throughout the cardiac cycle for the BA_01 geometry with no device deployed 132
5.11 Indications of the approximate flow regime within the BA_01 geometry for steady state and transient flow simulations at mean flow rate. Clear recirculation is seen in the transient case with flow exiting and reentering through the aneurysm neck (dashed line) 133
5.12 Steady state simulations at mean and maximum flow rate 134
5.13 Comparing steady and transient velocity at mean flow to the development of a transient solution with stationary boundary conditions. Corresponding flow regimes are also indicated. 135
5.14 Comparing steady and transient velocity at maximum flow to the development of a transient solution with stationary boundary conditions. Corresponding flow regimes are also indicated. 136

6.1 Variation of contrast concentration with angiographic grayscale value experiment results 143
6.2 Calibration Card 144
6.3 Calibration Graph 145
6.4 Experimental aneurysm: aneurysm at surgical creation by vein graft of the CCA(left), 2D angiography showing aneurysm in-vivo 3 weeks post-creation(centre) and 3D STL reconstruction of the aneurysm from 3D rotational angiography 3 weeks post-creation(right) 146
6.5 Contrast residence in an experimental aneurysm, each image is separated by a time interval of 0.4 seconds 147
6.6 Segmentation of the aneurysm dome in 2D angiography 148
6.7 Contrast washout curves for the four experimental aneurysms 149
6.8 Decay curves of all four experimental aneurysms with an exponential line of best fit 150
6.9 Trimmed simulation geometry and details of mesh resolution 151
6.10 Multiple independent contrast pulses introduced at the geometry inlet 153
6.11 Multiple independent pulses introduced at the geometry inlet combine to create a cycle-averaged contrast bolus (unity over one cardiac cycle) 154
6.12 Human ICA flow profile generated from a 1D model of the arterial tree 155
6.13 Flow streamlines at mean parent vessel flow rate in the ‘No Device’ simulated geometry 156
6.14 Total absolute contrast value within the aneurysm dome for all eight contrast pulses 157
6.15 Contrast pulse residence and decay for all eight pulses in the ‘No Device’ geometry 157
6.16 Cycle-averaged simulated contrast residence and decay for the ‘No Device’ geometry 158

6.17 Comparing experimental and simulated (cycle-averaged) contrast bolus residence and decay curves. Both sets of curves are centred on peak concentration. 159
6.18 Virtual and in-vivo angiography (images taken at 0.40 second intervals from peak contrast concentration) with no device deployed. Images are aligned to the peak aneurysm contrast concentration at 0.80 seconds 161
6.19 Total contrast pulse value in the aneurysm domes for the 'High Re' and 'Low Re' simulations 163
6.20 Relative contrast pulse distributions for the 'High Re' and 'Low Re' simulations . 164
6.21 Relative contrast pulse decay for the 'High Re' and 'Low Re' simulations 164
6.22 Cycle-averaged contrast bolus residence and decay for the High Reynolds number simulation 165
6.23 Cycle-averaged contrast bolus residence and decay for the Low Reynolds number simulation 166
6.24 Aneurysm inflow across the cardiac cycle for the initial, 'High Re', and 'Low Re' simulations 167
6.25 Velocity magnitude at the aneurysm neck for the initial 'No Device', 'High Re', and 'Low Re' simulations 168
6.26 Different degrees of flow infiltration and vortex position in the 'High Re', and 'Low Re' simulations at mean parent vessel flow rate 168
6.27 Experimental and simulated contrast bolus concentration decay including 'High Re' and 'Low Re' simulations 169
6.28 Vessel (red) and catheter (blue) model cross-sections 172
6.29 Velocity profiles of pressure-driven flow in the blocked vessel lumen at mean and maximum ICA flow rates 173
6.30 Catheter and vessel flows mixing at mean ICA flow conditions 174
6.31 Catheter and vessel flows mixing at maximum ICA flow conditions 174
6.32 Total absolute contrast pulse values for the 'High Q' and 'Low Q' simulations . . 175
6.33 Relative contrast pulse distributions for the 'High Q' and 'Low Q' simulations . . 176
6.34 Relative contrast pulse decay for the 'High Q' and 'Low Q' simulations 177
6.35 Cycle-averaged contrast bolus residence and decay for the high flow rate simulation 177
6.36 Cycle-averaged contrast bolus residence and decay for the low flow rate simulation 178
6.37 Aneurysm inflow across the cardiac cycle for the original, high flow rate, and low flow rate simulations 179
6.38 Velocity magnitude at the aneurysm neck for the initial 'No Device', 'High Q', and 'Low Q' simulations 180
6.39 Different degrees of flow infiltration and vortex position in the 'High Q', and 'Low Q' simulations at mean parent vessel flow rate 180

6.40 Experimental and simulated contrast concentration decay, including 'High Q' and 'Low Q' simulations . . . 181
6.41 Contrast decay rates for all three simulations ('No Device', 'High Q', and 'Low Q') conducted at different parent vessel flow rates . . . 181
6.42 Contrast residence and decay curves for experimental and all cycle-averaged simulations . . . 183

7.1 Reconstructions based on 3D angiography before and after flow-diverter deployment 187
7.2 Reduced contrast infiltration is seen in both aneurysms after flow-diverter device deployment . . . 187
7.3 Contrast infiltration and decay after device deployment. Images are separated by 0.4 seconds. . . . 188
7.4 Contrast washout curves for both experimental aneurysms implanted with a flow-diverter . . . 188
7.5 Decay portions of the experimental contrast residence curves with an exponential decay trend line fitted . . . 188
7.6 Flow-diverter device used experimentally (a) and the same device modelled virtually (b) . . . 189
7.7 Simulated flow streamlines in the 'With Device' case at mean parent vessel flow rate . . . 190
7.8 Absolute value for all eight contrast pulses in the With Device geometry . . . 191
7.9 Evolution of Pulse 7 for the 'With Device' simulation in the proximal region of the aneurysm neck. The contrast pulse concentration is shown at times 2.60 seconds (systole), 2.80 seconds (diastole), and 3.00 seconds . . . 191
7.10 Relative contrast residence and decay for all eight contrast pulses in the 'With Device' geometry . . . 192
7.11 Cycle-average contrast bolus residence and decay in the 'With Device' geometry . 193
7.12 Simulated instantaneous aneurysm inflow with and without a flow-diverter device deployed . . . 193
7.13 Maximum and mean aneurysm inlet velocity with and without device (in-silico) . 194
7.14 Total contrast volume in the aneurysm dome with and without a device deployed 195
7.15 Flow streamlines at mean flow for the 'No Device' geometry with a flow-diverter deployed . . . 196
7.16 Total absolute value for all eight contrast pulses in the 'No Device' geometry with a flow-diverter deployed . . . 197
7.17 Relative residence and decay for all eight contrast pulses in the 'No Device' geometry with a flow-diverter deployed . . . 197

7.18 Contrast bolus residence and decay in the 'No Device' geometry with a flow-diverter deployed 198
7.19 Simulated instantaneous aneurysm inflow with and without a flow-diverter device deployed in both the with and without device geometries 199
7.20 Flow pattern at peak systole for the 'No Device' simulation and the No Device geometry implanted with a flow-diverter device 199
7.21 Maximum and mean aneurysm inlet velocity with and without a flow-diverter device deployed in both the with and without device geometries 200
7.22 Comparing experimental and simulated contrast decay with and without device . 201
7.23 Virtual and in-vivo angiography (images taken at 0.40 second intervals from peak contrast concentration) with a flow-diverter device deployed. Images are aligned to the peak aneurysm contrast concentration at 0.80 seconds 202
7.24 Virtual and in-vivo angiography (images taken at 0.40 second intervals from peak contrast concentration) with no device deployed. Images are aligned to the peak aneurysm contrast concentration at 0.80 seconds 203
7.25 Effect of increased mean parent vessel flow rate and Reynolds number (consistent with a 50% concentration of Omnipaque 240) on aneurysm flow pattern 204
7.26 Comparing experimental and simulated contrast decay with and without device . 206
7.27 Virtual and in-vivo angiography (images taken at 0.40 second intervals from peak contrast concentration) with a flow-diverter device deployed in the 'No Device' geometry compared to the experimental case after device deployment. Images are aligned to the peak aneurysm contrast concentration at 0.80 seconds 207
7.28 Overlapped flow patterns within the aneurysm dome with a flow-diverter deployed for the 'no device' geometry (blue) and the 'with device' geometry (red) at mean and maximum flow rate 208

List of Tables

3.1 Relative inlet pressure boundary condition by geometry. Pressures are derived from geometries with no device deployed and a volumetric flow rate of 230ml/min 51
3.2 Flow-Diverter parameters 60
3.3 Vessel diameter and Flow-Diverter sizing 62

6.1 Contrast Properties 162
6.2 Summary of contrast mixture properties 162
6.3 Exponential contrast decay constants for the 'High Re', 'Low Re', and initial 'No Device' simulations 166
6.4 Inflow summary for the 'High Re', 'Low Re', and initial 'No Device' simulations . 167
6.5 Flow reductions due to catheter occlusions 172
6.6 Exponential decay time constants for the 'High Q', 'Low Q', and original simulations 178
6.7 Mean and range of aneurysm inflow for the original, high and low inflow simulations 179
6.8 Exponential decay constants: experimental and all cycle-averaged simulations . . 183

7.1 Aneurysm Inflow With and Without a Flow-Diverter Deployed 194
7.2 Experimental and simulated contrast decay rates 200

Nomenclature and Abbreviations

α: Womersley Number

ACA: Anterior Cerebral Artery

BA: Basilar Artery

BPM: Beats per Minute

β: Weighting Factor

CCA: Common Carotid Artery

CFD: Computational Fluid Dynamics

CT: (X-ray) Computed Tomography

De: Dean Number

ϵ: Weighting Factor

ECM: Extracellular Matrix

FEA: Finite Element Analysis

γ: Weighting Factor

Γ: Diffusivity ($m^2\ s^{-1}$)

ICA: Internal Carotid Artery

μ: Dynamic Viscosity (Pa s)

MCA: Middle Cerebral Artery

MR(I): Magnetic Resonance (Imaging)

ϕ: Generic Scalar Quantity

p: Pressure (Pa)

Q: Flowrate ($m^3\ s^{-1}$)

ρ: Density ($kg\ m^{-3}$)

ρ^*: Spearmans' Rank Correlation Coefficient

R: Coefficient of Determination

Re: Reynolds Number

SAH: Subarachnoid Haemorrhage

t: time (s)

u: Velocity ($m\ s^{-1}$)

VA: Vertebral Artery

WSS: Wall Shear Stress (Pa)

Chapter 1

Introduction and Physiological Background

In this chapter the cardiovascular system and the structure of the artery are introduced in section 1.1; blood properties are discussed in section 1.2; details of aneurysm types and risks are given in section 1.3; treatment options, including minimally invasive options, and specifically flow-diverters, are detailed in section 1.4; flow-diverter devices currently in use and under development are considered in section 1.5; finally, hemodynamic factors corresponding to successful aneurysm treatment with a flow-diverter device are commented on in section 1.6

1.1 The Cardiovascular System, the Structure of the Vasculature, and Vascular Disease

At the turn of the millennium, ischemic heart disease and cerebrovascular disease were the leading cause of death worldwide; a trend that shows no sign of abating. [93]

The vital importance of a healthy cardiovascular system was recognised as early as the ancient Egyptians, but the correct function of the basic anatomy was not known until the work of Harvey in 1628. [57] The human cardiovascular system comprises a number of elements: the heart, which acts as a centralised pump that pressurises and ejects blood in a pulsatile manner; the arteries and arterioles, which transport oxygenated blood throughout the body; the capillaries, microscopic

vessels that deliver oxygenated blood and allow gas exchange with the surrounding tissue; the veins and venules, which transport deoxygenated blood back to the heart under low pressure; and finally, the pulmonary circulation, which transports blood from the heart to the lungs to be oxygenated before returning to the heart. The entire cardiovascular system is regulated by the sympathetic nervous system, which ensures an adequate pressure and flow rate of oxygenated blood to all tissue by varying heart-rate and the lumen size of the arterial network. Even brief dysfunction of any element of the cardiovascular system can lead to complications, which can cause severe disability or death, in only a matter of minutes.

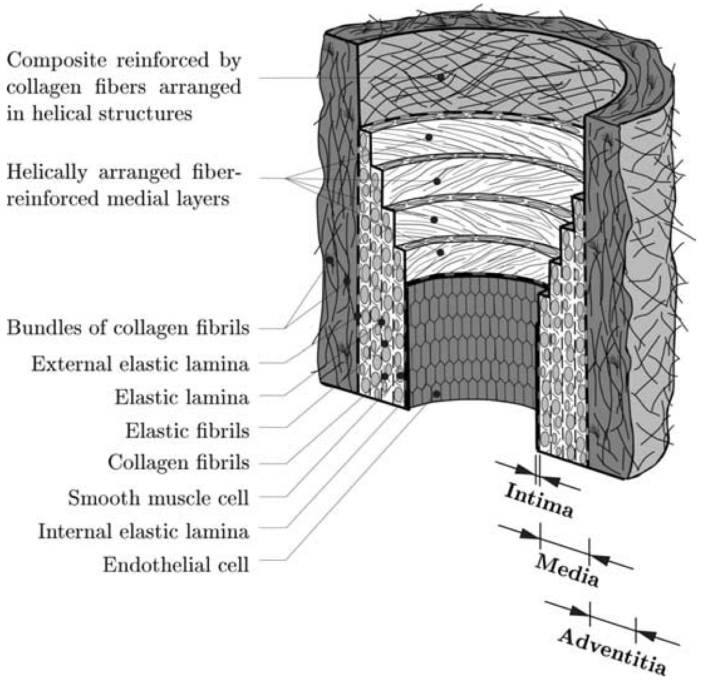

Figure 1.1: *Layers of healthy arterial wall. Adapted from Holzapfel et al.* [60]

Much vascular disease is associated with the arterial network, where the vital movement of oxygen-rich blood risks being restricted. A healthy cerebral artery has three layers as shown in figure 1.1. The innermost layer, the intima, is composed of a lower membrane that acts as a base for the attachment of a layer of endothelial cells, which are exposed directly to the bloodflow. Changes in the intima are often seen as a result of ageing and vascular disease. The media, the intermediate layer, is separated from the intima by an elastic laminae. The media comprises a network of elastic fibres, collagen fibres and smooth muscle cells. The media is usually the thickest portion of the vessel wall and contributes to the bulk of the mechanical properties of

the vessel. Finally, the outermost layer of the vessel is the adventitia, which is separated from the media by an external elastic laminae. The adventitia is a relatively stiff outer sheath made up of helical collagen fibres. The thickness of the adventitia varies depending on the arterial function, with the adventitial layer in cerebral vessels being relatively thin. [157] [60]

The overall mechanical properties of the artery are dictated by the elastin-collagen matrix and the relative proportions of each constituent; collagen fibres are typically unloaded and coiled, providing high tensile strength, while the elastin fibres give the vessel flexibility and elasticity. [60]

1.2 Properties of Blood and Arterial Blood Flow

Blood is a highly complex fluid that flows at scales from centimetres to micrometers within the human body in both a steady and pulsatile fashion. The structure of blood is majority water with a mix of cells, proteins and ions, and approximately 40% of the fluid by volume is comprised of red blood cells. The viscosity of blood is largely dictated by the presence of red blood cells, with the interactions between the small, semisolid particles raising the viscosity of blood to approximately 4x that of water. [76]

This particle-based source of viscosity makes blood a non-Newtonian fluid especially at very low shear rates and in small diameter vessels and capillaries. However, blood flow in relatively large arteries, such as the major arteries of the cerebral circulation, is considered to be Newtonian. [111] Areas of low shear rate present in the tip of an aneurysm dome can result in a localised increase in blood viscosity due to aggregation of red blood cells [76], however, the effect of this localised departure from Newtonian behaviour on aneurysm flow pattern and velocity has been shown to be small. [101] At such scales, a constant dynamic viscosity of 0.0035-0.004 Pa s is widely assumed in the literature. [63] A dynamic viscosity of 0.004 Pa s will be assumed throughout this study.

Given that blood is primarily composed of water, and the remaining constituents of blood are also majority water, the density of blood and water are very similar. The small fraction of blood constituents that are more dense than water do increase blood density but only by a

few percent. A relatively narrow range of blood densities of 1000-1050kgm^{-3} is assumed in the literature. [119] [141] In this study, blood is modelled as having a density equal to water (1000kgm^{-3}).

Blood flow in the arterial network experiences a wide range of pulsatility effects. Cardiac output from the heart is characterised by a high flow during systole and zero flow in the diastole phase of the cardiac cycle. Flow immediately downstream of the heart in the aortic arch resembles a smoothed step function with the flow rate falling to approximately zero for the second half of the cardiac cycle (diastole.) (See figure 1.2) Instability from localised flow reversal and a high Reynolds number (≈4000) result in flow entering the turbulent regime in the aorta. [115]

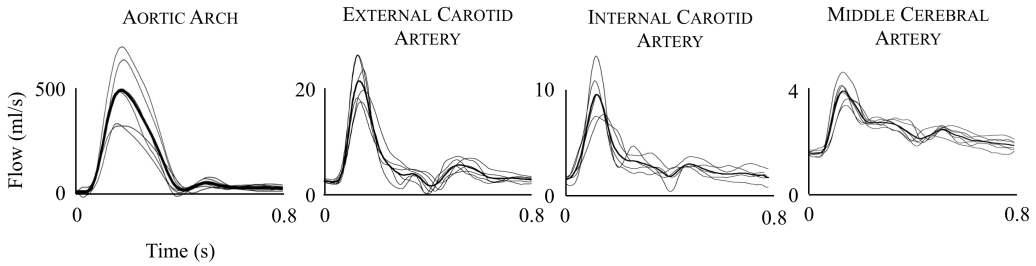

Figure 1.2: *Flow magnitude and pulsatility from the aorta to the middle cereal artery (average in bold of in-vivo measurements in healthy volunteers). Adapted from Reymond et al. [123]*

Flow in medium-sized vessels (≈1-6mm diameter), like the major cerebral arteries, is characterised by pulsatility that begins to dissipate deeper into the vasculature (compare the ICA and MCA distributions in figure 1.2) and a non-zero flow rate throughout diastole. Flow is laminar and localised flow reversal in diastole is very minor and limited to larger vessels.

Finally, flow in very small vessels, arterioles, and capillaries is laminar and pseudo-steady with an almost complete loss of any pulsatility. In vessels below 1mm diameter non-Newtonian effects become significant with viscosity dominating the flow characteristics. At a finer scale, flow in capillaries is dictated by interactions at the cellular level and the assumption of treating blood as a fluid with uniform properties breaks down.

Variation in the waveforms of figure 1.2 is due to attenuation resulting from both the resistance of the arterial bed and the capacitance of the arterial elasticity. Simplified models of pressure and flow rate in the vasculature that incorporate these resistive and capacitive elements may be used to approximate 'typical' flow characteristics anywhere in the vasculature. These models

are discussed further in the Boundary Conditions section of the following chapter.

Wall shear stress (WSS) is an important quantity of viscous flow in pipes, and is especially important in the dynamic system of flow in arteries. There is a well-established relationship between WSS and endothelial cell function, with WSS acting as a primary pathway for sensing mechanical stimuli within the vasculature. [121] Normal WSS in the cerebral vascular is considered to be approximately 2-5Pa. This value is then altered by disease and local stenosis, vessel curvature, non-circular arterial sections, secondary flow effects, and flow pulsatility. WSS is discussed in greater detail with reference to aneurysms in section 1.6.5.

Finally, arteries are not a static system; vessels contract and dilate to ensure constancy of blood flow rate and pressure. This auto-regulatory function in the cerebral arteries is particularly strong as supply of blood to the brain needs to remain relatively constant despite a cardiac output that may triple during intense exercise. However, accurately modelling such effects falls outside the scope of this study. Changes in flow conditions due to heart rate have been quantified in the literature by Bowker et al. [11], although overall flow patterns were not found to change considerably due to changes in pulse. In this study, typical 'at rest' conditions are assumed for a healthy individual with a heart rate of 75 BPM. Cerebral arteries are also assumed rigid in this study. Such an assumption is common throughout the literature for two reasons. First, accurately modelling the arterial distension is problematic due to the complex anisotropic structure of the vessel wall and is consequently very computationally costly. Second, flexible vessels have been shown to have little effect on overall flow patterns and haemodynamic indices within the vasculature. Instead, distensible vessels mainly act to reduce peak values of WSS due to deformation at areas of flow impingement. [39]

1.3 Intracranial Aneurysms

Intracranial aneurysms are localised dilations in the wall of the cerebral arteries, most often occurring in the region of the Circle of Willis, shown in figure 1.3. Although aneurysms are relatively innocuous and often entirely asymptomatic malformations, their occurrence in such close proximity to the brain poses a risk of severe complications and leads to a *very* challenging treatment environment.

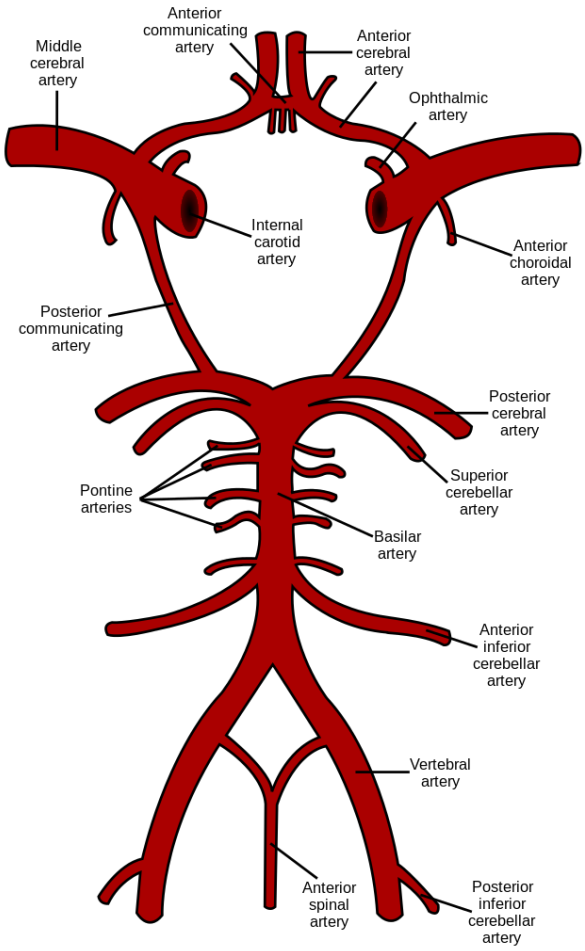

Figure 1.3: *The arteries of the cerebral circulation located at the base of the brain, which form the Circle of Willis. The cerebral circulation is fed by blood from the Vertebral and Internal Carotid arteries, which originate at the aorta. (Image: WikiCommons)*

1.3.1 Aneurysm Prevalence and Risks

The estimated prevalence of intracranial aneurysms in the general population is around 1-5%. [12] [153] Some variation in this rate is attributed to ethnicity, gender and a number of risk factors including smoking, hypertension, alcohol abuse and sympathomimetic drug use. [159] [29] [75]

A major risk to a patient presenting with an intracranial aneurysm is from subarachnoid haemorrhage (SAH) resulting from aneurysm rupture. During SAH bleeding spreads into the subarachnoid space, the cerebrospinal fluid filled cavity separating the meninges that surround the brain, and triggers an often catastrophic response. The increased intracranial pressure activates the sympathetic nervous system, which dramatically increases blood pressure. This leads

to further compression of the neural matter and vasculature, resulting in widespread ischemia. Approximately 85% of all spontaneous SAH cases are due to aneurysm rupture. [53]

Although the estimated aneurysm rupture rate is relatively low, with an annual rate around 3%, the effects of SAH can be catastrophic. Aneurysm-rupture induced SAH has a mortality rate of 25-45% and a severe disability rate of 17%. [94] [67] Additionally, 5-15% of all strokes are attributed to aneurysms. [8] Gender and age are also thought to play a role in aneurysm rupture with the rate of SAH in women being twice that of men, and the highest prevalence seen between 55 and 60 years of age. [159]

Clinical management of intracranial aneurysms is key as only an estimated 20-50% of cases pose a risk of rupture during a patient's lifetime. [29] Aneurysm treatment is often complex and is not without risks, consequently many patients may be monitored for a long period of time before treatment is proposed. A conservative approach is also necessitated by the often irreversible nature of many treatment procedures. The issue of appropriate monitoring and management is compounded further by the fact that most aneurysms are entirely asymptomatic and are increasingly being discovered incidentally during unrelated imaging procedures. [153]

As such, the fields of interventional neurology and neuroradiology have adopted imaging and modelling techniques at a considerable pace in an attempt to elucidate the complex and visually obscured phenomena that dictate aneurysm management.

1.3.2 Aneurysm Formation and Growth

Inflammation has been found to play a significant role in the inception and growth of cerebral aneurysms. [3] Such inflammation may result from disease, most notably polycystic kidney disease, or local blood pressure and complex flow conditions. [122] [24] [25] [157]

The mechanism of aneurysm growth after inception is highly complex and dominated by the load-bearing relationship of collagen and elastin fibres in the extracellular matrix (ECM) of the vessel. Under normal conditions, the collagen fibres are unloaded in a crimped configuration and fibres are being continually deposited and degraded with a half life of around 4 weeks. Aneurysms develop and grow as medial smooth muscle cells die, elastin fibres within the vessel wall rupture, and load is transferred to the collagen fibre network. The loss of elastin and smooth

muscle cells in the medial layer is also accompanied by the accumulation of lymphocytes. [48] The rate of elastin regeneration in the ECM is very slow, with a typical half life of 70 years, which leads to a vanishing proportion of arterial wall load being borne by elastin fibres. In order to compensate for the loss of elastin and maintain equilibrium, additional collagen fibres must be deposited in the ECM. [61] The relatively high turnover of collagen allows for progressive growth and remodelling of the aneurysm, which may stabilise or continue to grow. [157] The layer of intimal endothelial cells remains as the aneurysm grows but reorganises according to local flow conditions at the wall. This can lead to both a highly uniform pattern of cells or a highly irregular structure associated with intimal thinning. [133]

1.3.3 Aneurysm Types and Locations

Aneurysms may be classified into two broad types: saccular or fusiform.

Saccular aneurysms result from localised vessel wall degradation that does not affect the entire vessel circumference. A typical sidewall saccular aneurysm is shown in figure 1.4 (left), an isolated 'berry-like' out-pouching forms on straight vessel sections and may have a wide or narrow neck. Bifurcation aneurysms are saccular aneurysms that form at or near arterial bifurcations as shown in figure 1.4 (centre). Bifurcation aneurysms often have complex shapes, which may have a wide or narrow neck, or no clearly defined region neck due to aneurysm and vessel coalescence.

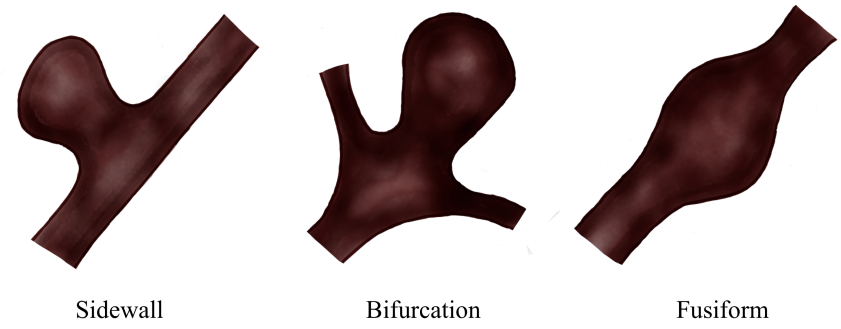

Figure 1.4: *Typical aneurysm types: Saccular, bifurcation, and fusiform.*

Fusiform aneurysms form at locations where the entire circumference of the vessel wall is degraded. Consequently, fusiform aneurysms are amorphous with no visible neck and often form a highly irregular shape. (See figure 1.4) Fusiform aneurysms often form as dissecting aneurysms,

where a partial tear in the vascular wall is enlarged by flow infiltrating and separating the layers of the wall and collapsing the original vessel lumen. Fusiform aneurysms are comparatively rare, especially in the cerebral vasculature, with approximately 90% of all intracranial aneurysms being saccular in presentation.

Aneurysms may form anywhere in the vascular network, but they are especially prevalent in the cerebral circulation. [12] Common intracranial aneurysm locations are shown in figure 1.5.

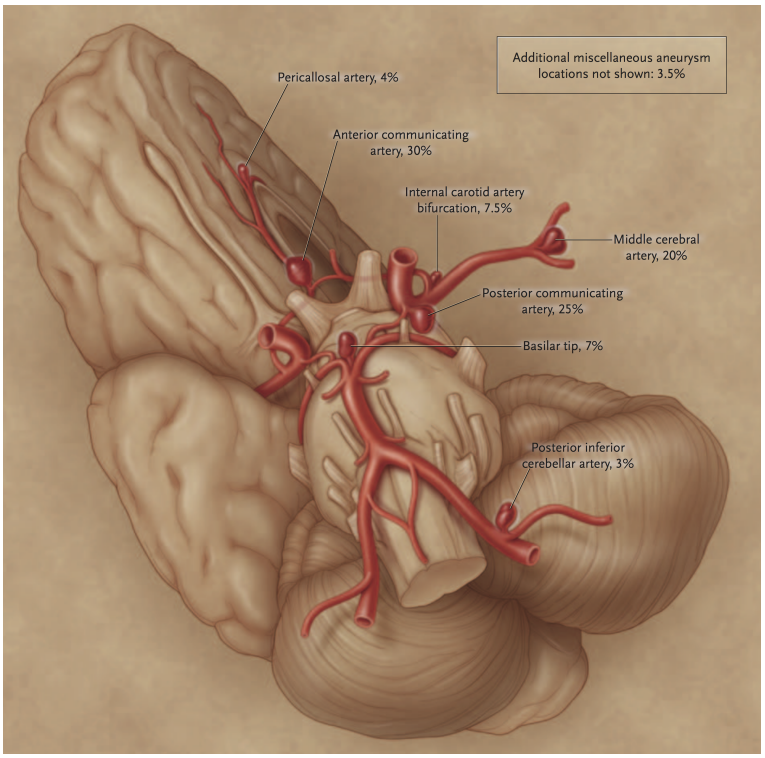

Figure 1.5: *Typical aneurysm locations in the cerebral vasculature of the general population (from Brisman et al. [12])*

Cerebral aneurysms commonly form at vessel bifurcations and areas of high tortuosity due to the prevailing flow conditions. [135] The variation in cerebral anatomy within the population also influences aneurysm location. Only around 50% of individuals share a 'text book' Circle of Willis. In others, one or more vessels (typically communicating branches) may not be patent to blood flow or may be absent entirely. [62] Hence, blood flow patterns and pressures are often highly patient-specific, resulting in susceptibility to aneurysm formation. [137] [36] Also, additional aneurysms may develop in up to 30% of patients who already have one cerebral aneurysm. [151] [12]

1.3.4 Factors Affecting Rupture Risk

The mechanisms that initiate aneurysms rupture are complex and poorly understood. However, a number of clinical metrics have been linked to increased aneurysm growth and rupture risk.

-Aneurysm Size: A number of studies have indicated that large aneurysms (with a major diameter greater than ≈7-8mm) enlarge more over time and pose a higher rupture risk than smaller aneurysms. [14] [81]

-Aneurysm Shape: Many shape factors linked to aneurysm rupture risk have been posited in the literature. Some measures are relatively simple relations, such as aneurysm aspect ratio (height/neck width), aneurysm to vessel diameter ratio, bottleneck factor (max diameter/neck width), etc [59] [40] [145] [81]; others, such as Zernike moments, capture complex geometric harmonics. [97] In one striking example, Ujiie et al. showed that 80% of ruptured aneurysms had an aspect ratio (AR) greater than 1.6, compared to only 10% of all unruptured aneurysms. [146] Irregular and multi-lobed aneurysms with non-spherical shapes are also associated with rupture. While a wide aneurysm neck and an aneurysm angle that creates an inflow rate typical of the parent vessel both exacerbate the rupture risk. [36] Broadly, the flow distributions of many at-risk geometries are characterised by either high degrees of flow jetting or acute areas of flow stagnation.

-Aneurysm Location: Aneurysm location has been linked to increased ruptured risk in a number of studies with rupture observed in areas of naturally occurring cross-flow and other complex flow patterns. Specifically, aneurysms located at the basilar apex, posterior communicating artery, posterior inferior cerebellar artery, and anterior communicating artery have all been linked to increased risk of rupture. The risk of rupture was also elevated in aneurysms located in a partial or highly asymmetric vasculature. [23]

The mechanisms associated with each of these factors will be discussed in detail in section 1.6.

1.4 Aneurysm Treatment Methods

Aneurysms at risk of rupture or further growth are treated by isolating the delicate lesion from the vasculature. Treatment methods reduce flow entering the aneurysm dome, which leads to thrombosis of the aneurysm and a reduced risk of rupture. Both surgical and minimally-invasive techniques may be used to treat an at-risk aneurysm, as detailed below:

1.4.1 Clipping

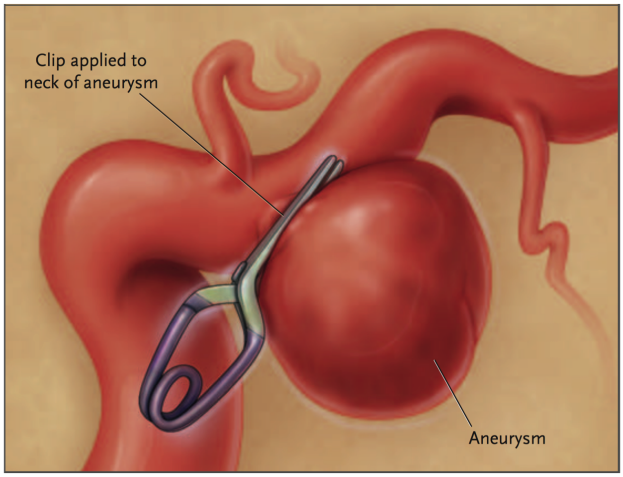

Figure 1.6: *Aneurysm treatment by clip ligation (clipping) (from Brisman et al. [12])*

Unlike other treatments, aneurysm clip ligation (clipping) is performed during open-surgery, after removing a portion of the skull in a craniotomy. During treatment the aneurysm dome is isolated from the parent vessel by placing a small metal clip over the aneurysm neck, as shown in figure 1.6. When appropriate, the aneurysm dome is then drained of blood. The clip remains permanently in place after the skull has been closed with local endothelialisation at the closed aneurysm neck returning the vessel to normal function.

The procedure was first performed by Dandy in 1937 [33] and until around 1990, clipping remained the only treatment option for cerebral aneurysms. Advances in surgical technique and microscope imaging have improved success rates but the procedure has remained largely unchanged. Regrowth and delayed bleeding are rare following clipping, but aneurysm remnants have been observed in 4-18% of patients. [18] A major disadvantage of treatment by clipping is the highly invasive nature of the procedure, and access can be problematic for aneurysms

in certain locations. Clipping is often considered the most cost effective treatment option for giant aneurysms compared to endovascular methods, where treatment cost scales with aneurysm volume.

1.4.2 Endovascular Coiling

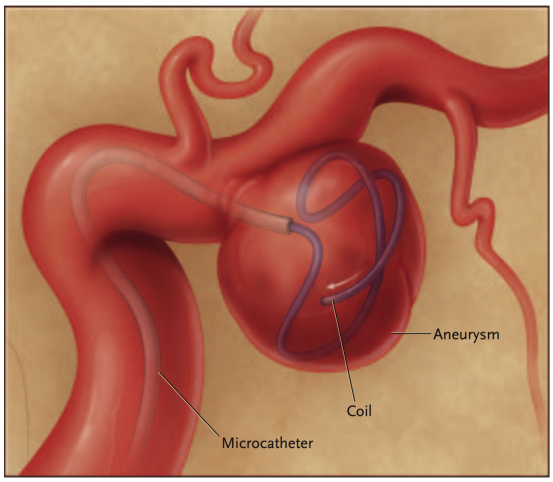

Figure 1.7: *Aneurysm treatment by endovascular coiling (from Brisman et al. [12])*

Historically, as early as the 1880s, attempts had been made to treat cases from within the vasculature to isolate aneurysms by filling with wires. [120] However it was the development of the Guglielmi detachable coil one hundred years later in the late 1980s that substantially improved and standardised the procedure to make it a viable clinically option. [55]

Unlike clipping, endovascular coiling is performed in an entirely minimally-invasive manner. A puncture is made in the femoral or radial artery and a micro catheter fed through the circulation, via the aortic arch, to the site of the aneurysm. A number of platinum coils are then passed along the tubular catheter and deposited into the aneurysm sac as shown in figure 1.7. The coils are manufactured with a 'memory' that encourages packing into an approximate sphere with known diameter; sequential coils are selected with tighter packing radii until the aneurysm is filled to a typical packing fraction around 30-100% by volume. [102] [70] Flow within the aneurysm dome is substantially reduced after coil placement, which is followed by thrombosis and aneurysm isolation.

A major advantage of coiling over clipping is the minimally-invasive nature of the procedure.

Recovery and procedure times are reduced and risk of infection is lowered. [66] A randomised trial between clipping and coiling ruptured aneurysms, the International Subarachnoid Aneurysm Trial (ISAT), found that disability-free outcome was higher in cases of coiling. [99] However, there have been reports of increased risk of rebleeding in aneurysms treated with coils due to coil compaction. [1]

Coiling is not a viable treatment option in aneurysm geometry shapes that are not capable of securely containing the coils and risking occlusion of the parent artery. Very large aneurysms require many coils (>50) for adequate isolation, which can lead to very high treatment costs. Additionally, large aneurysms are often symptomatic due to a 'mass effect' whereby the enlarged aneurysm dome rests on a nerve within the skull or restricts blood flow in a neighbouring vessel. Coiling treatment cannot reduce such symptoms as the size of the aneurysm is not reduced after filling with coils and thrombosis.

1.4.3 Stent-Assisted Coiling

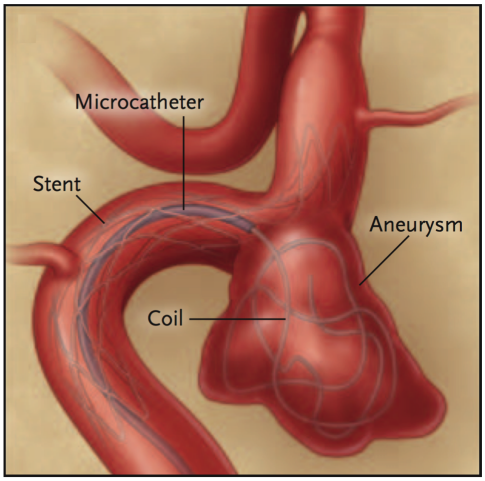

Figure 1.8: *Stent-assisted endovasular coiling of a wide-necked cerebral aneurysm (from Brisman et al. [12])*

A major limitation of conventional endovascular coiling lies in the risk of coil prolapse and subsequent occlusion of the the parent vessel, especially in wide-necked aneurysms. The technique of stent-assisted coiling, illustrated in figure 1.8, uses a high porosity cerebral stent to act as a scaffold within the vessel lumen that prevents coil prolapse. The stent is delivered first by micro catheter in the same manner as the subsequent coils. The aneurysm is then isolated by throm-

bosis, as in conventional coiling, and the stented lumen is reconstructed by re-endothelialisation at the stent struts.

Stent placement can be problematic in complex bifurcation geometries, and occasionally, two stents deployed in a 'Y' configuration may be required. [128] Reports in the literature indicate an increased risk of in-stent thrombosis and emboli transport, especially in complex multi-stent cases, but this risk is small. [65]

1.4.4 Flow-Diverter

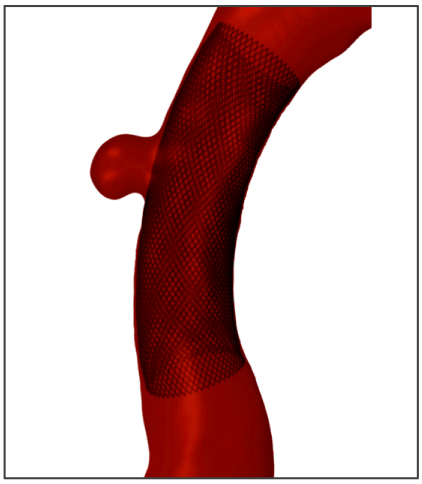

Figure 1.9: *Flow-diverter treatment of a sidewall aneurysm*

Developed from conventional high-porosity stents used for stent-assisted coiling and to remedy arterial stenosis, flow-diverters are low-porosity stents that can be used in isolation to treat a cerebral aneurysm.

Porosity is defined in equation 1.1 below as the fraction of a device mesh that is open and not obscured by struts or wires.

$$Porosity = \frac{Area\ of\ Mesh\ Pores}{Total\ Mesh\ Area} = 1 - \frac{Area\ of\ Device\ Wires}{Total\ Mesh\ Area} \tag{1.1}$$

For regular intracranial stents the value of porosity is around 85-95% and the device functions primarily as a structural scaffold. [134] The lower porosity of a flow-diverter device, typically around 60-70%, gives rise to sufficient resistance to flow that the device alone may be used to

treat an aneurysm. [64]

A flow-diverter is delivered minimally-invasively in the same manner as high porosity stents. Designs of current clinical devices are constructed from interwoven filaments that may be collapsed into the catheter and unsheathed progressively at the site of the aneurysm neck. The device may be fully retrieved with up to 90% of the flow-diverter length deployed. [17] The reduced flow into the aneurysm dome leads to thrombosis. Fully-thrombosed aneurysm domes treated by flow-diverter have been observed to shrink and be slowly reabsorbed over time, thereby reducing any aneurysm mass effect. [104]

Flow-diverters offer a very elegant method of aneurysm treatment with the delicate aneurysm dome left untouched and the device itself eventually being fully endothelialised into the vessel lumen. Additionally, aneurysms of all shapes, sizes and neck-widths may be treated by flow-diverter, as no portion of the device enters into the potentially delicate aneurysm dome. There are mixed results in the literature regarding the use of flow-diverters to treat bifurcation aneurysms and thereby risking the jailing one or more daughter vessels with the low-porosity mesh. [2]

Given that the low porosity of the flow-diverter mesh blocks the aneurysm neck entirely, no other endovascular methods, such as coiling, may be subsequently used if the aneurysm obliteration is not complete by flow-diverter alone. There are examples in the literature of 'telescoping' multiple flow-diverter devices inside one-another to locally reduce the porosity further. In order to mitigate the risk of partial thrombosis, current EU guidelines favour the use of flow-diverters for adjunct coiling where coils are placed into the aneurysm dome in addition to deploying a flow-diverter. This method increases the likelihood of complete thrombosis of the aneurysm dome but, as with conventional coiling, any reduction in mass effect benefits are lost. [17]

Finally, the increased risk of in-stent thrombosis in the low porosity mesh of the flow-diverter requires patients to adhere to a substantial anti-platelet regime both pre- and post-intervention and in some cases, this regime can last up to a year.

1.4.5 Other Treatment Methods

Onyx (Micro Therapeutics Inc., Irvine, CA) is a liquid embolisation agent that when injected into the vasculature precipitates to form a soft, sponge-like semi-solid. Although traditionally used to treat arteriovenous malformations (AVMs), Onyx may be injected into an aneurysm dome to isolate it from the vasculature. Clinical use of Onyx for aneurysm treatment is unusual and often only occurs after other methods have failed. That said, aneurysm occlusion rates with Onyx are similar to those achieved with coils.The procedure is complex and involves inflating and deflating an occlusion balloon multiple times in addition to deploying the agent. [100]

Finally, a true treatment of last resort is parent vessel occlusion, whereby the blood supply to the at risk aneurysm is cut-off entirely. The technique is only used in cases for which all other treatment options have been exhausted, and when there is sufficient collateral blood flow from the remaining vessels in the Circle of Willis for there to be little risk of ischemic damage. [32]

1.5 Commercially Available Flow-Diverter Devices

This study focuses specifically on flow-diverters for aneurysm treatment. Such devices offer an elegant treatment solution as well as great potential for design variation and customisation, which is neglected in current clinically used examples.

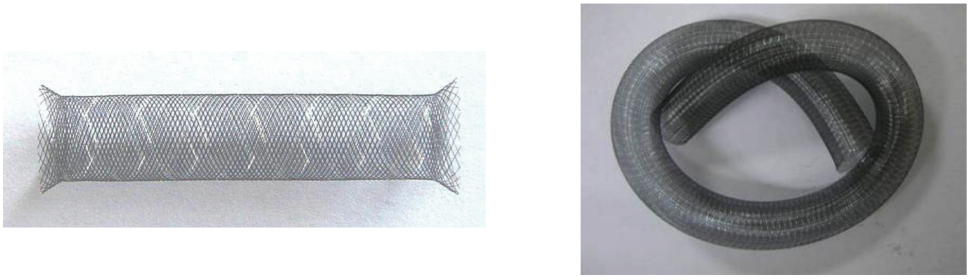

Figure 1.10: *Dominant flow-diverter devices in clinical use: the Silk flow-diverter and Pipeline Embolization Device (Images: Balt Extrusion and EV3 promotional material)*

There are two dominant flow-diverter devices currently (2015) under clinical use: the Silk flow-diverter (SILK; Balt Extrusion, Montmorency, France) and the Pipeline Embolization Device (PED; EV3/Covidien, Irvine, CA). Both devices are of a very similar design and are shown in

figure 1.10. The PED was approved for use by the FDA in 2011, and both the PED and SILK were 'CE' mark approved for use in Europe in 2007. The salient features of the SILK and PED are detailed below.

SILK: Device is braided from 44 Nitinol (Nickel-Titanium alloy) wire strands and 4 platinum marker strands, approximately 35μm diameter. The overall structure is an interwoven tube with flared ends and rhomboid-shaped pores with a typical pore diameter of 110-250μm. The device is manufactured in a range of diameters (2-5.5mm) and lengths (15-40mm.) A deployed device has a porosity varying from 45-65% depending on device deployment configuration. Later versions of the SILK have been introduced, known as the SILK+, which have an increased radial force and are available in tapered diameters.

PED: Also of braided construction with 48 wires all made from platinum-nickel-cobalt alloy making the entire device partially radio-opaque. The woven structure is entirely straight and forms a tube with diameters from 2.5-5.0mm and lengths from 10-35mm. The porosity range of the PED is more narrow, falling between 65-70%, and it has a pore diameter of 140-225μm.

Both devices are deployed via similarly sized micro catheters in slightly different manners: the SILK is deployed by unsheathing, whereas the PED features a rotating 'pusher' delivery wire.

The family of WEB devices (Sequent Medical, Aliso Viejo, CA) are also approved for European use in patients after receiving a CE mark in 2013. The WEB (single-layer mesh) and WEB II (double-layer mesh) are dedicated devices designed to treat bifurcation aneurysms, including wide-necked cases.

The WEB device, shown in figure 1.11, resembles a cylindrical flow-diverter with both open ends crimped closed to create a small mesh ball that may be expanded inside the aneurysm sac. The device is available in diameters between 5 and 11 mm and is constructed from a braided mesh comprising 108 or 144 wires, depending on the device size. For the WEB II device two layers of mesh are employed, one inside the other, resulting in flow resistance from a total of 216 or 288 wires. The largest mesh pore diameters observed are in the range of 100-180μm, depending on device size. [113] The device has a variable porosity across the face intended to fill the aneurysm neck due to the gathering of the woven mesh at the device centre. Consequently, the device's

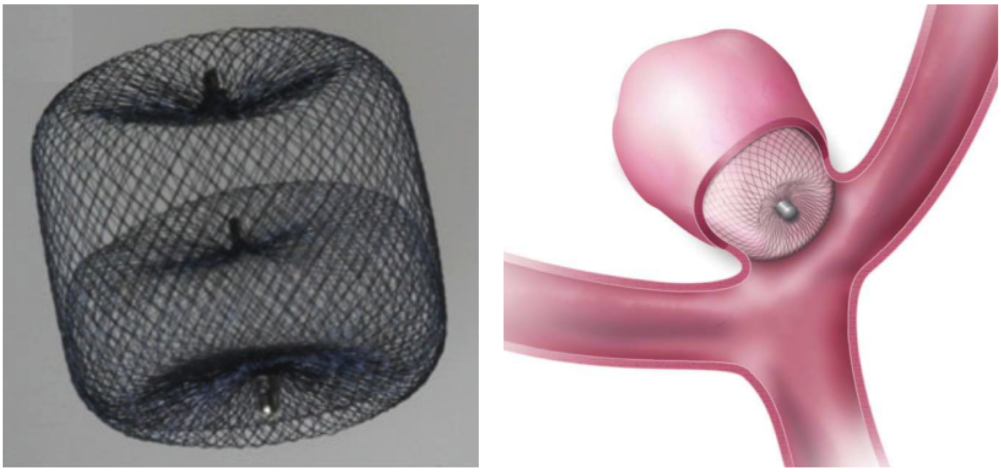

Figure 1.11: *WEB II device (Image: Pierot et al. [113])*

porosity varies from 0% at the device centre to 78% at the edges. [74]

There are a number of other woven flow-diverter device concepts in various stages of development, known to the author at the time of writing, which are summarised below.

The Surpass flow-diverter (SURPASS; Stryker Neurovascular, Fremont, CA) was 'CE' mark approved in Europe in 2011 and is currently undergoing clinical trials. The device is similar in size to both the SILK and PED but features a variable number of wire strands, from 48 to 96, ensuring approximately constant pore size over the rage of device diameters.

The Flow Re-Direction Endoluminal Device (FRED; MicroVention, Tustin, CA) received a CE mark for European use in 2013 and is also currently undergoing trials. The FRED design features highly flared ends for security and a dual-layer woven mesh with a low-porosity 48-strand inner device and a high porosity 16-strand outer device, resembling a flow-diverter deployed in a conventional stent. [116]

The Tubridge Revascularization Device (TUBRIDGE; MicroPort Neurotech, Shanghai, China) is also undergoing trials in China. The device is similar in size to the SILK and PED with flared ends and between 46 and 62 strands, resulting in a porosity of 65-70%. [163]

Finally, the Luna Aneurysm Embolization System (LUNA AES; NFocus Neuromedical, Palo Alto, CA) is an ovoid braided device designed to be deployed inside an aneurysm dome, in a similar fashion to the WEB family of devices. The device is formed from a double-layer of woven

Nitinol mesh encapsulated at the proximal and distal ends of the device by platinum markers. To date, the device has been trialled in animal models [80] and a small cohort of patients [114], which reported an aneurysm occlusion rate of 50% at 6-months follow-up and no parent vessel stenosis.

1.6 Thrombosis and Hemodynamic Factors

The goal of flow-diverter intervention is to promote the growth of stable thrombus within the aneurysm dome and thereby reducing the risk of rupture. The biochemical pathway to initiation, growth and stabilisation of thrombus is a highly complex process that is beyond the scope of this work. Comprehensive review and discussion of such processes can be found in the work of Furie and Furie. [51] [52]

This study focusses on the hemodynamic conditions linked to the magnitude and quality of thrombus formation after flow-diverter deployment. In the clinical setting, the effectiveness of a flow-diverter is initially assessed immediately after deployment by observing the reduction in angiographic contrast infiltrating the aneurysm dome. Follow-up MRI imaging at a later date (typically 3-12 months) is then used to assess the degree of aneurysm obliteration.

Although thrombosis following coiling is almost instantaneous, the lack of any obstruction within the aneurysm dome following flow-diverter treatment renders thrombosis slower and more incremental, often taking weeks or months to reach full occlusion. Rates of occlusion *in-vivo* vary significantly, often due to variation in administered anti-platelet regime, with complete occlusion after 3-6 months being common in 49-95% of cases. [112] [17]

1.6.1 Complete and Partial Occlusion

Aneurysm thrombosis is widely accepted to be a safe and effective means of isolating an at-risk aneurysm from the vasculature. However, incomplete thrombosis has frequently been linked to aneurysm recurrence and *increased* rupture risk. [16] Incomplete occlusion has been attributed to the hemodynamic environment within the aneurysm dome with chaotic flow-patterns linked to increased rupture risk. [21] Partial occlusion is also observed in large and giant aneurysm

geometries and in cases with high aspect ratio; in these cases, localised regions of sluggish flow adjacent to higher speed flow lead to isolated areas of thrombus formation. [77] These flow conditions can prevail after flow-diverter treatment and contribute to the increased rate of delayed rupture in large aneurysms. [17] Aneurysm rupture following flow-diverter treatment in giant aneurysms has been shown in the literature to be especially catastrophic, with a fatality rate of up to 80%. [42]

1.6.2 Aneurysm Inflow and Turnover Time

Increasing the degree of stasis in the aneurysm dome has been widely documented as promoting thrombus initiation and growth. [13] Many authors have linked a reduction in either aneurysm inflow or mean aneurysm sac velocity to stable thrombus formation. [50] [69] [84] Increases in turnover time before and after FD placement (turnover time = aneurysm sac volume/inflow rate) have also been linked to thrombus formation. Unlike pure inflow, turnover time also allows for comparisons between aneurysms with different sac geometries. [64]

1.6.3 Flow Residence Time

A more sophisticated measure of propensity towards thrombus formation is the residence time of flow within an aneurysm dome. While turnover time is calculated from bulk velocity and represents the average time blood remains in the aneurysm sac, residence time varies throughout the aneurysm sac. Residence time may be calculated for specific aneurysm regions, thus highlighting areas of local recirculation that would promote thrombus formation.

Sadasivan et al. [132] modelled aneurysm inflow in the two distinct components of diffusion and convection. Under this regime, decay time constants representing the range of residence times within the aneurysm may be calculated, which gave a 'virtual contrast' capability to the CFD simulations, allowing direct comparison of simulated results with patient angiograms. A later study conducted in rabbits confirmed the link between increase in contrast residence time and greater thrombus formation within the aneurysm dome. [131] Contours of residence time were also investigated by Butty et al. [15], where some regions of a simulated aneurysm exhibited a flow residence time around 5x longer than the corresponding turnover time.

1.6.4 Velocity and Flow Jetting

Flow jetting and areas of high flow-impingement have been correlated with increased risk of rupture and incomplete aneurysm thrombosis. In a large CFD study of 62 aneurysms, Cebral et al. [21] showed that geometries with a concentrated jet and a small impingement zone were over 6x more likely to rupture than cases with a diffuse inflow jet. Castro et al. [19] confirmed a similar pattern in a smaller study of 40 terminal aneurysm cases. A strong correlation between persistent aneurysm jets and partial thrombosis leading to delayed aneurysm rupture was observed clinically by Kulcsar et al. following flow-diverter deployment in 11 aneurysms. [77] High aneurysm aspect ratio has been widely correlated with aneurysm rupture and is often attributed to the concentrated flow jetting seen in geometries with a large AR. [135]

1.6.5 Wall Shear Stress

Wall shear stress (WSS) is the shear force acting at a direction tangential to the fluid boundary, which results from localised velocity deceleration at the vessel wall. WSS for a Newtonian fluid is defined in equation 1.2. As discussed previously in section 1.2, the influence of WSS on the vessel wall is a complex phenomenon with both physical and biochemical interactions.

$$WSS = \mu \left(\frac{\partial u}{\partial y} \right)_{vessel\ wall\ (y=0)} \tag{1.2}$$

where μ = dynamic viscosity, u is the velocity parallel to the vessel wall and y is the distance from the wall.

As WSS arises from the velocity gradient at the vessel wall, the value of WSS is highly dependent upon cross-sectional velocity; flow pulsatility, geometry curvature, and changes in lumen cross-sectional shape and area can all dramatically alter localised WSS values. For Poisseulle flow in a straight vessel, the WSS magnitude is uniform and scales linearly with flow rate, as described in equation 1.3.

Normal physiological values of WSS magnitude in the cerebral vasculature fall in the 2-5 Pa range. Large deviations from these values within the aneurysm dome are thought to alter the aneurysm wall integrity and increase the risk of rupture. [92] Specifically, outside of this

normal range, WSS has been linked to changes in vessel neointima thickness [76], and with very high (>≈40Pa) or very low (<≈1.0Pa) values of WSS linked to activation of endothelial cell apoptosis. [136] [49]

$$|WSS|_{straight\ pipe} = \frac{32\mu Q}{\pi d^3} \tag{1.3}$$

where Q is flow rate (m^3s^{-1}) and d (m) is vessel diameter. For conditions typical of mean flow in the ICA (230ml/min, 4mm diameter), equation 1.3 yields a WSS magnitude of 2.44Pa.

WSS is linked to endogenous inhibitors of platelet aggregation such as Prostacyclin (PGI_2) and Nitrous Oxide (NO). A high WSS is linked to NO release while both a high and pulsatile WSS distribution promotes Prostacyclin production. [125] Within the literature there are two schools of thought linking aneurysm rupture and wall shear stress: high-WSS and low-WSS induced rupture. [135] [95]

Proponents of high-WSS induced rupture link raised WSS with endothelial damage that initiates wall remodelling. The mechanism of failure involves the release of NO, initiated by the elevated WSS, which then lowers the arterial wall tone. The imbalance between blood pressure and vessel wall stiffness then leads to a ballooning of the weakened vessel. [103]

Low-WSS induced rupture theory cites the dysfunction of flow induced NO, caused by the flow stagnation inside the aneurysm sac, leading to intimal damage via platelet aggregation. This damage then allows the local infiltration of white blood cells and fibra into the endothelial surface. Inflammation follows leading to degeneration of the vessel wall encouraging the stretching and thinning of the surface and allowing the aneurysm sac to enlarge. [54]

Evidence to support both theories is widespread. Pathological examination confirms the white blood cell infiltration suggested by the low-WSS theory. [31] The location of the majority of aneurysm rupture, which is commonly in the main body of the aneurysm sac where WSS most often falls to its lowest value, also supports a low-WSS rupture mechanism. [143] Conversely, a key piece of evidence supporting the elevated WSS hypothesis is the high proportion of aneurysms located at vessel bifurcations where flow separation causes elevated WSS and high rates of aneurysm growth. [135]

The link between WSS and thrombus formation is less controversial. The partial thrombosis of giant aneurysms in areas of low shear gave rise to a number of thrombus formation models based on a WSS threshold. [51] [52] [107] [109] These models assume thrombus forms below a strain rate threshold of $100s^{-1}$ (corresponding to a WSS magnitude around 0.4Pa) and does not form above this threshold. Although the predictions of such a model are unverified, the thrombus initiation and growth predicted in different aneurysm sizes is consistent with generalised clinical observations. [107] [109] Hence, it is assumed that, independent of any factors related to rupture risk, low WSS within the aneurysm dome promotes thrombus formation.

Other metrics that are related to variation in WSS magnitude and direction, such as WSS Gradient (WSSG), Oscillatory Shear Index (OSI), and Gradient Oscillatory Number (GON) have also been linked to aneurysm growth and rupture risk in the literature. However, the mechanisms underpinning such hypotheses are often more opaque and poorly verified than those associated with WSS magnitude alone. [69] [27]

Chapter 2

Numerical Methods

In this chapter the concept of computational fluid dynamics in the field of biofluidics is introduced in section 2.1, with a brief discussion of the numerical basis for the Finite Volume Method; geometry discretisation and mesh generation are discussed in section 2.3; both flow regime and boundary condition choice are considered in section 2.5 and section 2.6; finally, device deployment by finite element simulation and simplified algorithms are discussed in section 2.7.

2.1 Computational Fluid Dynamics and the Finite Volume Method

The birth of computational fluid dynamics (CFD) in the 1930s focussed on the highly-specific problem of 2D aerofoil design. [98] The rapid development of computational hardware in the 1960s and 1970s soon lead to the integration of CFD methods into many diverse research fields. [98] From its inception, biomedical engineering, and specifically biofluidics, have naturally adopted CFD techniques due to the complex and highly non-linear nature of the physical characteristics governing physiology. All CFD codes exclusively address the solution to some variant of the Navier-Stokes equations, with few exceptions. The CFD methodology is divided into three distinct components, which are detailed below.

Pre-processor: The flow geometry is defined and discretised into sub-domains, all fluid and any other physical properties must be defined or approximated, and appropriate boundary conditions applied.

Solver: The governing equations of flow are discretised and simplified by the substitution of localised approximations to flow variables. The resulting system of equations is solved iteratively by reducing the error resulting from the approximate solution, which only partially satisfyies the governing equations.

Post-processor: Solver-generated data is output and visualised with scalar surface plots, particle tracking, vector plots, etc. as well as raw alphanumeric output.

This chapter focuses on each of these three elements in the context of the Finite Volume Method, the formulation that underpins the majority of commercially available CFD codes.

2.1.1 The Navier-Stokes Equations

The Navier-Stokes equations may be cast by considering conservation of momentum in a fluid, supplemented by mass continuity. First, a finite fluid volume in cartesian space is defined, as shown in figure 2.1.

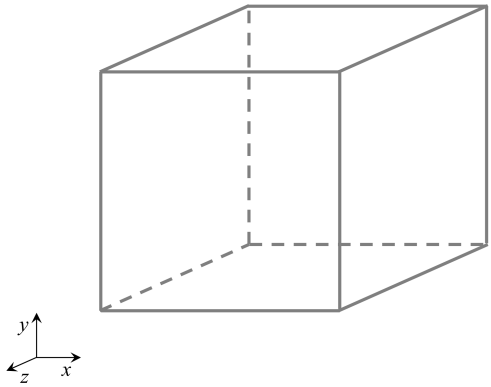

Figure 2.1: *A generalised fluid control volume, CV*

The mass continuity equation for the fluid volume is detailed in equation 2.1 whereby the increase in mass of the volume is equal to the net mass flow into that volume.

$$\frac{\partial \rho}{\partial t} + \bigtriangledown \cdot (\rho \mathbf{u}) = 0 \tag{2.1}$$

where ρ =density, t=time and $\mathbf{u}$=velocity.

For an incompressible fluid equation 2.1 reduces to equation 2.2.

$$\bigtriangledown \cdot (\mathbf{u}) = 0 \tag{2.2}$$

Newton's second law considered over the finite volume states that the change in momentum on the fluid volume is equal to the sum of forces acting on the volume.

$$\rho \left(\frac{\partial \mathbf{u}}{\partial t} + \mathbf{u} \cdot \bigtriangledown \mathbf{u} \right) = - \bigtriangledown p + \bigtriangledown \cdot \overline{\mathbf{T}} + \mathbf{S} \tag{2.3}$$

where $\mathbf{u}$ = velocity field, p = pressure, ρ = density, $\overline{\mathbf{T}}$ = stress tensor, and $\mathbf{S}$ is the momentum source term.

Equation 2.3 must be supplemented by an equation of state to link deformation and stress in a given fluid element. As discussed in section 1.2, blood is considered to behave as a Newtonian fluid under the flow conditions considered in this study. As such, the viscous stress in the fluid can be considered linearly proportional to the local strain rate i.e. the viscosity does not depend on the stress state or the velocity of the fluid. Hence, assuming an isotropic Newtonian fluid, the stress tensor term of equation 2.3 can be simplified as indicated in equation 2.4.

$$\bigtriangledown \cdot \overline{\mathbf{T}} = \mu \bigtriangledown^2 \mathbf{u} \tag{2.4}$$

where $\mathbf{u}$ = velocity field, $\overline{\mathbf{T}}$ = stress tensor, and μ = dynamic viscosity.

The conservation of momentum equation may be cast in a cartesian coordinate system for an isotropic Newtonian fluid and is indicated for the x, y, and z directions in equations 2.5, 2.6, and 2.7.

$$\frac{\partial (\rho u)}{\partial t} + \bigtriangledown \cdot (\rho u \mathbf{u}) = -\frac{\partial p}{\partial x} + \bigtriangledown \cdot (\mu \bigtriangledown u \ ) + S_{Mx} \tag{2.5}$$

$$\frac{\partial (\rho v)}{\partial t} + \bigtriangledown \cdot (\rho v \mathbf{u}) = -\frac{\partial p}{\partial y} + \bigtriangledown \cdot (\mu \bigtriangledown v \ ) + S_{My} \tag{2.6}$$

$$\frac{\partial (\rho w)}{\partial t} + \bigtriangledown \cdot (\rho w \mathbf{u}) = -\frac{\partial p}{\partial z} + \bigtriangledown \cdot (\mu \bigtriangledown w \ ) + S_{Mz} \tag{2.7}$$

where u, v, and w are the velocity components of $\mathbf{u}$ in the x, y, and z directions respectively,

p = pressure, ρ = density, μ = dynamic viscosity, and S is the momentum source term in the respective x, y, and z directions.

These momentum equations, known generally as the Navier Stokes Equations, combined with equation 2.2 govern incompressible, isotropic, Newtonian, unsteady fluid flow in three dimensions. Although the set of equations is of closed-form, analytical solutions are only achievable for highly simplified flow conditions. A general solution, and even proof of such a solution, is elusive. In order to solve the Navier-Stokes equations for a non-trivial problem, it is necessary to approximate the solution over discretised volumes and solve the approximated governing equations iteratively.

2.1.2 The Scalar Transport Equation and Finite Volume Method

By introducing a general variable, ϕ, the generalised form of the fluid flow equations, including the equations governing scalar quantities such as temperature, may be cast in the form of equation 2.8—known as the scalar transport equation.

$$\frac{\partial (\rho\phi)}{\partial t} + \bigtriangledown \cdot (\rho\phi\mathbf{u}) = \bigtriangledown \cdot (\Gamma_\phi \bigtriangledown \phi\ ) + S_\phi \tag{2.8}$$

where ϕ = generic scalar quantity, Γ_ϕ = the scalar-specific diffusion coefficient and S_ϕ = any scalar source terms.

Thus, the three dimensional momentum equations may be represented in equation 2.8 by setting ϕ equal to one of the cartesian components of the velocity field (u, v or w) and setting Γ equal to the dynamic viscosity. Also, by setting ϕ equal to 1, equation 2.8 yields the continuity equation. The general form of equation 2.8 then forms the basis of computationally solving all equations of fluid flow using the Finite Volume Method.

Many other numerical techniques are available to solve the Navier-Stokes equations, including Finite Difference, Finite Element and Particle Methods, but Finite Volume Methods are dominant in commercial CFD packages owing to general robustness over a large range of Reynolds number, low memory usage and fast solution speed.

In the Finite Volume Method, equation 2.8 is integrated over the generic control volume, CV,

illustrated in figure 2.1 to form equation 2.9:

$$\int_{CV} \frac{\partial (\rho\phi)}{\partial t}\ dV + \int_{CV} \bigtriangledown \cdot (\rho\phi \mathbf{u})\ dV = \int_{CV} \bigtriangledown \cdot (\Gamma_\phi \bigtriangledown \phi\ )\ dV + \int_{CV} S_\phi\ dV \tag{2.9}$$

which, after applying Gauss' divergence theorem to the diffusive and the convective terms of equation 2.9, yields equation 2.10

$$\frac{\partial}{\partial t}\left(\int_{CV} \rho\phi\ dV\right) + \int_A \mathbf{n} \cdot (\rho\phi \mathbf{u})\ dA = \int_A \mathbf{n} \cdot (\Gamma_\phi \bigtriangledown \phi\ )\ dA + \int_{CV} S_\phi\ dV \tag{2.10}$$

where A is the area of the control volume face, and $\mathbf{n}$ is the corresponding normal vector of the face.

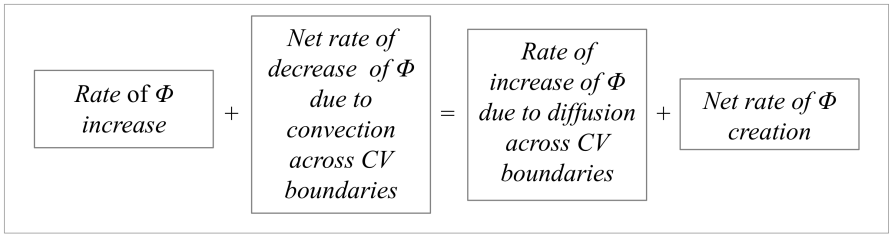

Figure 2.2: *The physical relationship expressed in equation 2.10*

In steady state equation 2.10 reduces to equation 2.11:

$$\int_A \mathbf{n} \cdot (\rho\phi \mathbf{u})\ dA = \int_A \mathbf{n} \cdot (\Gamma_\phi \bigtriangledown \phi\ )\ dA + \int_{CV} S_\phi\ dV \tag{2.11}$$

And, for time-varying problems over the interval Δt, equation 2.10 yields equation 2.12, the most generalised form of the governing equation:

$$\int_{\Delta t} \frac{\partial}{\partial t}\left(\int_{CV} \rho\phi\ dV\right)\ dt + \int_{\Delta t}\int_A \mathbf{n} \cdot (\rho\phi \mathbf{u})\ dA\ dt = \int_{\Delta t}\int_A \mathbf{n} \cdot (\Gamma_\phi \bigtriangledown \phi\ )\ dA\ dt + \int_{\Delta t}\int_{CV} S_\phi\ dV\ dt \tag{2.12}$$

2.2 Strategies for Solving the Discretised Equations

Integration of equation 2.12 over the control volume CV yields a discretised equation at the volume centre, C in figure 2.3.

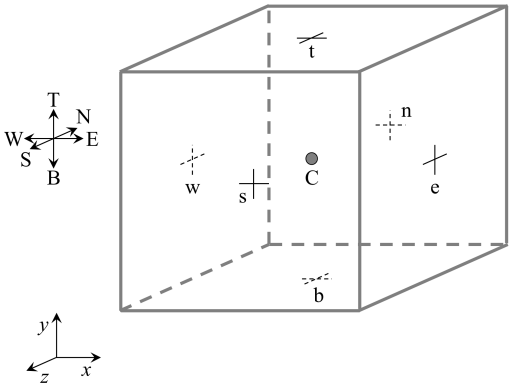

Figure 2.3: *The control volume, CV, indicated with north(n), south(s), east(e), west(w), top(t) and bottom(b) faces and corresponding neighbouring cell centres N, S, E, W, T and B in the directions indicated. (Figure adapted from: Versteeg and Malalasekera [154])*

The generalised solution method to the corresponding discretised equation is to address the discretisation of each term of the equation separately, before coupling pressure and velocity terms and iteratively solving the system of equations.

2.2.1 The Diffusion Term

The diffusion term of equation 2.12 can be discretised as shown in equation 2.13:

$$\int_A \mathbf{n} \cdot (\Gamma_\phi \bigtriangledown \phi \ ) \ dA = \left[\left(\Gamma A \frac{\partial \phi}{\partial x} \right)_e - \left(\Gamma A \frac{\partial \phi}{\partial x} \right)_w \right] + \left[\left(\Gamma A \frac{\partial \phi}{\partial y} \right)_s - \left(\Gamma A \frac{\partial \phi}{\partial y} \right)_n \right] + \left[\left(\Gamma A \frac{\partial \phi}{\partial z} \right)_t - \left(\Gamma A \frac{\partial \phi}{\partial z} \right)_b \right] \tag{2.13}$$

where A is the area of a given face, k, and $\left(\frac{\partial \phi}{\partial j}\right)_k$ is the gradient of ϕ in the j direction evaluated at face k.

Assuming a central difference method the gradient of ϕ in the j-direction at the k face may then

be linearly approximated with equation 2.14 with respect to the volume centre point, C, and the centre point of the adjacent cell, K:

$$\left(\frac{\partial \phi}{\partial j}\right)_k = \frac{(\phi_K - \phi_C)}{\delta j_{CK}} \tag{2.14}$$

where ϕ_K is the value of ϕ at the centre of the adjacent volume and δj_{CK} is the distance between the two volumes centres in the j direction.

Applying the central difference method to each term of equation 2.13 then yields equation 2.15.

$$\begin{aligned}\int_A \mathbf{n} \cdot (\Gamma_\phi \bigtriangledown \phi\ )\ dA = &\left[\Gamma_e A_e \frac{(\phi_E - \phi_C)}{\delta x_{CE}} - \Gamma_w A_w \frac{(\phi_C - \phi_W)}{\delta x_{WC}}\right] \\ + &\left[\Gamma_s A_s \frac{(\phi_S - \phi_C)}{\delta y_{CS}} - \Gamma_n A_n \frac{(\phi_C - \phi_N)}{\delta y_{NC}}\right] + \left[\Gamma_t A_t \frac{(\phi_T - \phi_C)}{\delta z_{CT}} - \Gamma_b A_b \frac{(\phi_C - \phi_B)}{\delta y_{BC}}\right]\end{aligned} \tag{2.15}$$

2.2.2 The Convection Term

The convection term of equation 2.12 is discretised as shown in equation 2.16:

$$\int_A \mathbf{n} \cdot (\rho \phi \mathbf{u})\, dA = \sum_{k=1}^{N} (\rho_k \phi_k u_k^n)\, A_k = \sum_{k=1}^{N} \dot{m}_k \phi_k \tag{2.16}$$

where N is the number of faces in the control volume CV, u_k^n is the velocity component normal to a given face k, and $\dot{m}_k$ is the mass flux through the face.

A number of different schemes are available to solve the discretised convection equations. [156] However, either the central difference or upwind schemes (or a combination of both schemes) are the dominant methods employed in most commercial finite volume codes.

The central difference scheme is employed in a similar manner to the treatment of the diffusive term; the value of ϕ at a face is approximated as the weighted average of the value of ϕ at the two cell centres, as shown in equation 2.17.

The central difference scheme is second order accurate but suffers from a lack of transportiveness and is consequently unstable at high flow velocities or coarse grid resolutions.

$$\phi_k = \gamma_k \phi_C + (1 - \gamma_k)\, \phi_K \tag{2.17}$$

where γ_k is a linear weighting factor incorporating the relative position of face k between the two cell centres K and C.

The upwind differencing scheme incorporates the flow direction through the control volume when approximating the value of ϕ at a cell face. The value of ϕ at the centre of the volume is thus propagated to the upwind face of the volume as described in equation 2.18:

$$\phi_k = \begin{cases} \phi_C \ when \ u_k^n < 0 \\ \phi_K \ when \ u_k^n > 0 \end{cases} \tag{2.18}$$

Accounting for flow direction in the upwind scheme makes the method more attractive for higher flow speeds than the central difference method. However, the accuracy of the upwind scheme is only first order. Additionally, given that the propagation term in the scheme is dependent upon the coordinate system, the upwind scheme produces erroneous results, known as false diffusion, when the flow direction is not well aligned with the mesh.

A combination of both schemes, known as the Hybrid scheme, is often used in commercial CFD code and is shown in equation 2.19. Such a scheme then incorporates the accuracy and multi-directional flow robustness of the central difference scheme with the stability and high-speed flow robustness of the upwind method.

$$\phi_k = \beta \phi_k^{Upwind} + (1 - \beta)\, \phi_k^{CentralDifference} \tag{2.19}$$

where β is a weighting factor with $\beta = 1$ corresponding to a pure upwind scheme and $\beta = 0$ corresponding to a pure central difference scheme.

In this study the value of β is set to 0.01 to maximise the accuracy of the central difference method for the multidirectional flow of the aneurysm dome, and to eliminate the false diffusion that would be seen in the Upwind method. The upwind component of the scheme is only utilised for mesh regions with high Péclet number, where the large ratio of advective to diffusive fluid transport would lead to numerical instability and slow simulation convergence for the central

difference scheme.

2.2.3 The Temporal Term

Many methods may be used to discretise the governing equations in time. A generic partial differential equation is shown in equation 2.20 for ϕ, which varies in time and one dimensional space. The variable ϕ is discretised in time and space as detailed in equation 2.21.

$$\frac{\partial \phi}{\partial t} = F\left(\phi, x, t, \frac{\partial \phi}{\partial x}, \frac{\partial^2 \phi}{\partial x^2}\right) \tag{2.20}$$

$$\phi\left(x,t\right) = \phi_i^n = \phi\left(i\Delta x, n\Delta t\right) \tag{2.21}$$

Hence, the generalised time-marching scheme for ϕ, from t to $t + \Delta t$ is given in equation 2.22, and may be fully implicit, fully explicit or a combination of the two.

$$\frac{\phi_i^{n+1} - \phi_i^n}{\Delta t} = \epsilon F_i^{n+1} + \left(1 - \epsilon\right) F_i^n \tag{2.22}$$

where i is the node under consideration and ϵ is the weight such that $\epsilon = 0$ results in a fully explicit scheme and $\epsilon = 1$ results in a fully implicit scheme.

Most CFD applications are dominated by either the Euler or Crank-Nicholson methods. The Forward Euler method ($\epsilon = 0$) is first order accurate and fully explicit, but only conditionally stable, while the Backward Euler method ($\epsilon = 1$) is first order accurate and fully implicit, rendering the scheme unconditionally stable. The Crank-Nicholson scheme ($\epsilon = 0.5$) is second order accurate and unconditionally stable.

In this study the Crank-Nicholson scheme is used exclusively for time-marching in transient flow problems due to the scheme's second-order accuracy.

2.2.4 Pressure-Velocity Coupling and Iterative Methods

The discretisation and solution methods discussed previously all assume a known local velocity distribution within the fluid domain, a condition which is not true in all practical implementations of the method. Additionally, the pressure gradient forms the most significant momentum source, S_M in equations 2.5, 2.6 and 2.7, in most engineering flows but there is no equation to directly obtain the pressure gradient.

Instead, the pressure distribution must be solved for using pressure-velocity coupling or pressure correction. The generalised pressure correction methodology is detailed in figure 2.4. First, a pressure field is guessed, which is used to solve for the velocity field. This velocity field satisfies the momentum equations but not the continuity equation. A pressure correction term is then calculated from the linearised continuity equation. The velocity and pressure fields are then iteratively updated until the simulation convergence criteria is reached.

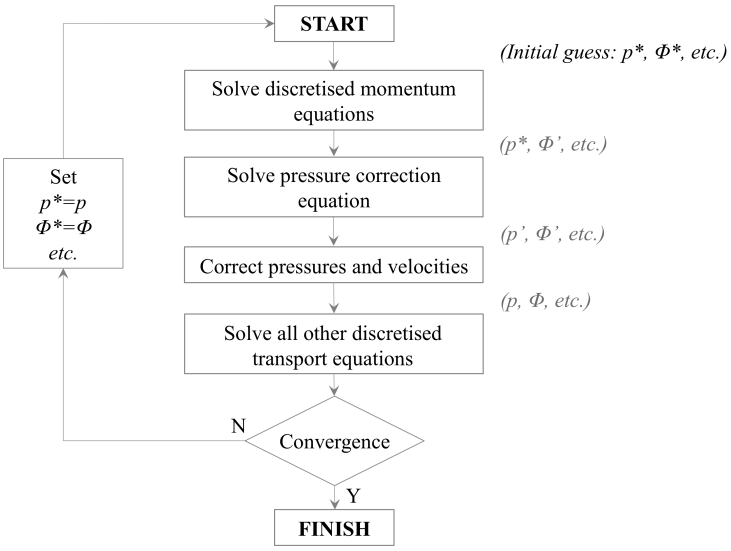

Figure 2.4: *Generalised pressure correction algorithm methodology*

A number of pressure correction algorithms are implemented in commercial CFD code including variants of the SIMPLE (Semi-Implicit Method for Pressure-Linked Equations) and PISO (Pressure Implicit with Splitting of Operators) schemes. [46] [108] [154]

In this study a SIMPLEC (SIMPLE-Consistent) pressure correction scheme is used. [41] [105] The SIMPLEC scheme is very similar to the schematic of figure 2.4 but with an additional initial step whereby pseudo-velocities are calculated prior to calculating a pressure-correction

term, which is then used to solve the momentum equations.

Finally, solution convergence is accelerated in this study with the use of an algebraic multi grid method (AMG). The speed of convergence is increased by interpolating a solution between meshes of varying fineness. Initially a number of solution iterations are made on the full resolution fine mesh, the resulting residuals are then imposed on a more coarse grid and getting progressively coarser until the most coarse grid is reached. The coarse grid solution is then reimposed onto the finest grid and the process repeated. The technique allows for the reduction of errors across many wavelengths and scales simultaneously, which significantly increases the speed of convergence for the grid. The coarse grids are defined algebraically by a system matrix and are not defined by the geometry of the original mesh. [46] [158]

2.3 Meshing and Mesh Independence

The dicretised equations discussed in the previous section are formulated to be solved over a mesh of finite volumes. Such a mesh may be propagated through the simulation geometry in either a structured or unstructured fashion.

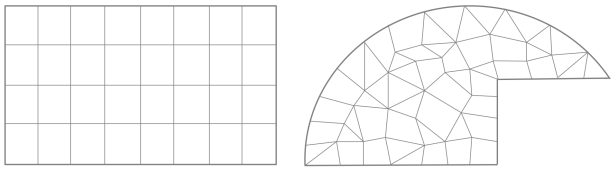

Figure 2.5: *Idealised meshing schemes: (a) structured and (b) unstructured*

2.3.1 Structured Meshes

The elements of a structured grid have regular connectivity, and each node of the mesh has a unique index value with physically adjacent nodes indexed sequentially, making the grid very memory efficient. An idealised structured mesh is shown in figure 2.5. Structured meshes have the advantage of substantially increased computational efficiency but are not suitable for complex geometries with large variation in boundary curvature, such as human vasculature.

2.3.2 Unstructured Meshes

Conversely, the elements in an unstructured grid are categorised by their irregular connectivity. Consequently the unstructured grid is significantly less memory efficient as neighbouring cell relationships must be stored explicitly. An unstructured mesh is also shown in figure 2.5. A major advantage of unstructured meshes is the ease with which the mesh may be fitted to complex geometries and easily refined in areas of complex flow behaviour.

2.3.3 Mesh Quality and Refinement

The accuracy of a discretised solution is dependent on both the method of approximating the variation between the centre points of discrete volumes (as discussed in section 2.2) and the distance between the centre points. For large volumes the assumption of linear variation between cell centres breaks down, and the resulting discrete approximation becomes unrealistic and often unstable. Thus, in regions of complex flow it is vital to ensure a grid with sufficiently high-resolution to accurately approximate local gradients as piece-wise linear. Mesh quality is also important for ensuring solution accuracy; the discrete volume geometries must be regulated to minimise distorted and skewed cells, which introduce errors from assumptions of consistency across the cell face.

Studies in the literature [21] [4] show the importance of adaptive meshing techniques for creating high quality grids that are also memory-efficient. Valen-Sendstad et al. [147] detailed a discussion of mesh resolution typical for CFD simulations of human vasculature and the resulting impact of solution accuracy. Although such discussion is general, it is noted that within the literature an average element size for accurately converged meshes is in the range of 2000-5000 cells/mm^3 for arterial flow within the cerebral circulation.

In this study the presence of highly irregular surfaces, complex vessel bifurcations, and the embedding of very small diameter device structures within the mesh require the use of unstructured meshes exclusively. All grids are meshed in three dimensions in a projected single domain and an Omnitree cartesian tree type with three cartesian layers for high fidelity boundary layer resolution. Mesh independence studies are performed for each specific analysis case, and mesh independence is confirmed at mesh densities around 4000 cells/mm^3 in all cases.

2.4 Comparison to Other Studies in the Field

Across CFD studies in the literature that focus on aneurysm haemodynamics, it is difficult to compare solution strategies and solver settings, as such details are rarely fully reported by authors. [147] In light of both this discrepancy and the growing controversy regarding the accuracy of some published simulations, [152] a number of standardisation and parameterisation tests have been conducted and reported in order to compare the results of different research groups in the field. These specific studies are summarised below as an illustration of the current 'state of the art' and serve as a benchmark for this study.

Radaelli et al. 2008 [119] (2007 Virtual Intracranial Stenting Challenge) A summary of six separate submissions to the challenge with both stented and unstented models simulated. Mesh resolution of ≈500 cells/mm^3 with additional grid refinement at the location of stent struts. No details of solver setting are given but the majority of submissions utilised commercial CFD codes, for which default settings are typically first-order schemes in space and time.

Cito et al. 2014 [28] (2011 Virtual Intracranial Stenting Challenge) Summary of six separate submissions covering both stented and unstented models. Typical mesh resolution of ≈600 cells/mm^3 for unstented models with local mesh refinement to ≈8000 cells/mm^3 in the stented cases. No solver settings are given but the majority of submissions utilised commercial CFD codes.

Steinman et al. 2013 [141] (2012 ASME CFD Challenge) Study reporting 27 separate submissions of unstented aneurysm models only. Average mesh resolution of ≈350 cells/mm^3 (interquartile range: 2-2000 cells/mm^3). No solver settings are listed but the majority of submissions utilised commercial CFD codes.

Janiga et al. 2015 [63] (2013 CFD Rupture Challenge) Summary of 26 separate submissions covering unstented models only. Median reported simulation mesh size was 2.1 million elements (283,000-18,000,000 range). No solver settings are given but the majority of submissions appear to have utilised the defaults of commercial CFD codes.

Finally, Valen-Sendstad et al. [147] reported a study simulating flow in 12 aneurysms, which was completed with both 'Normal' and 'High' resolution setups. The 'Normal Resolution' solution

utilised a mesh resolution and solver parameters typical of those reported in the literature (first-order spatial and temporal (fully implicit) solvers, and a mesh density of ≈1500 cells/mm^3). 'High Resolution' simulations were conducted with a setup considered approximately an order of magnitude finer than the 'Normal' case (second-order discretisation in space and time with a mesh density of ≈10,000 cells/mm^3). The study concluded that while the resolution of most computations reported in the literature is adequate to predict the rupture risk of untreated aneurysms, such studies may not adequately capture complex indices linked to biochemical stimuli.

In summary, the setup of the simulations conducted in this study, and the criteria for mesh-independence, meets or exceeds the resolution of most current 'state of the art' computations.

2.5 Flow Regime and Features

Blood flow within human cerebral arteries is generally accepted to be laminar, given a typical Reynolds number (2.23) well below the transitional case for steady pipeflow. [50] [73] [160] However, flow pulsatility and vessel curvature, especially at bifurcations, may reduce the stability of the flow and lower the effective transitional Reynolds number. [127]

$$Re = \frac{\rho u l}{\mu} \tag{2.23}$$

where Re is the Reynolds number, ρ = density, u = velocity, l =length scale (pipe diameter) and μ = dynamic viscosity.

The pulsatility effects of blood flow were extensively studied by Womersley, who showed that pulsatile pipe flow adopts an increasingly non-parabolic flow profile with increasing flow frequency. [56] [161] The tendency for flow to depart from the steady-state profile and adopt a plug profile increases with the Womersley number, defined in equation 2.24.

This effect is small at a Womersley number typical of the small blood vessels supplying the brain (where typically $\alpha < 5$). Flow profiles for the ICA and similar sized vessels have been validated with 3D Doppler measurements and show little departure from a parabolic flow dis-

tribution. [117] [71] Hence, most studies in the literature model the inlet of a vessel geometry as a parabolic velocity profile consistent with steady, pressure-driven flow in a pipe (Poiseuille flow). Consequently, all vessel inlet velocity boundary conditions in this study are chosen to be parabolic.

$$\alpha = \frac{l}{2}\sqrt{\frac{\omega\rho}{\mu}} \tag{2.24}$$

where α is the Womerlsey number, l =length scale (pipe diameter) ρ = density, ω =flow oscillation angular frequency ($\omega = 2\pi/T$) and μ = dynamic viscosity.

Although the velocity profile of either steady or oscillating flow in a straight tube may be radially symmetric, curved tubes introduce vorticity into the cross-sectional plane of the flow. Such behaviour was first observed by Dean [38] [37] and may be quantified by the Dean number (equation 2.25).

$$De = \sqrt{\frac{r}{R}}Re \tag{2.25}$$

where De is the Dean number, r =vessel radius, R = vessel radius of curvature and Re is the Reynolds number.

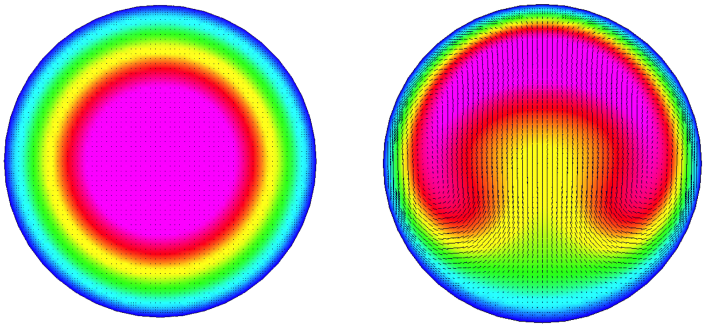

Figure 2.6: *Flow in 4mm diameter tubes at a constant Reynolds number and variable curvature, which results in different Dean numbers and the emergence of a pair of vortices in the case of a non-zero Dean number. In-plane flow is indicated with flow vectors while longitudinal velocity is colour coded.*

As Dean number increases, secondary flow causes a substantial departure from a radially symmetric velocity profile, as shown figure 2.6. In the figure the inside bend of the vessel curve is

orientated at the bottom of the image; flow instability resulting from the vessel curvature leads to secondary flow and the formation of a pair of counter rotating vortices indicated with vectors. Substantial changes in the distribution of the out-of-plane (longitudinal) velocity are seen as a result of the secondary flow.

Dean number ranges between approximately 0 and 100 in the human cerebral circulation suggesting that significant portions of vasculature harbouring aneurysm may have highly non-radially symmetric flow velocity profiles. As such, the radially symmetric inlet velocity profiles applied to simulations in this study are done so with caution. Geometry inlets are created at points in the vasculature that are downstream from relatively straight portions of vessel where momentum exchange has allowed a symmetric profile to develop.

2.6 Boundary Conditions

The time-varying flow rate and pressure profiles within the circulatory system must be incorporated into the boundary conditions of any flow simulation of the vasculature. Given the changes in vessel diameter, tortuosity, elasticity and the complex auto-regulatory nature of the vasculature, the variation in pressure and velocity is far from trivial. Typical profiles of pressure and flow rate in the Circle of Willis, measured *in-vivo* using ultrasound and tonometry probes, are shown in figure 2.7. [123]

However, such *in-vivo* measurements are unsuitable for modelling much of the vasculature that is inaccessible by non-invasive means. To obtain flow and pressure profiles that are valid throughout the vasculature it is necessary to approximate the propagation of blood flow though the circulatory system with an idealised model.

In the one dimensional model proposed by Reymond et al. [123] approximations to the continuity and momentum equations are created by assuming all arteries in the vasculature are straight, tapered, and viscoelastic segments. The Navier-Stokes equations are integrated along the longitudinal direction of the vessel with a Witzig-Womersley shear model accounting for both convective acceleration and wall friction. The resistance of the arterial bed is incorporated with a three-element Windkessel model. Selected examples of the resulting pressure and flow

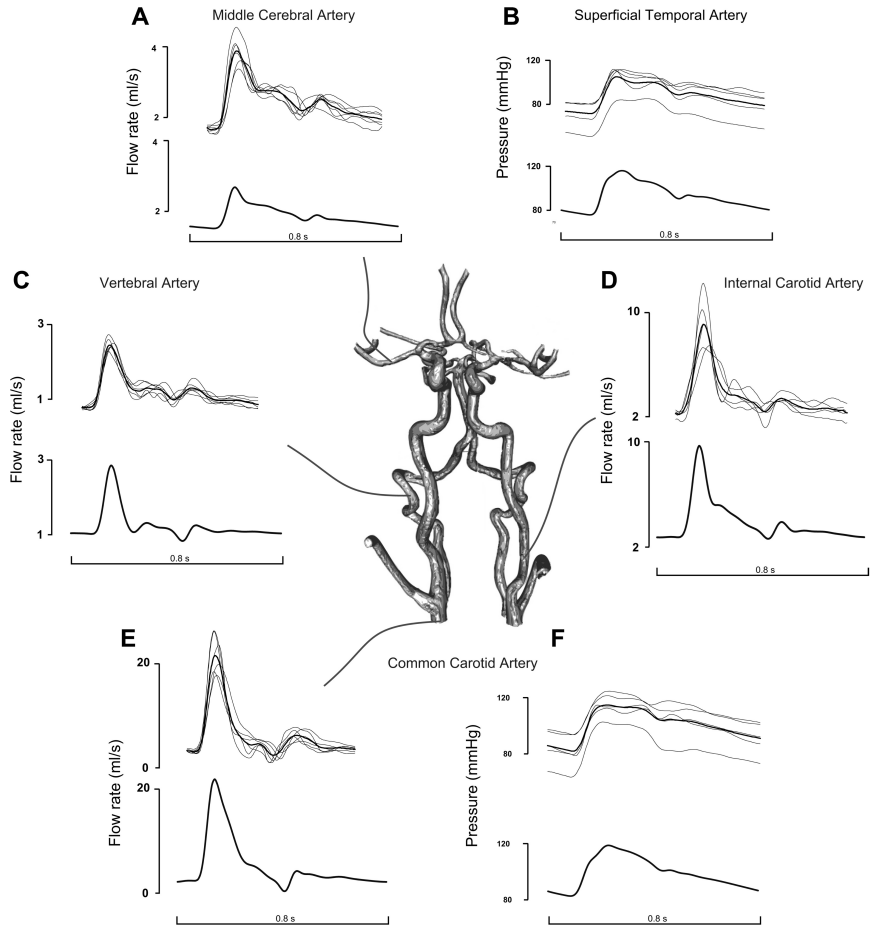

Figure 2.7: *Pressure and flow waveforms measured in-vivo (upper of each pair of plots) and the corresponding 1D analytical model prediction (lower of each pair of plots), at salient locations in the cerebral vasculature. Reproduced from Reymond et al. [123]*

curves are shown in figure 2.7 and are in good agreement with the average profiles measured *in-vivo*.

More sophisticated approximations of the vasculature, including 3D models, are available and are discussed widely in the literature. [124] Three dimensional models in particular are capable of capturing the complex flow at a regions of high vessel curvature and bifurcations. However, the exponential increase in computational cost of such schemes combined with little increase in accuracy renders the simpler 1D model the dominant modelling choice.

All inlet velocity boundary conditions used in this study are scaled to fit the volumetric curves generated by the 1D model proposed by Reymond et al. [123]

In this study, pressure profiles based on a 1D model are not used in favour of a constant pres-

sure assumption at all daughter vessel outlets. This simplification is made for a number of reasons:

- Relatively short segments of vasculature are simulated, which reduces the number of daughter vessels in the geometry. Where only a single inlet and single outlet are present in a geometry, imposing a time-varying pressure outlet boundary condition unnecessarily slows simulation convergence.

- Many of the vessel geometries considered have daughter vessels resulting from symmetric bifurcations, which will also have symmetric (and equal) outlet pressures.

- A 1D model of pressure is calculated assuming an unobstructed vessel lumen. After deploying a flow-diverter device to treat an aneurysm, nearby perforators and daughter vessels are often jailed by the device with the effective resistance of such vessels increasing, invalidating the 1D pressure condition. Incorporating such an increase in resistance, and any subsequent vessel remodelling, into the outflow boundary condition is still an open question in the literature. Hence, for simplicity, a constant outflow pressure condition is assumed for all vessels, but further discussion of this assumption with reference to varying the outlet condition of a jailed vessel is presented in chapter 3

2.7 Flow-Diverter Device Deployment Methods

Finally, when modelling the effect of a flow diverting device on changes in aneurysm flow, it is necessary to virtually deploy such a device accurately within the model vasculature. In reality the deployment and placement of a device is a highly complex procedure, which is governed by the expansion of the super-elastic device material and highly non-linear vessel wall. A number of virtual deployment methods have been detailed in the literature from the most complex (full finite-element analysis with a distensible vessel wall) to the more simple (cylindrical projection-based fast deployment algorithms). All methods rely on the same three steps to mimic device deployment: crimping of the device to a diameter typical of microcatheter delivery, bending of the crimped device to fit the vasculature, and release of the crimped device. In all cases the vessel wall is assumed rigid. The three broad classes of virtual deployment model are summarised

below:

- Full Finite Element Analysis (FEA): Device wires are modelled as super-elastic solids undergoing large deformations; simulations are typically conducted using ABAQUS software (Dassault Systemes, Vélizy-Villacoublay, France). [35] [128] FEA offers the most accurate representation of device deployment and simulated 'unsheathing' bears good correspondence with *in-vitro* experiments. [89] Although the method is highly accurate, such accuracy comes at the price of large computation times. Modelling the device-vessel contact remains problematic with little verification in the literature and the limitations of a rigid vessel wall, which is a common source of simulation instability. FEA also becomes less attractive as a method for deploying device designs with a high pore-density, which substantially increases computational load due to both the increase in resolution required and the increased degrees of freedom in the simulation.

-Projection-based Deployment Algorithms: The device deployment is modelled as the deformation of a meshed smooth cylinder, onto which the device texture is projected. The deployed texture is then used to reconstruct the 3D geometry of the device deployed within the vasculature as shown in figure 2.8. [21] [4] [5] The technique is very computationally efficient but does not incorporate the physical properties of the device. The accuracy of localised device deformation is questionable, especially in devices with large and irregular pores and at the aneurysm neck.

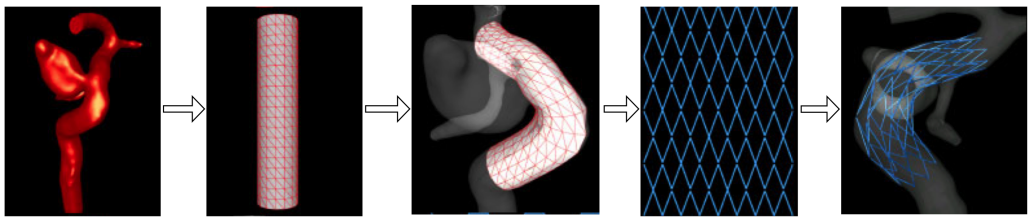

Figure 2.8: *Cylindrical projection deployment of a flow-diverter with a vessel. Adapted from Appanaboyina et al. [4]*

- Spring-based Deployment Algorithms: The Fast Virtual Stenting method (FVS) proposed by Larrabide et al. [82] [83] is a modified form of a projection-based scheme that incorporates local stent structure. The nodes of the device that are projected onto the underlying cylindrical mesh are given longitudinal and torsional stiffness as indicated in figure 2.9.

Devices deployed with the FVS method show good correlation with *in-vitro* deployments in vessel

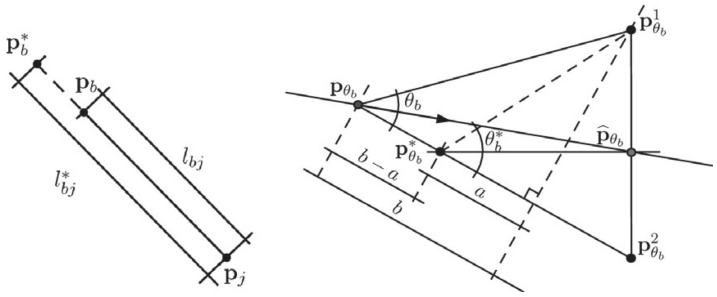

(a) Strut length force ($\mathbf{f}_l$) (b) Strut angle force ($\mathbf{f}_a$)

Figure 2.9: *In the FVS method the projected device geometry is given localised stiffness. Adapted from Larrabide et al. [82]*

phantoms, even at the aneurysm neck and with irregular device cell structures. [82] [83]

A similar algorithm developed by Spranger et al. [140] also utilises a spring analogy to give individual device struts stiffness, as shown in figure 2.10. However, in this case the underlying cylindrical mesh is removed entirely, which has the effect of each strut being represented as a simplified 1D finite element.

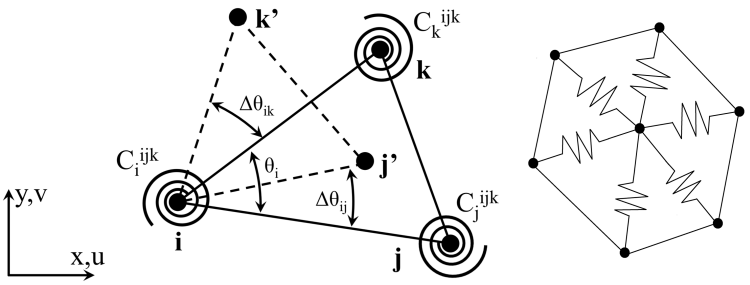

Figure 2.10: *Longtitudinal and torsional spring analogy of the deployment scheme proposed by Spranger et al. Figure adapted from Blom [10] and Farhat et al. [44]*

As with the FVS method, device placement is improved compared to a projection method. The accuracy of the scheme also compares favourably to a full FEA deployment. [139]

Both of these spring-based methods represent a substantial increase in accuracy with little increase in computational load when compared to projection-based deployment schemes.

Finally, in a study by Bernardini et al. [9], the relative accuracy of different FEA and FVS deployment methods was evaluated. Simulations incorporated both rigid and distensible vessel walls, 1D and 3D descriptions of device struts, and both full FEA and simplified FVS deployment methods. Little difference was seen in device positioning, resulting flow pattern, or hemodynamic

indices across the different simulations. The study concluded that no significant loss of accuracy resulted from deployment of a device with a simplified algorithm and rigid vessel walls.

In this study the algorithm developed by Spranger et al is used to deploy cylindrical flow-diverter designs. The method is chosen as a compromise between the computational speed of a fast deployment algorithm and the accuracy of a full FEA simulation. In chapter 4 the deployment of a number of non-cyclindrical flow-diverter devices is discussed. As these devices lack a coherent cell-based structure across their entire geometry, they are unsuitable for being deployed by the spring-based deployment algorithm and must be placed manually.

Chapter 3

Flow-Diverter Mesh Design and Large-Scale Flow Features

In this chapter the performance of different designs of flow-diverter are assessed through in-silico simulation. Previous work discussing the sensitivity of physiological flow (especially secondary flow features) to subtle design changes and the influence of mesh design is discussed in section 3.1. The remainder of the chapter is divided into two halves. In section 3.2 a number of mesh designs are modelled in idealised geometries; flow reduction and secondary flow effects of different mesh topologies are discussed. In section 3.3 the same flow-diverter designs are implanted into patient-specific aneurysm geometries. Flow reduction, secondary flow features, and wall shear stress are all compared across the different device designs and porosities.[1]

3.1 Introduction

Within the human vasculature, the effects of geometry on flow structure are complex and highly unpredictable; very subtle design features can induce large changes in flow regimes, velocities and stresses.

[1]The work presented in section 3.3 of this chapter has appeared as part of: T W Peach, M Ngoepe, K Spranger, D Zajarias-Fainsod, and Y Ventikos. Personalizing Flow-Diverter Intervention for Cerebral Aneurysms: From Computational Hemodynamics to Biochemical Modeling. International Journal for Numerical Methods in Biomedical Engineering, 30(11):1387-407, 2014 [109]

For example, the great clinical importance of the subtle variation in aneurysm flow patterns was emphasised by Cebral et al. [21]. In a study that retrospectively modelled 62 ruptured and unruptured aneurysms, small changes in flow pattern stability, flow impingement region size and flow jet size were all correlated with aneurysm rupture risk.

Similarly, Baek et al. [7] showed that relatively small variation in aneurysm geometry and flow rate may lead to flow patterns where areas of flow impingement in the aneurysm sac become unstable. Such oscillations resulted in localised, high-frequency variation in WSS magnitude and direction, that may correlate with aneurysm growth and rupture.

Cookson et al. [30] showed that a small helical twist in graft tubes, similar to the natural helical shape of human arteries, created radically different flow conditions when compared to straight tubes under the same boundary conditions. The helical tube flow field increased mixing across the pipe lumen, reduced peak velocities, increased flow stability and returned WSS distributions to more physiologically normal values.

The minimally invasive nature of vascular devices results in a dominant device construction of meshes woven from shape memory alloy wire, which allows the device to easily collapse and expand for delivery and deployment. However, with the development of a novel method of laser-cutting flow-diverter devices directly from hollow Nitinol tubing (shown in figure 3.1), non-woven mesh designs may be easily created. [90]

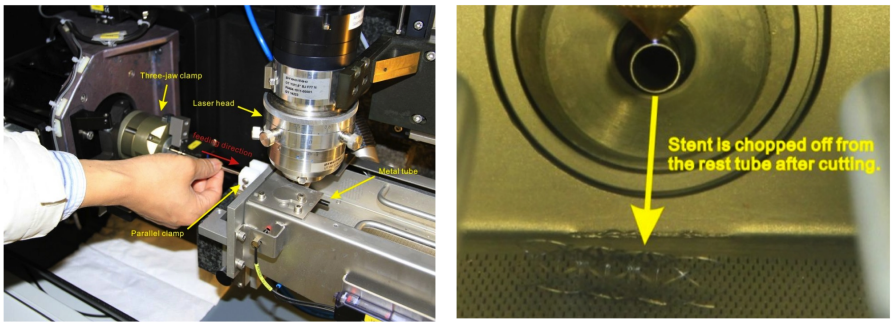

Figure 3.1: *Detail of the method used to laser-cut Nitinol hollow tubing into a flow-diverter device*

The technique allows for a flow-diverter with almost any mesh topology to be cut (see figure 3.2), providing the mesh is assigned to collapse down for crimping. An additional advantage of such laser-cut designs is a greater device flexibility but increased radial stiffness, arising from substantially reduced friction normally associated with a woven design. [90] This increased flexibility

allows smaller devices to be placed deeper into the cerebral vasculature, where vessels such as the MCA and ACA account for a disproportionate number of aneurysms at risk of rupture.

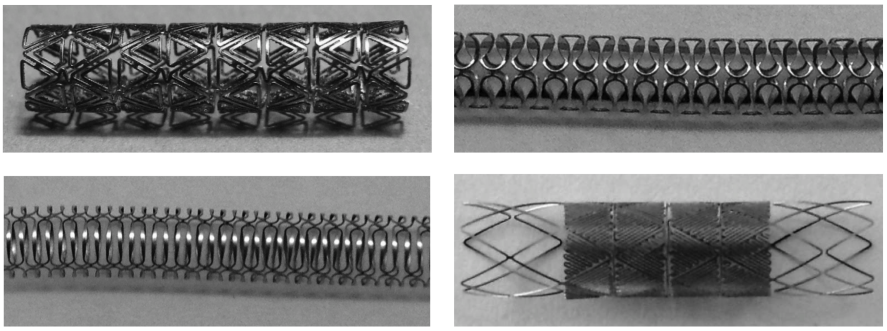

Figure 3.2: *Four of the almost infinite number of possible mesh designs that may be laser-cut*

However, the effect that significant variation in flow-diverter mesh topology will have on large-scale aneurysm flow features is currently unknown.

As discussed in chapter 1, there are currently two cylindrical designs of cerebral flow-diverter on the market that are approved for use in patients: the Pipeline Embolization Device, known as the PED (Covidien/ev3, Irvine, CA) and the SILK flow-diverter (Balt Extrusion, Montmorency, France). Both of these designs are almost identical and are constructed from a mesh of interwoven Nitinol wires. Clinical experience of both the PED [88] [104] and the SILK [79] [91] report good aneurysm occlusion in many different sac sizes and geometries. The body of research detailing clinical experience with both designs of flow-diverter continues to grow, with a total of over 800 interventions recorded in the literature.

The design considerations of such woven flow-diverter devices, with a fixed mesh shape, have been simplified to a balance of porosity alone. A high porosity mesh design increases device flexibility, reduces the risk of ischemia in healthy vessels covered by the device, and aids the collapse and subsequent delivery of the device. A low porosity mesh design provides maximum resistance to blood flow entering the aneurysm, reduces blood velocity in the aneurysm dome and encourages aneurysm isolation from the vasculature with fast, stable thrombosis. The balance of these factors has lead to current clinical devices alighting upon a common optimum porosity of 60-70%, with almost identical corresponding pore sizes and wire diameters.

However, once mesh design itself can be easily varied and is no longer confined to closed-cell woven patterns, the optimisation process is much more complex. A broad spectrum of stent

designs have been modelled in the literature ranging from the very abstract to the more familiar designs that are commercially available. At the most simple, Ohta et al. [106] investigated the effect of a single pair of stent struts and their orientation to the flow. The study concluded that the greatest reduction in inflow was achieved by the cancelling of local vortices when stent struts are placed perpendicular to the flow. Lieber et al. [84] reported the effect of strut size on intra-aneurysmal flow for a rhomboid mesh, finding that a stent reduced the vorticity in an aneurysm sac and that at a constant porosity, decreasing the filament diameter and hence increasing the number of struts across the aneurysm neck reduced inflow more. Liou et al. [86] investigated the influence of stent shape considering both helical and square mesh designs, with the most significant reduction in aneurysm inflow achieved with a helical stent. In two further studies, both Fu et. al [50] and Appanaboyina et al. [4] concluded that for a given porosity, the greatest reduction in aneurysm inflow was achieved with a 'zig-zag' design of flow-diverter, compared to helical and rhomboid designs.

Much of the literature also suggests that the performance of a flow-diverter device varies substantially with the angle of the flow impacting the mesh. Kim et al. [73] compared parent vessel curvature with aneurysm turnover time post-treatment for two different designs of flow-diverter stent; turnover time was found to increase by up to a factor of 16 after varying vessel curvature alone. Considerable variation in flow reduction, flow pattern and thrombolytic action with vessel curvature was also shown by Meng et al. [96]. Finally, a study by Augsburger et al. [6] suggested that flow-diverter success was not solely based on porosity but was highly influenced by variation in local vessel geometry.

3.2 Investigating Flow-Diverter Meshes in Idealised Flow Conditions

Initially in this chapter, different mesh topologies are investigated by simulating blood flow striking the mesh in an idealised geometry at three different angles. The flow reductions of each mesh are compared as well as any changes in flow pattern introduced by the mesh topology. The mesh designs are subsequently deployed in three anatomically accurate aneurysm geometries, and the relative flow-diverting action and performance are assessed in each case.

3.2.1 Mesh Designs

Three flow-diverter mesh designs are created in the 3D computer graphics package Blender (Stichting Blender Foundation, Amsterdam, The Netherlands) and modelled as 4mm diameter cylinders to represent novel and clinically used flow-diverter mesh topologies. The mesh configurations and respective porosities are summarised in figure 3.3.

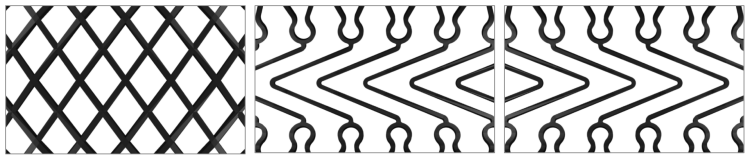

Figure 3.3: *Mesh designs to be tested for flow-diverting action (not to scale)*

The 'Rhomboid' mesh of figure 3.3 has a strut width of 30 micrometers and pore size of around 200 micrometers. The mesh design is similar to that of commercially available woven flow-diverter devices, such as the SILK and PED, and has a similar porosity around 70%.

The 'Converging' and 'Diverging' meshes in figure 3.3 are of a design developed in-house, which may be laser-cut from Nitinol tubing. The mesh has a strut width of 70 micrometers, an average space between the struts of around 500 micrometers, and a strut angle of 20 and 160 degrees from the direction of the flow for the diverging and converging cases respectively. The meshes both have a porosity of 80%.

A number of geometries are created to test the effective resistance of each mesh as the angle of the flow impacting meshes changes. Geometries with 90, 60 and 30 degree bends are shown in figure 3.4, which offer a flow jet striking the meshes at approximately the same respective angles. The geometries are of circular cross-section with a diameter of 4mm, chosen to be similar to that of a human ICA. An advantage of such curved geometries over the straight channel used in conventional hydraulic resistance tests is the creation of a more complex flow profile. The curved geometry introduces in-plane vorticity to the fluid flow, known as Dean Flow [38], and creates flow conditions more similar to the complex flow seen in human cerebral vessels with high tortuosity. The presence of vorticity in the flow also allows for quantifying the degree to which different mesh designs reduce or increase the vorticity of the flow they interact with.

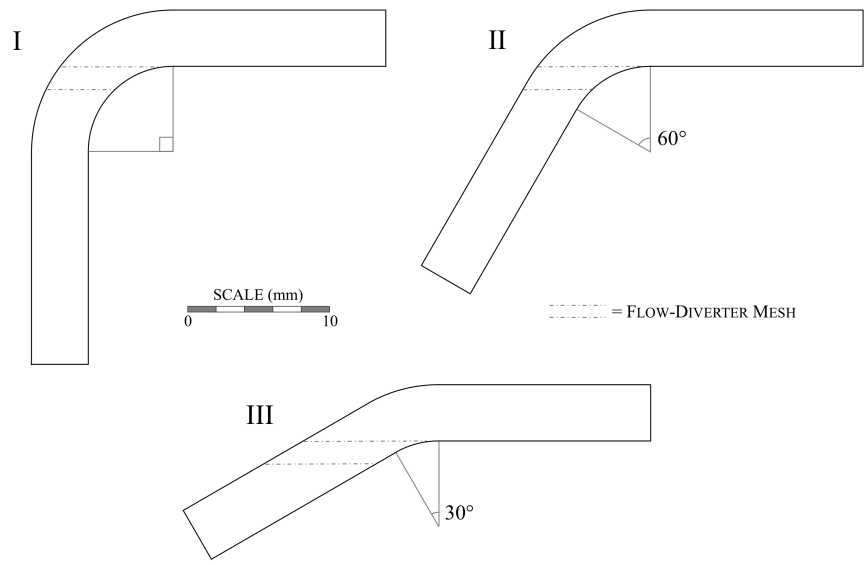

Figure 3.4: *Flow diverter testing geometries where the device is positioned between the dashed lines. I: 90 degree bend, II: 60 degree bend and III: 30 degree bend*

The test meshes of figure 3.3 are deployed as half-cylinders into each of the three geometries shown in figure 3.4. The Rhomboid mesh deployed in the 90 degree bend geometry is shown as a cutaway section for clarity in figure 3.5.

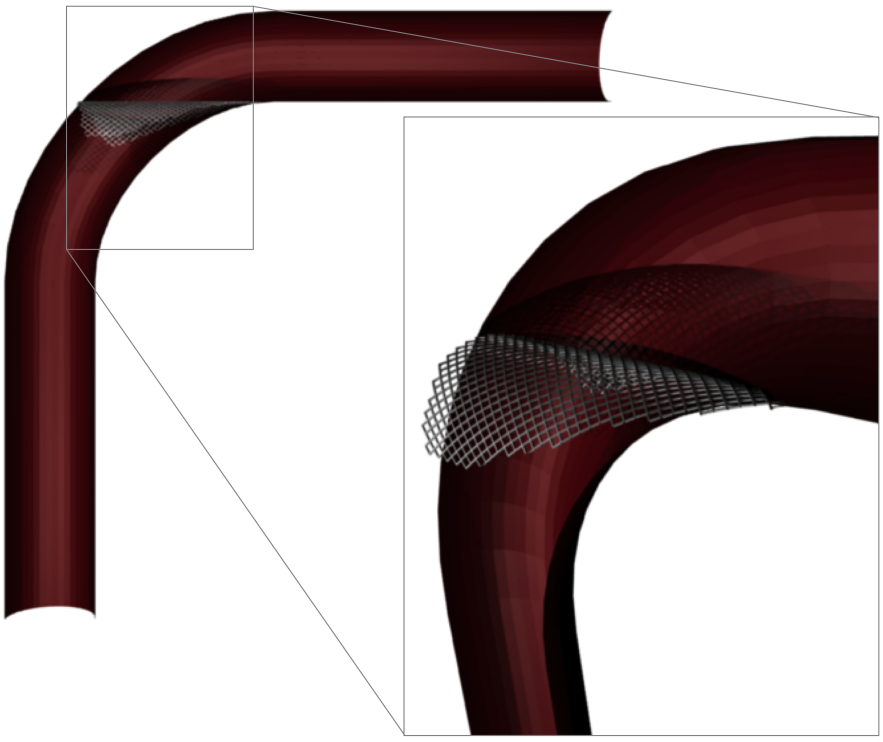

Figure 3.5: *Rhomboid mesh deployed in the 90 degree bend geometry (cutaway)*

3.2.2 Methodology

Simulations of each mesh and geometry combination are run in CFD-ACE+ (ESI Group, Paris, France) and are conducted with a fixed pressure drop boundary condition from inlet to outlet, as summarised in Table 3.1. These values of pressure are first calculated with a prescribed steady state flow rate of 230ml/min, a flow rate typical of the human ICA. Blood is modelled as incompressible and Newtonian, with a density of 1000kgm^3 and a dynamic viscosity of 0.004 Pa s. As previously discussed, a Central Differencing scheme is used, along with SIMPLE-Consistent (SIMPLEC) pressure correction [105] [41] and an algebraic multigrid method for convergence acceleration. [158] A constant, fixed-pressure inlet boundary condition is set for each geometry type, as listed in Table 3.1, in addition to an outlet boundary condition of zero relative pressure.

The effectiveness of each mesh is then assessed by the relative reduction in flow achieved under the same pressure gradient as was recorded for the unobstructed geometries.

Table 3.1: *Relative inlet pressure boundary condition by geometry. Pressures are derived from geometries with no device deployed and a volumetric flow rate of 230ml/min*

GEOMETRY	PRESSURE
90° Bend	180 Pa
60° Bend	143 Pa
30° Bend	131 Pa

Mesh independence tests are performed on the 90 degree bend geometry with the rhomboid mesh deployed. This mesh and geometry combination is chosen as a 'worse case' whereby the higher pore-density of the Rhomboid mesh and the greater change in flow direction of the geometry bend increase the subsequent flow's sensitivity to mesh quality. A fixed inlet and outlet boundary condition of 180 Pa and 0 Pa respectively are applied with the solver setting discussed previously. The geometry is imported into CFD-VisCART (ESI Group, Paris, France) to be meshed, which is completed with a Projected Single Domain mesh, an Omnitree Cartesian tree type, and three near-wall Cartesian layers to give a smooth and well-resolved boundary definition. Simulations are run on meshes with minimum cell densities from 1-50,000 cells/mm^3 resulting in mesh sizes from 12,000 to 13,200,000 elements. Results are shown in figure 3.6. From the figure it can be concluded that at a mesh density greater than 5,000 cells/mm^3, the error in flow rate falls

below 1%, when compared to the finest mesh available. This level of mesh refinement is therefore considered 'independent' for all other geometries. The two most coarse meshes did not converge as the close spacing of the rhomboid mesh cells was not accurately resolved by the coarse grid, resulting in complete occlusion of the vessel.

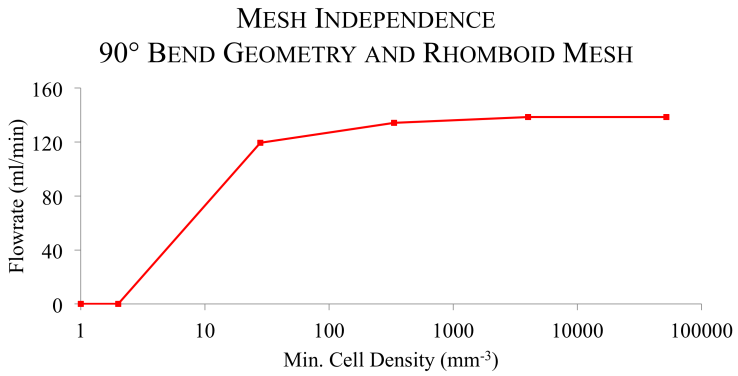

Figure 3.6: *Mesh independence tests*

Meshes generated at the chosen independent fineness level for all combinations of the three geometries and three mesh topologies result in simulation mesh sizes of 3,460,000 to 6,900,000 cells. The simulations are run on 8, 2.93 GHz cores, converging to five orders of magnitude residual reduction in around 500-1000 iterations in a typical solution time of 4-8 hours.

3.2.3 Simulation Results

Reductions in flow for each geometry due to the three different mesh topologies are summarised in figure 3.7.

The graph suggest that the flow-diverting behaviour of the meshes is dominated by porosity with little difference seen in the performance of the converging and diverging meshes, which differ only in shape. The lower porosity rhomboid mesh results in a greater reduction in pipe flow, as would be expected with a greater fraction of struts giving increased resistance. The rhomboid mesh offers reductions in flow of 38-47% compared to the 20-35% reductions seen for higher porosity meshes.

Figure 3.7 also suggests that there is a marked difference in behaviour of all the devices in the 90 degree geometry, with a substantial drop in flow reduction seen across the meshes. This is

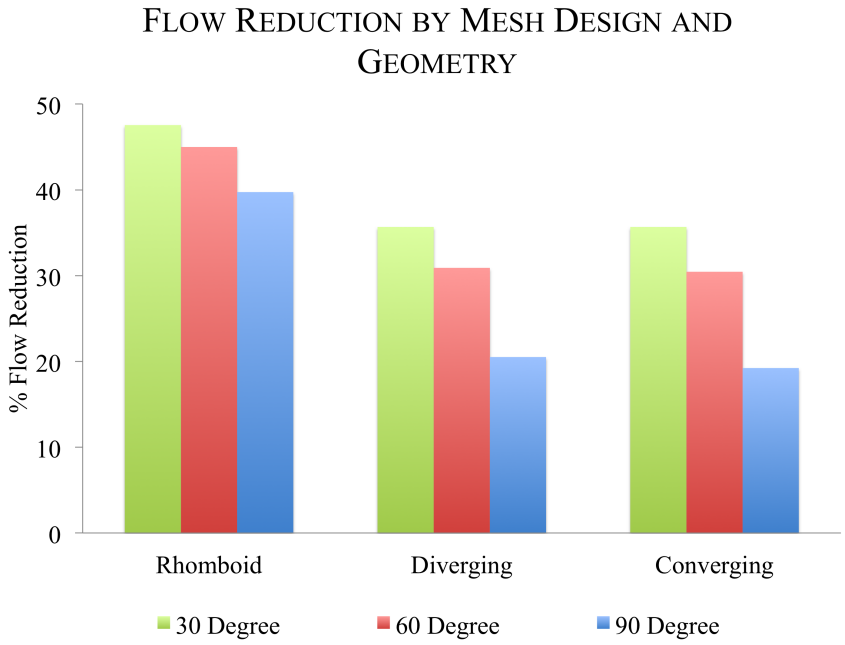

Figure 3.7: *Flow reduction by mesh topology type and geometry*

especially true of the converging and diverging meshes, where the flow reduction achieved almost halves between the 30 degree and 90 degree geometries. The precise mechanisms producing these flow-reductions are unclear from the changes in bulk flow alone.

In order to observe the changes in flow pattern induced by the different mesh designs, three planes are cut in each geometry: one at the end of the curved section, one at the geometry outlet and one at the mid-point between these two locations. The longitudinal velocity magnitude and direction of the in-plane velocity vector directions are indicated in addition to plots of the in-plane vorticity. These planes are shown for each geometry in figure 3.8, figure 3.9, and figure 3.10, and when a pair of counter-rotating vortices is clearly identifiable in the planes, the centre of the circulation is indicated with a black cross-hair. The longitudinal cross-section at the mid-point of each geometry is also shown, with velocity magnitude plotted. It should be noted that while the highly non-axially symmetric velocity profile leads to areas of low velocity along the cross-section (prominent for the Rhomboid mesh in each of the figures), mass continuity is not violated.

From the first diagram of each of the three figures (labeled (a)), it is clear that all three curved geometries introduce some degree of in-plane vorticity to the flow, as indicated by the vorticity

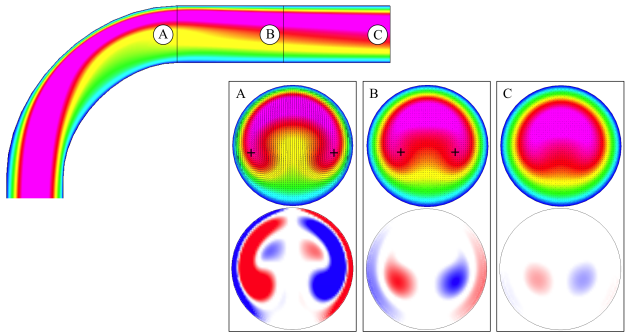

(a) *No Device*

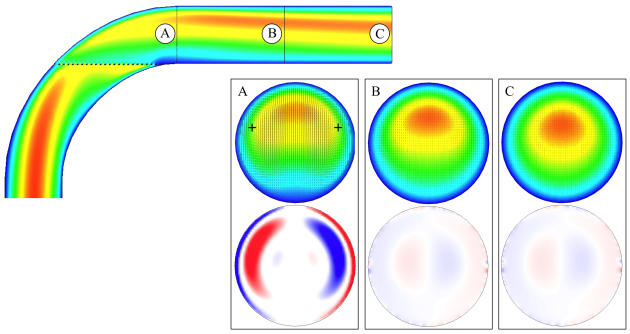

(b) *Rhomboid Mesh*

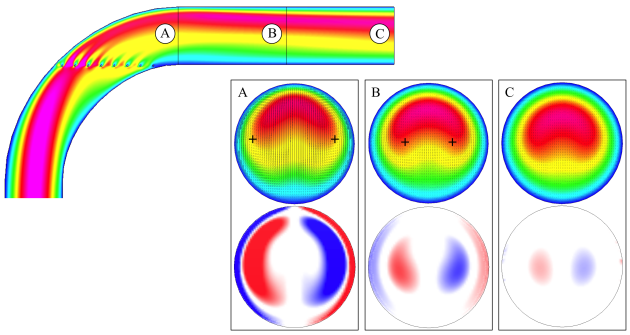

(c) *Convergent Mesh*

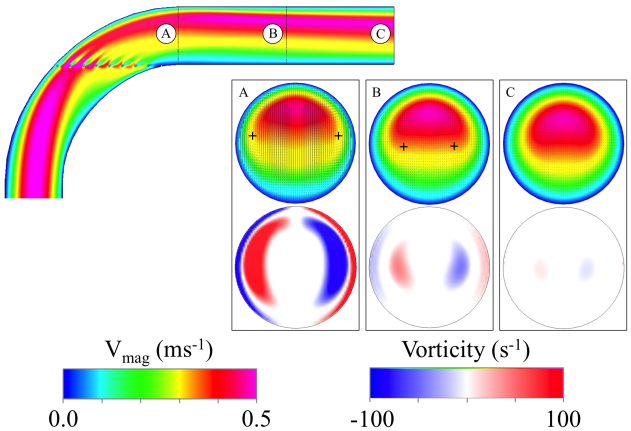

(d) *Divergent Mesh*

Figure 3.8: *Velocity and vorticity plots of the 90 degree bend geometry*

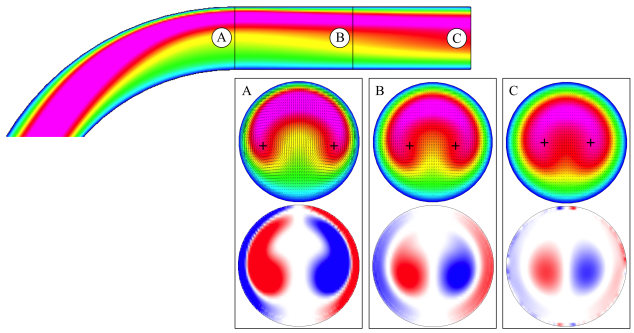

(a) *No Device*

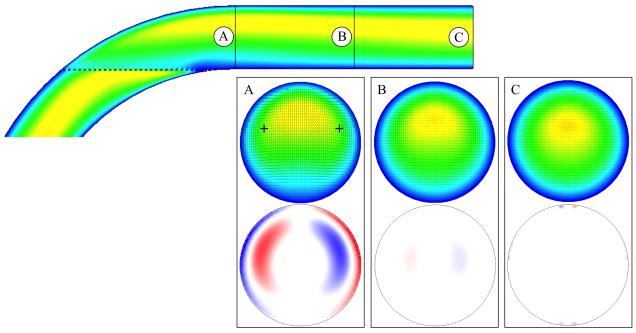

(b) *Rhomboid Mesh*

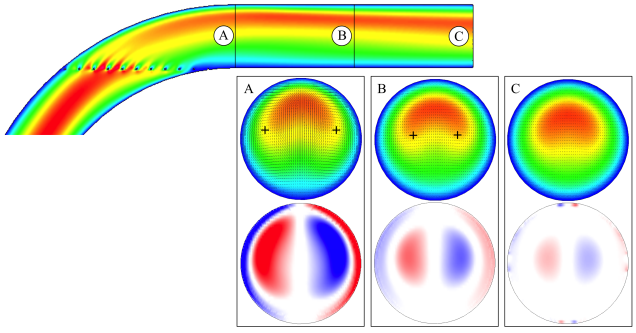

(c) *Convergent Mesh*

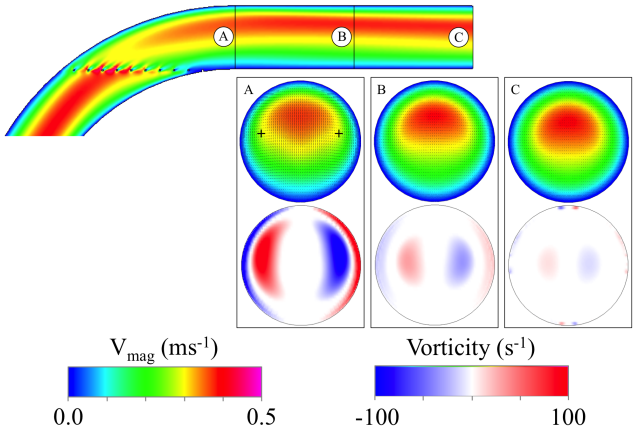

(d) *Divergent Mesh*

Figure 3.9: *Velocity and vorticity plots of the 60 degree bend geometry*

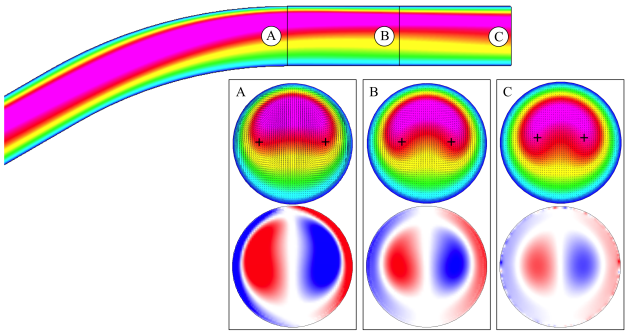

(a) *No Device*

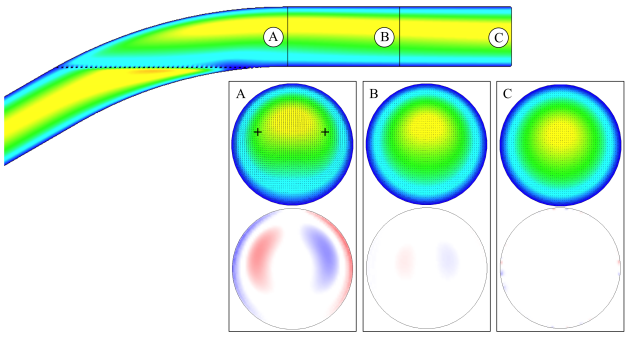

(b) *Rhomboid Mesh*

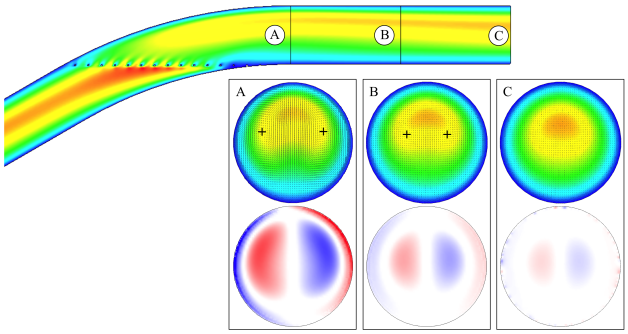

(c) *Convergent Mesh*

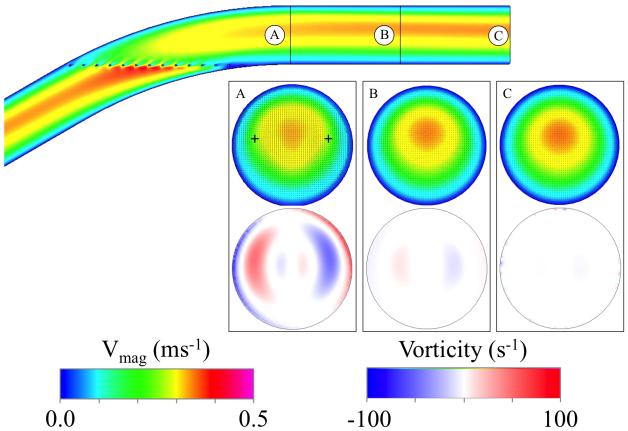

(d) *Divergent Mesh*

Figure 3.10: *Velocity and vorticity plots of the 30 degree bend geometry*

plots and the in-plane components of the velocity vectors. A classic, stable first-order 'Dean flow' profile is clearly visible where the concentric, radially-symmetric poiseuille profile has morphed into a pair of counter-rotating vortices moving fluid from the inside to the outside edge of the bend. This in-plane vorticity decreases further downstream in the straight section of the geometries as momentum transfer returns the flow towards a Poiseuille regime. Across all the geometries, the vorticity decays with the centres of circulation moving towards the mid-stream.

The Dean number (defined previously in Equation 2.25), and hence the degree of in-plane vorticity, is inversely proportional to the square root of the vessel radius of curvature. Although the 90 degree geometry creates the greatest in-plane velocity components immediately following the bend, it appears that the in-plane vorticity is less stable in the 90 degree geometry and the pair of vortices decay faster, reducing the vorticity at the geometry outlet to less than the 60 degree geometry case (compare outlet cross-sections of figure 3.8(a) and figure 3.9(a)). This increased vorticity decay in the 90 degree geometry is due to the emergence of two additional areas of local vorticity (visible in figure 3.8(a)), which are adjacent to and in the opposite direction of the two main concentrations, and lead to local vortex cancelling.

The Rhomboid mesh, indicated in (b) of figure 3.8, figure 3.9, and figure 3.10, appears to substantially reduce the peak velocity of the fluid across the geometries. The central core of the flow is clearly disrupted in all three geometries with all flow reduced to less than 0.2ms^{-1} in the centreline plane, immediately after the rhomboid stent mesh. The in-plane vorticity of the flow is also substantially reduced by the Rhomboid mesh, with almost all vorticity eliminated from the flow by the middle cross-sectional plane across all three geometries.

The higher porosity of the Converging and Diverging meshes results in less reduction in peak fluid velocity than the Rhomboid case. The Converging and Diverging meshes do not significantly reduce the high-speed core of the flow (velocity greater than 0.4ms^{-1}) in the 90 degree geometries, which may offer an explanation for the substantially reduced flow reduction seen in figure 3.7. By contrast, high-speed flow is almost entirely dissipated by the Converging and Diverging meshes in the 30 degree bend geometry, where the flow reduction achieved across all three mesh topologies only varies by around 10%.

Consistently, in-plane vorticity is more prevalent in the geometries with the converging mesh deployed (c) compared to the diverging mesh (d). The action of the converging mesh, which directs a single jet of flow centrally, reinforces the momentum of the flow moving around the curved geometry from the inside to the outside faces and thus reinforces the pair of vortices.

The diverging mesh appears to introduce a pair of counter rotating vortices (clearly visible in figure 3.10(d)), which rotate in the opposite directions to those introduced by the geometry curve. The result is a reduction in vorticity and a flow profile closer to the poiseuille solution for the divergent mesh. This is further reinforced by the angle of the flow passing through the meshes in each of the centre-line planes; in the converging case the flow infiltrates further, with a more vertical jet coincident with flow morphing from the inside to the outside of the bend, whereas flow passes through the diverging mesh with a flatter, more horizontal jet.

Finally, it should be noted that the local Reynolds number of flow at the device struts does not exceed ≈15, which is well below the critical Reynolds number (47 for a smooth cylinder) corresponding to the onset of Von Karman vortex generation.

3.2.4 Idealised Geometry Conclusions

From the results of the simulations in section 3.2.3, it is clear that in simple, curved-pipe geometries the resistance of a mesh are dominated by the mesh porosity alone. The greatest difference between the performance of the three meshes is seen in the 90 degree bend geometry. A substantial drop in the flow reducing capability of the Converging and Diverging meshes is seen, which corresponds to very limited reduction in the high-velocity flow passing through the mesh.

Different large-scale flow features are seen across the mesh topologies: the Rhomboid mesh eliminates almost all in-plane velocity from the flow passing through it, while both the Converging and Diverging mesh designs impart vorticity into the flow. In the Converging case, flow is directed into the centre of the vessel, encouraging a pair of vortices to form. The flow passing through the Diverging mesh is consistently 'flatter' and directed towards the outer edges of the vessel. In addition, a pair of vortices are introduced rotating in the opposite direction to the Converging case.

However, the flow conditions created by the curved pipe geometries are not a good representation of typical conditions at an aneurysm *in-vivo*. In particular, the flow rate passing through the mesh is unrealistically high compared to the flow entering a side-wall aneurysm. Also, the effect of the pulsatile nature of blood flow *in-vivo* on any flow vorticity introduced by a flow-diverter is unknown.

3.3 Anatomically Accurate Aneurysm Simulations

In the following section the same mesh topologies (Rhomboid, Convergent and Divergent) are investigated further. The meshes are deployed in anatomically accurate aneurysm geometries with physiologically consistent flow profiles. The effect of mesh porosity alone is also controlled for with designs of the same mesh design but varying porosity. Flow reduction and secondary flow effects are explored in addition to wall shear stress distributions.

3.3.1 Anatomically Accurate Geometries

To quantify the effect of different flow-diverter mesh designs on aneurysm hemodynamics, and to attempt to generalise the behaviour seen, a number of aneurysm types are simulated with different flow-diverter mesh designs. The different permutations of the aneurysm and device types allow for the isolation of specific features that have been linked in the literature to device effectiveness, such as device porosity, mesh design, parent vessel flow rate, aneurysm aspect ratio etc.

Three patient-specific vessel geometries, each presenting an aneurysm in a different location and of a different size and shape, are extracted from patient Computed Tomography Angiography (CTA) data (see figure 3.11).

The first geometry, ICA_Bifurc, represents a small saccular aneurysm of the Internal Carotid Artery (ICA) proximal to the vessel bifurcation. A second geometry, ICA_Giant, has a large saccular aneurysm present on the ICA, opposite the ophthalmic artery. Finally, the third geometry, MCA, shows a small but sessile aneurysm on the Middle Cerebral Artery (MCA).

Each vessel geometry is imported into Blender and trimmed to within ten vessel diameters

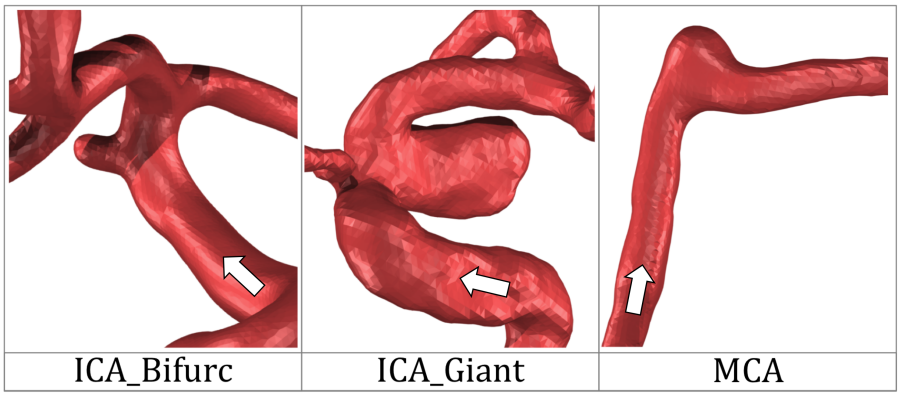

Figure 3.11: *Patient specific geometries with inlets and direction of inflow indicated*

upstream and downstream of the aneurysm location in order reduce the simulation mesh size and increase computational efficiency.

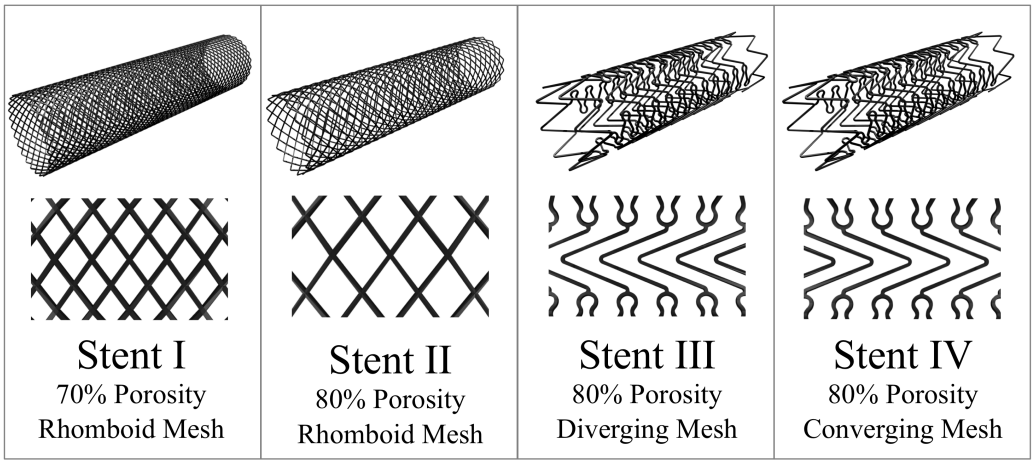

Figure 3.12: *Flow-diverter designs*

Table 3.2: *Flow-Diverter parameters*

Device	Porosity	Wire Diameter	Number of Strands	Pore Diameter
Stent I	70%	30µm	48	120-260µm
Stent II	80%	30µm	32*	130-280µm
Stent III	80%	70µm	n.a.	500µm (min)
Stent IV	80%	70µm	n.a.	500µm (min)
SILK/PED	~70%	~30µm	48	~110-250µm

*Number of strands chosen to preserve longitudinal axis angle (rhombus shape) of a 70% porosity 48 strand stent of the same diameter

Four different flow-diverters are created, with varying porosity and mesh designs, as shown in figure 3.12 and summarised in Table 3.2. The selection of stent designs is chosen to reflect both commercially available and entirely novel devices. Stent I is almost identical to the SILK (Balt

Extrusion, Montmorency, France) or PED (ev3/Covidien, Irvine, CA) with a rhomboid mesh at 70% porosity. This mesh of this device is identical to the 'Rhomboid' mesh discussed in the previous section. Stents III and IV have been previously discussed and are manufactured within the Oxford Engineering Science Department. Both 'Diverging' and 'Converging' meshes have a porosity of 80%. The remaining device, Stent II, acts as a control on both porosity and design, with an 80% porosity Rhomboid mesh. Using these designs it is possible to investigate the influence of stent porosity on inflow reduction alone by comparing Stents I and II whilst also investigating the influence of mesh design alone by comparing Stents II, III and IV. These stent designs are summarised in Table 3.2 and compared to the parameters of the commercially available SILK/PED. Because of the semi-open cell design of Stents III and IV, only the minimum pore diameter is given.

3.3.2 Simulation Methodology

Flow-diverters are sized to the geometries in accordance with current clinical guidelines recommended by the SILK/PED manufacturers, as detailed in Table 3.3. Each stent design is virtually crimped and deployed in each aneurysm geometry with an in-house fast deployment algorithm assuming a rigid vessel wall. [140] [139] [109]

The virtual crimping of the device is necessary to confine the device to within the vasculature prior to virtual deployment; this crimping is conducted in a purely radial fashion, hence the deployed length of the flow-diverter device remains unchanged. This method of crimping differs to the method of deployment used clinically whereby the device is compressed radially into the delivery catheter resulting in longitudinal lengthening. When the device is deployed radial expansion occurs coincident with longitudinal compression and the device shortens as it is deployed. As such the degree of foreshortening and the precise location of both the proximal and distal ends of the device, which are key parameters in successful clinical treatment [45], are not accurately predicted by the virtual deployment method. However, as discussed in section 2.7 the deployed position of the device at the aneurysm neck is virtually unaffected by the approximations of the virtual deployment method.

The virtually deployed flow-diverter geometries are trimmed to improve computational efficiency,

Table 3.3: *Vessel diameter and Flow-Diverter sizing*

VESSEL	VESSEL DIAMETER (DISTAL TO ANEURYSM)	VESSEL DIAMETER (PROXIMAL TO ANEURYSM)	DEVICE DIAMETER*
ICA_Bifurc	3.10-3.70mm	3.25-3.80mm	3.5mm
ICA_Giant	3.25-3.75mm	3.75-4.00mm	4.0mm
MCA	2.45-2.60mm	2.35-2.70mm	2.5mm

*Devices chosen according to current SILK/PED manufacturers' recommendation

leaving a stent length of approximately one aneurysm neck diameter upstream and downstream of the aneurysm neck for each geometry. Despite dramatically different mesh topologies of the devices, very little variation is seen between the deployed positions of the flow-diverter designs across the aneurysm geometries. Cutaway sections showing each flow-diverter device deployed in the ICA_Giant aneurysm geometry, which is the most tortuous case, are shown in figure 3.13. If Stents III and IV were to be deployed in a vessel with much greater curvature than that seen in the ICA_Giant geometry, it is likely that the 'chevron' portions of the design would collide with one another, making the device less flexible unless the stent struts were to overlap one another, a situation not encountered in the geometries simulated.

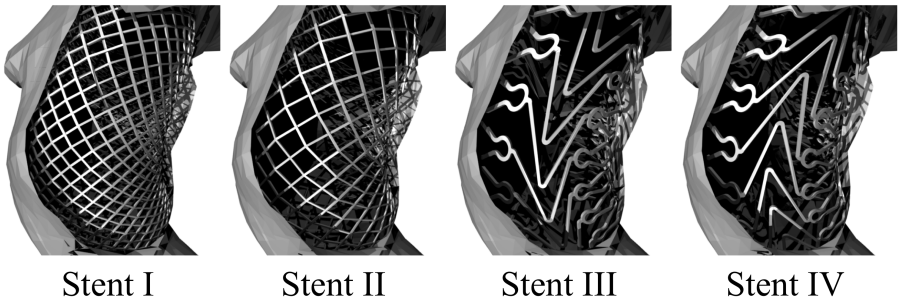

Figure 3.13: *All four flow-diverter devices deployed in the ICA_ Giant geometry*

Transient flow mesh independence tests are performed on each geometry with and without a stent deployed with meshes corresponding to minimum cell densities of approximately 1-60,000 cells/mm^3. The aneurysm geometries, with and without the Stent I device deployed, are imported into CFD-VisCART to be meshed. The meshing of each geometry is completed with a Projected Single Domain mesh, an Omnitree Cartesian tree type, and three near-wall Cartesian layers to give a smooth and well-resolved boundary definition. The results of these simulations are shown in figure 3.14.

A measurement plane is defined at the neck of each aneurysm, through which the aneurysm

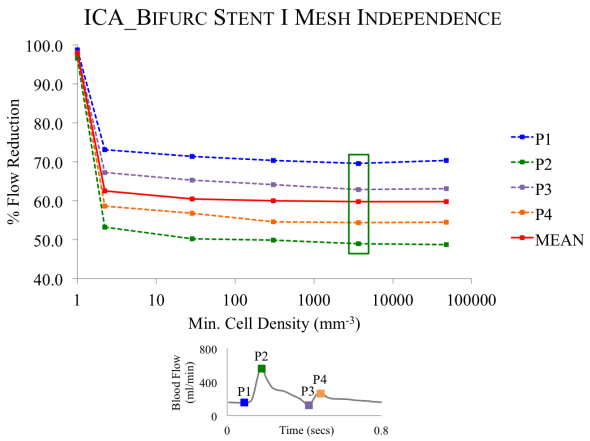

(a) *ICA_ Bifurc mesh independence*

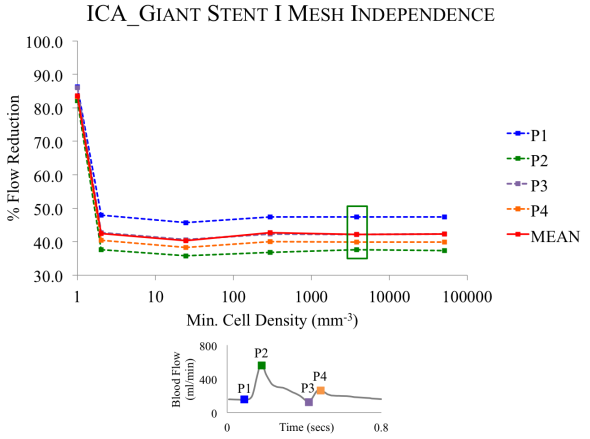

(b) *ICA_ Giant mesh independence*

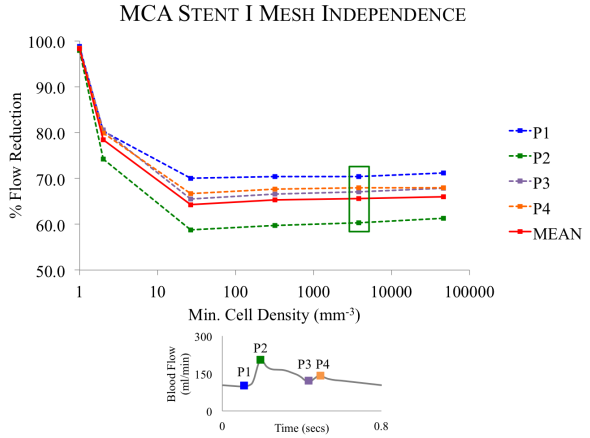

(c) *MCA mesh independence*

Figure 3.14: *Mesh independence plots*

inflow is recorded. The planes are placed as recommended by Kim et al. [73], and the number of mesh elements in the plane exceeds the recommendation of Jou et al. [69], to fully resolve flow features. Meshes are assumed independent when the variation in both mean and instantaneous

reduction in aneurysm inflow falls to less than 1% for two consecutive mesh fineness levels. This condition is met for all three aneurysm geometries at a cell density greater than 5,000 cells/mm^3, approximately the same as that calculated for the idealised pipe geometries in section 3.2.2. The resulting meshes, generated at this fineness level for all three geometries with each device deployed, fall in the range of 2,850,000 to 8,160,000 elements.

The simulation meshes are imported into the multi-physics suite CFD-ACE+. The Reynolds numbers of the flow in the parent vessel of each aneurysm geometry have a minimum around 160 at diastole and a maximum around 760 at systole, indicating laminar flow (verified in each case, by the lack of emergent high frequency oscillations, as interrogated in the high resolution computations). For all three geometries simulated with pulsatile flow at a frequency of 75 BPM, the Womersley number remains in the range of 1.3-2.2, which supports a parabolic inlet flow profile assumption. [56]

Blood flow is modelled as an incompressible fluid with unsteady 3D Navier-Stokes governing equations, with a Central Differencing scheme for spatial differentiations and interpolations as well as a Crank-Nicholson second order scheme for time-marching. A density of 1000kgm^{-3} and a dynamic viscosity of 0.004 Pa s are assumed. The SIMPLE-Consistent (SIMPLEC) pressure correction method [105] [41] and an algebraic multigrid method for convergence acceleration are used. [158]

A radially symmetric parabolic velocity profile is prescribed at the inlet of each aneurysm geometry. The periodic variation of the mean inlet velocity of each vessel is scaled to fit volumetric flow curves generated from a 1D model of the arterial tree. [123] The flow rate profiles for the Internal Carotid and Middle Cerebral Arteries are both shown in figure 3.15. Three full cardiac cycles are simulated with the flow distribution only measured in the third cycle in order to remove as many transient effects of the pulsatile flow profile as possible.

Simulations are run for each aneurysm geometry with and without the four different designs of flow-diverter implanted. Transient simulations are run with a time-step of 0.01 seconds for three cardiac cycles at 75 BPM, totalling 2.40 seconds. Time-step sensitivity studies at 0.05, 0.01 and 0.005 seconds indicated that a time-step of 0.01 seconds is appropriate for these flows and is typical of similar CFD studies. [69] [85] [149] All simulations converge to a stable solution with

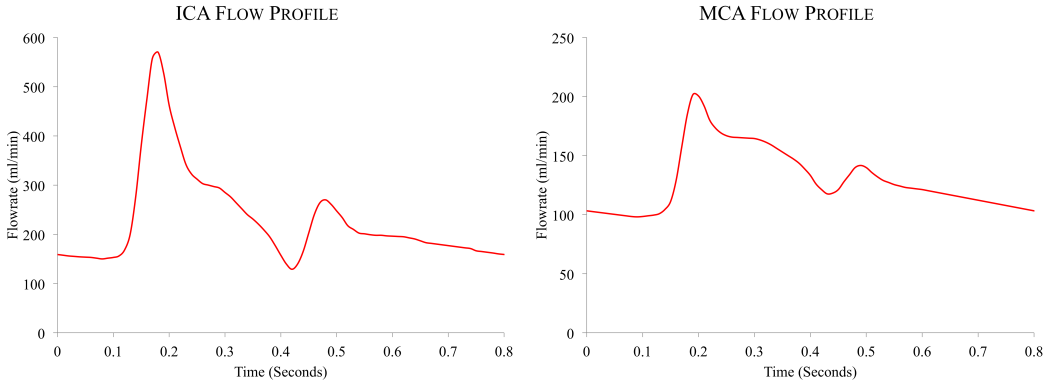

(a) *ICA Profile* **(b)** *MCA Profile*

Figure 3.15: *Parent vessel flow profiles*

a solution time for each time-step of around 40 minutes when run on up to 64 2.93GHz cores, depending upon mesh size. Each time-step of the simulations is found to typically converge to five orders of magnitude residual reduction in 50-100 iterations with no individual time-step exceeding 500 iterations.

A fixed pressure boundary condition is applied to all outlets of each geometry. It should be noted that this condition may be unrealistic for vessels that are subsequently jailed after stent deployment, when a higher back-pressure is likely. Although artery-specific pressure profiles based on 1D flow network calculations may be incorporated into simulations to represent the relative back-pressure of different vessel sizes and arterial beds, imposing these conditions on a vessel both pre- and post-intervention is problematic if the vessel is jailed by a flow-diverter. In order to investigate the sensitivity of predicted flow reduction to such a pressure change induced by vessel jailing, a series of steady state simulations are performed with Stent I deployed and an increasing back-pressure boundary condition imposed at the jailed outlet vessel. This test is only conducted on the ICA_Giant geometry as the other two geometries contain no vessels jailed by the flow-diverter.

Simulations are run with the same solver parameters discussed previously, but with a steady state inflow rate of 230ml/min. The outflow pressure boundary condition of the jailed ophthalmic vessel is increased up to +500 Pa (3.75 mmHg) in increments of 100 Pa. The aneurysm inflow rate for each outlet pressure is calculated, and the percentage reduction in aneurysm inflow calculated from the inflow recorded for the same geometry with no device deployed and a 0 Pa

outlet condition. This change in aneurysm inflow reduction is plotted in figure 3.16 in addition to the jailed vessel flow rate, relative to the flow rate seen in the simulation with a 0 Pa outlet pressure condition.

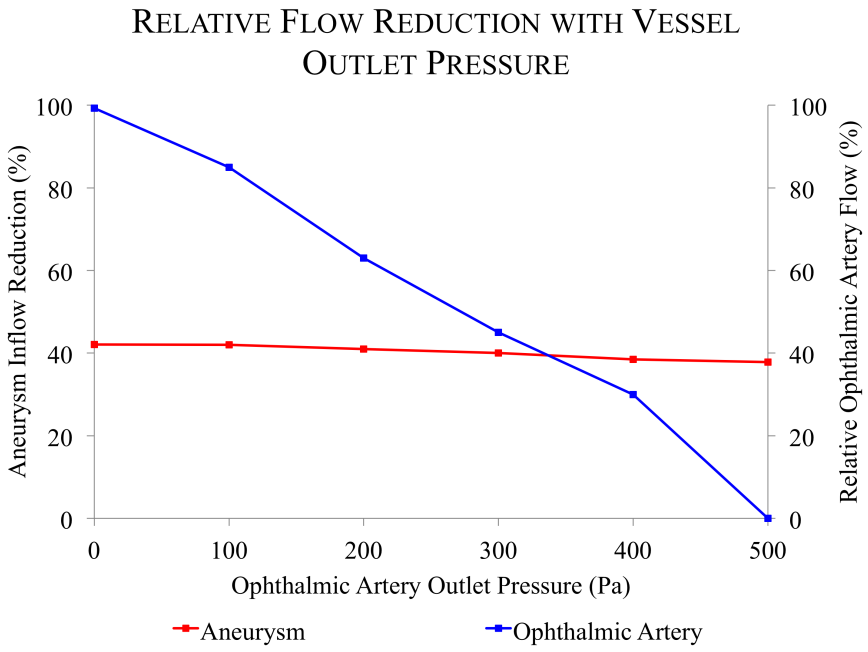

Figure 3.16: *Changes in both aneurysm inflow reduction and Ophthalmic artery flow due to variation in outlet pressure condition (Stent I)*

A variation of 4.3% is seen in aneurysm flow reduction for Stent I (42.1% reduced to 37.8%) despite a near 100% reduction in ophthalmic artery flow between the 0 Pa and +500 Pa simulations. Thus, the effect of the fixed pressure boundary condition at the jailed vessel can be considered small. The assumption of a constant fixed pressure outlet boundary condition for all vessels is further reinforced by the close correspondence to *in-vivo* measurements of the relative proportions of outflow seen in the daughter vessels of the ICA_Giant and ICA_Bifurc simulations with no device deployed. [123] [58] [126]

3.3.3 Results: Flow Reduction

The bar chart in figure 3.17 summarises the reduction over the cardiac cycle in aneurysm inflow due to each stent deployed in the respective geometry. The range of percentage flow reduction over the cardiac cycle is indicated in black on each mean value.

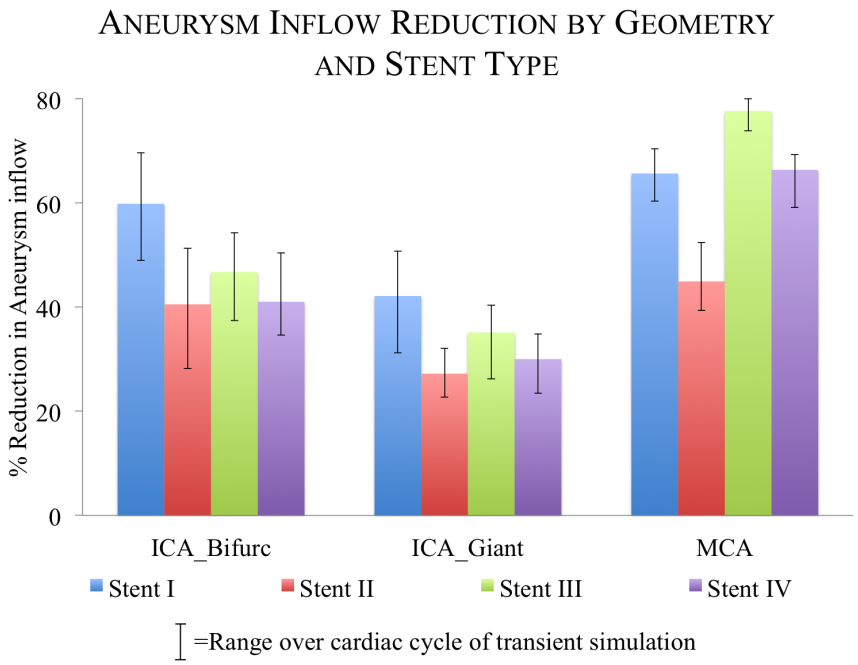

Figure 3.17: *Reduction in aneurysm inflow due to device deployment in each aneurysm geometry*

Across the three aneurysm geometries a considerable range in mean flow reduction (27.2-77.6%) is seen over all four stents, as shown in figure 3.17. An even greater range of instantaneous flow reduction is seen over the entire cardiac cycle with flow reduction as low as 22.7% and as high as 88.0% observed. Consistently across all three geometries and both parent vessel flow profiles (MCA and ICA), the lowest flow reduction is seen at peak systole, when parent vessel flow is at its highest. The greatest flow reduction is seen at the dicrotic notch, when parent vessel flow is at a minimum. The considerably higher range of parent vessel flow over the cardiac cycle seen in the ICA geometries (ICA: 130-570 ml/min, MCA: 95-205 ml/min) is also evident in the higher range of flow reductions (indicated in black on figure 3.17) seen in both ICA geometries. By contrast, the MCA geometry experiences the lowest variation in inflow reduction over the cardiac cycle.

The variation from the mean flow-rate over the cardiac cycle in both types of parent vessels (ICA and MCA) is markedly asymmetric, with flow maximums of 2.5x and 1.7x the mean flow for the ICA and MCA respectively, compared to flow minimums of 0.6x and 0.8x respectively. However, the variation of inflow reduction about the mean seen across all geometries and flow-diverter types appears considerably more symmetric; both the maximum and minimum inflow reductions fall approximately equidistant from the mean inflow reduction in all cases. The

largest percentage variation in inflow reduction is seen for the ICA_Bifurc geometry with Stent II deployed where an inflow reduction of 40% ± 12% is seen, despite a parent vessel flow that varies by +150% and - 40% from the mean value.

In the cases of Stents I and II, the assumption that a lower porosity stent produces a greater reduction in aneurysm inflow is supported, with the 70% porosity mesh of Stent I redirecting 15-20% more aneurysm inflow than the 80% porosity mesh of Stent II across all three aneurysm geometries. The lowest porosity device, Stent I, gives the greatest flow reduction in two-thirds of the geometries, but surprisingly in the MCA geometry, Stent III (80% porosity diverging mesh) outperforms Stent I (70% porosity rhomboid mesh). Stent III also outperforms the other 80% porosity devices in the remaining two geometries. This suggests that while generally a lower stent porosity results in greater inflow reduction for a given mesh design, certain mesh design traits may offer substantial increases and decreases in this performance.

The sensitivity of inflow reduction to mesh design seems to be aneurysm geometry specific with the greatest variation in device performance seen in the MCA geometry. This is further reinforced by the flow patterns seen in figure 3.18. Little difference in aneurysm flow patterns is seen between Stents I and III deployed in ICA_Giant, but for the MCA geometry, a substantially flatter flow profile that infiltrates the aneurysm sac much less is seen in the case of Stent III when compared to Stent I.

These differences in flow patterns are also visible in the aneurysm entry planes. Figure 3.19 shows both the velocity magnitude and vorticity of flow at the aneurysm neck of the MCA case. The velocity profile of the flow is shown for both mean and maximum parent vessel flow rate with darker areas indicating the region of aneurysm inflow.

For the MCA geometry the action of the different mesh topologies appears quite different, which results in substantial variation in flow pattern and inflow region shape. The rhomboid mesh of Stent I and (less so) Stent II confines aneurysm inflow to the proximal portion of the MCA aneurysm neck (left-hand side in figure 3.19), with flow exiting in the distal half of the neck. The vorticity in the inflow region is markedly lower for the rhomboid devices, and Stent I in particular, suggesting behaviour that is consistent with the results of section 3.2.3, with the high pore-density rhomboid mesh of Stent I eliminating almost all in-plane velocity components of

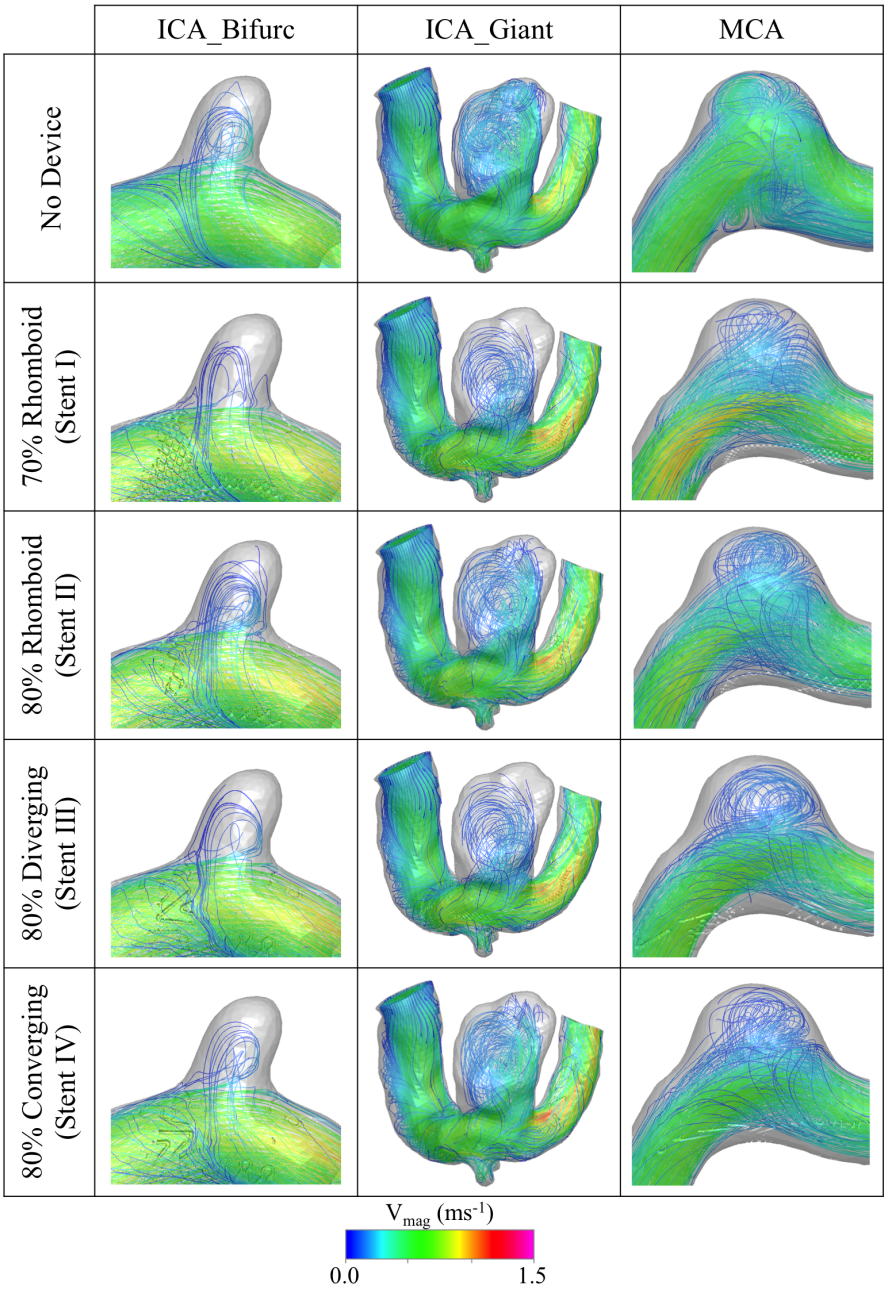

Figure 3.18: *Streamlines of flow (lines tangential to instantaneous velocity vectors) at mean parent vessel flow rate across all three aneurysm geometries with and without a flow-diverting stent deployed*

the aneurysm inflow.

In figure 3.19, substantial vorticity components are seen at the aneurysm neck for Stent III. In particular, these vorticity components appear to follow the angle of the diverging mesh and result in a chequerboard pattern of positive and negative vorticity. This pattern of vorticity suggests that Stent III generates locally adjacent areas of opposite vorticity, leading to flow being 'flattened' by the device (as shown in figure 3.18), and is subsequently either redirected

out of the aneurysm via the two 'sides' of the neck, or the flow forms the central vortex structure seen in figure 3.18.

In the Stent IV case, a similar magnitude of in-plane vorticity is seen to Stent III. However, the converging nature of the mesh design appears to concentrate the flow towards the centre of the aneurysm neck, and not towards the sides of the neck as in Stent III, which results in high velocity-magnitudes and greater flow infiltration into the aneurysm dome for Stent IV, as visible in figure 3.18.

Stent II appears to performs particularly badly in the MCA geometry for two reasons: firstly, the rhomboid mesh reduces the vorticity of the flow entering the aneurysm dome allowing the inflow to penetrate deeper into the aneurysm (compare Stent I and II with II and IV in figure 3.18) and effectively reducing the resistance to flow entering the aneurysm dome; secondly, the flow that does enter the aneurysm dome is substantially faster moving than for Stent I (compare Stent I and II in figure 3.19) owing to the higher porosity (80% vs. 70%) of the device.

The flow patterns of figure 3.19 show substantial variation in both velocity magnitude, shape and in-plane vorticity resulting from changes in mesh design alone, which reinforces the assertion discussed previously: that the performance of flow-diverter designs in the MCA geometry is governed by mesh design as much as by porosity.

Conversely, the vorticity and inflow region shape at the aneurysm neck of the ICA_Bifurc and ICA_Giant geometries, shown in figure 3.20, shows very little variation across the three different flow-diverter mesh topologies. From the detailed inflow and outflow patterns seen in figure 3.20 it is clear that for these two geometries, the success of the different flow-diverters is primarily determined by porosity and the subsequent degree of inflow velocity reduction. In the ICA_Giant case in particular the relatively identical inflow regions, vorticity and local velocity magnitude result in very little variation in flow reduction ($\approx$27-33%) across all three 80% porosity devices.

Finally, parent vessel flow at the vessel cross-section immediately before the aneurysm, is shown for each geometry in figure 3.21. Both velocity magnitude and vorticity are plotted for the plane indicated in each geometry. The MCA case in figure 3.21 shows a vorticity and velocity profile similar to a that of pressure-driven flow in a curved pipe, which is not surprising given the visual

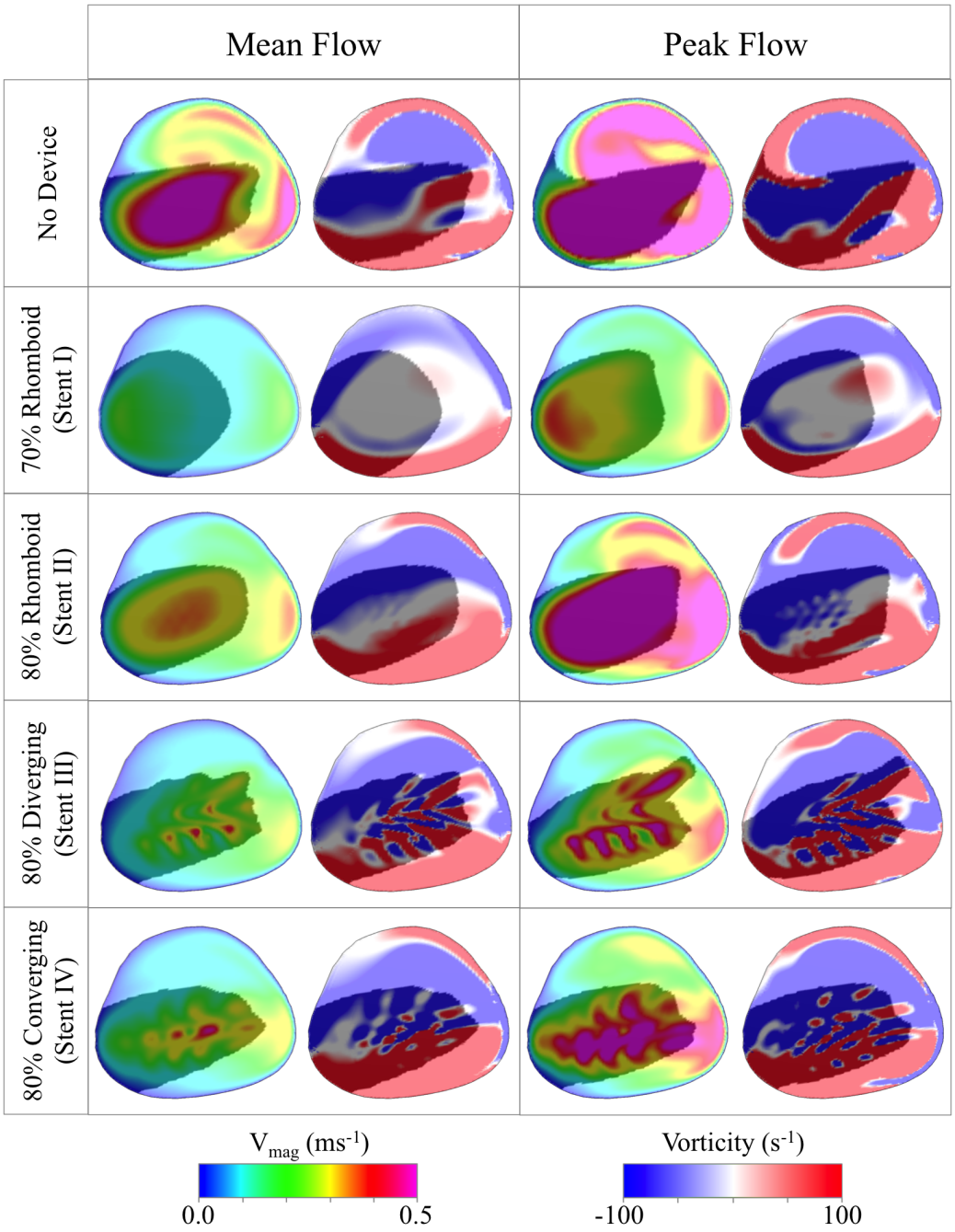

Figure 3.19: *Aneurysm inlet planes for the MCA geometry. Velocity magnitude and vorticity are indicated for mean and maximum flow rate. Darker areas correspond to the region of inflow.*

similarity between the MCA geometry and the curved pipe geometries discussed in section 3.2.3. The same is also true, but to a lesser degree, of the velocity profile, vorticity and vessel shape for the ICA_Bifurc geometry in figure 3.21. By contrast, the highly tortuous nature of the ICA_Giant vessel geometry creates a cross-sectional flow profile that is very distorted, when compared to a concentric Poiseuille regime.

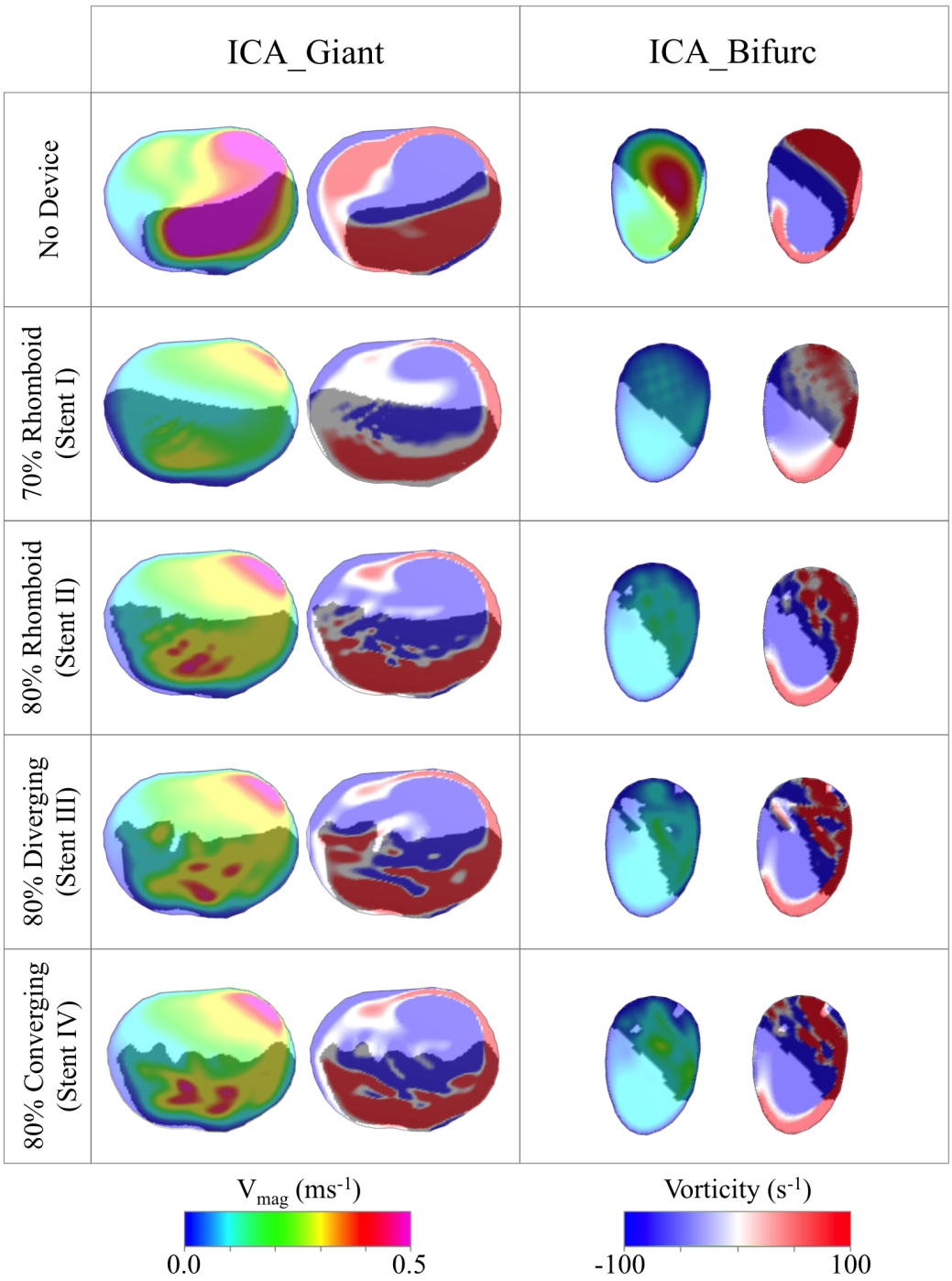

Figure 3.20: *Aneurysm inlet planes for the ICA_Bifurc and ICA_Giant geometries with velocity magnitude and in-plane direction indicated*

These differences in the shape and complexity of the flow immediately proximal to the aneurysm neck may provide an explanation for the increased influence of device mesh shape on aneurysm flow pattern seen in the MCA geometry. Additionally, the angle of flow striking the device mesh may be highly influential. In both the ICA_Bifurc and ICA_Giant cases, flow enters the

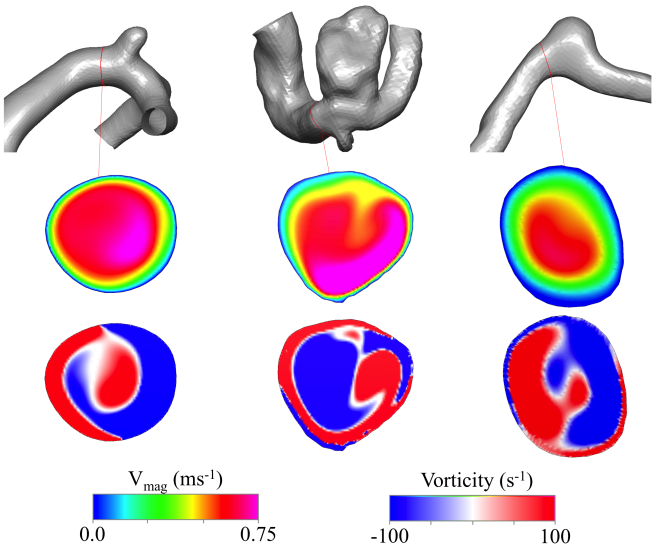

Figure 3.21: *Parent vessel velocity magnitude and vorticity profiles at mean flow rate for cross-sections proximal to each aneurysm*

aneurysm in a classic 'shear-driven' manner, with flow then striking the device mesh at a very shallow angle. In the MCA case, the flow entering the aneurysm strikes the mesh at an angle closer to that seen in the curved pipe geometries of section 3.2.3, where the mesh patterns of Stents III and IV were shown to add significant vorticity to flow.

The variation of aneurysm inflow reduction seen across stent designs and aneurysm geometries challenges the assumption that flow reduction of a device is primarily governed by mesh porosity and pore size. It is generally considered that for a given porosity a flow-diverter mesh design with a larger number of smaller filaments results in greater flow reduction. [84] This rationale assumes that the primary means of flow-diverter action is by a hydraulic resistance dominated by the increased skin friction of many small stent struts. The dramatically different performance of Stents III and IV, which have the same pore size, strut diameter and porosity, suggests that large-scale flow effects, influenced (if not dominated) by large stent mesh shape variation and features, may also have an important role to play in flow-diverter design. The action of flow-diversion appears to be quite different between Stents I and II and that of Stents III and IV: Stents I and II appear to resist flow by means of the fine mesh offering a frictional resistance to fluid passing through it. However, Stents III and IV appear to redirect or steer flow out of or into the aneurysm respectively. Considering the deployment of Stents III and IV across the aneurysm geometries, the Diverging or Converging mesh patterns alone appear to introduce

a variation in inflow reduction of 5-10%, with the Diverging pattern of Stent III consistently outperforming the Converging mesh of Stent IV.

3.3.4 Results: Wall Shear Stress

The aneurysm WSS distributions at mean arterial flow rate are shown in figure 3.22, where each geometry is indicated prior to placing a flow-diverter and also with each device design implanted. Across all the geometries, areas of elevated WSS correspond to regions of relatively high-speed flow impingement (see flow streamlines in figure 3.18.)

The WSS pattern in the aneurysm dome of the ICA_Bifurc geometry is relatively unchanged by either the presence or absence of a device or by different device designs that are implanted. The only significant change visible after deployment of any device design in the geometry is the elimination of an area of locally elevated WSS on the proximal face of the aneurysm dome (left-hand side of the dome in in the figure). However, this area of locally elevated WSS (around 3Pa) is well within the range of normal physiological values of WSS, hence the ICA_Bifurc geometry would be considered at a low risk of growth or rupture if left untreated. The removal of this local WSS peak and the general reduction of WSS throughout the ICA_Bifurc aneurysm to a very low value by all devices suggest that aneurysm isolation by significant thrombus formation would be likely regardless of the device implanted. Given that the flow pattern within the ICA_Bifurc aneurysm dome does not change substantially after device deployment, remaining as a classic shear-driven vortex in all cases, the change in WSS pattern is attributed to a reduction in flow velocity in the aneurysm dome alone (clearly visible in figure 3.18).

The spatially-averaged WSS values for the ICA_Bifurc aneurysm detailed in figure 3.23support the pattern seen visually, with a substantial reduction (greater than 75%) in mean WSS after deployment of any device design. The reduction in mean WSS achieved by Stent I (70% porosity) is considerably greater than that of Stents II-IV (80% porosity) and reduces the observed WSS to a value very close to zero. Given the small variation in WSS reduction across the three 80% porosity designs with varying mesh topologies, it appears that for the ICA_Bifurc case both inflow reduction are WSS reduction are primarily governed by device porosity.

The reduction in aneurysm inflow (and hence mean inlet velocity) achieved by the different

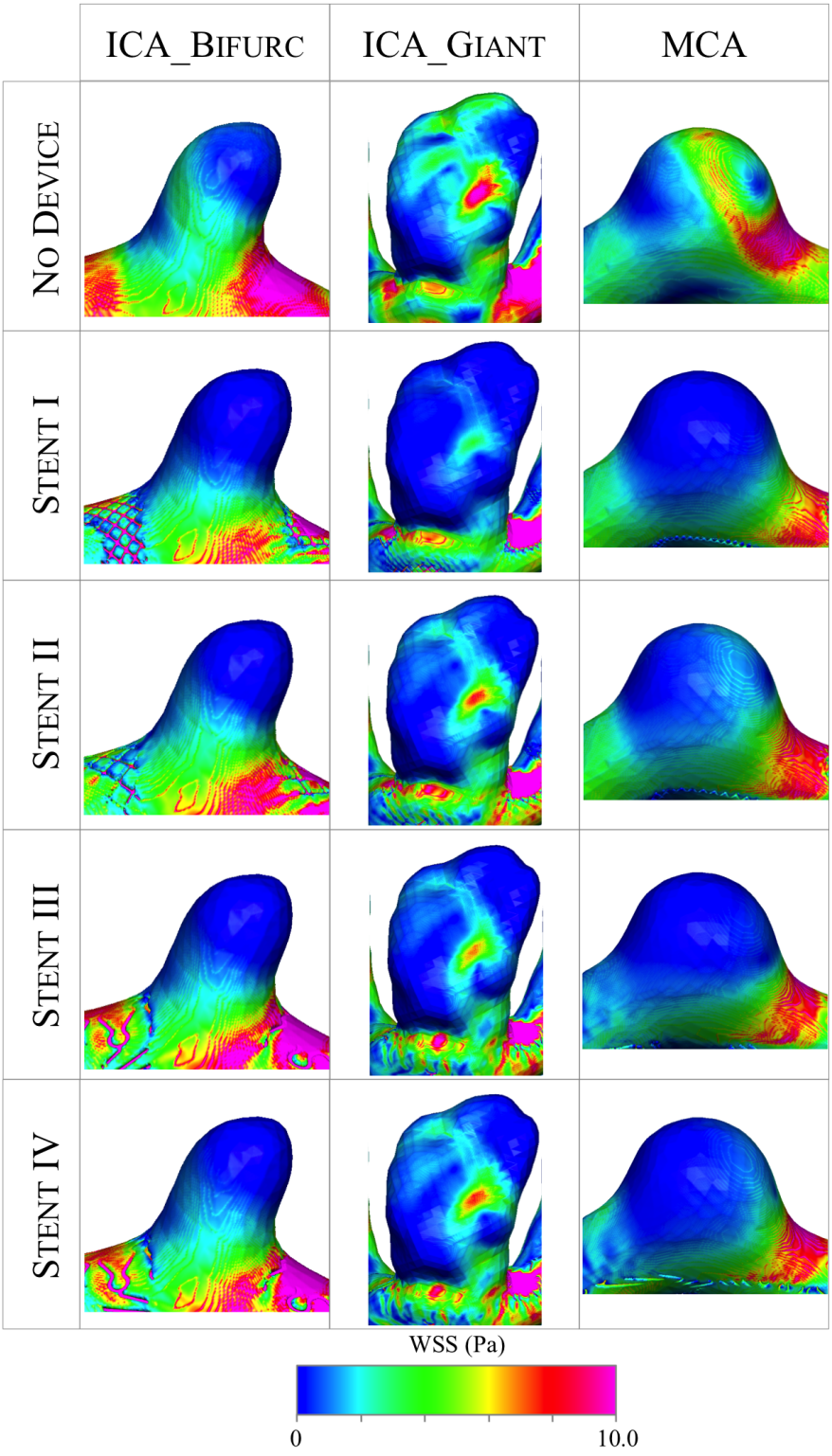

Figure 3.22: *WSS at mean flow rate*

devices is of the order of 40-60%, but the reduction in average WSS is around 75-94%. This reinforces the notion that even in this seemingly simple single-vortex flow pattern, flow within

the aneurysm dome is highly complex compared to Poiseuille-like flow environment, where WSS and flow rate are directly proportional.

Finally, the ICA_Bifurc aneurysm geometry would be considered low-risk by clinical metrics being a small, relatively narrow-necked, side-wall aneurysm, an assumption supported by the maximum and mean WSS values within the aneurysm dome falling in the range of a healthy cerebral vessel. [92]

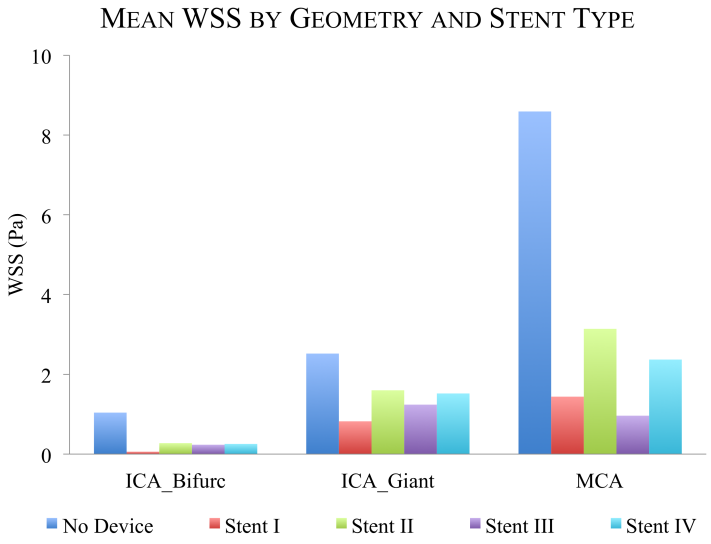

(a) *Mean WSS*

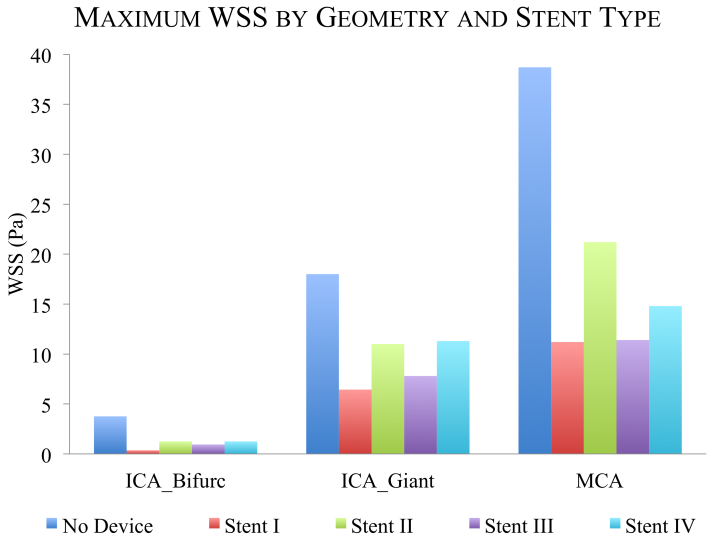

(b) *Maximum WSS*

Figure 3.23: *Spatially-averaged and maximum WSS values for the dome of each aneurysm at mean arterial flow*

Although the ICA_Giant aneurysm with no device deployed has a mean WSS value in the

normal physiological range, the clearly elevated area visible mid-way up the aneurysm dome may present some clinical concerns. All of the flow-diverter designs reduce the size and peak value of the elevated region, but in all cases the WSS in the region remains high with a peak value greater than 6 Pa (see figure 3.23).

The greatest reduction in both spatially-averaged and maximum WSS is achieved by the lower porosity flow-diverter, Stent I, which is consistent with the greater inflow reduction also seen. Across the three 80% porosity meshes (Stents II-IV) the WSS distribution is broadly unchanged, but the absolute value of WSS varies significantly. From figure 3.23 it is clear that the the performance of Stent II and Stent IV are almost identical in both mean and maximum WSS reduction, but Stent III creates a reduction in both mean and maximum WSS around halfway between the other two 80% porosity designs and the 70% porosity device. Visually, this greater reduction can be attributed to the reduced flow penetration into the aneurysm dome in the case of Stent III. This is especially noticeable in figure 3.18, where a small area of relatively fast-moving flow is present in the top-right corner of the aneurysm dome in the Stent II and Stent IV geometries but is entirely absent in the Stent I and Stent III cases.

It appears that unlike the ICA_Bifurc aneurysm geometry, for the ICA_Giant case, reduction in aneurysm dome WSS is governed by both porosity and mesh design. The reduction in mean WSS falls in the range of 37-67%, consistently higher than the corresponding reduction in aneurysm inflow of around 25-40%.

The WSS reduction achieved by each design of flow-diverter is quite different in the MCA geometry, although as before in both the ICA_Bifurc and ICA_Giant cases, the broad pattern of WSS remains relatively unchanged. The large fraction of high-speed flow entering the aneurysm dome in the 'No Device' case of the MCA geometry (see figure 3.18) results in highly elevated average and peak WSS values as shown in figure 3.23. Such a large departure in WSS from the 'physiologically normal' value of around 2 Pa would suggest the aneurysm is at risk of complications if not treated, consistent with the clinical metrics of low aneurysm-aspect-ratio and aneurysm location.

All four designs of flow-diverter reduce the mean WSS seen in the aneurysm dome to a value considered more typical of the vasculature, but the maximum WSS values seen remain very high

(greater than 10 Pa), especially in the case of Stent II.

From figure 3.23 it is clear that the greatest reduction in mean WSS is achieved by Stent III, despite having a higher porosity than Stent I. As previously discussed, regarding Stent I in the ICA_Giant geometry, here the reduced WSS values seen in the case of Stent III appear to visually correlate with reduced flow infiltration into the aneurysm dome (see figure 3.18). Additionally, the more coherent flow pattern introduced into the aneurysm dome by Stent III, with a single vortex centred on the approximate centre of the aneurysm dome, results in less flow impacting the aneurysm wall, which in-turn substantially reduces the WSS. In all other flow-diverter designs (Stents I,II and IV) the flow pattern within the aneurism dome is relatively unchanged from the 'No Device' case: a jet of flow enters the aneurysm and strikes the dome at the distal wall, leading to an elevated area of WSS. Significant variation in mean and peak WSS reduction is seen in the MCA geometry with changes in mesh design alone. Unlike in the previous two geometries, ICA_Bifurc and ICA_Giant, in this case, the flow-diverter performance appears to actually be dominated by mesh design over porosity, with a range of 20% reduction in mean WSS attributed to porosity variation, and a range of 26% attributed to changes in design. Once again, the reduction in mean WSS achieved (63-89%) is substantially greater than the corresponding reduction in aneurysm inflow alone (44-78%).

The maximum values of WSS shown in figure 3.23 may be somewhat spurious, and these values should be viewed with caution as they may not representative of the WSS pattern as a whole. Although areas of elevated WSS are common (such as the clearly elevated area of WSS seen in the ICA_Giant geometry), the maximum values in figure 3.23 for the ICA_Bifurc and MCA cases are commonly associated with the surface of a geometry that is not perfectly smooth. Evidence of this effect can be seen in high-WSS areas of the ICA_Bifurc and MCA geometries, where bands of mid-range and elevated WSS values create unrealistic contours of WSS resulting from artefacts of smooth continuous surfaces being represented by finite voxels. A similar WSS pattern emerges in areas of the mesh that adjoin the flow-diverter mesh; sharp edges of the flow-diverter are rendered as perfectly rigid arterial wall, resulting in highly elevated WSS, which would be substantially reduced *in-vivo* by mechanisms of vessel deformation and remodelling. Broadly, any maximum value of WSS from a rigid-wall simulation is likely to highly overestimate the absolute value of WSS when compared to that experienced in the *in-vivo* environment.

3.3.5 Anatomically Accurate Geometry Conclusions

The changes in aneurysm flow pattern after deployment of a flow-diverter device vary considerably over the three cases discussed. In the ICA_Bifurc aneurysm, all device designs resulted in little change in aneurysm flow pattern, but did induce an overall reduction in aneurysm velocity. The complex flow patterns within the ICA_Giant geometry showed some variation after device deployment with more successful devices reducing aneurysm inflow velocity and flow infiltration as well as creating a more coherent, and less chaotic, flow pattern. Finally, the MCA aneurysm showed the greatest variation in flow pattern after device deployment with the most successful device restructuring the flow pattern within the aneurysm dome from a high-velocity jet violently impacting the distal aneurysm wall to a relatively low-velocity single vortex with localised flow at a tangent to the aneurysm wall.

The WSS patterns seen within each aneurysm do not change dramatically from the WSS distribution with no device deployed. The deployment of a device reduces both the mean and maximum WSS magnitude within the aneurysm dome, and this reduction in WSS is consistently greater than the corresponding reduction in aneurysm inflow alone, suggesting the aneurysm WSS values are highly sensitive to the complex flow environment within the aneurysm dome.

3.4 Conclusions

A number of large-scale flow effects have been observed in both idealised pipe geometries and patient-specific anatomically accurate aneurysm geometries. In some cases these flow patterns remain un-altered after treatment with a flow-diverter, but in other cases the flow pattern varies as a result of subtle changes in the mesh design of the flow-diverter devices alone. Different flow-diverter mesh topologies have been shown to introduce varying degrees of vorticity into flow passing through the mesh. In some cases, dramatically different flow patterns within the aneurysm sac result from treatment with devices of identical porosity but very small changes in mesh design.

Rhomboid mesh designs, like that of existing flow-diverter devices, have been shown to act in a porosity-dominated fashion; the relatively small mesh pore size dissipates flow and removes

almost all vorticity, resistance to flow is achieved by a frictional reduction in velocity alone.

The shaped mesh topologies that have been discussed, the Converging and Diverging cases, produce different percentage reductions in aneurysm inflow despite having a common porosity. In one aneurysm geometry in particular, dramatically different aneurysm flow patterns, attributed to mesh topology alone, result from treatment with each device. The action of both the Converging and Diverging mesh designs is to both resist flow and to impart some degree of vorticity the flow passing through the meshes. The presence and directionality of this vorticity appears to be the determining factor in any changes in flow pattern observed. Flow reduction in these meshes is achieved by both frictional reduction of flow velocity and by a redirection of the flow into or away from the aneurysm dome.

Despite a reduction in the magnitude of maximum and mean WSS in the aneurysm dome after device deployment, the pattern of the WSS distribution remains relatively unchanged. Areas of peak WSS, most often associated with flow jetting and impingement, often remain in the same location after device placement. WSS and flow reduction are not simply linked, as would be the case for pressure-driven flow in a straight pipe. Consistently across all devices and aneurysm geometries, reductions in spatially-averaged and peak WSS at mean flow rate are reduced by a greater percentage than aneurysm inflow reduction, reinforcing the non-linear relation between inflow reduction and WSS reduction.

Finally, it is apparent that anatomically accurate aneurysm geometries can introduce highly complex flow patterns in both the parent vessel and aneurysm dome. Such complex flow renders the outcome of aneurysm treatment with a flow-diverter highly non-trivial. Hence, simple resistance-based metrics such as mesh pore-size and porosity offer very limited insight into treatment success.

Chapter 4

Alternative Flow-Diverter Design Concepts: the 'Sphere' Device

This chapter describes the development and testing of a novel, non-cylindrical flow-diverter device. The device concept is introduced in section 4.1 and investigated in an idealised aneurysm geometry in section 4.2. The analysis is extended to six anatomically accurate aneurysm geometries in section 4.3. Finally, the device performance is compared to the action of commercially available flow-diverter devices in section 4.4.[1,2]

4.1 Introduction

Current designs of cerebral flow-diverter in clinical use are exclusively of a cylindrical, tubular design. Both the PED (Covidien/ev3, Irvine, CA) and the SILK flow-diverter (Balt Extrusion, Montmorency, France) are formed of interwoven wires.

While such flow-diverter designs present an elegant treatment solution for sidewall aneurysms, treatment of bifurcation aneurysms with flow-diverters remains problematic. The closed-cell

[1]The work presented in section 4.3 of this chapter has appeared as part of: T W Peach, J F Cornhill, A Nguyen, H Riina, and Y Ventikos. The 'Sphere': A Dedicated Bifurcation Aneurysm Flow-Diverter Device. Cardiovascular Engineering and Technology, 5(4):334-347, 2014 [110]

[2]The work presented in section 4.4 of this chapter appears as T W Peach, K Spranger and Y Ventikos. Towards Predicting Patient-Specific Flow-Diverter Treatment Outcomes for Bifurcation Aneurysms: From Implantation Rehearsal to Virtual Angiograms. Annals of Biomedical Engineering (Forthcoming)

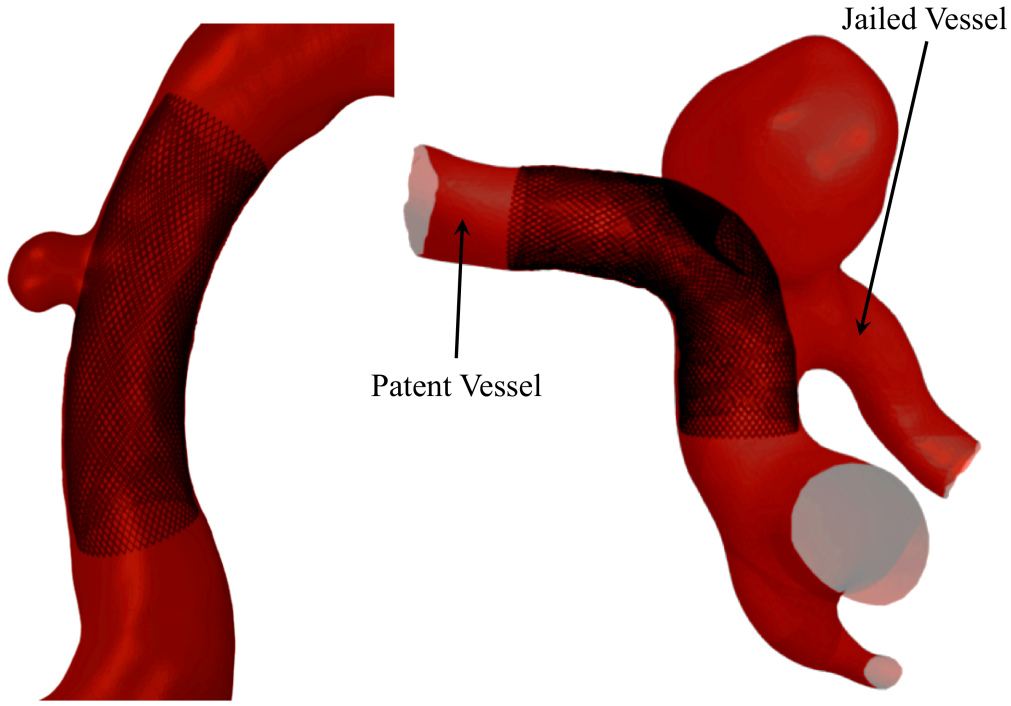

Figure 4.1: *Conventional flow-diverter design deployed in both a sidewall and bifurcation aneurysm*

cylindrical nature of current flow-diverter designs makes the jailing (covering of the vessel lumen with a device mesh) of all but one daughter vessel inevitable during treatment. This is illustrated in figure 4.1 (right).

These concerns have been replicated in the clinical cases reported in the literature. A study conducted by Saatchi et al. [130] included 46 'uncoilable' aneurysms that originated at vessel bifurcations. Although successful treatment with the PED was reported in 41 cases, in the five remaining cases (10.9%) complete occlusion of the daughter vessel was reported, which resulted in the death of one patient. Many of the early concerns related to flow-diverter treatment (risks of emboli transport and in-stent thrombosis as well as incomplete re-endothelialisation) are especially acute for the treatment of bifurcation aneurysms with flow-diverters. Perhaps as a consequence of this, there are very few examples in the literature of bifurcation aneurysms treated with either SILK or PED, but the cases that are presented have high variability in treatment outcome. [78] [87]

Alternative concepts to the conventional cylindrical flow-diverter have been proposed to better

address the treatment of bifurcation aneurysms and reduce treatment morbidity and mortality. The most significant alternative is the WEB device (Sequent Medical, Aliso Viejo, CA), as discussed in chapter 1. The WEB device is capable of treating a bifurcation aneurysm without daughter vessel occlusion by morphing a Nitinol mesh, similar to conventional cylindrical flow-diverters, into a collapsible ball that may be deployed within the aneurysm dome. [74] [113] The device is then secured within the aneurysm sac itself by expanding to oppose the vessel wall in a similar manner to conventional coiling. It is unknown whether or not a relatively high radial force device deployed inside the aneurysm dome alters any risk of aneurysm weakening, enlarging or rupture, as is the effect of such forces on wide-neck and giant aneurysms in particular.

In this chapter a design is proposed for a novel device with flow-diverting functionality, intended to specifically treat bifurcation aneurysms. The device, now known as the 'Sphere', is a Nitinol spherical frame that presents a high-density face to the aneurysm neck in order to reduce inflow. It is secured by 'legs' in the form of multiple open hoops that form part of the spherical frame, which are deployed in the parent vessel distal to the aneurysm. Thus, all bifurcation daughter vessels remain uncompromised following treatment, unlike some interventions using conventional cylindrical flow-diverters. In addition, the device is secured in a non-diseased portion of the artery where high radial force, of the order of conventional cylindrical flow diverters, is not a concern. Additionally, no portion of the flow-diverter device enters the delicate aneurysm dome.

4.2 Idealised Aneurysm Geometry Simulations

4.2.1 Aneurysm and Device Geometries

A prototype flow-diverter device is shown in figure 4.2 (left). The device is developed by the Minimally Invasive New Technologies (MINT) group based at Weill Cornell Medical School, New York. The flow-diverting action of the device is achieved by a dense, woven face that is secured at the neck of the aneurysm with four flexible legs.The device is constructed from a single loop of 0.104mm diameter Nitinol wire with an effective porosity of ≈70% at the device face and a face size of 4x5mm. The device is packaged for deployment by securing two of the legs

to a delivery catheter after the legs have been 'pulled apart' returning the device to its 'single loop' configuration. Upon releasing the two secured legs *in-vivo*, the device returns to the woven configuration of figure 4.2.

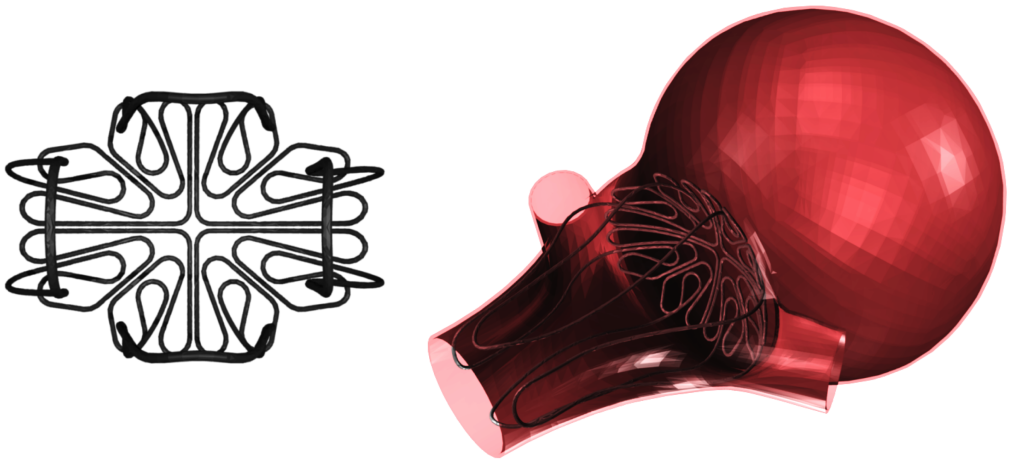

Figure 4.2: *Prototype device and the idealised bifurcation aneurysm geometry*

An idealised geometry, based on a Basilar tip bifurcation aneurysm, is used to test the device's performance. The geometry has a parent vessel of 3mm diameter representing the Basilar Artery (BA) and two daughter vessels of 2mm diameter corresponding to the posterior cerebral arteries (PCAs). The superior cerebellar arteries (SCAs) are not represented in the geometry. The aneurysm is modelled as an approximate sphere with a diameter of 11mm.

4.2.2 Simulation setup

The prototype device is manually deployed within the idealised aneurysm geometry in the 3D computer graphics package Blender. An entirely rigid vessel wall is assumed. The prototype device is shown deployed in the idealised aneurysm geometry in figure 4.2 (right).

The aneurysm geometry is imported into CFD-VisCART and meshed. Meshing is completed with a projected single domain con-conforming mesh, an omnitree cartesian tree type, and three near-wall cartesian layers to give smooth and well-resolved boundary definition.

The simulation meshes are imported into the multi-physics suite CFD-ACE+. Blood flow is modelled as an incompressible fluid with unsteady 3D Navier-Stokes governing equations, with

a Central Differencing scheme for spatial differentiations and interpolations, as well as a Crank-Nicholson second order scheme for time-marching. The blood fluid is assumed incompressible and Newtonian with a density of 1000 kgm^{-3} and a dynamic viscosity of 0.004 Pa s. A rigid arterial wall is assumed, as it has been shown to have little effect on the flow patterns seen when compared to simulations with elastic compliant walls. [39] The SIMPLE-Consistent (SIMPLEC) pressure correction method [105] [41] and an algebraic multigrid method for convergence acceleration are used. [158]

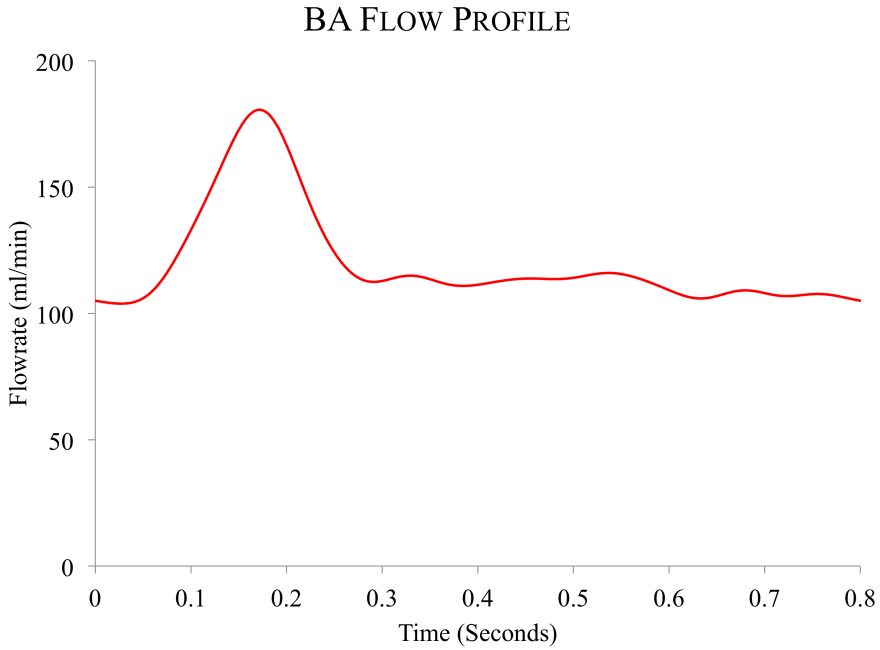

Figure 4.3: *BA flow profile*

The periodic variation of the parent vessel mean inlet velocity is scaled to fit volumetric flow curves generated from a 1D model of the arterial tree. [124] A typical flow profile for the Basilar artery is shown in figure 4.3, with a mean flow rate over the cardiac cycle of 120ml/min. Steady state simulations are run with mean flow of 120ml/min. Poiseuille flow is assumed and a parabolic, radially symmetric inflow profile prescribed. Inlet Reynolds numbers for the transient simulation fall in the range of 176-310, while the pulsatility of the flow results in a Womersely number of 2.10, which confirms that the flow remains laminar and approximately parabolic.

4.2.3 Mesh Independence

Transient flow mesh independence tests are performed on the idealised geometry with and without the device deployed. The grid independence test metric employed is the mean volumetric flow at the aneurysm neck. Meshes are generated at increasing levels of fineness with minimum cell densities in the range of 1-50,000 elements/mm^3. The solution is assumed mesh independent when the discrepancy between two consecutive meshes falls below 1% of the total inflow.

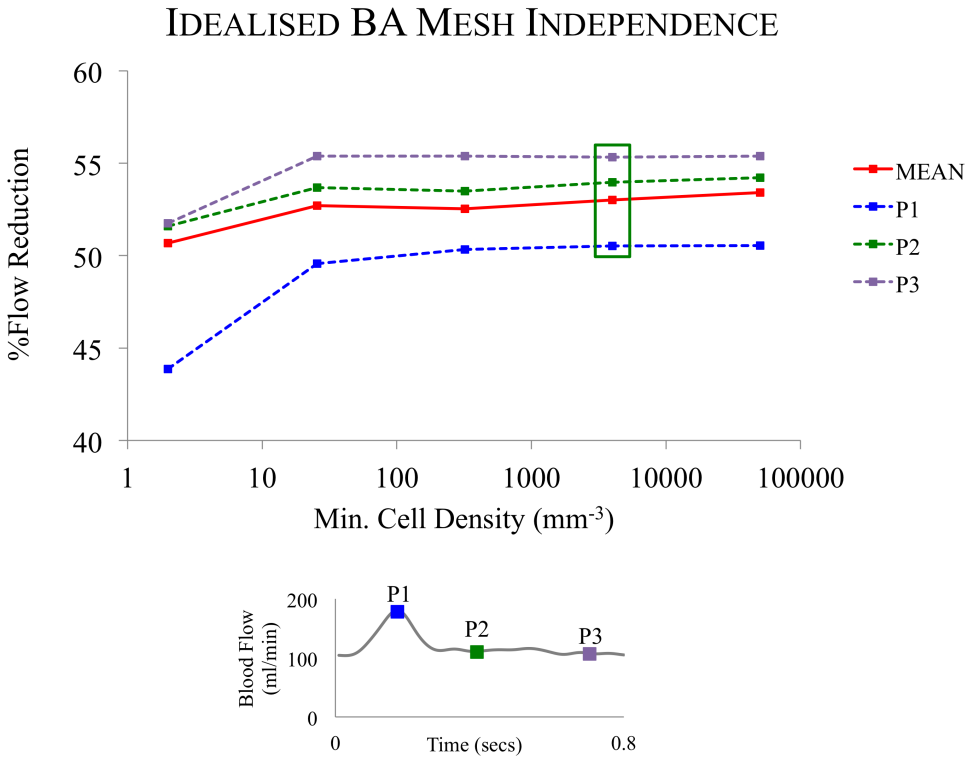

Figure 4.4: *Idealised bifurcation aneurysm geometry mesh independence*

Aneurysm inflow is measured at salient points in the cardiac cycle (peak systole, dicrotic notch etc.) with the mean aneurysm inflow computed over a single cardiac cycle. Three full cardiac cycles were simulated with results measured from the final cycle in order to remove transient effects. The study suggests mesh independence at meshes with a typical minimum cell density larger than 4000 elements/mm^3 as shown in figure 4.4. Additionally, at this level, the number of mesh elements in each geometry measurement plane exceeds the recommendation of Jou et al. [69] to fully resolve flow features. The resulting simulation meshes have sizes of 3,740,000 and 2,690,000 cells for the geometry with and without the device deployed respectively.

The independence of the transient flow solution with time-step size was also investigated. Simulations run at a time-step(Dt) of 0.05, 0.01 and 0.005 s respectively indicated that Dt = 0.01 s offered both good convergence of solution, unlike Dt = 0.05 s, and no significant change in flow pattern when compared to Dt = 0.005 s. Such a choice of time-step is consistent with similar CFD studies. [69] [85] [149] Aneurysm inflow is measured through a plane defined at the aneurysm neck. The plane must be placed as close to the natural neck of the aneurysm without falling too close to the device, which can lead to spurious results from local vorticity, as observed by Kim et al. [73] For the purpose of this analysis, this plane also defines the boundary between the aneurysm dome and parent vessel.

4.2.4 Steady and Transient Results

Transient simulations are run with a time-step of 0.01 seconds for three cardiac cycles at 75 BPM, totalling 2.40 seconds. The simulations are run on 32, 2.93 GHz cores with each time-step converging to five orders of magnitude residual reduction in around 50-100 iterations in a typical solution time of 40 minutes per time step. Steady simulations are run on 8, 2.93 GHz cores with a typical solution time around 20 hours to the same residual in under 2000 iterations. For both the steady state and transient solutions, the aneurysm inflow before and after device placement are compared to give a percentage flow reduction for a given time step.

The predicted flow-reduction due to the prototype device is summarised in figure 4.5 for both the steady state and transient simulations. For the transient simulation, the mean flow reduction is plotted in blue and the range of flow-reduction seen over the cardiac cycle is indicated in black.

From figure 4.5 it is clear that both the steady and transient simulations predict a device flow reduction of around 50%. The variation over the cardiac cycle of the flow reduction is small (4.8%), suggesting the pulsatility effects of the flow are also small, leading to good agreement between the flow reductions of the steady simulations with mean flow rate (50.5%) and the mean of the transient simulate flow reduction (53.0%).

The streamlines of figure 4.6 and figure 4.7 also suggest that there is little departure between the flow regime of the steady state solution and the instantaneous flow patterns seen throughout

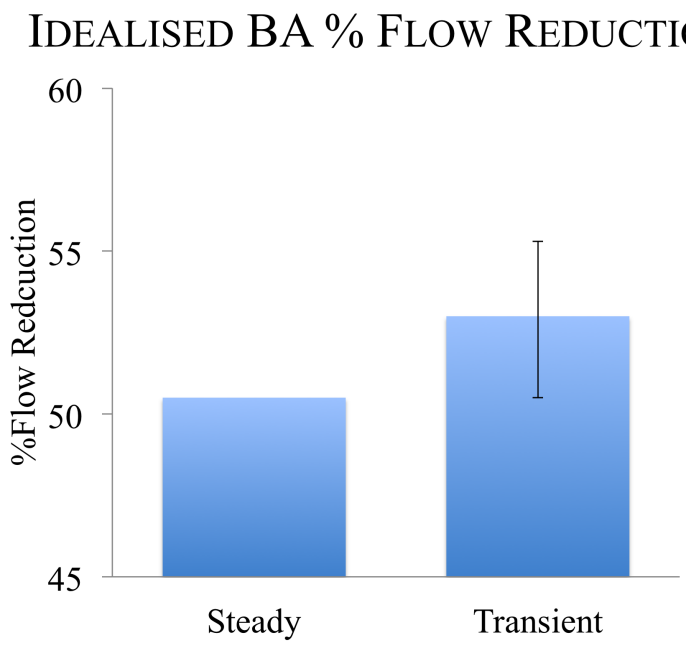

Figure 4.5: *Mean (and range of) aneurysm inflow reduction due to device deployment for the idealised BA geometry*

the cardiac cycle in the transient solution. In both the steady and transient computations of the geometry with no device deployed, the flow pattern in the aneurysm dome remains a single vortex. This flow pattern evolves from that seen in the first cardiac cycle of the transient solution. Initially, flow enters as a central jet leading to two counter-rotating vortices, by the third cardiac cycle this flow pattern has given way to the more energetically-preferential asymmetric single vortex pattern seen in the figure. This transition from the initially symmetric, but unstable, flow pattern into a more stable asymmetric regime is likely to be the cause of the very slow convergence of the steady state solution, taking almost 2000 iterations to reach convergence in the 'No Device' case.

Broadly, the action of the device appears to be to reduce the inflow into the aneurysm into four distinct jets, as shown in figure 4.6, corresponding to the four central spaces of the device. The jets have substantially reduced velocities compared to the 'No Device' case (mean inlet velocity falling from 0.402 to 0.207ms^{-1}), with the subsequent reduction in momentum destroying almost all of the vorticity seen in the aneurysm dome.

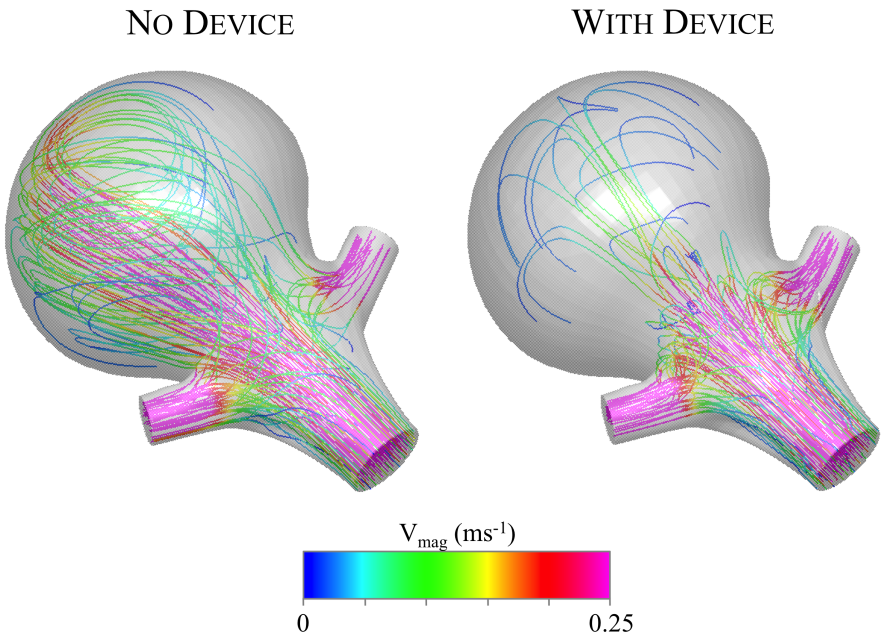

Figure 4.6: *Idealised BA geometry streamlines, steady state simulation*

4.2.5 Positioning Study

In order to quantify the sensitivity of the simulation results, a number of steady state computations are performed with the device rotated in three different planes as shown in figure 4.8. Simulations are repeated at the same mesh density and with the same solver settings as detailed in section 4.2.2. Given the good correspondence between steady and transient simulation results and the in the interests of computational efficiency, only steady state simulations are performed.

No dramatic changes in flow regime are seen, despite the device repositioning. A range of 47.5% to 54.5% flow reduction is seen across the three repositioned geometries, representing less than a 10% deviation from the 50.5% flow reduction predicted in the idealised positioned steady state simulation.

4.2.6 Conclusions: Prototype device and Idealised Aneurysm Geometry

The idealised aneurysm geometry used in the computations of section 4.2.1 is a reasonable tool for quantifying the generalised behaviour of a device, but there are some short-comings. In the idealised geometry, equal sized daughter vessels and a perfectly symmetric aneurysm dome result

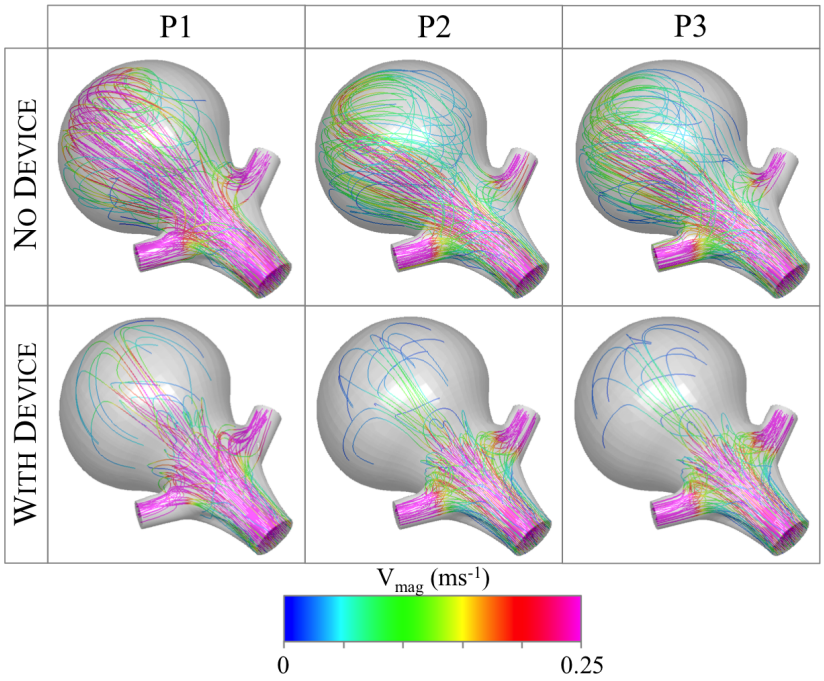

Figure 4.7: *Idealised BA geometry streamlines, transient simulation*

in a geometry that is 'too symmetric', leading to flow patterns that are symmetric but unstable and which decay into a more stable asymmetric flow regime. Such instability dramatically decreases the speed of convergence, and may lead to a lack of convergence in some cases where a solution may oscillate between a number of viable flow regimes.

For the idealised geometry, the steady state simulation at mean flow rate offers a good approximation to the flow reduction averaged over one cardiac cycle of the transient solution. Hence, considerable computational effort can be saved, but this good correspondence may not be true for anatomically accurate geometries and should be considered with caution.

Little change in flow reduction was seen as a result of device repositioning. This suggests that the precise positioning of the deployed device and the method of virtually deploying the device into position do not substantially effect the resulting flow patterns.

4.3 Anatomically Accurate Aneurysm Geometries

In following section, the previous analysis is extended to increase the accuracy and relevance of the flow environment experienced by the flow-diverter; the device is deployed in six patient-

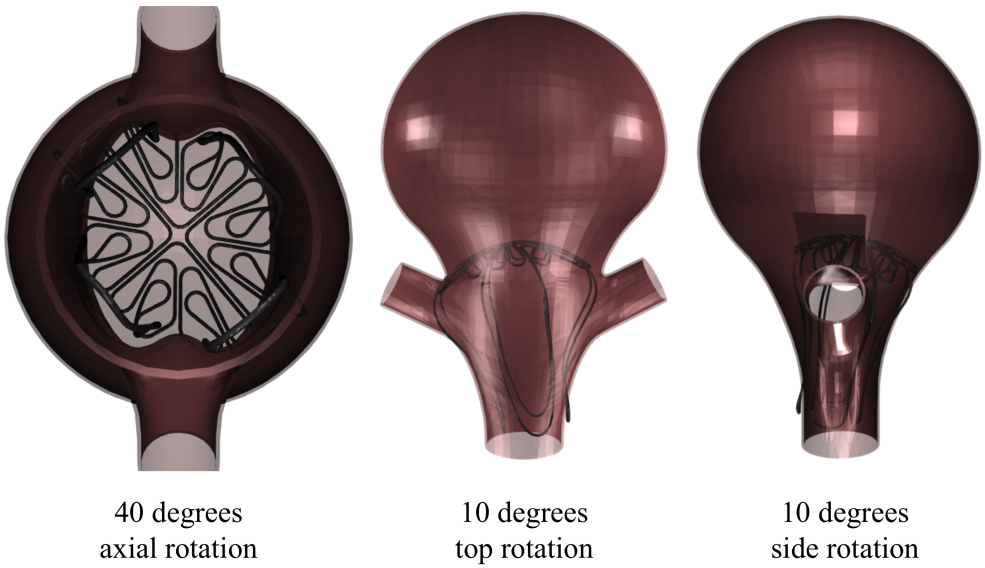

Figure 4.8: *Idealised BA geometry repositioned*

specific bifurcation aneurysms geometries with flow reduction and wall shear stress calculated. The design of the novel device is also altered to incorporate a lower porosity face, in the hope of increasing the flow-diverting action.

4.3.1 Aneurysm Geometries and Device Modifications

Six anatomically accurate, bifurcation aneurysm geometries are selected: three examples of a Basilar tip aneurysm and three examples of an Internal Carotid terminus bifurcation aneurysm. The geometries are segmented from CTA data in OsiriX(Freeware) and converted to STL format before being imported into Blender. The geometries are trimmed to result in vessel lengths of around five vessel diameters distal and proximal to the aneurysm location, as shown in figure 4.9.

A modified version of the prototype device is investigated, which is now known as the 'Sphere.' The new device has only two legs (compared to the four previously) to increase the ease of device deployment and a decreased face porosity to further increase the device's flow-diverting effect. The device is sized with a diameter between 4.50 and 6.50 mm, depending on aneurysm neck size and is constructed from a continuous Nitinol wire of 102μm (0.004") diameter. See figure 4.11 (left). The cap-like dense portion of the device is placed at the aneurysm neck, which is in turn

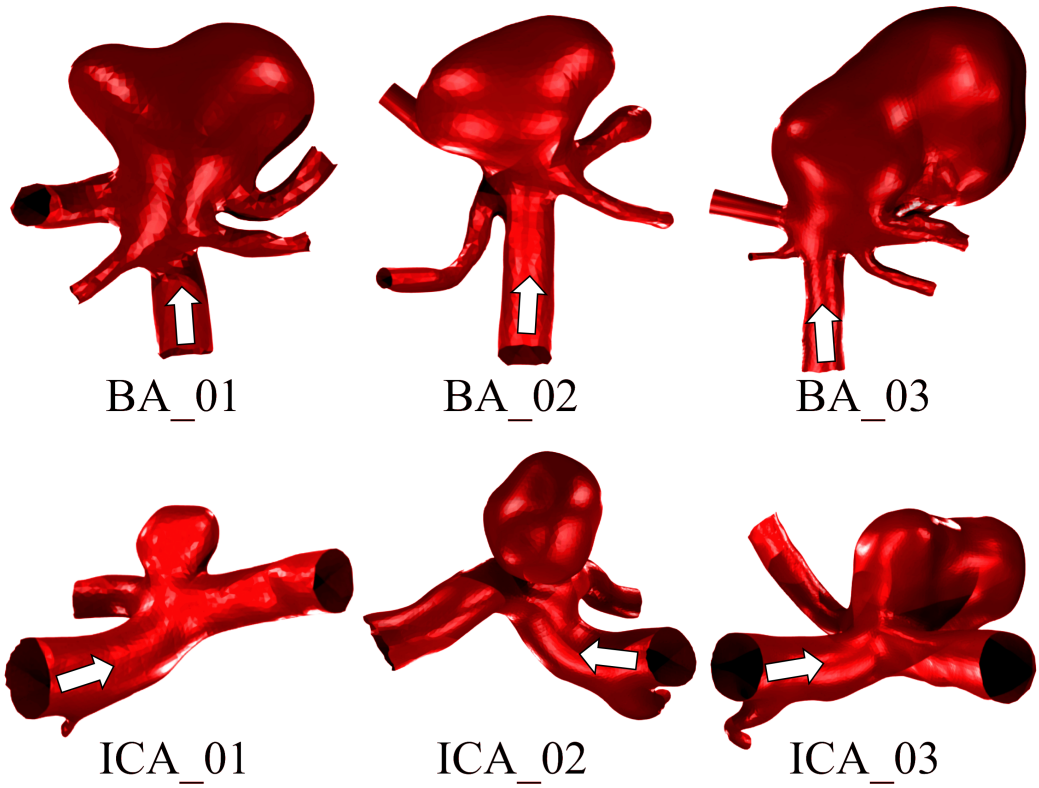

Figure 4.9: *Aneurysm geometries with inlets and direction of inflow indicated*

secured by the two device legs that are positioned in the parent vessel proximal to the aneurysm neck. The cap-like portion of the device used in this simulation, which blocks aneurysm inflow, has a porosity of 54%. A 'Sphere' device is virtually sized to both the aneurysm neck and parent vessel diameters before being virtually deployed.

4.3.2 Simulation Methodology

Modelling the deployment of the 'Sphere' device within a blood vessel is highly problematic. Fast deployment algorithms, such as that described in chapter 1, rely on a locally regular mesh-structure in order to accurately approximate the global position of the device. Such methods are therefore unsuitable for the large deflections of the irregular mesh pattern of the 'Sphere' device. An alternative method of virtual deployment is by full Finite Element Analysis (FEA), but solution stability is a concern, as discussed in chapter 1. The large deflections required to package and deploy the device combined with a lack of verified models for either vessel flexibility or vessel-device contact, render a FEA model of deployment highly complex and unstable. The

complexity and instability of the solution can be improved by assuming a rigid vessel wall and applying a substantial damping factor to the device's movement, but the resulting device position is entirely unrealistic.

In-vitro deployment rehearsals have been performed by micro-catheter delivery in silicone vessel phantoms with good device opening observed, as shown in figure 4.10.

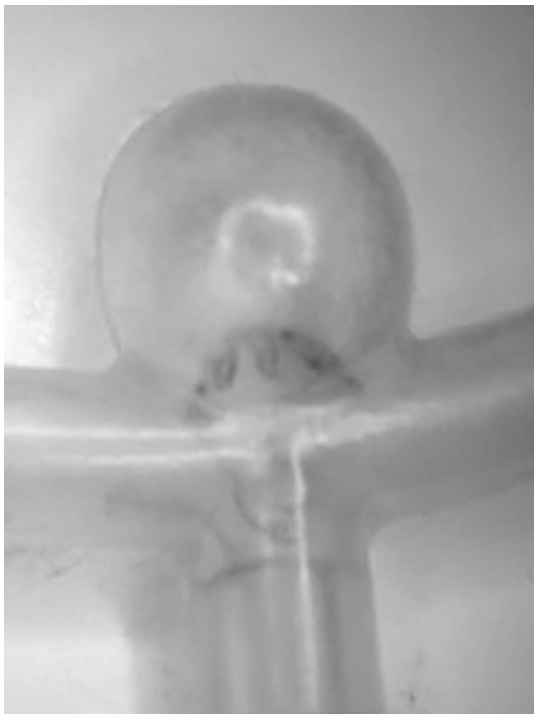

Figure 4.10: *Sphere device deployed in a silicone phantom*

Consequently, in this case, all devices are manually deployed in Blender assuming the vessel wall to be entirely rigid. The device is positioned assuming that the dense face is completely rigid and that the flexible legs, which provide device security and have no flow-diverting function, are positioned approximately. Visually, this virtual deployment method results in a device resting position very similar to that obtained experimentally.

A typical virtual device placement is shown in figure 4.11 (right).

The aneurysm geometries, with and without the device deployed, are imported into CFD-VisCART to be meshed. The meshing of each geometry is completed with a Projected Single Domain con-conforming mesh, an Omnitree Cartesian tree type, and three near-wall Cartesian layers to give a smooth and well-resolved boundary definition.

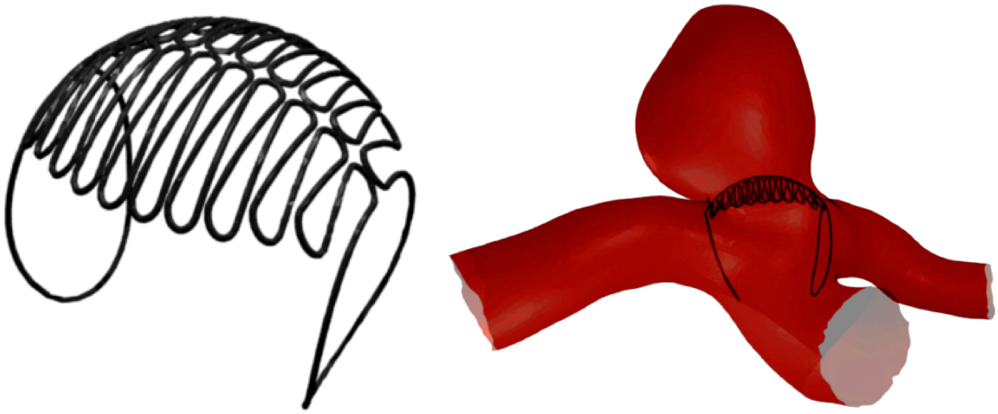

Figure 4.11: *Sphere device deployed in an aneurysm geometry*

The periodic variation of the mean inlet velocity of each vessel is scaled to fit volumetric flow curves generated from a 1D model of the arterial tree. [124] Typical flow profiles for the ICA and BA parent vessels over the cardiac cycle are shown in figure 4.3 and figure 4.12, with mean flow rates over the cardiac cycle of 230 and 120 ml/ min respectively. Steady state tests are run with mean flow of 230 ml/min for the ICA geometries and 120 ml/min for the BA geometries. Poiseuille flow is assumed and a parabolic, radially symmetric inflow profile prescribed. Inlet Reynolds numbers in the range of 274-392 are seen across the steady state simulations of the six geometries.

Transient studies are run with the same meshes but with a time-varying inflow based on the profiles of figure 4.3 and figure 4.12. A radially symmetric inlet velocity profile is prescribed and scaled to result in the same mean flow of the steady state study when averaged over the entire cardiac cycle. This results in transient simulations with mean inlet Reynolds numbers of 274-323 (range of instantaneous Re: 189-403) for the BA vessels and 306-392 (range of instantaneous Re: 169-980) for the ICA vessels. A parabolic inlet velocity profile is used as the relatively small Womersley number of the inflow (1.68-2.72) suggests little departure in velocity profile from a Poiseuille solution.

The option to include outflow boundary conditions derived from either experimentally measured flows or pressures, values originating from 1D models, or simple fixed pressure values was available. Given that the goal of this study was to compare conditions between untreated and treated

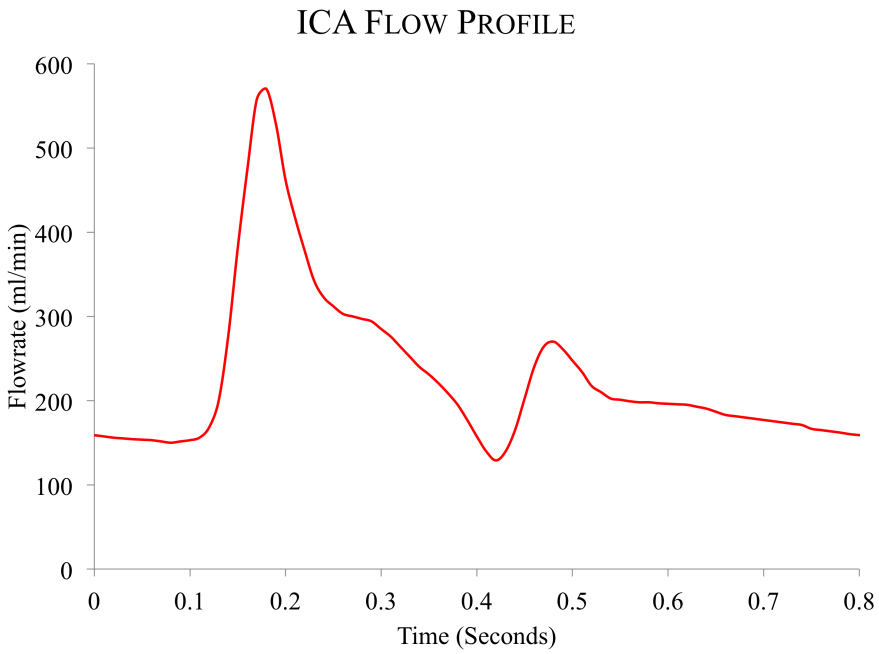

Figure 4.12: *ICA flow profile*

vessels and that access to measurements for the particular aneurysms studied was not available, the simplest possible outlet boundary condition was chosen to avoid spurious assumptions of downstream flow conditions after device deployment. Hence, in both the steady and transient computations, an outflow boundary condition of fixed pressure is prescribed at all daughter vessel outlets. Although such a condition may be less realistic than pulsatile 1D analogue models and not fully capture the different back-pressures of the circulatory branches, the relative proportions of outflow in each daughter vessel observed in this study do not differ substantially from *in-vivo* results recorded elsewhere in the literature. [58] [126]

4.3.3 Mesh independence

Transient flow mesh independence tests are performed on one aneurysm geometry from each location, with and without a device deployed (in this case geometries BA_02 and ICA_02). The grid independence test metric employed is the mean volumetric flow at the aneurysm neck. Meshes are generated at increasing levels of fineness with minimum cell densities in the range of 1-50,000 elements/mm^3. The solution is assumed mesh independent when the discrepancy between two consecutive meshes falls below 1% of the total inflow. Aneurysm inflow is measured

at salient points in the cardiac cycle (peak systole, dicrotic notch etc.) as well as computing a mean aneurysm inflow over a single cardiac cycle. Three full cardiac cycles were simulated with results measured from the final cycle in order to remove transient effects. The study suggests mesh independence at meshes with a typical minimum cell density larger than 4000 elements/mm^3 as shown in figure 4.13 and figure 4.14. Additionally, at this level, the number of mesh elements in each geometry measurement plane exceeds the recommendation of Jou et al. [69] to fully resolve flow features.

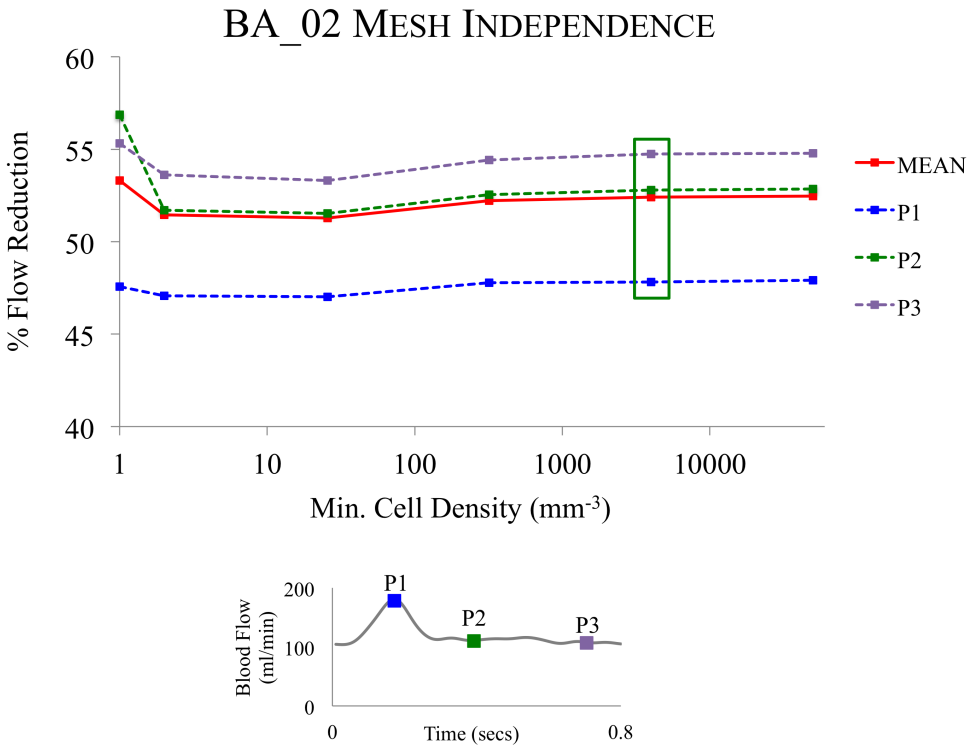

Figure 4.13: *BA geometry mesh independence*

Similar mesh independence tests were performed on all six aneurysm geometries, with and without the device deployed, but for steady-state simulation only. The simulations were run with an inlet velocity typical of the mean velocity seen across the cardiac cycle in the ICA and BA respectively. The steady-state mesh independence test suggested a similar independent cell density (4000 elements/mm^3) in five of the geometries. No convergent solution was found in the steady state for the ICA_01 geometry, possibly due to intrinsic strong unsteady flow patterns emerging due to flow instabilities, as reported by both Valen-Sendstad et al. [149] and Baek et al. [7] at high and low frequencies respectively. This extensive mesh independence analysis

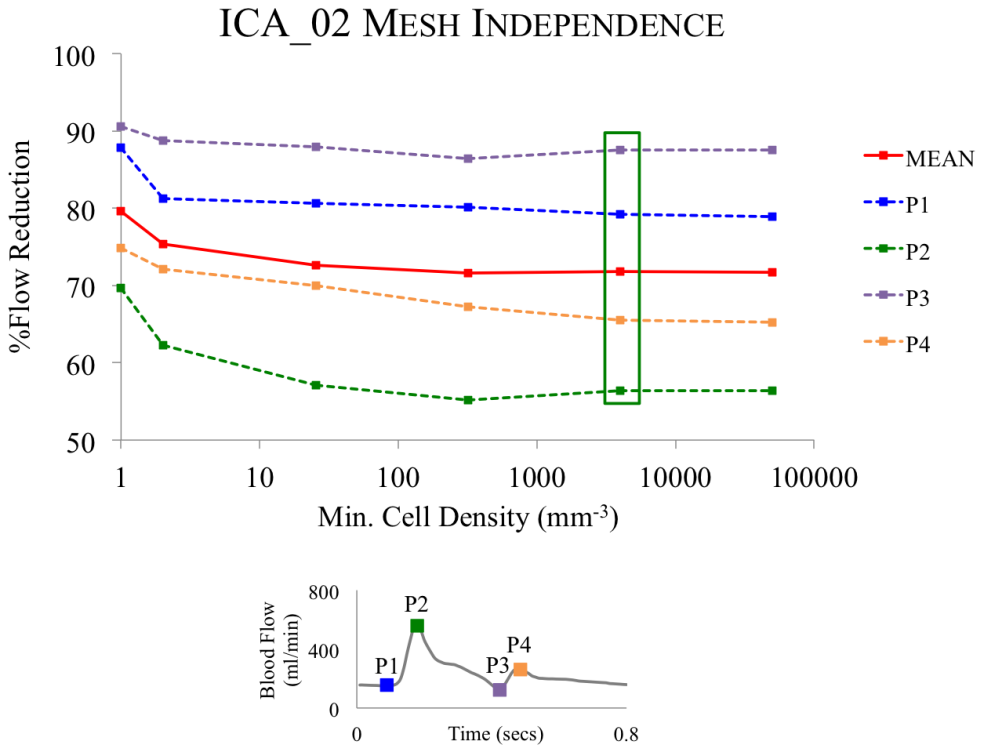

Figure 4.14: *ICA geometry mesh independence*

resulted in mesh size selections that vary between 3,410,000 and 6,520,000 elements across the geometries for both transient and steady state tests and for cases with and without the device implanted.

The independence of the transient flow solution with time-step size was also investigated. Simulations run at a time-step(Dt) of 0.05, 0.01 and 0.005 s respectively indicated that Dt = 0.01 s offered both good convergence of solution, unlike Dt = 0.05 s, and no significant change in flow pattern when compared to Dt = 0.005 s. Such a choice of time-step is consistent with similar CFD studies. [69] [85] [149]

4.3.4 Simulation Results

Transient simulations are run with a time-step of 0.01 seconds for three cardiac cycles at 75 BPM, totalling 2.40 seconds. The simulations are run on up to 32, 2.93 GHz cores with each time-step converging to five orders of magnitude residual reduction in around 50-100 iterations in a typical solution time of 40 minutes per time step. Steady simulations are run on up to 8,

2.93 GHz cores with a typical solution time around 20 hours to the same residual. No convergent steady-state solution at mean parent vessel flow rate was found for the ICA_01 geometry. An entry plane meeting the criteria previously set out is projected across each aneurysm neck, and the aneurysm inflow at each time step of the transient solution and for the steady state solution is calculated. For both the steady state and transient solutions, the aneurysm inflow before and after device placement are compared to give a percentage flow reduction for a given time step.

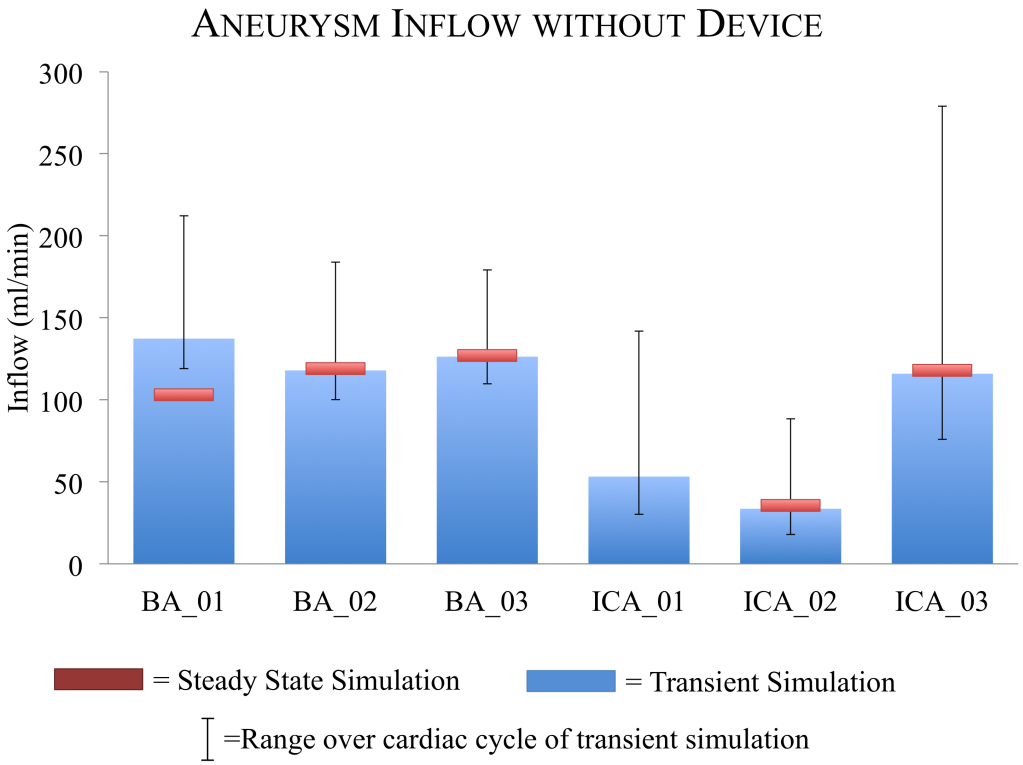

Figure 4.15: *'No Device' aneurysm inflow*

The steady state mean inflow with a device, without a device, and the subsequent flow reduction for each geometry, excluding ICA_01, are plotted in figures 4.15, 4.16, and 4.17, in red. The mean (over one cardiac cycle) inflow with a device, without a device and the subsequent flow reduction of a transient simulation is found by taking the mean of the flow reduction from each time-step and is plotted in figures 4.15, 4.16, and 4.17, in blue for each geometry. The range of inflow and flow reduction seen over the cardiac cycle for each geometry is also indicated in the figures, but in black.

The mean flow entering the aneurysm sac in the BA geometries is similar to the mean flow in

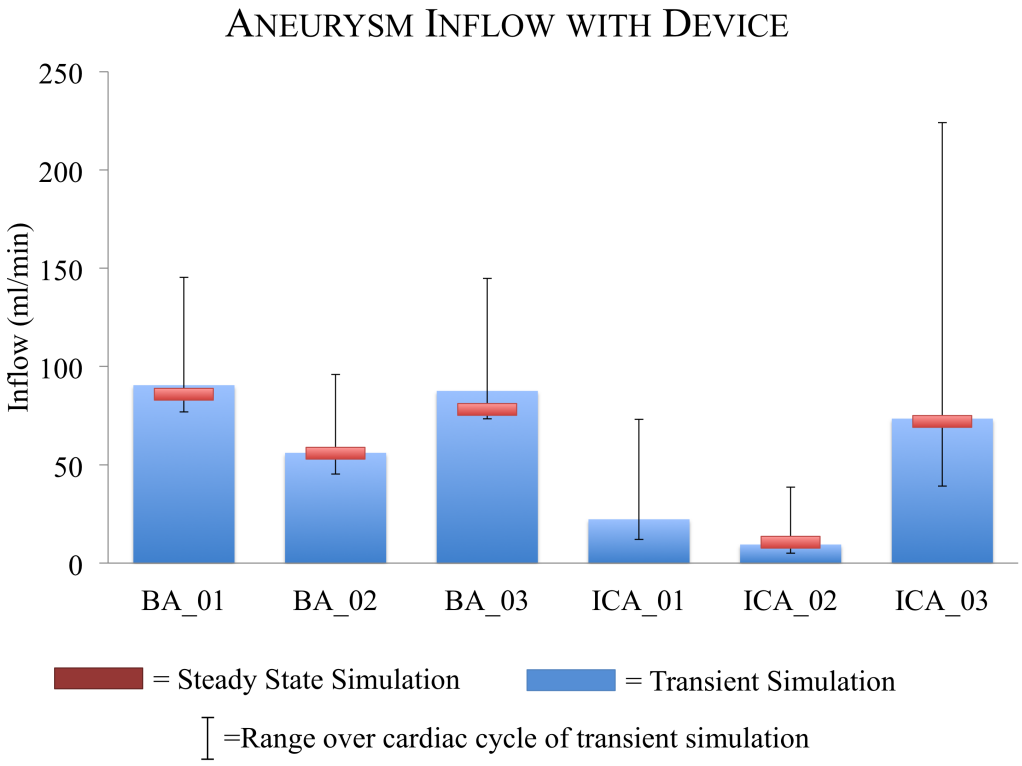

Figure 4.16: *'With Device' aneurysm inflow*

the parent vessel (120ml/min), suggesting almost all of the blood flowing in the parent vessel enters the aneurysm. The pattern in the ICA geometries is quite different. Although the mean flow in the ICA geometry parent vessels is almost twice that of the BA cases, at 230ml/min, the mean flow entering the aneurysm sac in the ICA geometries is equal or substantially less than for the BA cases. The ICA_03 geometry shows a mean aneurysm inflow of approximately half the parent vessel mean flow while the flow entering the aneurysm sac in the ICA_01 and ICA_02 cases is only 5-20% of the parent vessel flow.

A similar pattern is observed after device placement, as shown in figure 4.16. Again, the aneurysm inflow in the BA geometries, exceeds that of the ICA geometries despite the substantially higher parent vessel flow in the ICA cases. Both ICA_01 and ICA_02 also experience a very low level of aneurysm inflow after device placement, which, in the ICA_02 case, corresponds to a mean inflow of less than 5% of the parent vessel flow.

Figure 4.18 shows typical lines tangent to the instantaneous velocity vectors at a point of mean parent vessel flow in each transient simulation for the BA geometries with and without a device

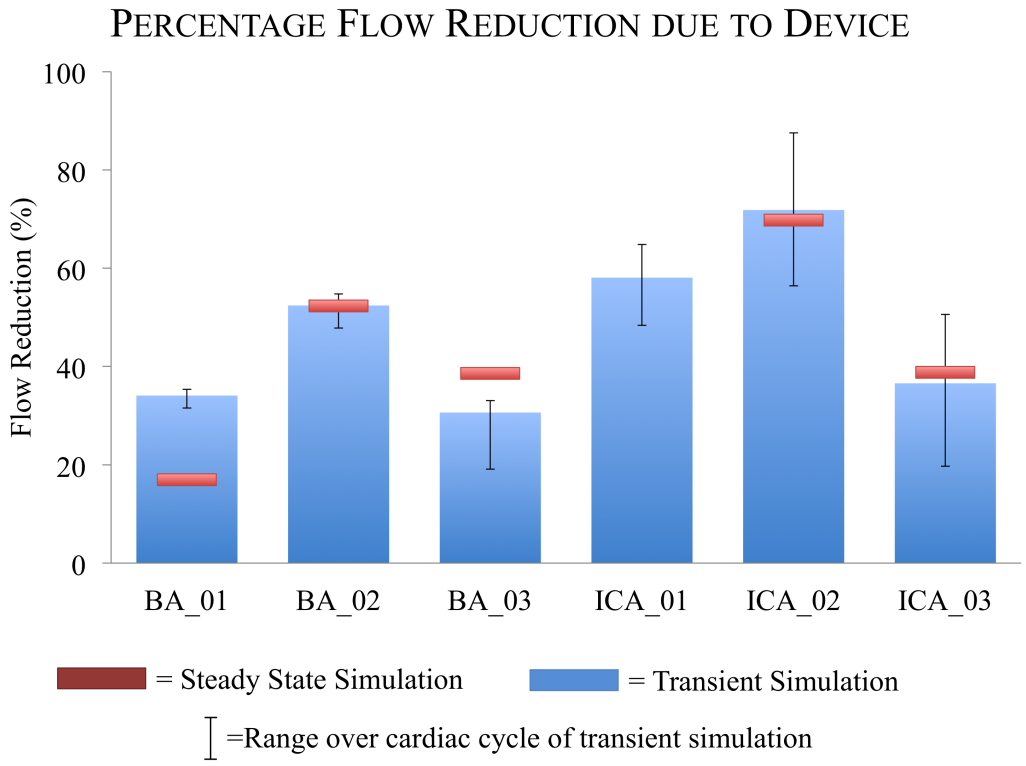

Figure 4.17: *Aneurysm inflow reduction*

deployed. In all three geometries, flow in the aneurysm sac before and after device placement is dominated by a single vortex with a small degree of, possibly, chaotic mixing. [138] A reduction in this mixing and both the mean and peak flow velocity in the aneurysm sac are seen after device deployment. The BA_02 geometry experiences the greatest reduction in aneurysm inflow and also appears to retain the simplest flow regime (a single vortex with little jetting) both before and after device deployment. The jetting seen in the BA_01 and BA_03 cases with no device is substantially reduced after 'Sphere' deployment but the flow reduction seen is some 20% less than for the BA_02 case. A more complex flow pattern remains after device deployment in these two cases, with flow violently striking the aneurysm wall before dissipating into a vortex. In all three geometries the device reduces the aneurysm inflow velocity at this mean parent vessel flow condition to typically less than 0.25 ms^{-1}.

Figure 4.19 shows typical lines tangent to the instantaneous velocity vectors for the ICA geometries with and without a device deployed. The mean flow reduction for each geometry is also indicated in both figures. The flow patterns within the aneurysm sac for the ICA cases are also dominated by a single vortex with a small amount of what is possibly chaotic mixing. The flow

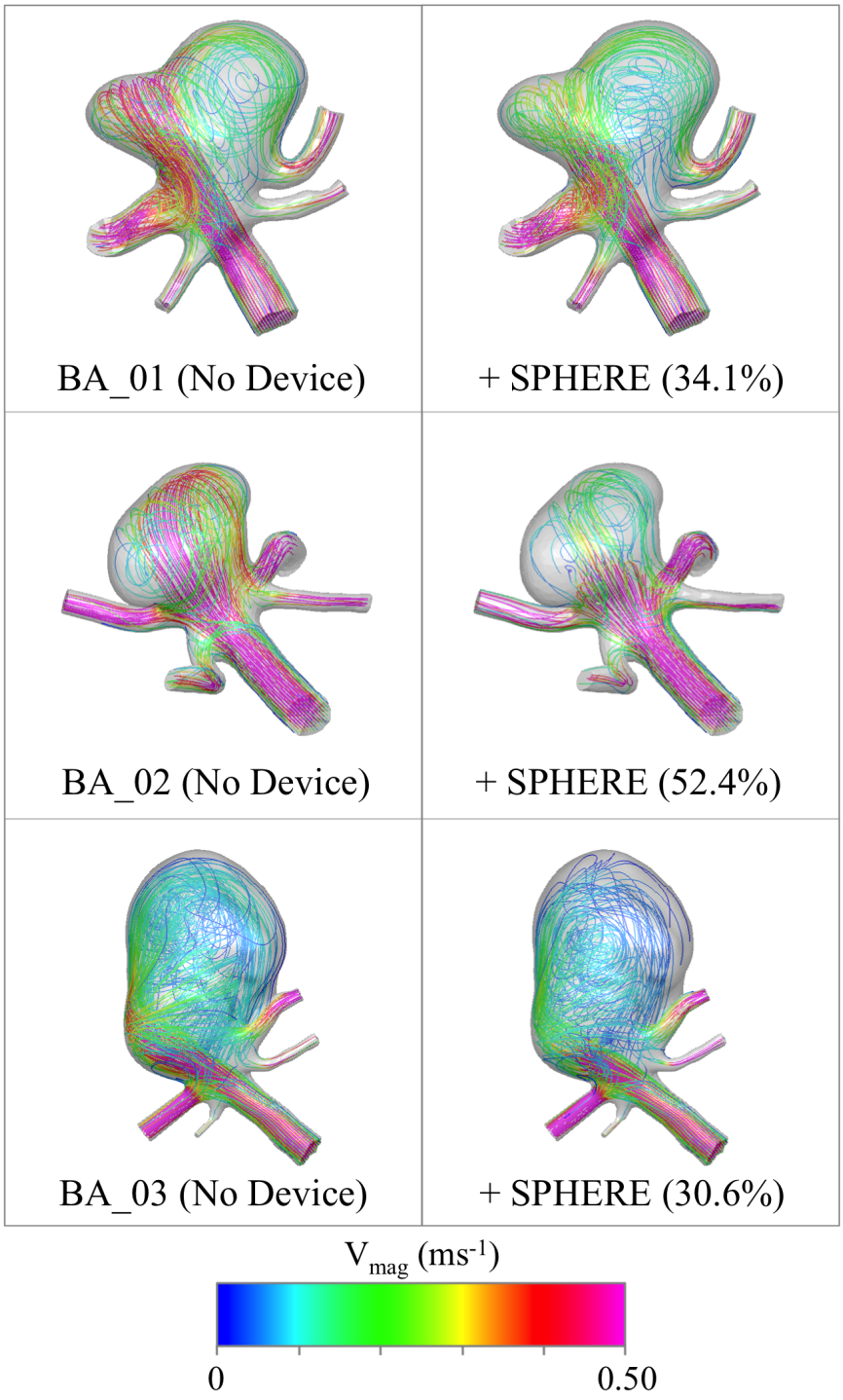

Figure 4.18: *Streamlines of flow (lines tangential to instantaneous velocity vectors) at mean parent vessel flow rate both with and without the Sphere device deployed in the BA geometries*

patterns appear less complex than for the BA cases, but a large variation (almost 40%) in inflow reduction after device, deployment is still seen. Flow velocities in the aneurysm sac are greatly

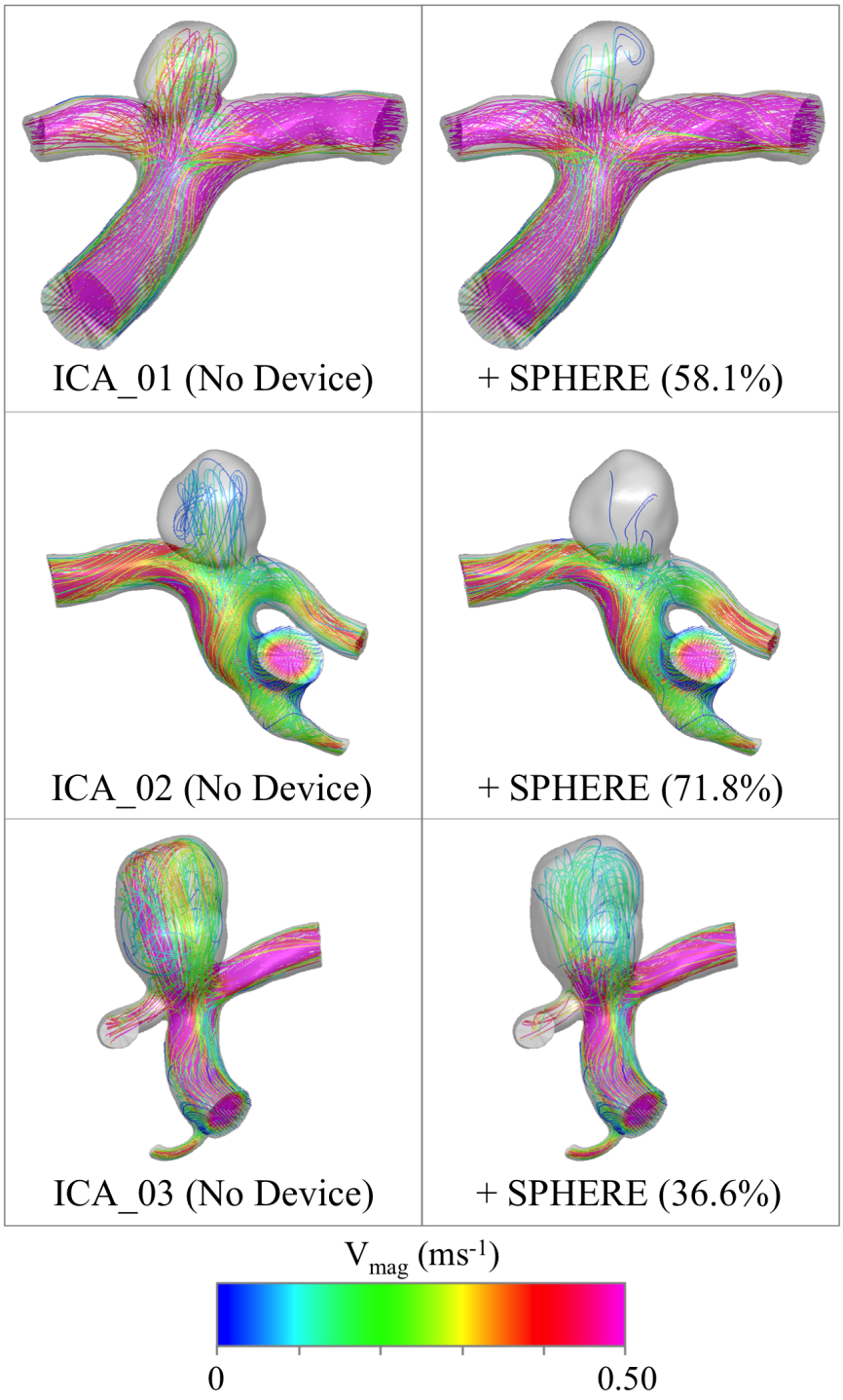

Figure 4.19: *Streamlines of flow (lines tangential to instantaneous velocity vectors) at mean parent vessel flow rate both with and without the Sphere device deployed in the ICA geometries*

reduced after placement of the device but the flow pattern of a single vortex appears unchanged, although this is less clear in the ICA_01 and ICA_02 cases with very low aneurysm inflow after

device deployment. The post-device reduction in flow velocity entering the aneurysm sac at mean parent vessel flow is greater than for the BA cases, with inflow reduced to approximately 0-0.15 ms^{-1}.

Considering figure 4.18 and figure 4.19, it appears the action of the 'Sphere' is to reduce the velocity and intensity of the flow entering the aneurysm sac with little change in the general flow pattern within the aneurysm, with the exception of BA_01 as previously discussed. In all geometries with no device deployed, the flow in the aneurysm sac appears to be dominated by a single vortex accompanied by a small degree of chaotic mixing, where the inflow jet first strikes the aneurysm wall, as also observed by Butty et al. [15] Such mixing appears less prevalent in the BA_02 and ICA_02 geometries, which both saw flow reduction in excess of 50% after device deployment. The ICA_01 geometry, however, which also saw a substantial flow reduction, has a flow pattern dominated by mixing that was subsequently reduced to a very slow moving single vortex after device deployment.

From the aneurysm inflow with no device deployed, shown in figure 4.15, it is clear that the BA and ICA geometries behave very differently with a much higher aneurysm inflow rate in the BA cases despite the lower parent vessel flow rate of the basilar artery. This phenomenon may be due to the anatomical differences in the BA and ICA termination bifurcations; in the BA cases each aneurysm is relatively wide-necked, with an aneurysm neck diameter larger than the parent vessel diameter, whereas the ICA cases are relatively narrow-necked and typically have an aneurysm neck smaller than the parent vessel. Consequently, the resistance to flow entering the aneurysm in the BA cases is much lower than in the ICA cases, which may explain the reduced flow entering the aneurysms in the ICA geometries despite a much higher parent vessel flow rate than the BA geometries. This hypothesis is also supported by the higher peak and mean velocity of the flow in the aneurysm sac of the BA geometries, despite similar parent vessel velocities between the two vessel types.

From the transient results shown in figure 4.17, it can be seen that the 'Sphere' device produces a large variation of flow reduction across the six geometries, with a range of 30.6-71.8% in mean reduction and flow reductions as low as 19.1% and as high as 87.5% seen at the peak systole and the dicrotic notch respectively. Consistently across the geometries, the greatest reduction in inflow is observed at the point of lowest parent vessel flow (dicrotic notch), and the least

reduction in inflow is observed at the highest parent vessel flow (peak systole). In the BA_01 and BA_03 geometries, there is a discrepancy between the mean of the transient prediction of flow reduction (blue) and the steady state flow reduction prediction (red) but otherwise the steady state predictions of mean flow reduction are very accurate for the remaining three geometries for which steady state solutions exist.

Finally, distributions of WSS magnitude are shown in figure 4.20. WSS magnitude is viewed from the front and back of each geometry and both with and without the device deployed. WSS plots are shown for maximum inflow at peak systole, and although the magnitude of the WSS varies, the WSS distribution remains approximately the same across the cardiac cycle. Across all geometries the 'Sphere' device reduces the overall WSS magnitude within the aneurysm dome. Peaks in WSS magnitude correspond to areas of flow impingement or jets with high velocity fields near the wall (see figure 4.18 and figure 4.19), and the reduction in flow jetting after device deployment is also apparent in the WSS distributions and is especially pronounced across the Basilar geometries and in ICA_03.

As previously discussed, the precise mechanisms of high or low WSS-induced aneurysm growth and rupture are still hotly debated; in this case, the 'Sphere' device appears to promote a healthier hemodynamic environment within the aneurysm sac by reducing the peaks of the WSS distribution to a more physiologically normal value (approx. 2 Pa), as shown in figure 4.20. The larger ICA flow rate results in increased blood flow velocity and hence higher WSS in the ICA cases. This is particularly noticeable in the ICA_01 geometry, which has a below-average vessel diameter (less than 3 mm) resulting is very large velocities (figure 4.19) and hence high WSS magnitude throughout the geometry. This effect is likely to be lessened physiologically with more elastic deformation of the larger ICA vessels, in turn reducing the WSS magnitude.

Also previously discussed, the geometries that experience the greatest flow reduction after device deployment appear to have less flow impingement/jetting in the aneurysm sac prior to device placement. This is reinforced by the WSS distributions of both the BA_02 and ICA_02 geometries where no high WSS (greater than 5 Pa) regions caused by flow jets occur in the aneurysm dome. Conversely, the three geometries that perform less favourably in terms of device flow reduction (BA_01, BA_03 and ICA_03) also have high WSS distributions with peaks from flow jets in the aneurysm sac before device placement. The ICA_01 case does not fit this pattern

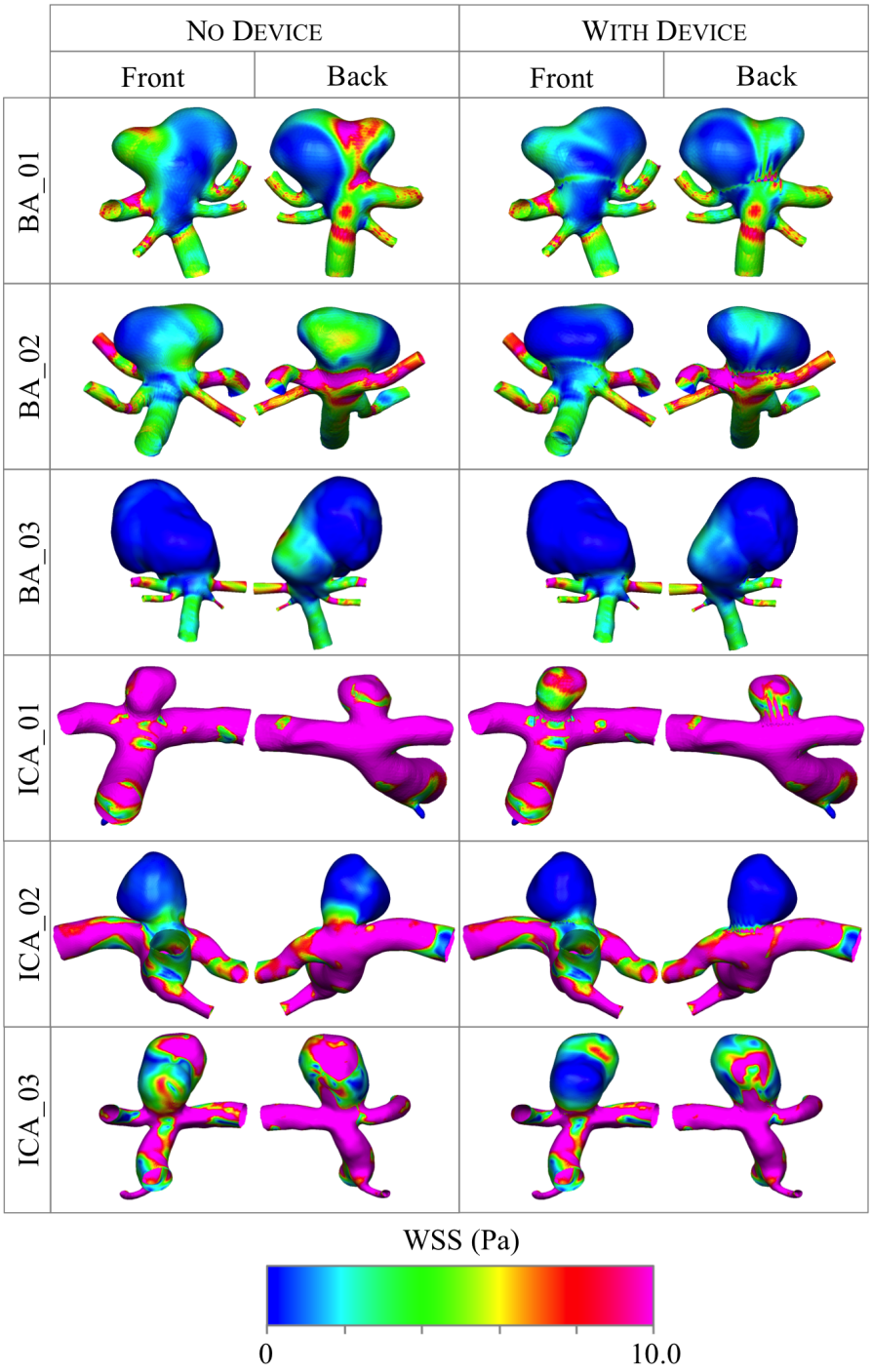

Figure 4.20: *WSS plots of all six aneurysm geometries with and without the Sphere device deployed at peak parent vessel flow rate*

of high WSS in the aneurysm sac corresponding to poor flow reduction by the device, but the smaller size of the ICA_01 aneurysm (with a height and width roughly equal to the parent vessel diameter) results in less flow jetting generally and a flow pattern in the aneurysm that is more similar to the BA_02 and ICA_02 geometries. It is also apparent that higher aneurysm inflow,

either with or without the device (figure 4.15 and figure 4.16), does not appear to correlate with increased WSS magnitude in the aneurysm sac.

The correlation between a number of geometric and flow features, and the resulting flow reduction achieved by the device was briefly investigated and summarised in figure 4.21.

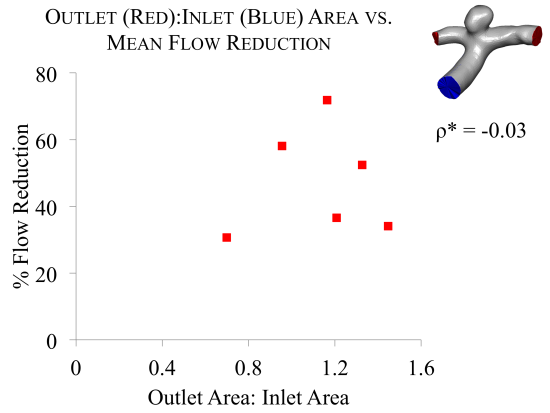

(a) *Geometry Inlet and Outlet Area Ratio and Flow Reduction*

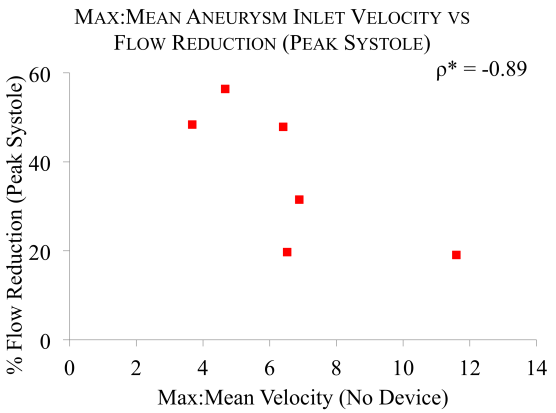

(b) *Ratio of Max:Mean Aneurysm Inlet Velocity and Flow Reduction*

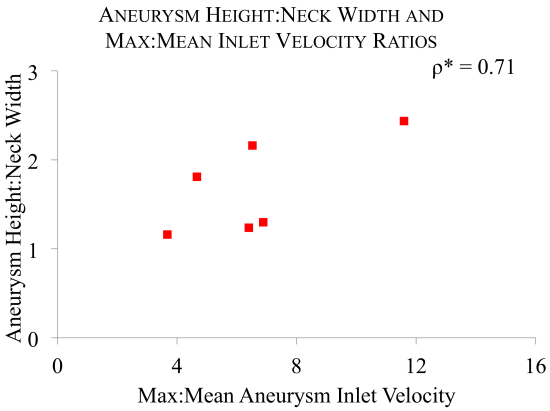

(c) *Correlating flow jetting and aneurysm aspect ratio*

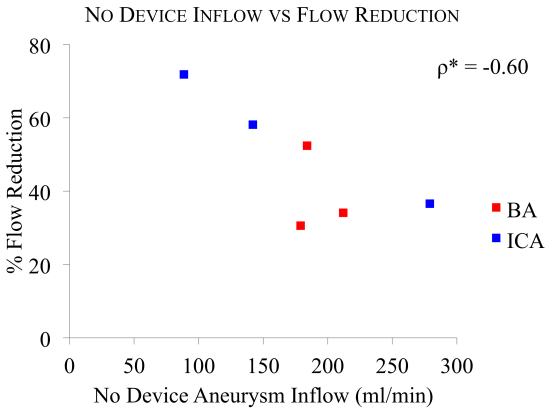

(d) *No Device Aneurysm Inflow and Flow Reduction*

Figure 4.21: *Plots of Flow Reduction and Geometry Metrics with Spearman's Rank Correlation Coefficient*

The ratio between the outlet and inlet areas of the geometry was chosen as a metric to approximate flow resistance in the geometry. A low outlet:inlet area ratio would imply constriction of the flow, increased flow acceleration and a large pressure gradient to accelerate the flow, conditions that are likely to 'drive' flow into the aneurysm dome, reducing device effectiveness. However, no correlation is seen between the ratio of geometry inlet to outlet area and the mean

flow reduction of the device, as shown in figure 4.21a.

Secondly, a number of metrics were chosen to investigate any correlation between device effectiveness and aneurysm flow that was of a high magnitude or was concentrated in a jet. Previous studies in the literature have suggested such a link, with Ujiie et al. [146] concluding that an aneurysm aspect ratio (average aneurysm height / average neck width) greater than 1.6 was correlated with an increased risk of rupture attributed to flow jetting.

The 'peakedness' (defined as the ratio of maximum velocity to mean velocity and similar to the kurtosis in this case) of the flow profile entering the aneurysm at peak systole with no device is plotted against peak systole flow reduction due to the device in figure 4.21b. A strong negative correlation is seen (Spearman's rank = -0.89) suggesting that aneurysm inflow with a strong jet reduces the effectiveness of the device. Additionally, the plot of figure 4.21c supports the assertion made by Ujjie et al. that this flow jetting and aneurysm aspect ratio are correlated, although a consistent measure of 'aspect ratio' is problematic with non-standard aneurysm shapes like many of the geometries considered here.

The mean aneurysm inflow with no device and the subsequent flow reduction achieved by the device are plotted in figure 4.21d. Although a weak negative correlation is observed (Spearman's Rank=-0.60) the correlation, at least at this small sample size, does not appear consistent across the BA and ICA geometries.

The results of all of these metric hypotheses must be considered inconclusive given the lack of statistical significance from such a small sample size (six cases), however, the stronger correlations observed warrant investigation with a larger data set in the future.

Plots of pressure for each vessel before and after device deployment are shown in figure 4.22 and figure 4.23.

Across all six geometries, very little change in pressure is seen after device deployment, the exception being a small increase in inlet pressure after device deployment, corresponding to the increased resistance to flow in the vessel. Such an increase in inlet pressure is likely to be sufficiently small to be considered insignificant and not effect device performance or risk of aneurysm rupture. The large increases in aneurysm sac pressure correlated with aneurysm rupture, which were observed by Cebral et al. [20] following FD deployment, would not be

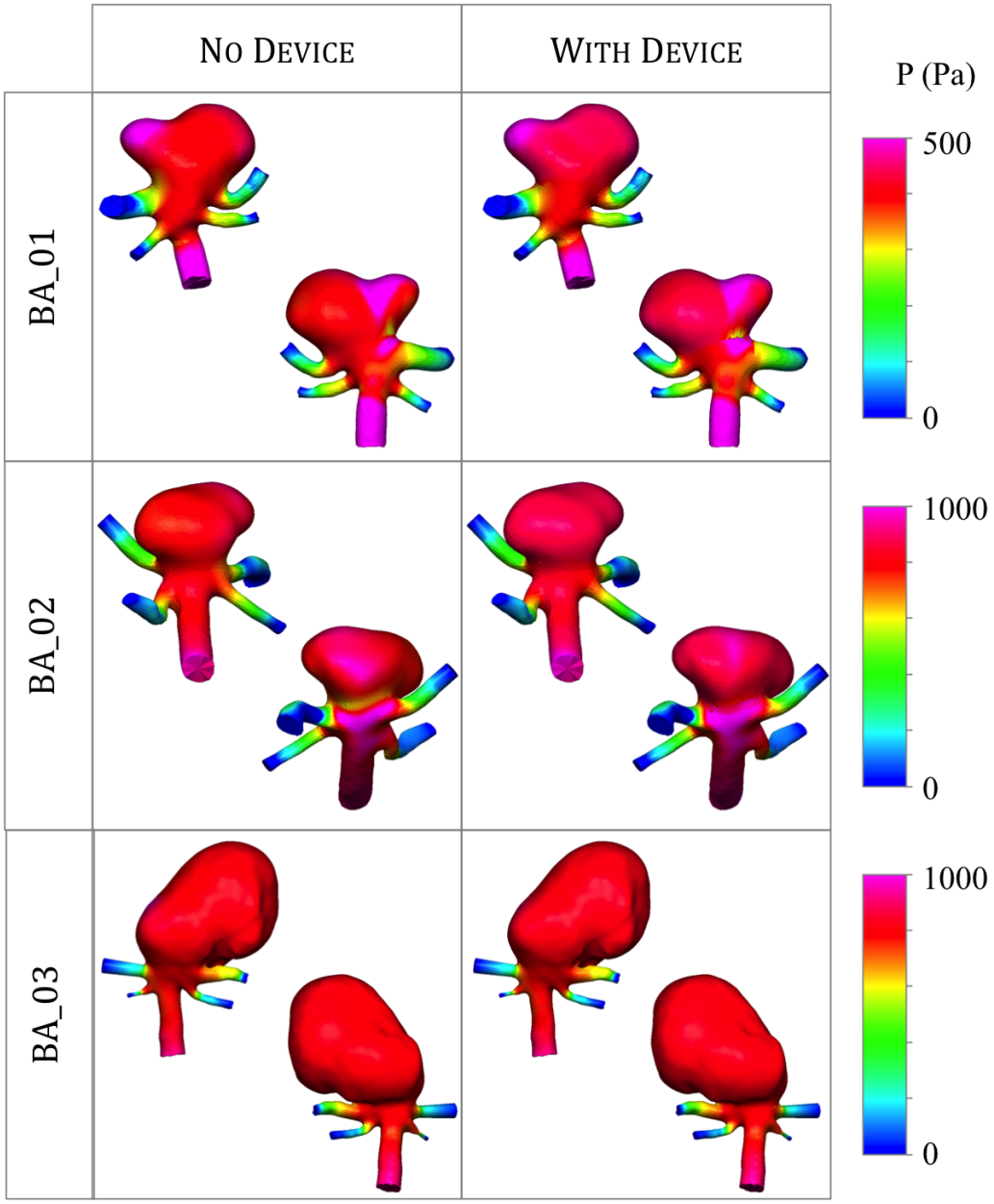

Figure 4.22: *BA pressure plots*

detected in this study. Such a pressure increase was attributed to the reversal of parent vessel stenosis, which cannot be modelled when assuming a rigid vessel wall as in the case of the current study.

As previously discussed, no convergent solution for the ICA_01 geometry was reached for a steady state simulation of mean parent vessel flow. The steady state simulations of the five other geometries give similar results to the mean result of the corresponding transient simulations with

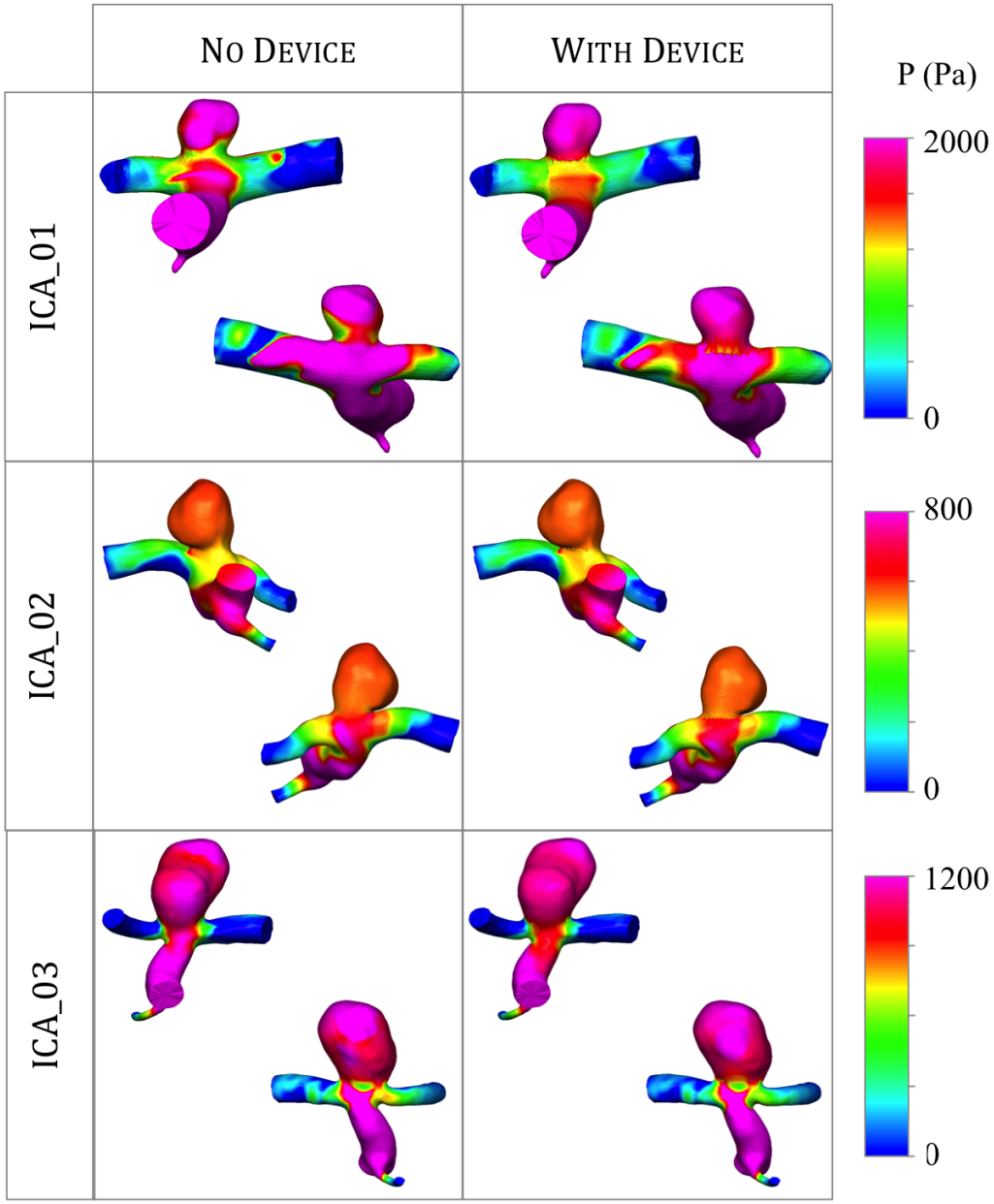

Figure 4.23: *ICA pressure plots*

the exception of the BA_01 'No Device' and BA_03 'With Device' cases. Both the mean and maximum aneurysm inflow with no device predicted by the transient simulation of BA_01 are of note in that they appear non-physical, exceeding the corresponding mean and maximum parent vessel flow rates. An explanation for this discrepancy and the underlying mechanism causing it are discussed in detail in the following chapter (chapter 5).

4.4 Comparing the 'Sphere' to the Performance of a Conventional Flow-Diverter

Current clinical practice would be to treat the aneurysms discussed in the previous section with either coils or a conventional flow-diverter device (SILK or PED). In many of the aneurysm geometries discussed, the presence of a wide aneurysm neck would also require the deployment of a high porosity stent for a stent assisted coiling procedure as conventional coiling would risk vessel occlusion by coil prolapse.

In this section, the same six aneurysm geometries are virtually implanted with a conventional flow-diverter to assess the flow reduction achieved by the novel 'Sphere' device compared to a likely clinical alternative. However, bifurcation aneurysms present significantly more clinical difficulties than sidewall cases, and the treatment of bifurcation aneurysms with conventional flow-diverters is often seen as a treatment of last resort. [78] Concerns of vessel occlusion following daughter vessel jailing with a conventional flow-diverter device are detailed in the literature and were previously summarised in section 4.1. If fears expressed over daughter vessel occlusion are warranted, the possibility of using the 'Sphere' device to treat bifurcation aneurysms, particularly difficult wide-necked cases such as the BA_01 geometry, without daughter vessel jailing is highly desirable.

4.4.1 Simulation Setup

The transient flow simulations of section 4.3.2 are repeated with a conventional flow-diverter implanted into each geometry. The flow-diverter used is almost identical to the commercially available SILK or PED with the same number of braided strands, strand diameter, pore density, pore shape, and range of lengths and diameters (see 'Stent I' in chapter 3). For convenience, this custom conventional flow-diverter is referred to as 'SILK'. Devices are implanted along the vessel centrelines indicated in figure 4.24, hence all daughter vessels apart from those congaing the centreline indicated are jailed by the device.

The length and diameter of the implanted device is chosen in accordance with manufacturer recommendations and virtual deployment is achieved with in-house fast deployment routines

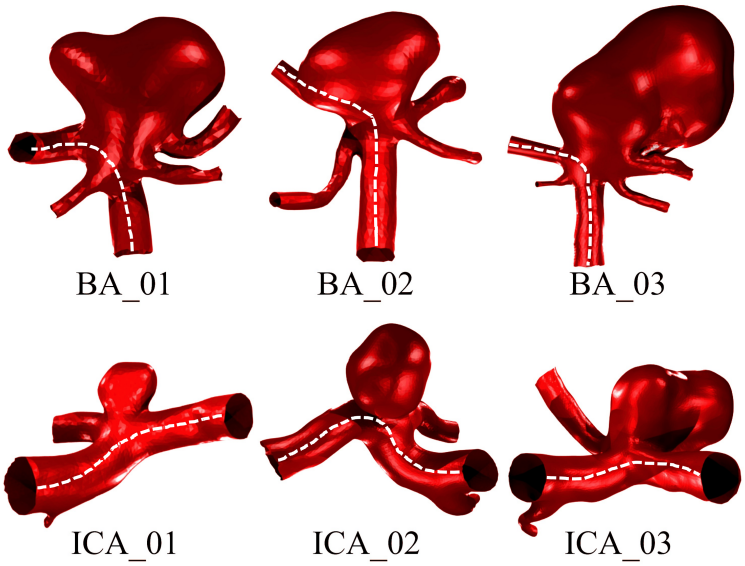

Figure 4.24: *Approximate vessel centrelines (white dashes) along which the SILK flow-diverter is deployed for each bifurcation geometry*

based on a virtual spring analogy as discussed in the previous chapter. [140] [139]

The resulting geometries are meshed to the fineness level discussed in section 4.3.3, yielding mesh sizes in the range of 4,700,000-6,470,000 elements. Simulations use the same solver settings, boundary conditions and time step as those detailed in section 4.3.2, and convergence to five orders of magnitude is achieved in less than 100 iterations and around 45 minutes for a given time step, with simulations run on 32, 2.93GHz cores.

4.4.2 Simulation Results

As before, the simulation results are post-processed in CFD-VIEW software with aneurysm inlet planes identical to those of the previous section defined.

Aneurysm inflow after SILK deployment is shown in figure 4.25, where the average inflow over the cardiac cycle is indicated is blue and the range of instantaneous inflow is indicated in black. The range of inflow seen over the cardiac cycle is similar to that seen for the 'Sphere' device (see figure 4.16), but the value of mean inflow is markedly reduced in half of the geometries (BA_01, BA_03 and ICA_03) implanted with the SILK flow-diverter. The average and range of percentage flow reduction achieved by the SILK device is displayed in figure 4.26. The flow-diverting effect of the SILK flow-diverter is broadly similar to that of the 'Sphere', but

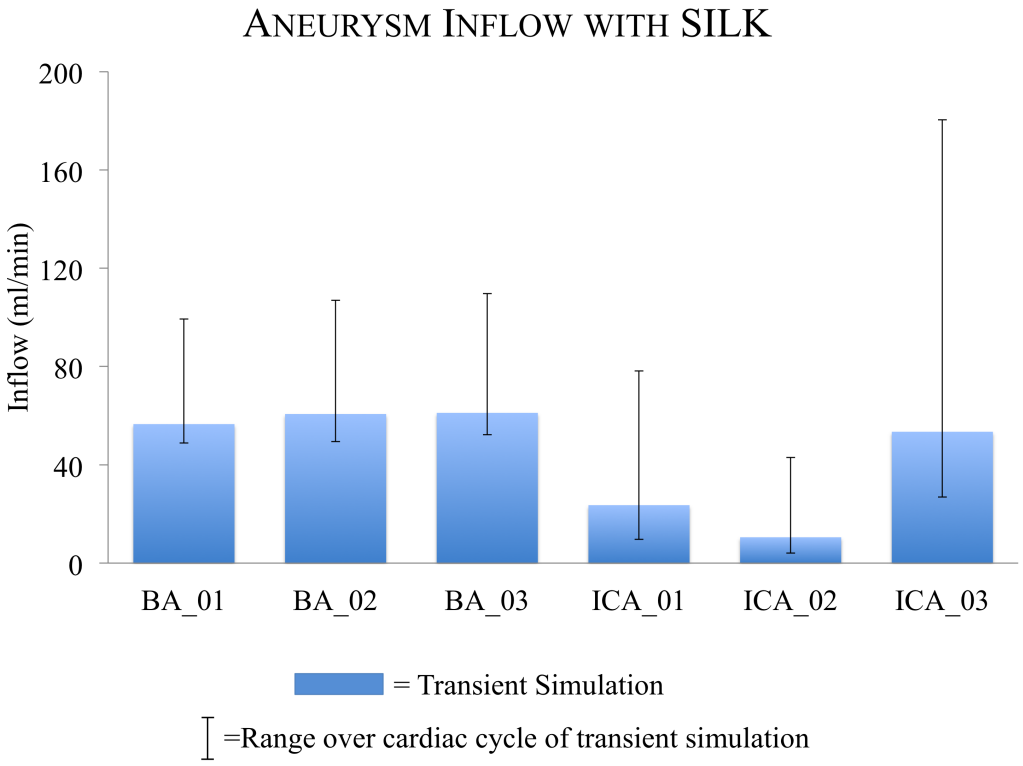

Figure 4.25: *Aneurysm inflow with conventional flow-diverter device (SILK) implanted*

in the BA_01, BA_03, and ICA_03 geometries, the SILK device outperforms the 'Sphere' by approximately 20%. The flow reduction achieved by the SILK shows less variation than that of the 'Sphere'; a flow reduction in the range of 50-70% is shown across all six geometries for the SILK compared to a range of 30-70% for the 'Sphere' (see figure 4.17 for comparison.)

The uniformity of the performance of the SILK flow-diverter when compared to the 'Sphere' is likely attributed to the action of the SILK, which is to reconstruct the flow into a distinct cylindrical section (bounded by the flow-diverter) regardless of the anatomical variation around the aneurysm neck. The flow patterns, and hence subsequent flow reduction, seen post-treatment with the 'Sphere' device are less disrupted and show more natural variation due to differences in the aneurysm geometries.

Lines tangent to the instantaneous velocity vectors are shown for the SILK device in all six geometries in figure 4.27 and figure 4.28.

As may be expected, the aneurysm flow patterns are almost identical in the geometries where very little difference was seen in the flow reduction achieved compared to the 'Sphere', namely

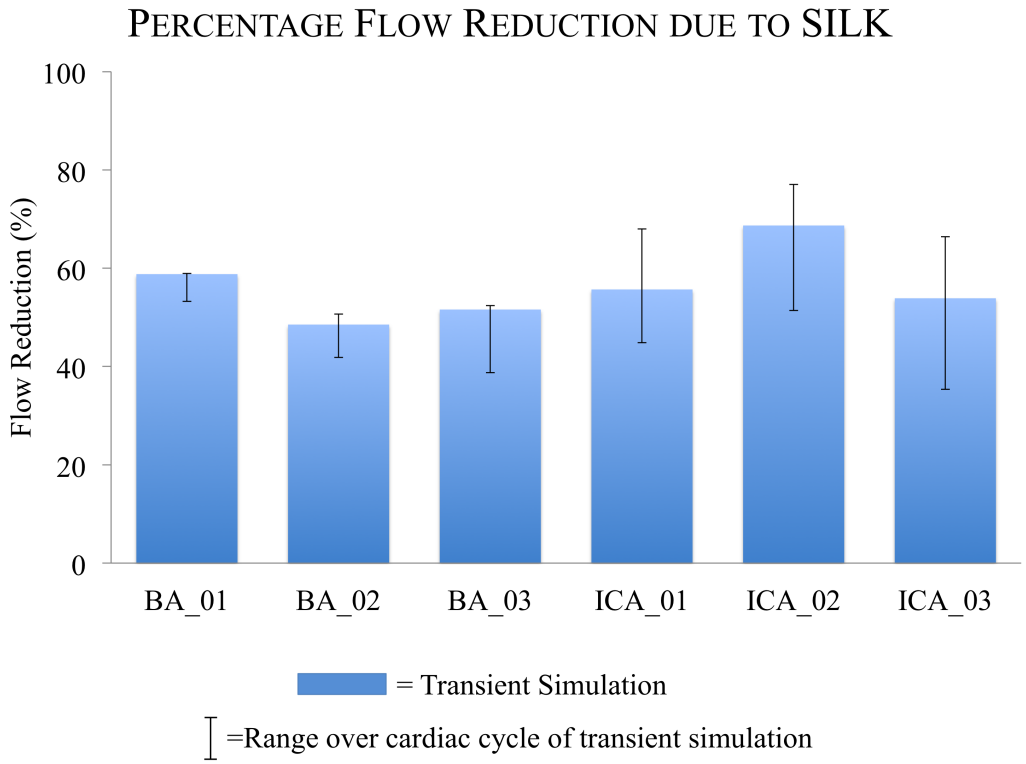

Figure 4.26: *Inflow reduction with SILK device*

BA_02, ICA_01, and ICA_02. In all three of these cases the 'Sphere' device marginally outperforms the current clinical standard of the SILK offering a slight increase in aneurysm inflow reduction. In the remaining geometries, BA_01, BA_03, and ICA_03, the SILK device substantially reduces both the aneurysm inflow and the flow velocity within the aneurysm dome. Across these three aneurysm geometries the flow patterns within the aneurysm dome after implantation with the SILK also appear more coherent and less chaotic than the flow after the 'Sphere' implantation.

In all six geometries the parent vessel flow is substantially more altered by the SILK device, with a clear 'core' of flow seen within the device struts and very little flow with a significant velocity entering the aneurysm neck. Although such a flow pattern is likely to be highly beneficial to encouraging aneurysm thrombosis, the resulting reduction in flow of other daughter vessels that are jailed by the conventional flow-diverters may be a concern. In order to quantify any such change of flow rate in the jailed daughter vessels, the flow rate in the dominant daughter vessel of each geometry (the vessel chosen for stenting) is plotted in figure 4.29.

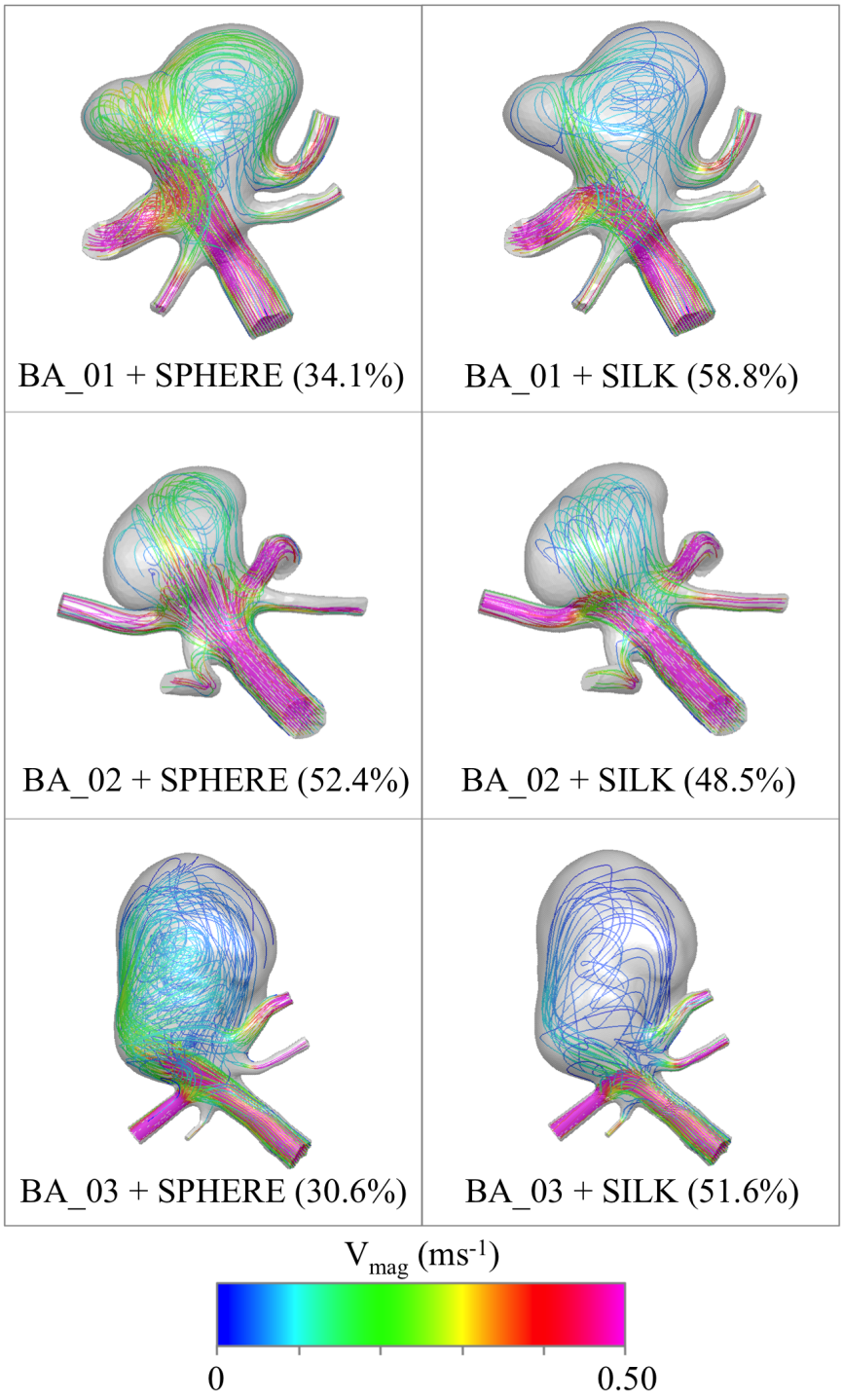

Figure 4.27: *Streamlines of flow (lines tangential to instantaneous velocity vectors) at mean parent vessel flow rate across the BA aneurysm geometries with a Sphere or a SILK device deployed*

From figure 4.29 it appears that although the SILK device alters the local flow pattern more than the 'Sphere', there is no substantial change in the proportion of the flow exiting the stented

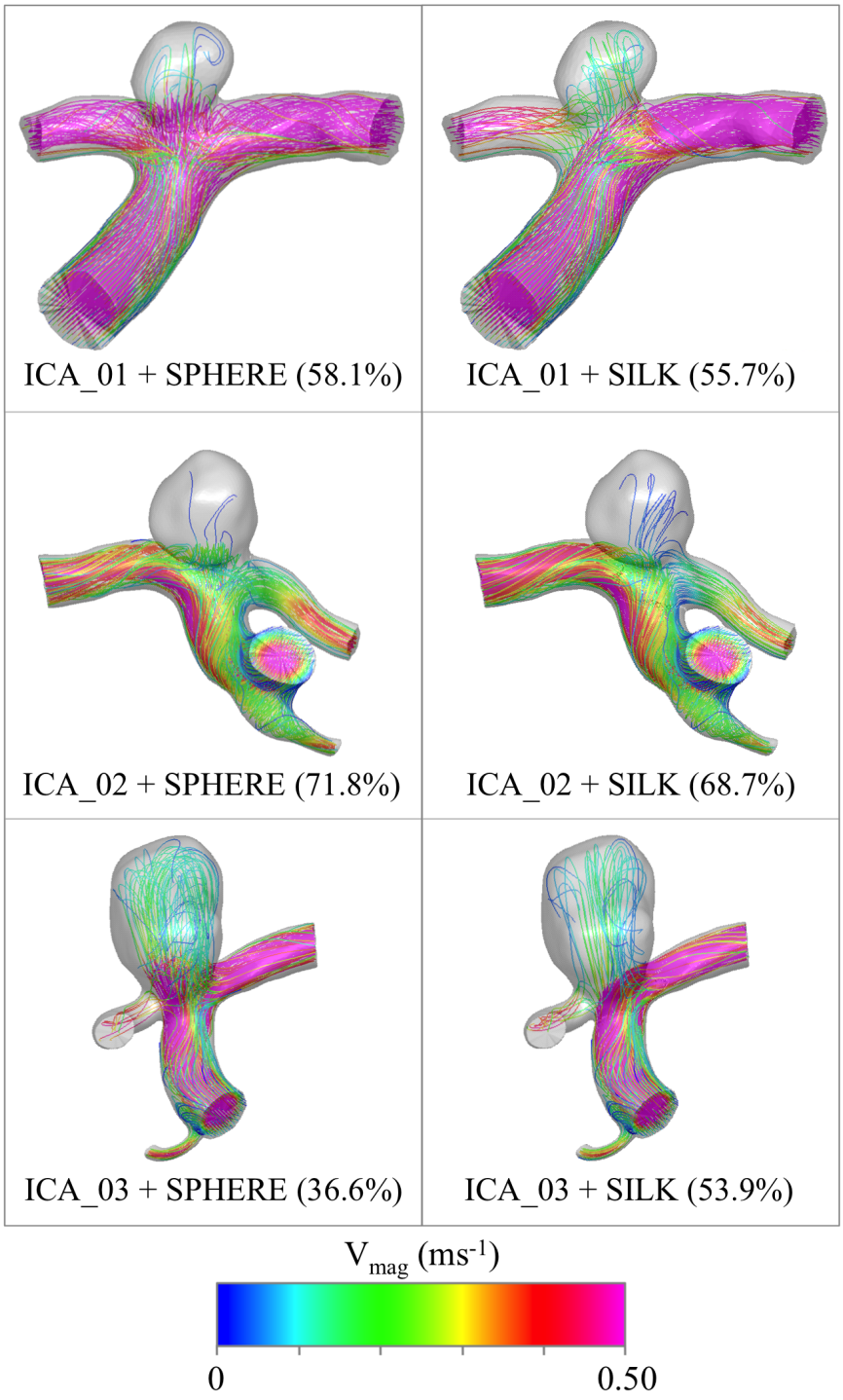

Figure 4.28: *Streamlines of flow (lines tangential to instantaneous velocity vectors) at mean parent vessel flow rate across the ICA aneurysm geometries with a Sphere or a SILK device deployed*

daughter vessel after the placement of either device. This in turn implies that the remaining daughter vessels, which are jailed by the conventional flow-diverter, do not experience a substan-

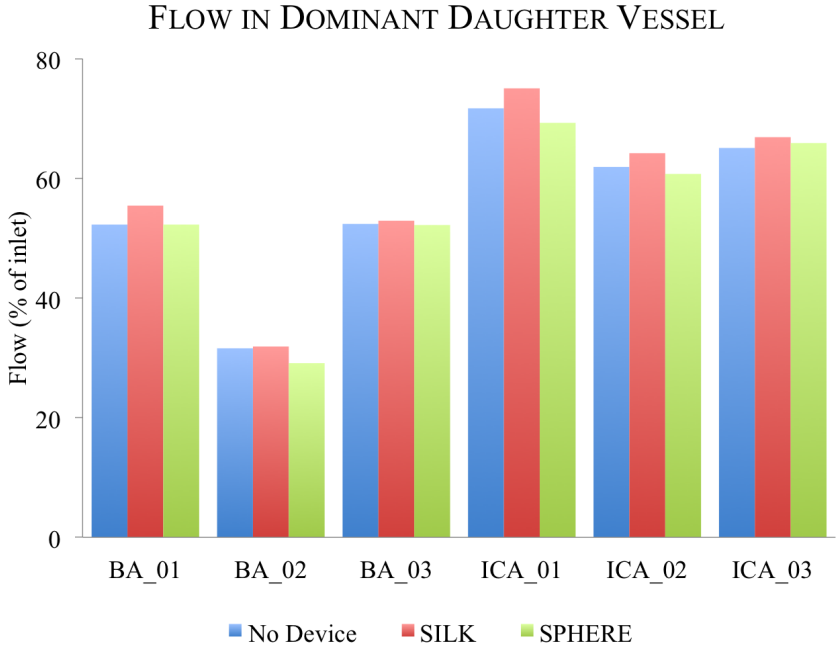

Figure 4.29: *Mean percentage of inflow leaving the dominant daughter vessel (the vessel selected for flow-diverter placement) with no device, the SILK, and the Sphere deployed*

tial reduction in flow after SILK implantation. The variation in daughter vessel flow rate after SILK device implantation observed in these simulations is of a similar order of magnitude to that observed in the literature *in-vitro*. [144] These results should be viewed with some caution, as after some time, the formation of neo-intima on the-flow diverter mesh may further reduce the flow to jailed vessels, causing vessel narrowing or partial occlusion and leading to higher vessel resistance and subsequent reduction in vessel flow.

Finally, the WSS distributions at maximum flow conditions (peak systole) in the geometries after implantation with each device are shown in figure 4.30.

In all six aneurysm geometries, virtual treatment with the 'Sphere' device results in elevated WSS values in the aneurysm dome, compared to treatment with the SILK device. Even in cases where the device flow reduction is similar, such as ICA_01, the WSS distribution within the aneurysm dome is more elevated after 'Sphere' implantation. This suggests that the substantial reduction in aneurysm velocity magnitude as well as in aneurysm inflow achieved by the implanted SILK device results in the reduced WSS distributions for the geometries.

In four of the six aneurysm geometries, the WSS patterns within the aneurysm dome are very

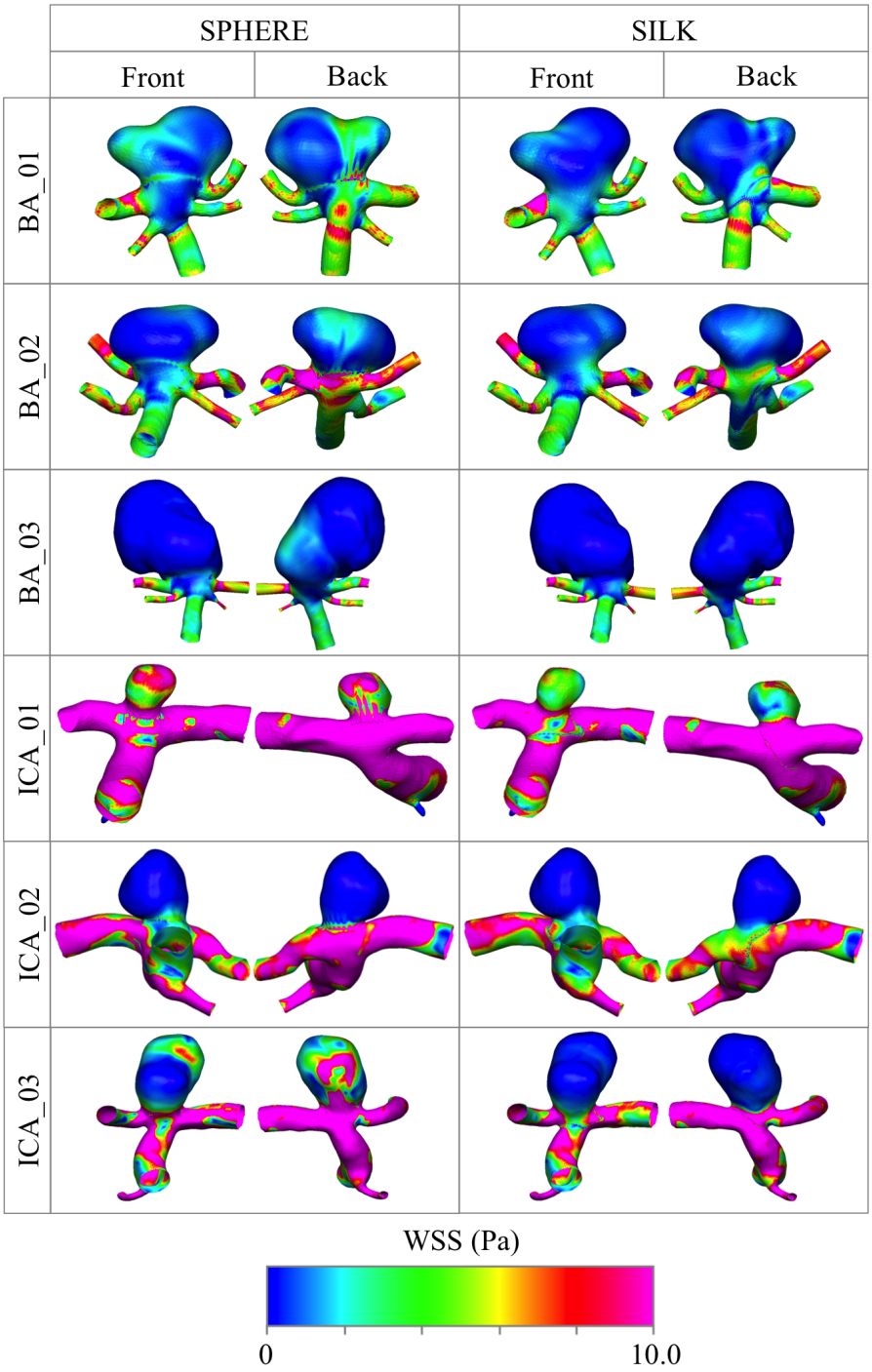

Figure 4.30: *Comparing WSS distributions at peak systole (max flow rate) for all geometries implanted with the SPHERE and SILK devices*

similar after treatment with either device. However, in the ICA_01 and ICA_03 geometries considerable variation in the aneurysm flow pattern and inlet velocity between the two devices (see figure 4.28) has resulted in substantially different WSS patterns, with concentrated areas of high WSS seen in both geometries after implantation of the 'Sphere.' As was discussed

previously, this is very surprising in the ICA_01 geometry where the performance of the two devices is almost identical when considering flow reduction alone.

The same three metrics previously discussed in figure 4.21 are repeated for the geometries with the SILK flow-diverter implanted and summarised in figure 4.31.

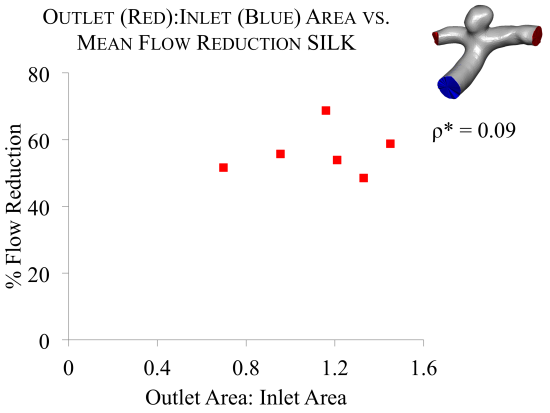

(a) *Geometry Inlet and Outlet Area Ratio and Flow Reduction*

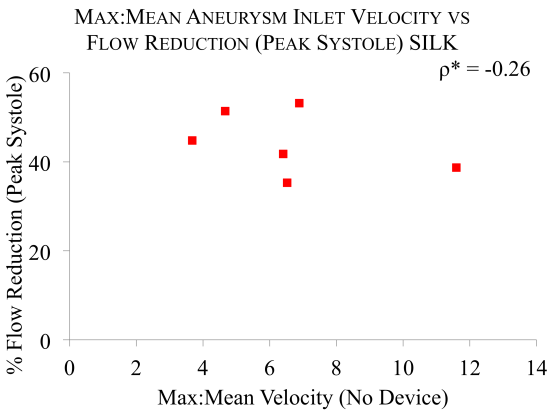

(b) *Ratio of Max:Mean Aneurysm Inlet Velocity and Flow Reduction*

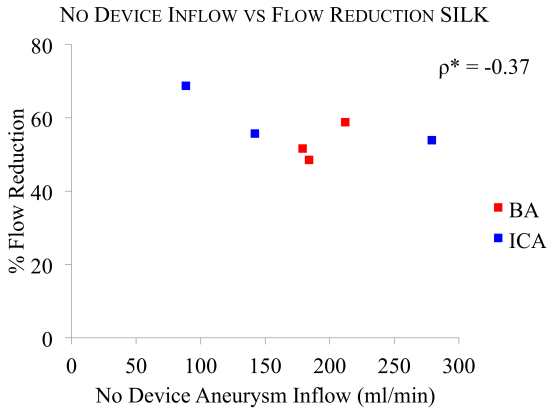

(c) *No Device Aneurysm Inflow and Flow Reduction*

Figure 4.31: *Plots of Flow Reduction and Geometry Metrics*

Compared to the same plots for the 'Sphere' device shown in figure 4.21, no correlation is seen between any of the flow or geometry metrics and the subsequent flow reduction of the SILK device. This lack of correlation is likely due to the strong influence of the SILK device geometry on the local aneurysm flow pattern after implantation, which then renders any metric that is based on the flow regime prior to device implantation effectively independent of device performance. Additionally, the flow reduction achieved by the SILK device is also relatively

independent of aneurysm geometry; the 'Sphere' device produced a range in flow reduction of approximately 45% across the six geometries, compared to the SILK device with a range of less than 20%.

4.5 Conclusions

This chapter has summarised the design evolution of a novel device that has been shown to provide substantial reduction in aneurysm inflow when virtually deployed to treat a number of patient-specific bifurcation aneurysms. The novel device, the 'Sphere', was also compared to the current conventional flow-diverter device that is widely used clinically. The flow reductions achieved by the 'Sphere' and SILK devices are summarised in figure 4.32.

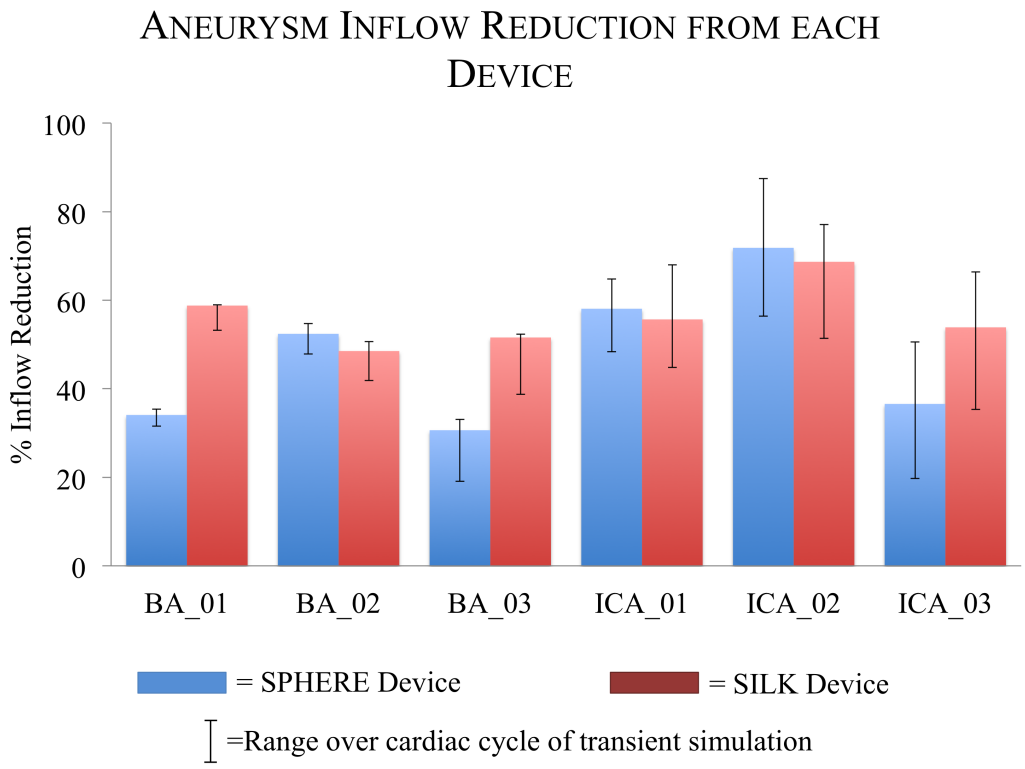

Figure 4.32: *Aneurysm inflow reduction for both the Sphere and SILK devices*

The novel 'Sphere' device compares favourably to the current clinical standard, although the SILK appears more effective in reducing the aneurysm peak velocity and inflow in a number of aneurysm geometries. The 'Sphere' device reduces the inflow into the aneurysm sac without substantially altering the geometry flow regime. Similar proportions of flow leave each daughter

vessel before and after device placement, reducing the risk of stroke or other ischemic neurological damage. Despite more dramatic changes in local flow regime and velocity following virtual treatment with the SILK device, the proportion of flow in each daughter also shows little variation. These findings suggests that the importance of a major design feature of the 'Sphere' device, the lack of daughter vessel jailing and risk of loss of patency, may have been overestimated. However, the long-term differences in the performance of the two devices is less clear, as a risk remains of vessels jailed by flow-diverter struts succumbing to a loss of patency over time.

Both the 'Sphere' and the SILK devices reduce the magnitude of the WSS distribution within the aneurysm dome as a result of reducing both the aneurysm inflow rate and the peak velocity of the inflow. In 4/6 of the geometries the aneurysm WSS patterns do not differ substantially following the virtual deployment of either device. However, in two cases, differences between flow regime and peak aneurysm inlet velocity after device deployment result in a significantly greater reduction in WSS for the SILK device. It appears that while the 'Sphere' device provides good reduction of elevated WSS in the aneurysm dome, the device is not as effective as the conventional cylindrical design of flow-diverter.

Both the 'Sphere' and SILK devices show no substantial effect on vessel pressure or pressure gradient after virtual deployment.

The current study has shown the 'Sphere' device to have a good flow-diverting ability in a number of bifurcation aneurysm geometries. However, significant aspects of the device's design have not been analysed: chiefly, the device's manufacture, deliverability, and the mechanical deformations experienced by both device and vessel wall that govern device security. Of these elements, the question of device security and the prevention of unintended migration is of paramount importance and deserves thorough investigation in the future.

Chapter 5

Flow Instabilities in the Aneurysm Dome

In this chapter, a number of inconsistencies between steady state and transient flow simulations from the previous two chapters are discussed. Patterns of instability seen in the literature are first discussed in section 5.1. Two geometries from chapter 3 and chapter 4, for which no steady state solution was found, are examined further in section 5.2, with consistent resonant behaviour seen in one case. Finally, one geometry from chapter 4 is investigated in section 5.3; two equilibrium flow patterns are discovered, with one unstable pattern found to decay into the second stable regime.[1]

5.1 Introduction

In three of the geometries simulated in the previous two chapters a discrepancy has been observed between the steady state simulations conducted at mean flow rate and the point of mean flow rate in the corresponding pulsatile simulations. All three of these cases are of aneurysm geometries with no device implanted, as summarised in figure 5.1.

In two of the cases, the MCA geometry in chapter 3 and the ICA_01 geometry in chapter 4,

[1]The work presented in section 5.3 of this chapter appears as part of: T W Peach and Y Ventikos. Stable, Unstable and Pseudo-Stable Aneurysm Flow Regimes in Steady State and Transient Simulations (in preparation)

	 MCA	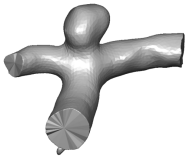 ICA_01	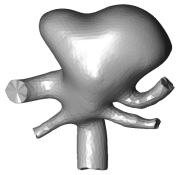 BA_01
Aneurysm Inflow (Steady State)	DNC	DNC	103 ml/min
Mean Aneurysm Inflow (Transient)	99.1 ml/min	53.2 ml/min	137 ml/min

DNC: Did Not Converge after 2,000 iterations

Figure 5.1: *Summary of the results of steady state and transient simulations for the three geometries discussed (aneurysm inflow rate)*

convergence was not reached in the steady state simulations. However, the same meshes did converge in the transient simulations at mean and maximum flow rates, which suggests that the lack of convergence in steady state was not due to insufficient mesh resolution.

In the remaining case, the BA_01 geometry in chapter 4, a fully converged solution was found at mean flow rate in both the steady state and transient simulations, but the flow pattern differed substantially in each case with a 33% greater aneurysm inflow rate predicted in the transient simulation.

The predominant suggestion in the literature is that steady state simulations of aneurysm flow represent a good approximation to the time-averaged behaviour of the corresponding pulsatile simulations. Studies [72] [142] cite the relatively low Womersley number of cerebral arterial flow as evidence that aneurysm velocity, pressure, and WSS distributions only vary in magnitude under pulsatile flow conditions, with no change in flow pattern or vorticity.

The discrepancy observed in the three simulations discussed here would stand in stark contrast to this assumption and could challenge any conclusions in the literature that have been derived from steady state simulation results alone. In light of this, in the following chapter, these three simulations are investigated further and compared to the emerging body of literature documenting aneurysm flow instability.

5.1.1 Aneurysm Flow Instability in the Literature

Although these effects have not been widely investigated, there are a number of examples in the literature that discuss oscillatory behaviour in cerebral aneurysms.

In the study by Chatziprodromou et al. [26], two sacular aneurysms present on the same segment of the internal carotid artery were simulated with a pulsatile flow profile. It was observed that one aneurysm was very sensitive to the unsteady nature of the flow; inflow and outflow regions of the aneurysm changed dramatically in addition to there being large variation in secondary flow features (cross-flow vectors). The second aneurysm was found to be highly insensitive to flow pulsatility, with little change in inflow and outflow regions observed.

Baek et al. [7] performed a transient flow study on a number of aneurysms across three patient-specific artery geometries with varying flow rates. Instabilities were observed in the deceleration phase of the flow profile, giving rise to oscillations in the 20-50Hz frequency range. The onset of this instability was found to vary across the different geometries but occurred at physiologically normal flowrates in 2/3 of the geometries. These oscillations were seen in velocity as well WSS magnitude and direction, with the greatest instability observed at points of flow impingement. Despite the instabilities observed, no significant change was seen in the global flow pattern within the aneurysm dome (vorticity, inlet and outlet regions etc.).

Finally, in a number of publications, Valen-Sendstad et al. also elucidated the presence of flow instability in aneurysms with the use of ultra-high-resolution computations. [148] [147] [150] Instabilities in velocity and WSS in the 1-500Hz range were observed, also corresponding to the deceleration phase of the cardiac cycle. Transient simulations conducted with stationary inflow conditions also showed the emergence of flow oscillations in a number of aneurysm geometries, specifically in bifurcation aneurysms and not sidewall cases.

5.2 Lack of Convergence in Steady State

As previously discussed, no convergence is seen after 2,000 iterations for steady state simulations at mean flow rate for either the MCA or ICA_01 geometries. However, the simulations do not diverge, but instead they 'plateau' with subsequent solver iterations failing to reduce the

simulation residuals to the specified criterion (5 orders of magnitude.) The lack of convergence in steady state with little residual reduction implies a flow regime within the geometry that varies in time, despite boundary conditions that do not. Such a condition could be met in one of two ways:

1.) No steady state solution exists: the flow pattern within the aneurysm is unstable with flow that oscillates at a resonant frequency or mixes chaotically.

2.) Multiple steady state solutions exist: the flow pattern within the aneurysm is unstable and alternates randomly between multiple flow regimes that all satisfy equilibrium. In this case, no one flow configuration is more energetically preferable than any other *or* the energetic preference is so marginal that many solution iterations are needed to damp other regimes and resolve a single stationary solution.

Both of these hypotheses are tested in the following simulations.

5.2.1 Simulation Setup

The MCA and ICA_01 geometries are both simulated as a transient simulation with constant mean inflow rates (120ml/min and 230ml/min respectively). All other solver parameters (second order schemes in time and space for minimal dissipation) and boundary conditions are unchanged from the setup in chapter 3 and chapter 4. Running a transient simulation in this manner with constant inflow rate allows the development of aneurysm flow pattern to be observed in addition to any emerging instabilities, as detailed by Valen-Sendstad et al. [150] A time step of 0.01 seconds is used, and all time steps have a convergence criterion of five orders of magnitude residual reduction.

Additionally, the steady state simulations of the MCA and ICA_01 geometries are also repeated but allowed to run for up to 10,000 iterations (5x longer than in previous steady simulations.) Allowing a large number of solver iterations may then lead to the isolation of the most stable stationary flow regime, as suggested in the second point of the previous section, which may have not been possible in the maximum 2,000 solver iterations of the standard steady state solutions discussed in chapter 3 and chapter 4.

5.2.2 Results and Discussion

5.2.2.1 MCA Geometry

The transient simulation is run on 16 processors with a solution time around 20 minutes per time step and convergence typically achieved in less than 150 iterations per time step. A monitor point is seeded in the approximate centre of the MCA geometry aneurysm dome and close to the main jet of flow entering the aneurysm. The corresponding velocity magnitude at this point and its variation in time for the transient simulation is plotted in figure 5.2.

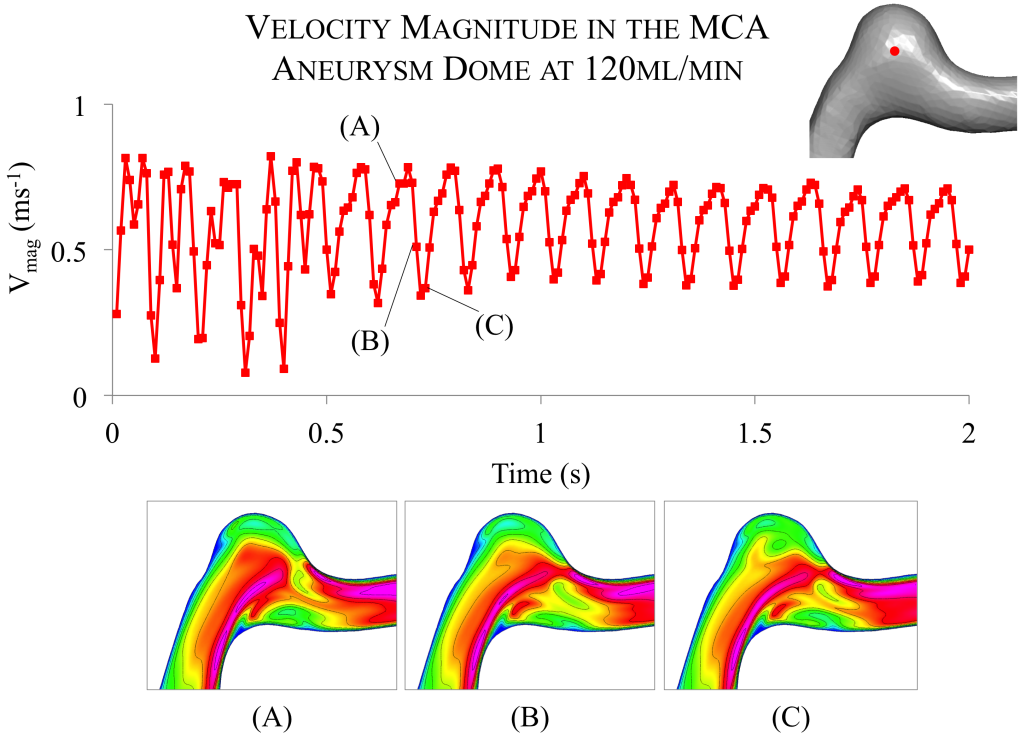

Figure 5.2: *Significant oscillations are seen in the velocity magnitude of flow within the aneurysm dome at a constant inflow rate*

In the figure, early transient behaviour can be seen with erratic variation in velocity for the first 0.5 seconds of the simulation, corresponding to approximately 15 'flow-throughs' based on the arterial bulk flow rate. After 0.5 seconds, a distinct pattern emerges with the velocity magnitude oscillating between a minimum and maximum value of approximately 0.4ms^{-1} and 0.75ms^{-1}, at around 10Hz. These velocity oscillations continue for the remaining 1.50 seconds of the simulation with a low rate of decay, if any. These fluctuations correspond to the oscillation

of the jet of flow entering the aneurysm as shown in the cross-sectional, velocity magnitude contour-plots also included in figure 5.2.

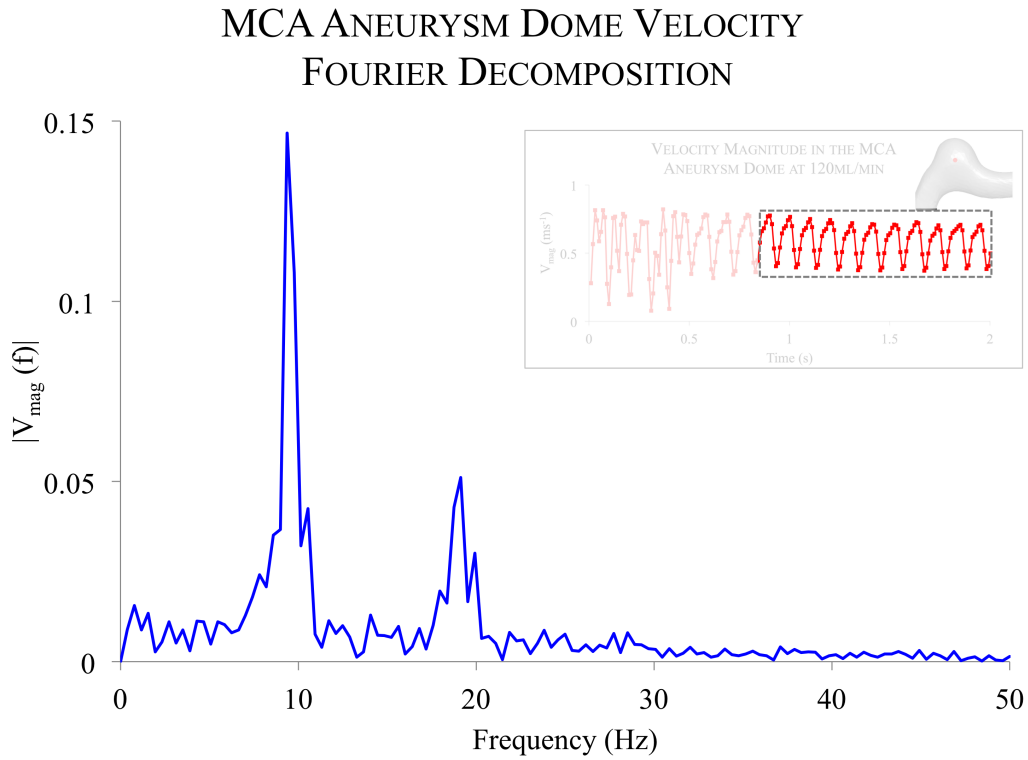

Figure 5.3: *Fourier decomposition plot for the indicated portion of the oscillating velocity magnitude plot shown in figure 5.2*

A Fourier decomposition of the consistent oscillations seen in figure 5.2 is shown in figure 5.3. The significant peak in the plot at around 10Hz confirms the dominance of the 10Hz signal clearly visible in figure 5.2, but the plot also shows an additional harmonic component in the velocity oscillations at around 20Hz. Higher frequency oscillations may be present in the oscillations but remain undetectable due to the simulation time step size limiting the maximum detectable frequency to 50Hz. Although other studies in the literature have suggested the emergence of oscillations with a frequency of up to 500Hz, most recorded cases have fallen in the 1-50Hz range. [7] [148]

Experimental studies performed on the same aneurysm geometry (MCA) at a similar flow rate show almost identical behaviour. Figure 5.4 illustrates two flow regimes observed experimentally from PIV analysis. The jet of flow entering the aneurysm dome oscillates, moving in and out of the plane shown. Visual, frame-by-frame inspection of the video recordings from the experimen-

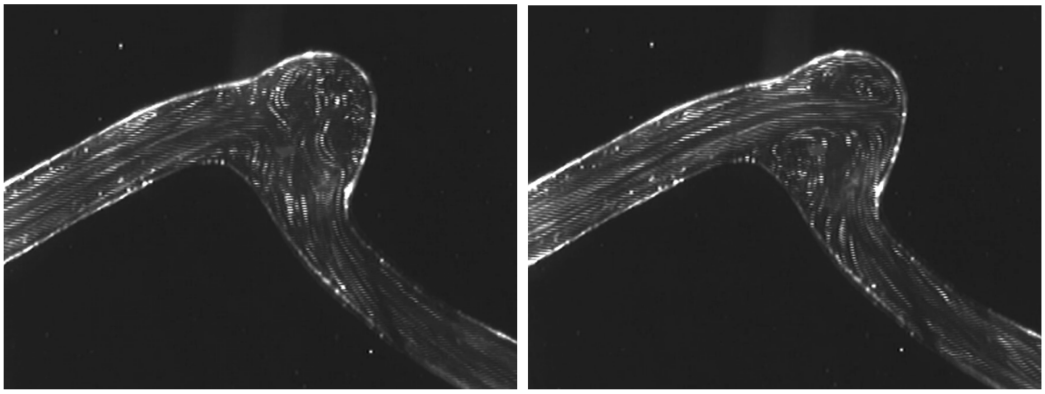

Figure 5.4: *Two distinct flow regimes observed in a particle image velocimetry (PIV) study of the MCA geometry at mean flow rate. Image credit: Dr. Jianhua Zhai*

tal study reveal a dominant oscillation of around 5Hz. The presence of similar oscillations in the PIV analysis confirm that the simulated flow oscillations seen are not the result of numerical instability or mesh quality.

It appears that this resonance oscillatory behaviour of the aneurysm inflow jet results in the lack of convergence in steady state as no stable, stationary flow regime may be found in the aneurysm dome. Finally, the steady state simulation of the MCA geometry is re-run but no convergent solution is reached after 10,000 iterations; reinforcing the assumption of an unstable and non-stationary flow regime within the aneurysm dome, despite stationary boundary conditions.

5.2.2.2 ICA_01 Geometry

Transient simulations are run on 16 processors with a full convergence at each time step achieved in around 20 minutes and typically in less than 100 iterations. As in the previous section, a monitor point is seeded in the ICA_01 geometry close to the main jet of flow entering the aneurysm dome. The variation in velocity magnitude at this point is plotted in figure 5.5.

Unlike the previous graph for the MCA geometry, figure 5.5 shows the flow distribution in the ICA_01 aneurysm dome quickly settling upon a stable configuration. A small degree of initial transient mixing persists for approximately 0.1 seconds (around three 'flow-throughs') but this quickly subsides with convergence onto a stationary flow regime. The rapid rate of convergence seen in figure 5.5 suggests that any instability leading to a lack of convergence in steady state is unlikely to be located in the main aneurysm dome. However, the method of seeding a monitor

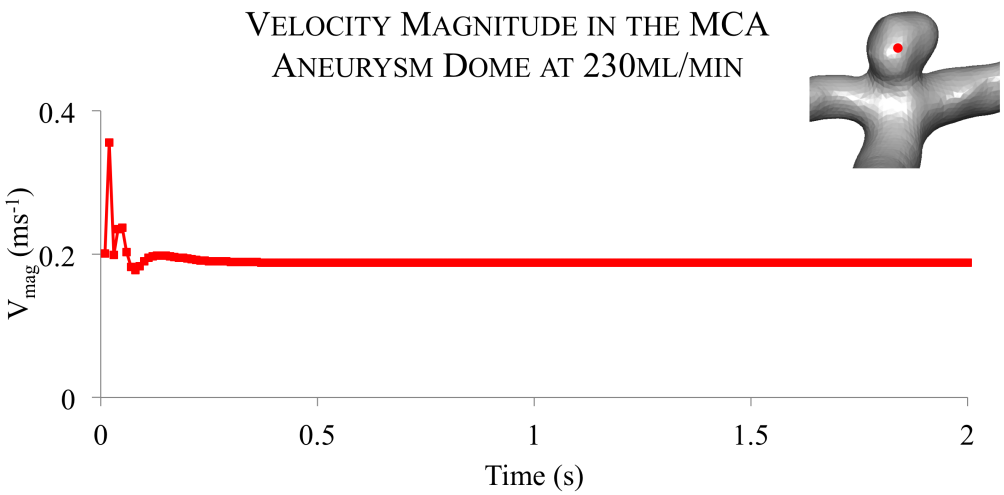

Figure 5.5: *No significant oscillations are seen for the ICA_01 geometry*

point adjacent to the main inflow region of the aneurysm only allows the stability of the overall jet to be monitored; small areas of instability may remain undetected.

The steady-state simulation of the ICA_01 geometry is repeated, reaching convergence to five orders of magnitude residual reduction in approximately 2800 iterations. The resulting flow regime and aneurysm inflow rates for the steady state and transient solutions are summarised in figure 5.6.

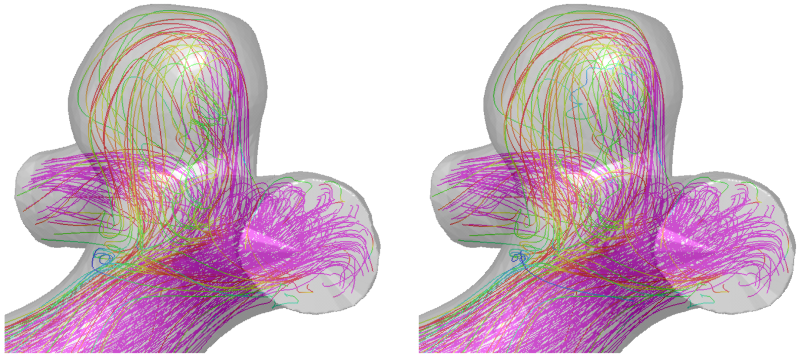

Figure 5.6: *Steady state and transient (stationary boundary conditions) simulations of the ICA_01 geometry with no device deployed, and corresponding aneurysm inflow rates*

It appears that the lack of steady state convergence seen initially in the ICA_01 geometry in chapter 4 can actually be attributed to a very slow rate of convergence. The large number of iterations (some 2800) required to reach convergence of the flow field in steady state suggests

that localised instability or high velocity gradient may be dramatically slowing convergence, but any such instability decays in a few thousand iterations at steady state. The relatively small vessel diameters in the ICA_01 geometry combined with the large ICA flow rate result in maximum velocities of up to 1.06ms^{-1} at mean flow. This value is higher than in any other geometry simulated in this study, and may contribute to the very slow convergence rate.

5.2.3 Conclusions: Lack of Convergence in Steady State

Two distinct cases of lack of convergence in steady state have been explored. In one case, a convergent steady state solution was subsequently found, with the initial lack of convergence attributed to a very slow rate of convergence linked to either under-damped local instability or large local velocity gradients. In the second case, sustained flow oscillations have been observed in the aneurysm dome, despite stationary boundary conditions, which suggests that no steady state solution exists at such a flow rate in the geometry. However, in both of these geometries fully convergent transient flow solutions with pulsatile inflow were found with relative ease, as detailed in chapter 4. As such, it is unclear whether the resonant behaviour seen in the MCA geometry is an unusual anomaly or whether it may be indicative of a underlying flow mechanism contributing to rupture risk.

Aside from the emergence of consistent oscillatory behaviour, the dissipation rate of initial transient effects also varied considerably between the two geometries; erratic transient effects subsided in approximately three 'flow-throughs' for the ICA_01 case but remained for around 15 'flow-throughs' in the MCA case, before giving way to coherent oscillations. For context, a similar study (transient analysis with stationary boundary conditions) by Valen-Sendstad et al. [149] classified aneurysms as either stable or unstable depending on whether or not initial transient effects persisted after five 'flow-throughs.' For the 12 aneurysms studied, 100% of unruptured cases were classified as 'stable' while 71% of ruptured cases were considered 'unstable.'

5.3 Variation Between Steady State and Transient Solutions

As summarised in figure 5.1, the pattern of behaviour seen for the BA_01 geometry is quite different to the previous two cases; a convergent steady state solution to the flow regime was found, but the regime is radically different to that predicted at mean flow rate in the transient simulation. This effect is illustrated in figure 5.7 and figure 5.8.

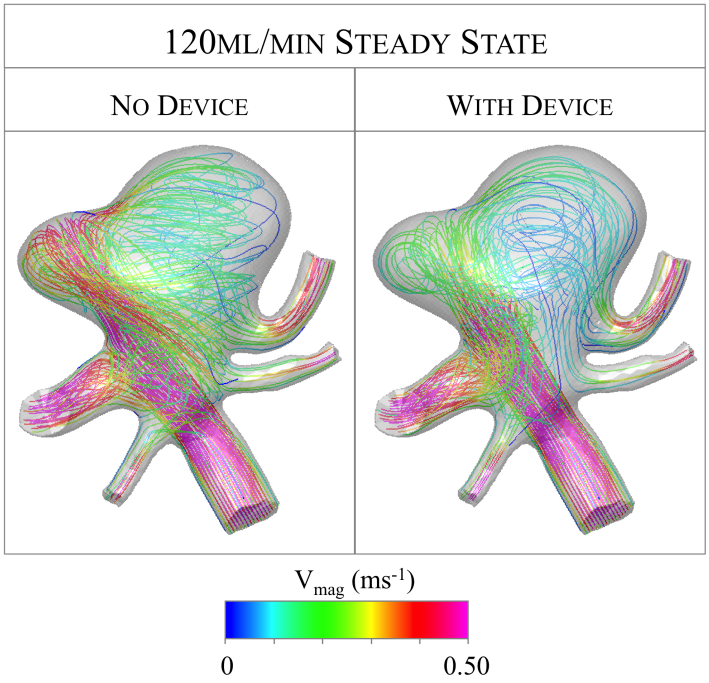

Figure 5.7: *Steady state simulation of BA_01 with and without a 'Sphere' device*

For the steady state prediction (figure 5.7), flow in the aneurysm dome with no device deployed is dominated by a jet impingement zone and a single vortex. The impingement area falls squarely in the smaller of the two lobes that make up the aneurysm dome. After the initial impact, the flow either quickly exits the aneurysm in the left-hand portion of the dome, or circulates in the larger lobe of the aneurysm in the right-hand portion. This movement sets up a helical vortex pattern within the aneurysm dome rotating about the axis indicated in figure 5.9(left).

In the transient case with no device deployed (figure 5.8), the overall flow structure in the aneurysm dome is similar: a single impingement zone concentrated on the smaller lobe and a slower speed vortex circling in the larger lobe. However, the direction of this vortex is aligned perpendicular to that produced in the steady state simulation, as shown in figure 5.9. This flow

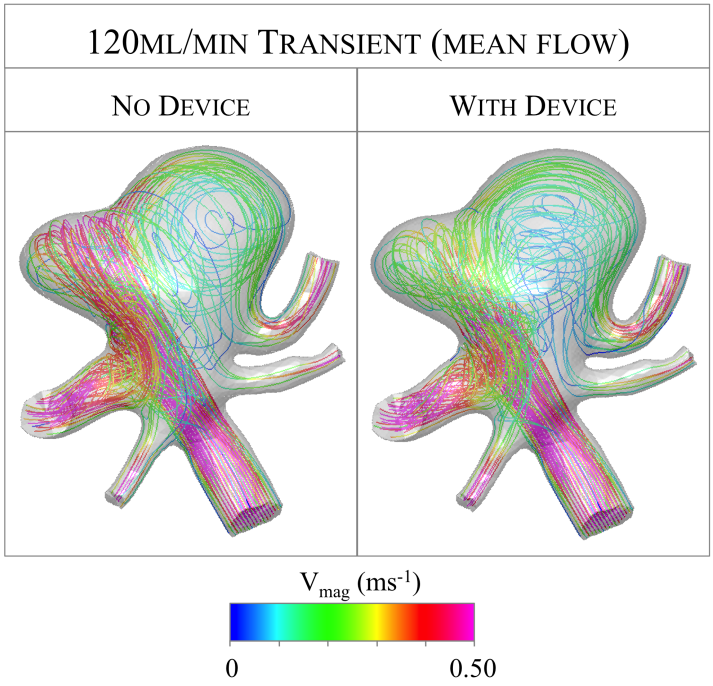

Figure 5.8: *Steady state simulation of BA_01 with and without a 'Sphere' device*

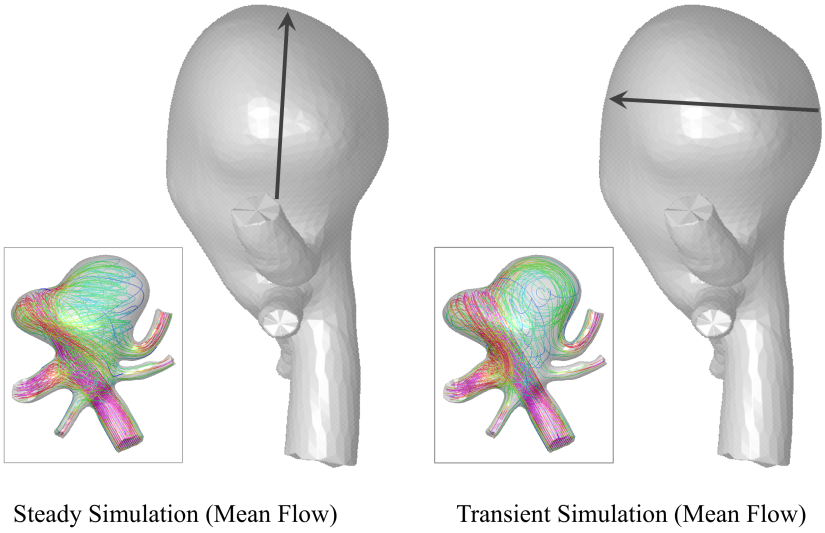

Figure 5.9: *Approximate vector directions of the circulation within the aneurysm dome of BA_01 with no device in both steady state and transient simulations*

pattern observed at mean flow rate in the transient simulation persists throughout the cardiac cycle, clearly showing a clockwise circulation at all flow rates as shown in figure 5.10.

It should be noted that little difference is seen between the steady and transient simulations with the 'Sphere' device deployed, as indicated in figure 5.7 and figure 5.8. There is also little variation

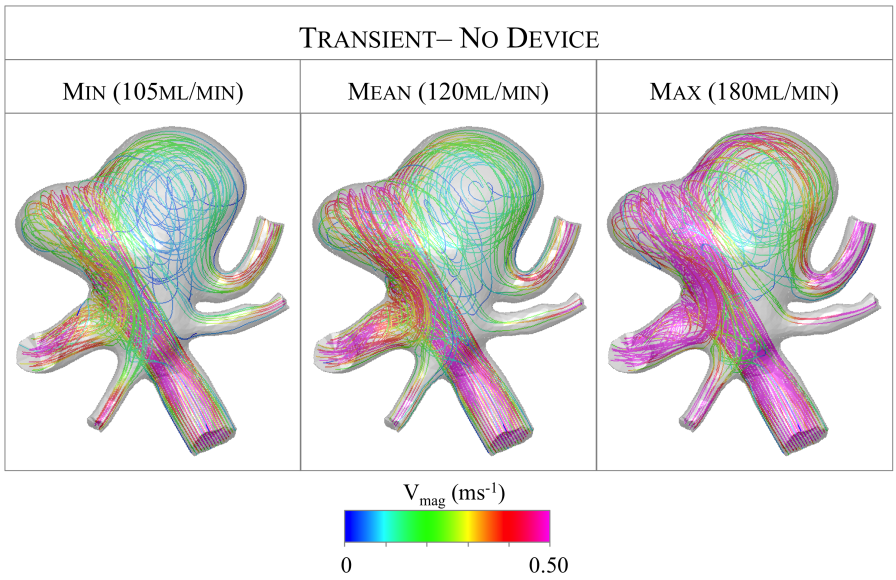

Figure 5.10: *Confirmation of the same flow pattern throughout the cardiac cycle for the BA_01 geometry with no device deployed*

in the predicted mean inflow rates for the two cases, at 86ml/min and 90ml/min respectively. Steady state simulations were not conducted for the same geometry with the conventional SILK flow-diverter deployed, and so no further comparison is possible.

The result of the slight change in flow pattern within the aneurysm dome for the 'No Device' case is dramatic. The effect of the discrepancy is to produce a predicted average aneurysm inflow that is 33% greater in the transient simulation when compared to the steady state simulation. Additionally, the predicted average aneurysm inflow in the transient case, 137ml/min, at first-sight appears non-physical, as it exceeds the average parent vessel inflow rate of 120ml/min. The cause of this seemingly non-physical inflow appears to be a region of recirculation.

The transient 'No Device' simulation of BA_01 (figure 5.8) reveals recirculation behaviour in the right-hand portion of the aneurysm dome with flow both exiting and re-entering the plane defined at the aneurysm neck. This behaviour is not present in the steady state flow regime, shown in figure 5.7. In the steady case, the helical vortex that transports flow out of the right-hand portion of the aneurysm encourages flow that only exits the aneurysm in this region and immediately moves towards a daughter vessel outlet, as shown in figure 5.11. However, the recirculation seen in the transient case results in flow re-entering the aneurysm dome for a second time adjacent to the original inflow jet. This secondary inflow leads to an increase in

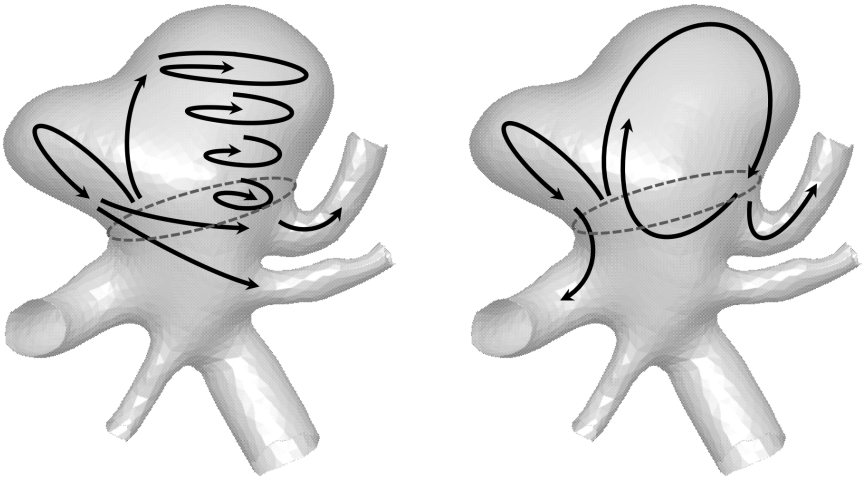

Figure 5.11: *Indications of the approximate flow regime within the BA_01 geometry for steady state and transient flow simulations at mean flow rate. Clear recirculation is seen in the transient case with flow exiting and reentering through the aneurysm neck (dashed line)*

total aneurysm inflow of the order of 17ml/min and results in the seemingly non-physical average aneurysm inflow rate of 137ml/min (114% of parent vessel flow) for the transient simulation. Details of this recirculation behaviour and the variation in flow regime between steady state and transient simulations are shown in figure 5.11.

The source of such a discrepancy in flow regime between the steady and transient simulations is not immediately clear. However, as previously discussed, once the 'Sphere' device is deployed in the aneurysm geometry, the difference between the steady and transient simulations is almost undetectable. Given the substantially reduced aneurysm inflow following device deployment, and the corresponding lower flow velocity and flow momentum in the aneurysm dome, the different flow regimes in the 'No Device' case may be momentum dependent. The vortex pattern for the steady 'No Device' simulation is similar to the lower momentum flow pattern seen after device deployment; the vortex pattern of the transient 'No Device' case may correspond to a higher momentum regime, where the mean flow regime is dominated by the higher flow rate portions of the cardiac cycle.

To interrogate this hypothesis, a number of simulations are conducted. Steady and transient simulations are run with stationary boundary conditions corresponding to the conditions at peak and mean flow rate across the BA cardiac cycle. It is suspected that two distinct flow patterns

will emerge: one corresponding to lower aneurysm dome momentum and one to higher aneurysm dome momentum.

5.3.1 Simulation Setup

Steady state simulations at both mean and peak flow rate are conducted with the same solver parameters as detailed in section 4.3.2 of chapter 4. Additionally, transient simulations are run with stationary boundary conditions corresponding to mean and maximum flow rates, as detailed in section 4.3.2, for a total of 200 time steps corresponding to 2 seconds of flow realtime. Both sets of simulations are run on 16 cores and with a convergence criterion of 5 orders of magnitude residual reduction.

5.3.2 Results and Discussion

The steady state simulations at both mean and maximum flow rate converged to the specified criterion in around 10 hours and 1800 iterations. The corresponding flow regimes predicted in the aneurysm's dome are shown in figure 5.12.

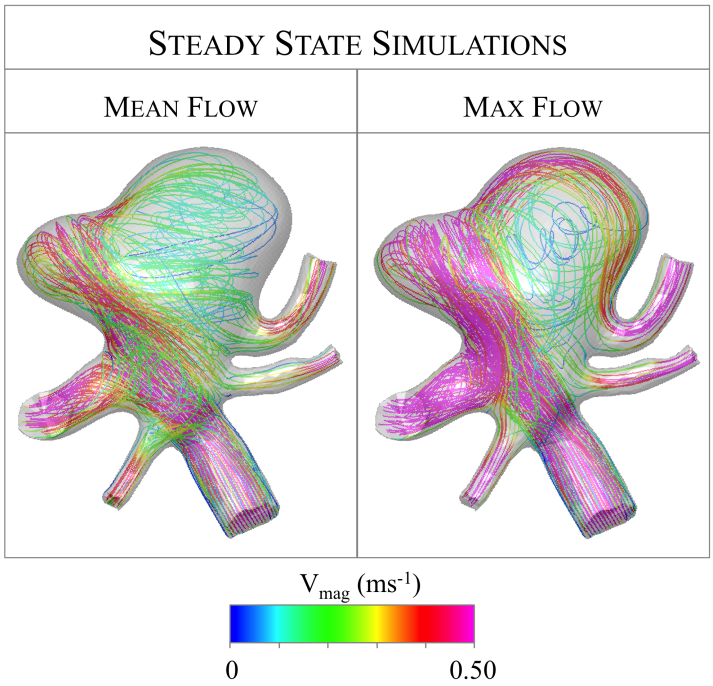

Figure 5.12: *Steady state simulations at mean and maximum flow rate*

The steady state solutions clearly show the two different flow regimes: a slower, helical vortex structure at mean flow rate and a faster vortex rotating in the perpendicular direction for maximum flow rate.

Each time step of the transient simulations converged in around 80-100 iterations, taking approximately 30 minutes per time step. The evolution of the velocity magnitude at a monitor point in the aneurysm dome is shown for mean and maximum flow in figure 5.13 and figure 5.14 respectively.

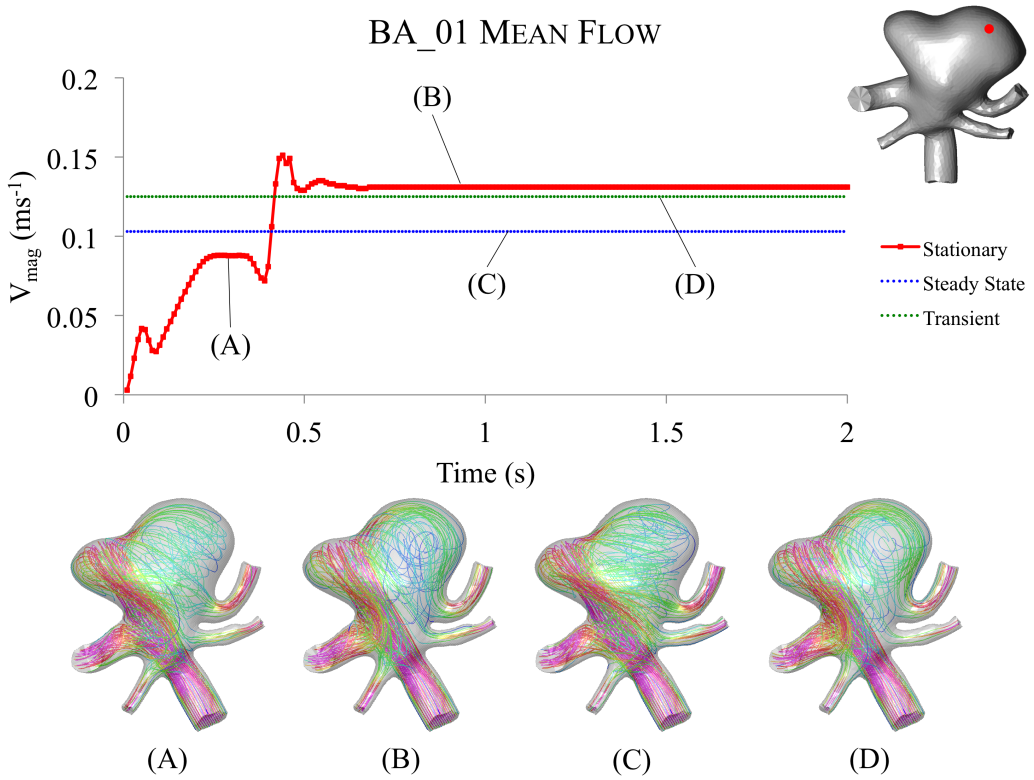

Figure 5.13: *Comparing steady and transient velocity at mean flow to the development of a transient solution with stationary boundary conditions. Corresponding flow regimes are also indicated.*

Figure 5.13 details the transient evolution of flow within the aneurysm dome under stationary conditions corresponding to mean flow rate. From the plot it is clear that two flow regimes exist. Although both of these regimes satisfy equilibrium, one regime (A) is unstable and features a helical vortex pattern, while the second regime (B) is stable with a vortex rotating in the perpendicular plane.

The first, unstable equilibrium configuration (A) is similar to the steady state solution at mean flow (C), but the slight variation in the axis of rotation between (A) and (C) leads to the

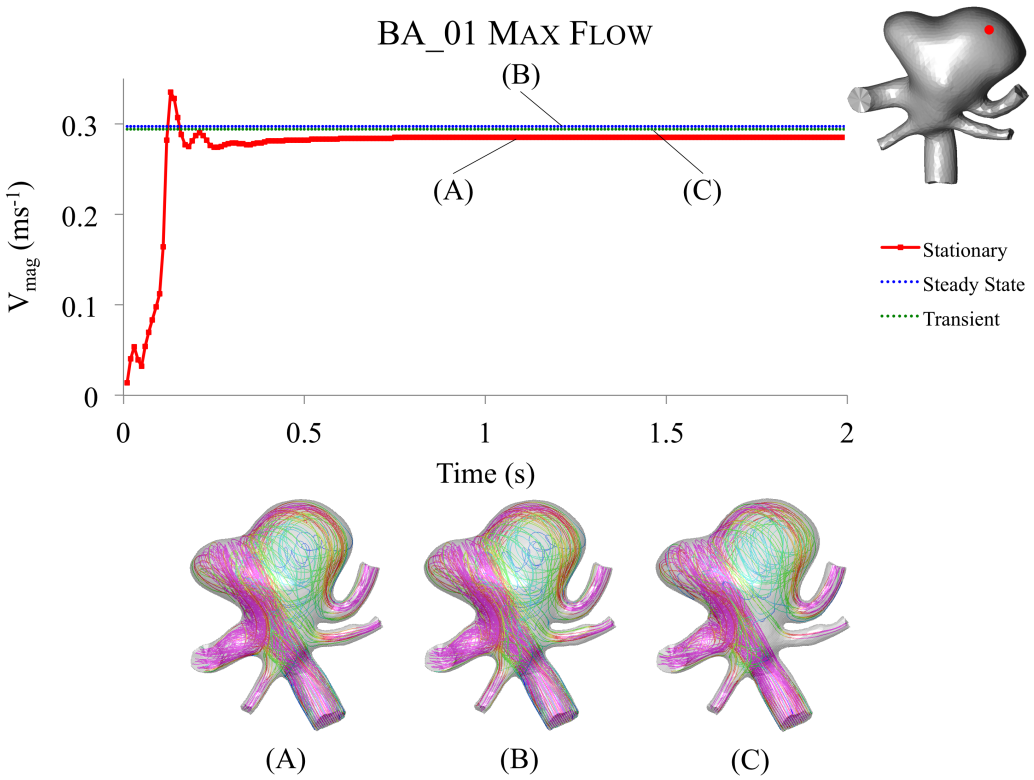

Figure 5.14: *Comparing steady and transient velocity at maximum flow to the development of a transient solution with stationary boundary conditions. Corresponding flow regimes are also indicated.*

velocity discrepancy seen in the plot of figure 5.13. This initial flow regime, (A), persists for around 0.2 seconds (around 6 'flow-throughs') before instability occurs. The instability gives way to the second, stable equilibrium configuration (B) that resembles the flow regime seen at mean flow rate in the transient case (D). This second regime appears to be associated with increased velocities and flow momentum in the right-hand lobe of the aneurysm dome.

The corresponding velocity evolution for the same point under maximum flow conditions is shown in figure 5.14, where a single, stable equilibrium flow regime is quickly converged upon. The flow regime at maximum flow rate for the transient simulation under stationary conditions (A), steady state simulation (B), and transient simulation (C), all appear identical. This common flow regime resembles the stable case at mean flow rate ((B) in figure 5.13), with a single vortex rotating clockwise in the aneurysm dome.

From figure 5.13 it appears that there are two possible flow regimes that co-exist in the BA_01 aneurysm geometry, these rival regimes are both shown in figure 5.12. One regime is unstable and persists under conditions of low flow momentum in the right-hand portion of the aneurysm dome.

The other regime is stable and corresponds to increased flow momentum in the same location. Although unstable, this first regime would likely be the first equilibrium state encountered by a flow solver that is given an initial condition of zero flow, as in the case of the steady state simulation at mean flow rate. Given the similarity between the mean flow, steady state regime predicted and the unstable stationary regime, (A), it appears that the steady state convergence criterion is met before instability occurs.

5.3.3 Conclusions: Steady State and Transient Inconsistencies

An initial discrepancy between the flow regime for a specific aneurysm predicted by steady state and transient simulations has revealed multiple steady state flow solutions. Although both an unstable and stable flow regime were highlighted, it has been shown that full convergence may be reached in steady state for the unstable regime. This behaviour has not been documented in the literature to date and depending on its generalisability, it may present a serious challenge to the validity of representing time-averaged transient behaviour of blood flow in aneurysms with steady state analyses. In the BA_01 aneurysm geometry discussed, this variation in flow regime has been shown to underestimate the true aneurysm inflow rate by 25% for the steady state solution.

5.4 Conclusion

In this chapter three patient-specific aneurysms have been discussed that challenge the conventional wisdom that steady state flow simulations accurately represent time-averaged transient simulations in the cerebral vasculature. Of the three geometries, one case was found to simply exhibit very slow convergence in steady state, but the remaining two cases both showed time-dependent flow behaviour under stationary boundary conditions, which has not been reported in the literature to date.

The implications of these flow phenomena on the hemodynamic and biochemical environment of an aneurysm dome both pre- and post-treatment by flow-diverter are entirely unknown. It is also unknown how representative the geometries discussed here may be of the general

population of cerebral aneurysms. As both of the aneurysms that exhibited unstable behaviour are wide-necked, a more comprehensive study is needed to determine whether such behaviour is generalisable, or very rare and limited to these select cases alone.

Much of the behaviour seen in these three aneurysm geometries supports the cautious conclusions of Valen-Sendstad et al. [147], which suggested that many important but subtle flow-effects may be masked in the body of CFD simulations in the literature due to poor spatial and temporal resolution and the use of overly dissipative solvers.

Chapter 6

Development of a Virtual Contrast Model

In this chapter, an in-silico model of angiographic contrast agent transport is developed. Examples of similar models in the literature are discussed in section 6.1, along with the limitations of such models, specifically focussing on contrast viscosity and density. A methodology for in-vivo verification of contrast residence is introduced in section 6.2, with in-vivo contrast decay of a porcine aneurysm model calculated in section 6.3. An in-silico model of contrast transport is set up in section 6.4 and compared to the in-vivo gold standard in section 6.5. Finally, the influence on the model of contrast density and viscosity, as well as parent vessel flow rate, are quantified in section 6.6 and section 6.7 respectively.[1]

6.1 Introduction

6.1.1 Motivation: the Need for a Virtual Contrast Model

The focus of the vast majority of the literature in the field, and this thesis thus far, has been to investigate 'surrogate' measures for successful obliteration of an aneurysm after treatment with a flow-diverter. As previously discussed in chapter 2, the precise mechanisms leading to successful

[1]The work presented in this chapter appears as part of: T W Peach et al. In-vivo Validation of a CFD Virtual Contrast Model (in preparation)

aneurysm occlusion are poorly understood, but appear to be flow-dominated. [20] [112]

Conventional 'surrogate' measures such as aneurysm flow rate, mean and maximum inlet velocity, WSS, WSSG, OSI and GON are all calculated from *in-vitro* and *in-silico* studies in the hope of striking upon a variable, often in the absence of any clear mechanism, that might govern thrombus formation. The rationale supporting a correlation between some of these measures and treatment success is reasonable: reduced flow and velocity are assumed to promote increased aggregation of platelets and thrombin, leading to a likely increase in thrombus proliferation. However, the importance of other more complex measures remains little more than conjecture.

A major limitation of the development of a hemodynamically driven thrombus formation model is the lack of a method to accurately measure these 'surrogate' indices under realistic conditions. On one hand, *in-vitro* and *in-silico* simulations with high spatial accuracy, fail to capture the complex biochemical nuances of the hemodynamic environment, and conversely, accurate measurement of such metrics is impossible in fully biochemically consistent *in-vivo* studies.

Limited methods do exist that can begin to verify simpler flow metrics *in-vivo*; the velocity and flow rate of blood in vessels may be estimated with MR imaging to a good degree of accuracy. [162] However, the validity of measuring more complex hemodynamic variables with MR techniques is questionable, as current MR imaging is undermined by a lack of resolution with relatively small numbers of voxels (around 5-10) spanning a vessel cross-section. [118] The effect of this under-resolution is exaggerated in the complex flow environment of the aneurysm dome, where there is no fixed flow direction, areas of vorticity are common, and large temporal variations may be experienced. The direct measurement of more sophisticated hemodynamic variables, such as WSS and other vector-based measures, is completely impossible by MR techniques without at least an order of magnitude increase in both spatial and temporal resolution. [34]

Angiography is currently the only imaging technique with the temporal and spatial resolution to begin to accurately infer the flow conditions experienced within the aneurysm dome *in-vivo*. As a result, all attempts to verify computationally simulated aneurysm flow patterns with *in-vivo* behaviour have inevitably focussed on the means of visualising blood flow angiographically: the

transport of contrast agent.

6.1.2 Contrast Transport Models in the Literature

A brief survey of virtual contrast models that have been proposed in the literature is summarised below.

Ford et al. 2005 [47] Methodology: A quantitative comparison between clinical (2D, 2fps) and virtual angiography. Contrast is modelled as an independent scalar. Bolus injections are modelled as both a idealised 'rectangular' function and a profile fitted to angiographic data. Inlet boundary condition are based on MRI data of age and sex matched volunteers, and modified to account for contrast injection rate. Results were visualised using 3D x-ray projection software and mapped into 2D. Conclusions: The best agreement between results was seen using the angiographically derived bolus profile. The aneurysm contrast decay predicted was accurately fitted to an exponential profile. Inaccuracies were attributed to not modelling contrast-blood density and viscosity mismatch, but these concerns were largely eliminated by heavily diluting the experimental contrast agent. It was shown that the contrast injection perturbed normal blood flow, suggesting that angiographic imaging may not represent normal conditions.

Cebral et al. 2007 [22] Methodology: A qualitative comparison between clinical (2D, 7.5fps) and virtual angiography. An injected bolus of dye was modelled as an independent scalar quantity, with an inlet profile inferred from angiography. Average vessel flow rates were assumed at the inlet. Virtual angiograms were aligned into a similar orientation as the clinical angiography, and the results inspected visually. Conclusions: Good correspondence was seen between major aneurysm flow features, approximate aneurysm fill and washout rates and areas of vorticity. The greatest discrepancy between virtual and real angiography was attributed to not modelling the density and viscosity differences between blood and contrast.

Sadasivan et al. 2009 [131] Methodology: A quantitative comparison of angiography from a rabbit model (2D, 30fps, pre- and post- FD implantation) and a previously developed [132] analytical model of contrast washout. An angiographic washout factor was proposed, which was correlated with aneurysm thrombosis at 6 months follow-up. Conclusions: A reduction in contrast washout curve amplitude and an increase in decay time constant were seen after stent

implantation. Reduced contrast infiltration and time constant increase were linked to more successful aneurysm thrombosis.

Endres et al. 2012 [43] Methodology: A quantitative comparison between clinical (2D, 30fps) and virtual angiography. Contrast was modelled as an independent scalar. Bolus injection was matched to heart state (position in cardiac cycle) and the bolus profile was matched to angiography. The inlet boundary condition period was matched to angiographic heart rate, and inlet flow rate was matched to angiographic contrast residence. Results were visualised using 3D x-ray projection software and mapped into 2D. Conclusions: Good correspondence was seen between clinical and simulated results. The importance of matching bolus injection point in the cardiac cycle is stressed, with large variation in contrast decay seen otherwise. The greatest errors in predictions are attributed to not modelling contrast viscosity and density.

Jou et al. 2012 [68] Methodology: A quantitative comparison between simulated aneurysm inflow and aneurysm inflow derived from clinical angiography (2D, 30fps). Mean flow rates are used for inlet boundary conditions. Conclusions: Correlation between results is good, but the CFD model consistently underestimates aneurysm inflow by 20%. Error was attributed to variations in density and viscosity of the blood/contrast that were not modelled *in-silico*.

Across the models in the literature, three factors emerge that appear to account for the majority of inaccuracies in *in-silico* models: blood/contrast density mismatch, blood/contrast viscosity mismatch, and instantaneous flow rate at the contrast introduction.

6.1.3 Proposed Contrast Model

In this chapter, a virtual contrast model is proposed that may be easily appended to transient CFD simulations. The basis of the model is to approximate angiographic contrast medium as an independent scalar quantity that is introduced at the geometry inlet boundary condition, similar to the injection of a dye. Initially, the scalar quantity is assumed to have the same viscosity and density as the simulated blood, but the effect of varying viscosity and density is explored. Finally, the effect of both inlet boundary condition flow rate and the presence of a catheter in the vessel lumen are investigated. The model is validated with *in-vivo* angiography from a porcine study.

6.2 The Basis of *In-vivo* and *In-silico* Contrast Validation

When comparing actual and predicted contrast washout we are confronted with an inconsistency: *in-vivo* data consists of angiographic pixel grayscale values representing the indirect measurement of contrast concentration projected into the 2D plane, while simulated results comprise absolute concentrations of virtual contrast medium distributed in 3D. Although the projection of the 3D virtual contrast distribution into the same 2D plane as the angiography is trivial, the correlation between absolute contrast concentration and grayscale value is more problematic.

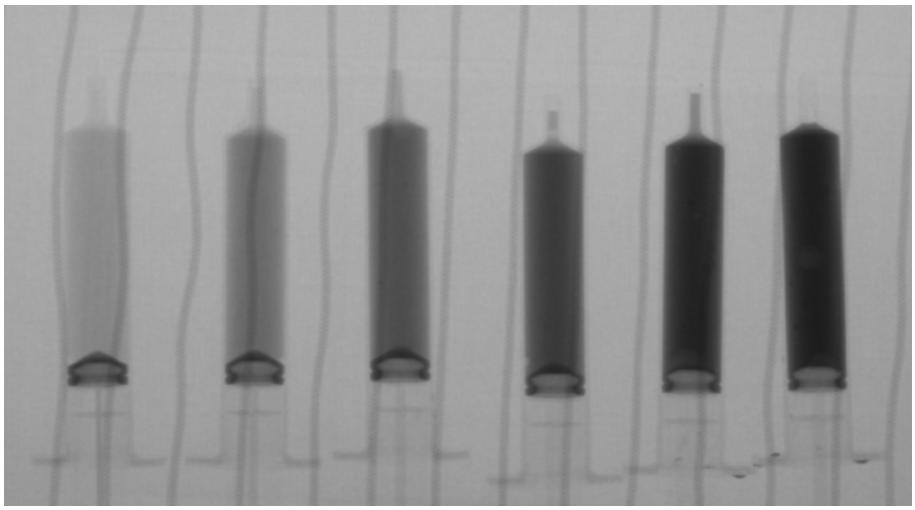

Figure 6.1: *Variation of contrast concentration with angiographic grayscale value experiment results*

The grayscale value seen in an individual angiographic pixel is the result of attenuation of the x-rays by contrast or surrounding tissue or bone. As a result of the subtraction phase of digital subtraction angiography (DSA), higher density regions, such as bone and contrast, appear dark, and lower density soft tissue appears light. Although the grayscale value of a pixel will be proportional to the local contrast concentration (more contrast will attenuate more radiation, resulting in a darker pixel), the relationship is complex and highly non-linear. It is also unclear if any post-processing (smoothing, contrast enhancement, rescaling of the dynamic range etc.) of the x-ray image occurs with software onboard the imaging unit; the effect such manipulation may have on the correspondence between contrast concentration and the corresponding pixel value may be substantial.

There are examples in the literature of full 3D calculations reconstructing angiography from inferred x-ray attenuation models interacting with contrast media. [47] [43] However, in the

interest of reducing computational complexity and creating a contrast model that can be incorporated into even basic angiography, a simple mapping of contrast concentration to angiography grayscale value is investigated in this case. A calibration experiment is performed whereby a number of 5ml syringes are filled with a mixture of saline and Omnipaque^{TM} 240 contrast medium corresponding to contrast concentrations of 0-50%. These syringes are then placed between two 1000ml bags of saline (to provide background x-ray absorption similar to soft tissue) and imaged with DSA protocols typical for adult cerebral/neck vessels. The resulting 2D angiographic image is shown in figure 6.1 .

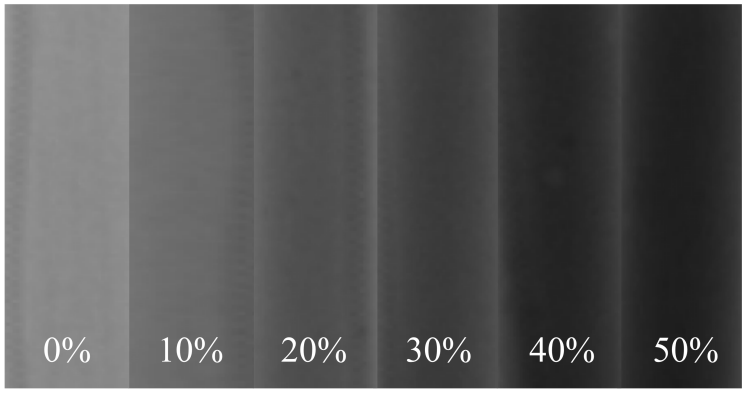

Figure 6.2: *Calibration Card*

There is clear differentiation between the grayscale values across the different concentrations. A windowed sample of the grayscale values of each syringe is taken from figure 6.1, as show in figure 6.2, and the mean grayscale value is plotted against contrast concentration in figure 6.3.

There appears to be a linear relationship between contrast concentration and grayscale value. It is likely that the very high density of the contrast (specifically the high electron-density of the iodine) results in very large relative changes between contrast concentrations, rendering any non-linear effects insignificant.

The plot suggests that once the background grayscale values of the angiography are subtracted entirely, the grayscale value of a pixel is linearly proportional to the contrast concentration. Hence, plots of variation in grayscale value of angiography can be considered analogous to plots of relative contrast concentration.

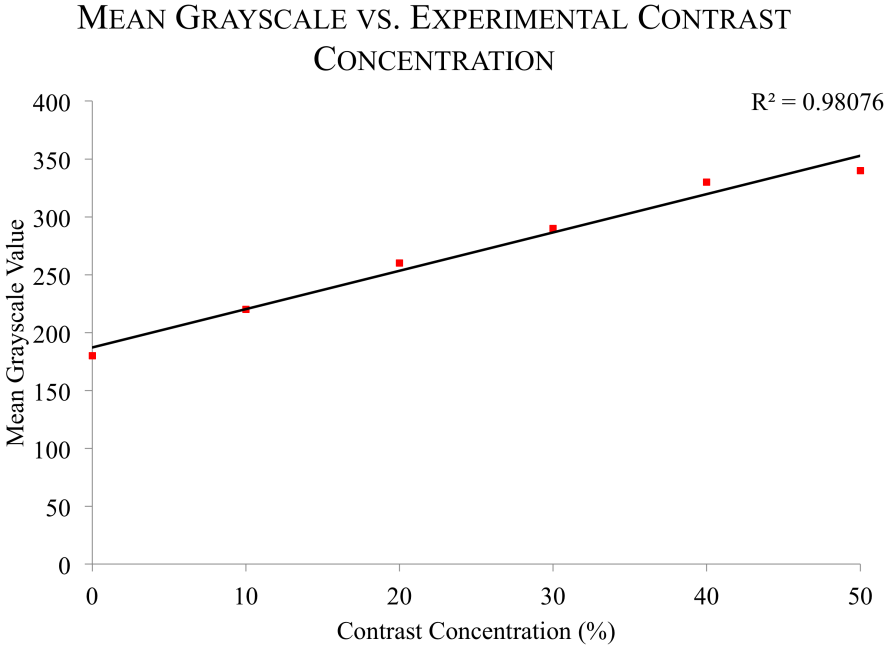

Figure 6.3: *Calibration Graph*

6.3 *In-vivo* Experiment

In order to assess the accuracy of the proposed virtual contrast model the simulation must be compared to an *in-vivo* aneurysm. The variability of the size, shape, and flow conditions of clinically presented cerebral aneurysms do not make them ideal test cases for investigating such a contrast model in the first instance. Instead, an animal model is proposed whereby a number of identical sidewall aneurysms may be created surgically, imaged, and treated by flow-diverter.

The target artery diameter (approx. 4mm), heart rate (70-80BPM resting), total cardiac output (approx. 6L/min) and animal size (60-70Kg) make the porcine model a good approximation to the flow conditions typical of a human internal carotid artery (ICA). The alternative to the porcine model, the rabbit-aortic-arch aneurysm model, has a heart rate closer to 200BPM and risks turbulent transition and high Womersley number effects such as flow reversal, which are not seen in the human cerebral circulation.

All animal experiments discussed in this study were performed by James Byrne and Rafik Rizkallah (Nuffield Department of Surgical Sciences, University of Oxford), assisted by Zhong You, Jiayao Ma and Thomas Peach (Department of Engineering Science, University of Oxford).

All experiments were performed following Oxford University ethics board approval and with financial support from the Wellcome Trust and EPSRC under grant number WT 088877/Z/09Z.

6.3.1 Experimental Methodology

6.3.1.1 Experiment

Experimental aneurysms are created in a porcine animal model using two, female large white pigs of 60-65 kgs. Each sidewall aneurysm is formed surgically by vein graft using the jugular vein cut at 45 degrees forming an anastomosis on the common carotid artery (CCA) with continuous 8/0 stitching. One aneurysm is formed on each CCA in two animals giving a total of four experimental aneurysms of near identical size and shape. The CCA is observed to have a diameter of around 4mm in both animals and the resulting sidewall aneurysms had a 5mm diameter, 15mm length and 7mm neck diameter. After creation, the aneurysms are allowed to heal for three weeks to allow for any local swelling to dissipate and for endothelialisation at the anastomosis site to stabilise. Both animals are given Aspirin and Clopidogrel as anti-platelet therapy following the surgical procedure to reduce spontaneous thrombosis and risk of ischemia, as would be standard practise in the clinical setting.

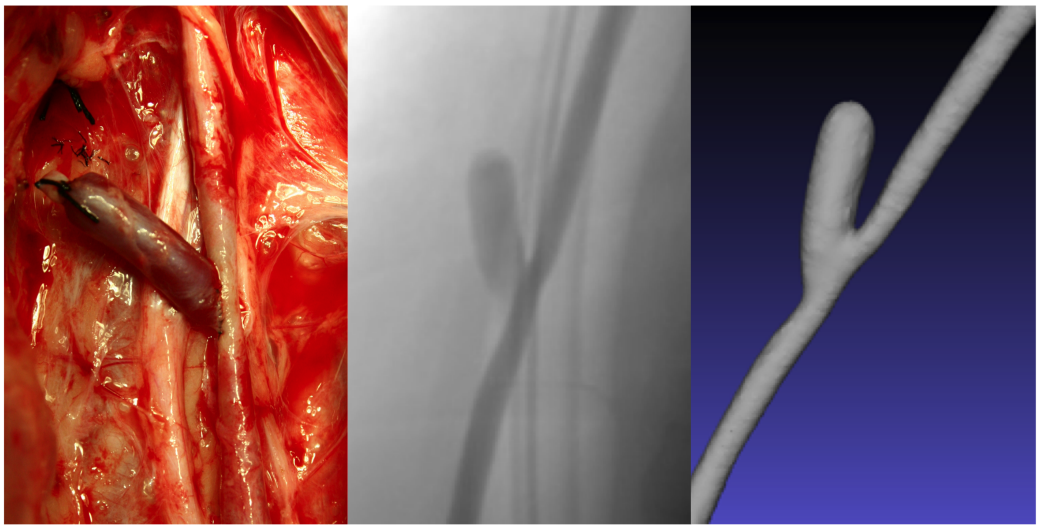

Figure 6.4: *Experimental aneurysm: aneurysm at surgical creation by vein graft of the CCA(left), 2D angiography showing aneurysm in-vivo 3 weeks post-creation(centre) and 3D STL reconstruction of the aneurysm from 3D rotational angiography 3 weeks post-creation(right)*

An aneurysm at surgical creation is shown in figure 6.4 (left). A catheter is inserted into

the femoral artery and angiography performed; 3D rotational angiography is used to accurately reconstruct the vessel and aneurysm geometry while 2D angiography is used to verify the patency of each aneurysm and observe angiographic contrast washout in the aneurysm dome. The 3D rotational runs are performed at a rotation speed of 20 degrees a second with a 20ml contrast injection, and the 2D runs are conducted at 7.5 frames per second with a 10ml contrast injection. A 2D angiographic image showing aneurysm patency with contrast filling the dome is shown in figure 6.4 (centre.)

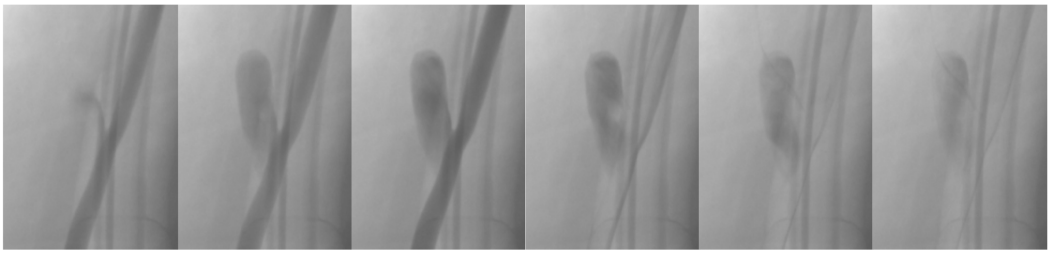

Figure 6.5: *Contrast residence in an experimental aneurysm, each image is separated by a time interval of 0.4 seconds*

6.3.1.2 Postprocessing

DICOM post-processing is completed in OsiriX, where 3D geometries are segmented using the default segmentation algorithm, and the resulting vascular surfaces are exported as .STL files. A 3D reconstruction of an experimental aneurysm is shown in figure 6.4 (right). Good correspondence is seen between the measured vessel and aneurysm size at surgical creation and the 3D reconstruction created from angiography three weeks post-creation. A small degree of thrombosis occurred in all four experimental aneurysms at the distal tip of the aneurysm dome in the area of the vein ligation; this is to be expected and results in a more clinically realistic smooth hemispherical aneurysm tip, rather than a sharp point.

Visually, the flow patterns between the four experimental aneurysms appear identical, with flow entering the aneurysm neck distally and circulating around the whole aneurysm dome, forming one large vortex. Typical flow can be seen in figure 6.5, where each DICOM image is separated by 0.4 seconds. The presence of flow recirculation results in contrast remaining in the aneurysm for 3-4 seconds after all contrast has left the parent vessel.

The 2D angiography DICOMs are exported as .tiff files and later segmented in Matlab (Math-

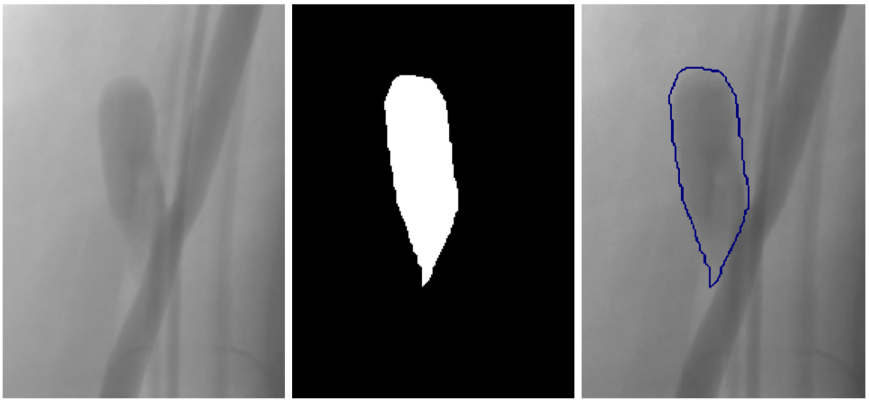

Figure 6.6: *Segmentation of the aneurysm dome in 2D angiography*

Works, Natick, MA). A segmentation window isolating the aneurysm dome from the parent vessel is created manually for each experimental aneurysm, as shown in figure 6.6 (left), and the mean grayscale value in the aneurysm dome is calculated for each DICOM in the time series.

6.3.2 *In-vivo* Results

The variation in time of the mean grayscale value in the aneurysm dome for each experimental aneurysm is plotted in figure 6.7. In each case, the mean grayscale value is normalised by the maximum mean grayscale seen in each geometry. The curves are presented with the background grayscale value (from the aneurysm with no contrast present) subtracted, and hence the grayscale value at a given time point is the result of contrast alone. As previously discussed in section 6.2, the approximately linear correspondence between grayscale value of a 2D DICOM pixel and the corresponding contrast concentration within the aneurysm, projected into the plane of the DICOM, allows for the plots of figure 6.7 to be considered analogous to aneurysm contrast concentration curves.

The plots in figure 6.7 show a similar contrast concentration curve shape to other studies. [43] A high rate of contrast infiltration is clearly visible, followed by a lower contrast decay rate that appears approximately exponential, suggesting the contrast decay is dominated by convective transport. Some variation can be seen across the four curves, which may be due to a number of factors: variation in contrast injection speed; variations in flow speed at the time of injection,

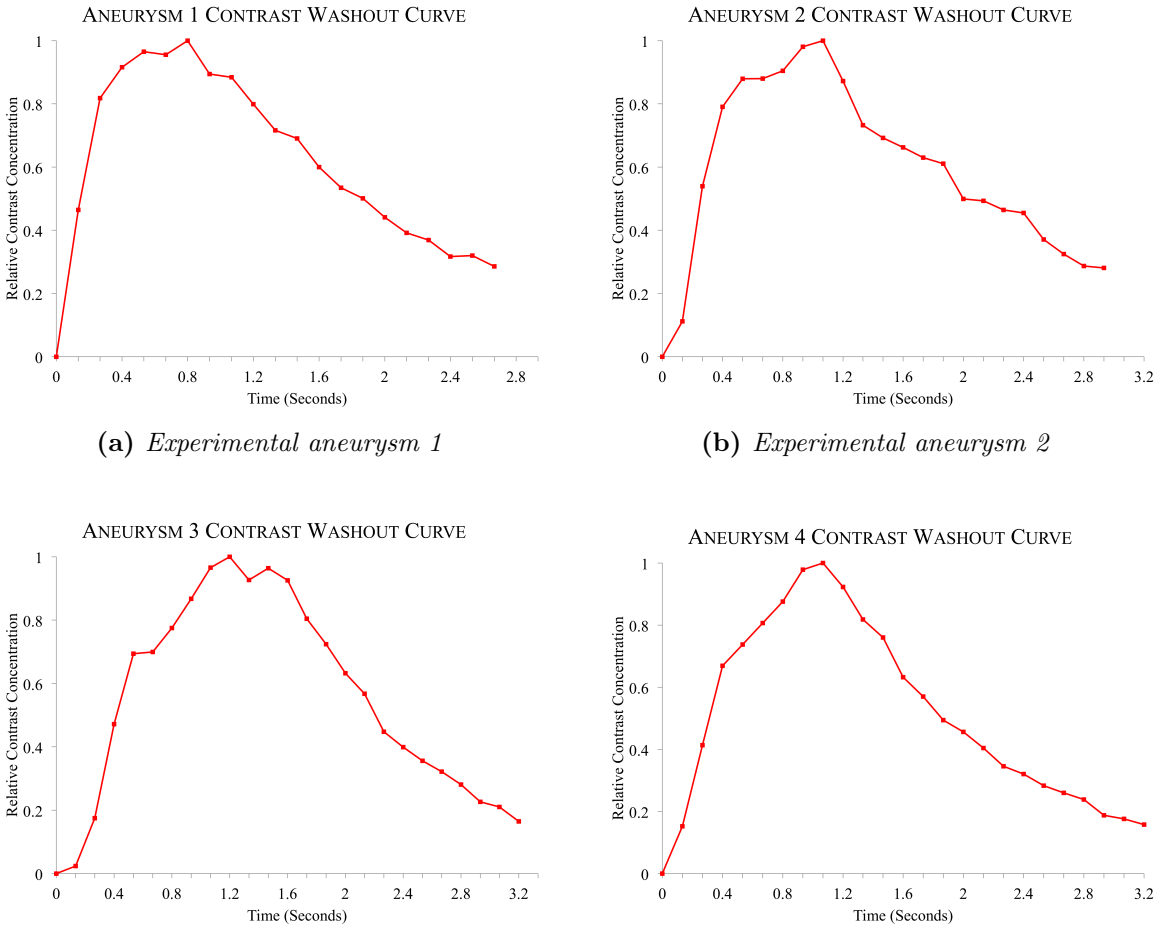

(a) *Experimental aneurysm 1*

(b) *Experimental aneurysm 2*

(c) *Experimental aneurysm 3*

(d) *Experimental aneurysm 4*

Figure 6.7: *Contrast washout curves for the four experimental aneurysms*

depending on the position in the cardiac cycle; differences in parent vessel blood flow rates both between left and right CCAs in each animal and between the two animals; and finally, variations in actual aneurysm size. However, all of these effects appear small, as the shape and scale are fairly constant across all four plots. The curves are easily split into two parts: firstly, contrast enters the aneurysm from the parent vessel at a high rate for the first 0.8-1.0 seconds (approximately one heart beat), and secondly, the contrast level then peaks before beginning to fall, as the contrast washes-out of the aneurysm at a much lower rate than it entered, falling to approximately 25% of the peak value in a further 2.0 seconds. The volume of contrast remaining in the aneurysm two to three cardiac cycles after the peak contrast concentration suggests high variation in flow velocity in the aneurysm sac and the high likelihood of areas of flow recirculation as is seen in figure 6.5.

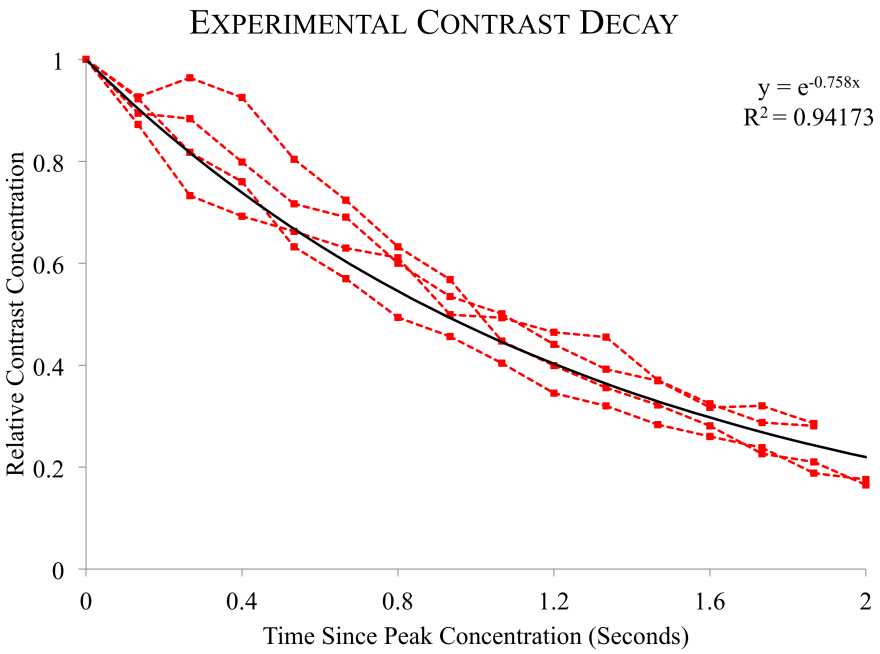

Figure 6.8: *Decay curves of all four experimental aneurysms with an exponential line of best fit*

Although the contrast concentration curves are fairly smooth, small fluctuations are seen, and these variations occur across the inflow and outflow portions of the curves. The variations appear approximately periodic, falling every 0.8-1.0 seconds (around one heartbeat) and most likely correspond to sudden changes in parent vessel flow rate, such as at peak systole. Among the four plots of figure 6.7, there appears to be greater variation in shape in the inflow portion, rather than the outflow portion, of contrast concentration. This is likely due to the influence of contrast injection time and speed on contrast infiltration but not contrast decay. Also, the increased speed of the contrast infiltration (and hence shorter infiltration time of the order of one heart beat) makes the distribution more sensitive to periodic variations in parent vessel flow. Conversely, the outflow portion of the plots shows little variation across the aneurysms and is approximately that of exponential decay, where contrast washout is driven by blood flow alone, and any periodic effects of the cardiac cycle are averaged-out by the slower rate of decay.

The decay portion of the contrast concentration curve gives a more accurate representation of the flow conditions in the aneurysm sac than the contrast inflow curve. In the contrast decay, the influence of external factors such as contrast injection volume, speed, and timing are reduced, and flow-recirculation behaviour, which is very common in aneurysms, can be captured. Hence, focussing on the decay portion of the contrast concentration curve is natural

for any study attempting to correlate simulated flow conditions with *in-vivo* contrast enhanced angiography.

The decay portions of the contrast concentration curves for the experimental aneurysms are plotted in figure 6.8 and show good similarity across all four geometries. An exponential decay trend line (assuming a contrast concentration of 1 at t = 0) is fitted to the data with a decay constant of 0.764 s^{-1}.

6.4 *In-silico* Experiment

6.4.1 Simulated Geometry

Given the similarity in geometry size, flow patterns and contrast concentration curves between the four experimental aneurysms, and in the interest of increasing computational efficiency, the 3D geometry of one aneurysm is selected for the computational study and is assumed to be representative of the behaviour seen in all four experimental aneurysms.

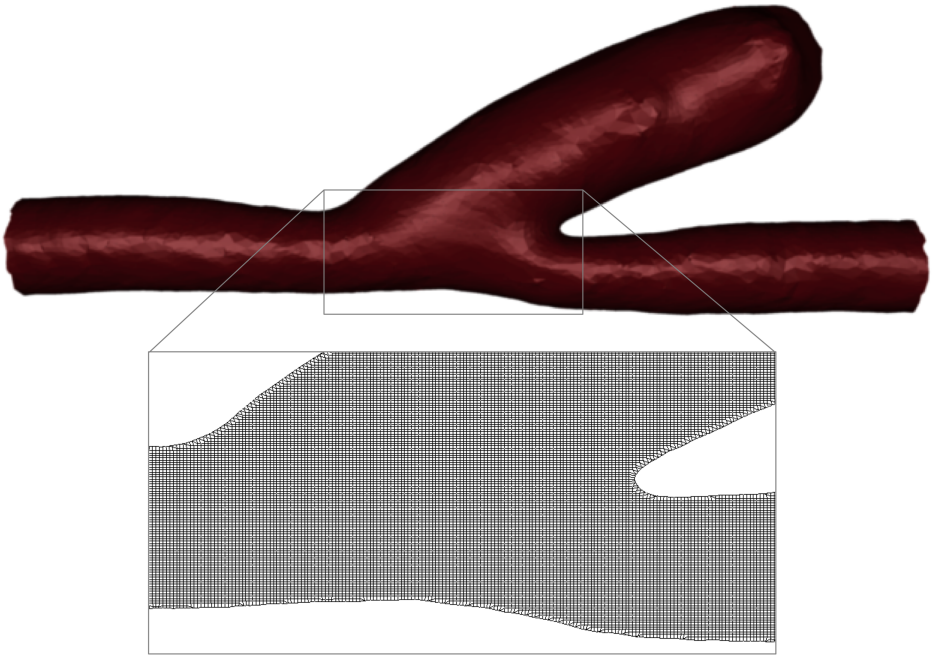

Figure 6.9: *Trimmed simulation geometry and details of mesh resolution*

In order to reduce the simulation mesh size, the reconstructed 3D geometry shown in figure 6.9 is trimmed to reduce the parent vessel portion of the geometry to a length of approximately 10 vessel diameters. The aneurysm geometry is imported into CFD-VisCART and meshed. Meshing is completed with a projected single domain con-conforming mesh, an omnitree cartesian tree type, and three near-wall cartesian layers to give smooth and well-resolved boundary definition. A minimum mesh density of 4,000 elements/mm^3 is prescribed to ensure a mesh-independent solution to the margin discussed in chapter 3 and chapter 4, which results in a mesh size of 4,290,000 elements.

6.4.2 Modelling Contrast *in-silico*

Contrast is modelled computationally as an independent scalar quantity introduced at the simulation inlet and transported in the bulk flow in a similar manner to dye particles. Although this method is a major simplification of what is, in reality, a two-fluid mixing problem, the reduction in both computational cost and the complexity required to characterise true two-fluid flow is considerable. The same independent scalar approximation is made in all of the virtual contrast models detailed in the literature with little loss of accuracy reported, as discussed in section 6.1.2.

$$\frac{\partial (\rho\phi)}{\partial t} + \bigtriangledown \cdot (\rho\phi \mathbf{u}) = \bigtriangledown \cdot (\Gamma_\phi \bigtriangledown \phi\ ) + S_\phi \tag{6.1}$$

where ϕ = local contrast concentration, Γ_ϕ = the diffusion coefficient of contrast in blood and S_ϕ = contrast concentration inlet boundary condition incorporated as a source term

Transport of the contrast is governed by equation 6.1, previously discussed in chapter 2. The contrast does not alter the simulated blood density or viscosity and has a diffusivity in blood of $1.0\text{x}10^{-7}\text{m}^2\text{s}^{-1}$, an order of magnitude estimate based on the diffusivity of tracer particles in blood flow. [129] The dominance of convection over diffusion in the flow is likely to render the effects of any inaccuracy in estimating the diffusivity small.

Previous studies in the field [43] and the experimental results in section 6.3.2 confirm the influence of contrast bolus injection speed and timing on the resulting aneurysm contrast con-

centration curve. The correlation between *in-vivo* and *in-silico* contrast residence curves may be greatly improved by 'matching' the real and virtual contrast injections to the same point in the cardiac cycle. [43] However, this approach relies on high-quality angiography with fine temporal-resolution (<0.1 seconds), which is likely to limit its clinical relevance. Moreover, without repeating the contrast injection *in-vivo* at another point in the cardiac cycle, there is a risk that 'matching' the two results reduces the virtual model's generalisability with a contrast washout curve that is not representative of the cardiac cycle as a whole.

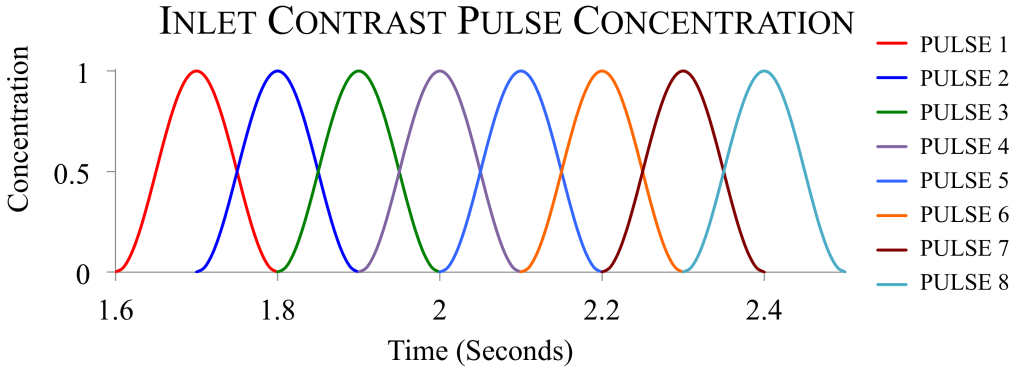

Figure 6.10: *Multiple independent contrast pulses introduced at the geometry inlet*

In this study, in order to increase generalisability and to quantify the influence of the cardiac position at the time of contrast injection, a series of sequential injections of contrast are made at intervals across the whole cardiac cycle, as shown in figure 6.10. The contrast particles from one injection have no interaction with the contrast particles from another pulse. This allows for the contrast concentration curve resulting from contrast injection at *any* point (to the nearest $1/8^{th}$ fraction of the cardiac cycle) to be estimated. It also quantifies any changes in contrast concentration due to variation in the cardiac position at the bolus injection. Each contrast pulse has a non-zero value for 0.2 seconds with eight separate pulses at 0.1 second intervals covering the entire 0.8 seconds of one cardiac cycle. The contrast pulse concentration is sinusoidal in time with zero gradient at maximum and minimum contrast concentration. The plots of figure 6.10 show the value of each contrast pulse at the inlet boundary of the geometry over time.

From these eight independent contrast pulses, any length of angiographic bolus administered at any $1/8^{th}$ fraction of the cardiac cycle may be modelled with a linear combination of the corresponding eight pulse decay curves. For example, the aneurysm contrast decay curve for a

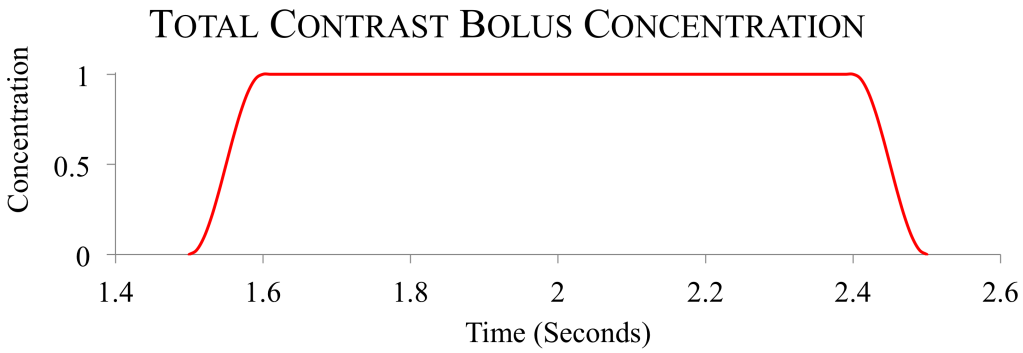

Figure 6.11: *Multiple independent pulses introduced at the geometry inlet combine to create a cycle-averaged contrast bolus (unity over one cardiac cycle)*

uniform bolus of contrast spanning the entire cardiac cycle (shown in figure 6.11) is calculated at each time step from the sum of the instantaneous values of all eight contrast pulses ('Pulse 1' to 'Pulse 8') plus the the value of 'Pulse 8' shifted forward in time by 0.8 seconds.

The uniform contrast bolus shown in figure 6.11 (with a value of unity over the entire cardiac cycle) is used in this study as the resulting contrast residence profile represents typical contrast residence averaged over one cardiac cycle—a 'cycle-averaged' profile. Then, given reasonable self-similarity of each contrast pulse residence profile (i.e. the volume of contrast entering the aneurysm varies in time, but the underlying rate of infiltration and decay remain constant), the cycle-averaged residence profile infiltration and decay rates can be considered representative of any bolus length, shape, and start time. The validity of such an assumption, and specifically the self-similarity of the different contrast pulse distributions, is discussed in detail in the following sections.

Finally, as discussed in section 6.3.2, the effects of contrast bolus injection times are more acutely seen in the infiltration portion of the aneurysm contrast concentration curve. Consequently, the infiltration portion of the curve is quantitatively ignored in this virtual model in favour of concentrating on the more robust decay portion, as shown in figure 6.8.

6.4.3 Simulation Setup

The simulation mesh discussed in section 6.4.1 is imported into the multi-physics suite CFD-ACE+. Blood flow is modelled as an incompressible fluid with unsteady 3D Navier-Stokes

governing equations, with a Central Differencing scheme for spatial differentiations and interpolations, as well as a Crank-Nicholson second order scheme for time-marching. The SIMPLE-Consistent (SIMPLEC) [105] [41] pressure correction method and an algebraic multigrid method for convergence acceleration are used. [158] A time step of 0.01 seconds is used in agreement with the time-step independence tests of chapter 3 and chapter 4. Blood is modelled as a Newtonian fluid (assuming non-Newtonian effects are small in arteries with a diameter greater than 0.5 mm [111]) with a density of 1000 kg m^{-3} and a dynamic viscosity of 0.004 Pa s. A rigid arterial wall is assumed.

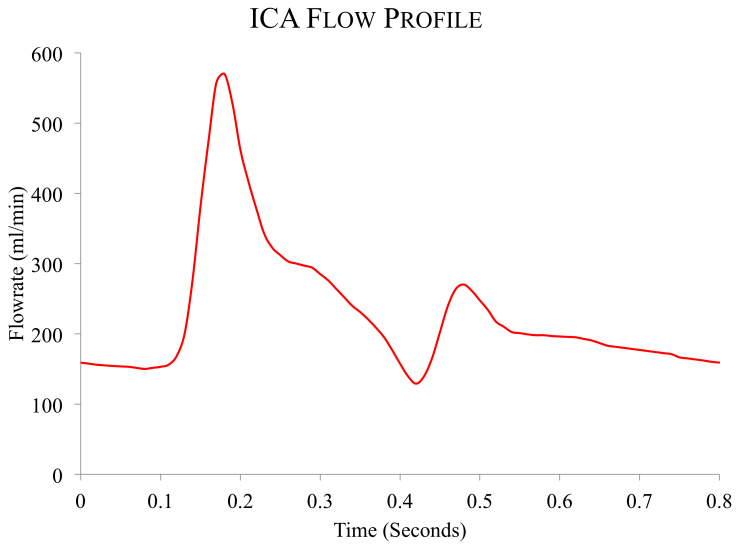

Figure 6.12: *Human ICA flow profile generated from a 1D model of the arterial tree*

The transient simulation is run with a time-varying inflow based on the profile of flow in the human ICA, as shown in figure 6.12. [124] As an accurate profile of flow in a porcine CCA is not available, it is concluded that the similarity in flow rate, artery diameter and distance from the heart between the porcine CCA and the human ICA make this assumption reasonable. A radially symmetric inlet velocity profile is prescribed at the inlet and scaled to give a mean flow rate of 230ml/min. The resulting simulation has a maximum and minimum Reynolds number of 680 and 120 respectively and a Womersley number of 1.40, confirming that the flow is confined to the laminar regime. A parabolic inlet velocity profile is used, as the relatively small Womersley number of the inflow suggests little departure in velocity profile from a Poiseuille solution. An outflow boundary condition of fixed pressure is also applied.

The simulation is run on 32, 2.93 GHz cores with each time-step converging to five orders of

magnitude residual reduction in around 50-100 iterations in a typical solution time of 30 minutes per time step. The contrast pulses are introduced after two full cardiac cycles (1.60 seconds real time) to reduce the influence of initial transient flow effects. The simulation is run for a further three cardiac cycles after the introduction of the final contrast pulse, giving a total simulation time of six cardiac cycles (4.80 seconds real time).

6.4.4 *In-silico* Results

The typical flow regime within the aneurysm dome is shown in figure 6.13 for mean parent vessel flow rate. A large vortex dominates the aneurysm dome, driven by flow entering in the distal portion of the neck and driving circulation in the counter-clockwise direction. A small area of recirculation can be seen in the tip of the aneurysm, where low-speed flow rotates in the clockwise direction. This flow pattern persists throughout the entire cardiac cycle.

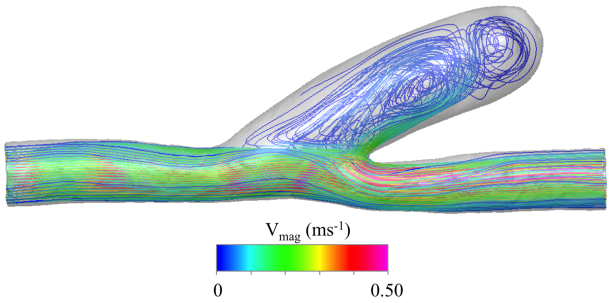

Figure 6.13: *Flow streamlines at mean parent vessel flow rate in the 'No Device' simulated geometry*

The 3D distribution of each of the eight independent contrast pulses is exported for every fourth time step ($1/20^{th}$ of a cardiac cycle) to aid computational efficiency. The 3D contrast pulse distributions are then imported into Matlab, where the 3D distributions are projected into the same 2D plane as the experimental DICOMs from section 6.3. The total contrast value in the aneurysm dome is calculated for each independent pulse, at each time point, and is plotted in figure 6.14.

In figure 6.14, large variation can be seen in the magnitude of the contrast value between the eight different introduction times; less than half the quantity of contrast is washed into the aneurysm for the contrast pulse introduced 0.6 seconds into the cardiac cycle (Pulse 6) when compared to the pulse introduced at 0.1 seconds (Pulse 1). This variation suggests that the

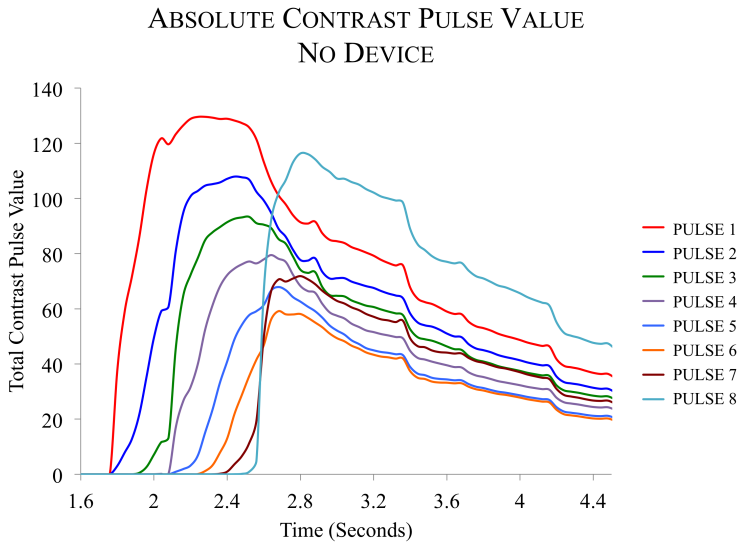

Figure 6.14: *Total absolute contrast value within the aneurysm dome for all eight contrast pulses*

absolute magnitude of contrast washed into the aneurysm varies considerably across the cardiac cycle under 'normal' flow conditions.

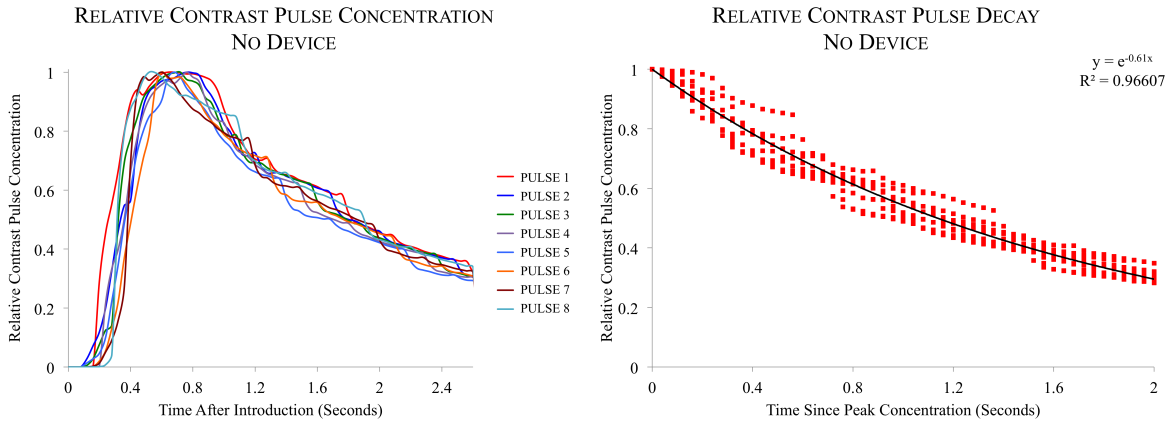

(a) *Relative contrast pulse concentration* **(b)** *Relative contrast pulse decay*

Figure 6.15: *Contrast pulse residence and decay for all eight pulses in the 'No Device' geometry*

Small peaks and troughs are seen in the the plots for all eight pulses. These occur at fixed times, mainly at 2.10, 2.90, 3.40, 3.70 and 4.20 seconds, all of which are either 0.2 or 0.5 seconds from the start of a cardiac cycle and correspond to the two peaks seen in the ICA flow profile (figure 4.12). The same effect is seen in the experimental contrast concentration plots of figure 6.7.

Despite the large variation in absolute value of the eight contrast pulses, when the relative contrast concentrations are plotted against the time after the pulse first enters the aneurysm,

as in figure 6.15a, all the plots have a very similar shape. The shape of the plot shows strong similarity to the experimentally obtained contrast washout curves of figure 6.7. In both the experimental and simulated cases, the time from contrast first entering the aneurysm to reaching peak concentration is around 0.8 seconds, and in both cases the contrast concentration falls to 30-40% of the peak value around 2.0 seconds after the peak.

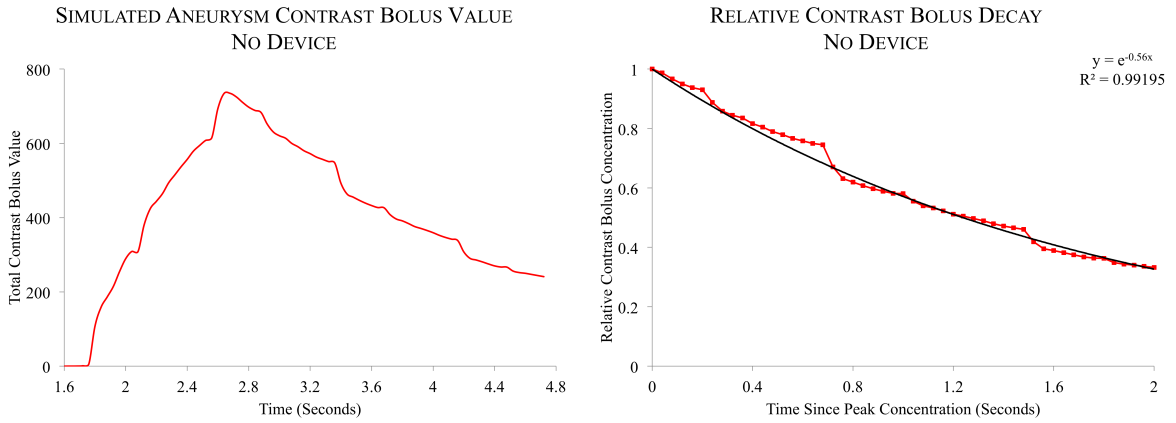

(a) *Absolute contrast value* **(b)** *Contrast decay*

Figure 6.16: *Cycle-averaged simulated contrast residence and decay for the 'No Device' geometry*

As for the experimental data, the decay portion of the separate contrast pulse curves may be isolated and plotted in figure 6.15b. An exponential trend line is fitted (assuming a contrast concentration of 1 at t = 0) with a decay constant of 0.610 s^{-1} and representing the average decay rate of the eight contrast pulses. The high R^2 value and corresponding low degree of scatter of the data around the trend line suggest that the decay rate, unlike the absolute contrast value, is relatively constant over all eight pulses, and hence, across the cardiac cycle.

A contrast residence curve corresponding to the injection bolus described in figure 6.11 (unity over the entire cardiac cycle for one cycle) may be constructed from a linear sum of the contrast pulse decay curves as detailed in section 6.4.2. The corresponding contrast bolus residence curve is shown in figure 6.16a. The simulated contrast infiltration time (time to peak concentration) of around 0.8-1.0 seconds is similar to that seen experimentally.

The decay portion of the simulated contrast bolus curve is plotted in figure 6.16b and fitted with an exponential decay trend line having a decay constant of 0.561s^{-1}. The similarity between the simulated contrast decay constant (0.561 s^{-1}) and the mean constant of the individual

contrast pulse's decay (0.610 s^{-1}) reinforces the assertion that the rate of contrast decay remains approximately constant across the cardiac cycle and that decay at any given time is well described by an exponential decay curve.

6.5 Comparing *in-vivo* and *in-silico* Results

Curves of both the experimental and the simulated contrast bolus concentration are plotted in figure 6.17a, and the corresponding decay portions with exponential trend lines fitted to the data are shown in figure 6.17b.

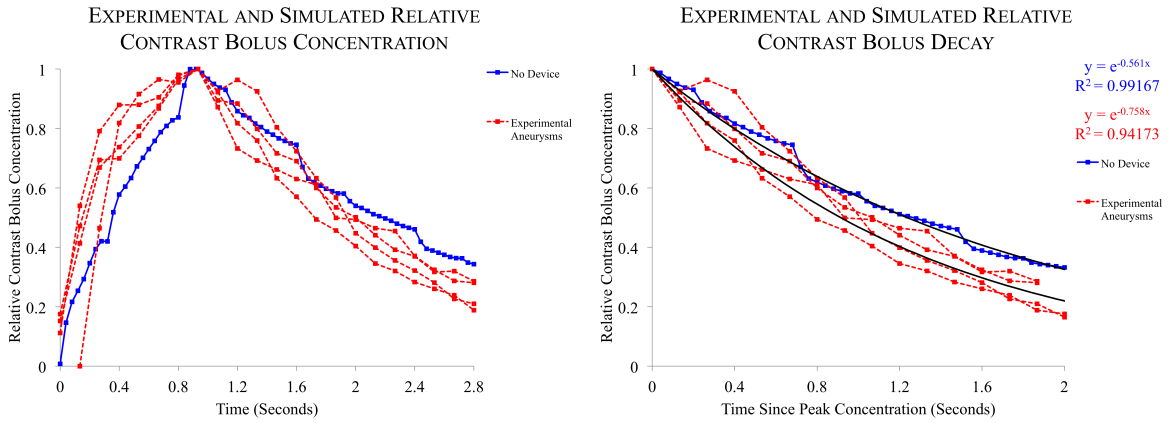

(a) *Contrast concentration* **(b)** *Contrast decay*

Figure 6.17: *Comparing experimental and simulated (cycle-averaged) contrast bolus residence and decay curves. Both sets of curves are centred on peak concentration.*

In both the overall contrast residence curve and the decay portion specifically, the correlation between the *in-vivo* data and the simulated profiles is good. The simulated decay curve falls within the scatter of the experimental data for the first 0.80 seconds (one cardiac cycle) of the decay, but by 2.00 seconds, a difference in contrast concentration of around 0.10 can be seen. The simulation underestimates the rate of contrast decay; after a contrast decay time of 2.0 seconds the experimental and simulated models show a relative concentration of 22.0% and 32.6% respectively. The simulated prediction of the experimental contrast decay constant is underestimated by 26% with an experimental and simulated decay constant of 0.758s^{-1} and 0.561s^{-1} respectively.

The magnitude of pulsatility in both the simulated and experimental data appear similar; given

that such pulsatility has been attributed to variation in parent vessel flow rate, the similarity suggests that the *in-vivo* flow profile in the porcine CCA and the assumed human ICA flow profile in the simulations are of a similar shape. In figure 6.17a, an initially high rate of contrast infiltration giving way to a smoother contrast peak in the experimental case suggests an experimental contrast bolus profile in time with a less well-defined end-point and a smoother decay, similar to that reported in the literature. [43]

Virtual angiograms are generated from the *in-silico* model, as shown in figure 6.18, where the total virtual contrast concentration is projected into a 2D plane approximately identical to that seen experimentally. The visual correspondence between the *in-vivo* and simulated contrast flow patterns is also good: in both cases the contrast enters the aneurysm at the same neck location, the degree of initial jet infiltration is similar, and the contrast decay rate is greatest in the lower-distal portion of the aneurysm.

Although the correlation between the simulated and experimental contrast behaviour is good, errors remain. Such errors should be linked to the assumptions of the model, namely parent vessel flow rate, contrast viscosity, and contrast density. The influence of these assumptions is discussed and quantified in the following sections.

6.6 Accounting for Contrast Viscosity and Density

In order to quantify the influence of contrast media properties (density and viscosity) on contrast washout, the *in-silico* simulations of the previous section are repeated with a range of densities and viscosities that are seen in clinically used angiographic contrasts. Given that a significant effect of contrast density and viscosity is to locally change the Reynolds number of the blood flow (Reynolds number being proportional to the density:viscosity ratio), the greatest influence on the flow will be seen from contrast media with the highest and lowest density:viscosity ratios.

6.6.1 Simulations Incorporating Contrast Viscosity and Density

The extremes of properties seen in clinically used contrast agents are summarised below in table 6.1. It should be noted that it would be clinically unusual to use either of these contrasts

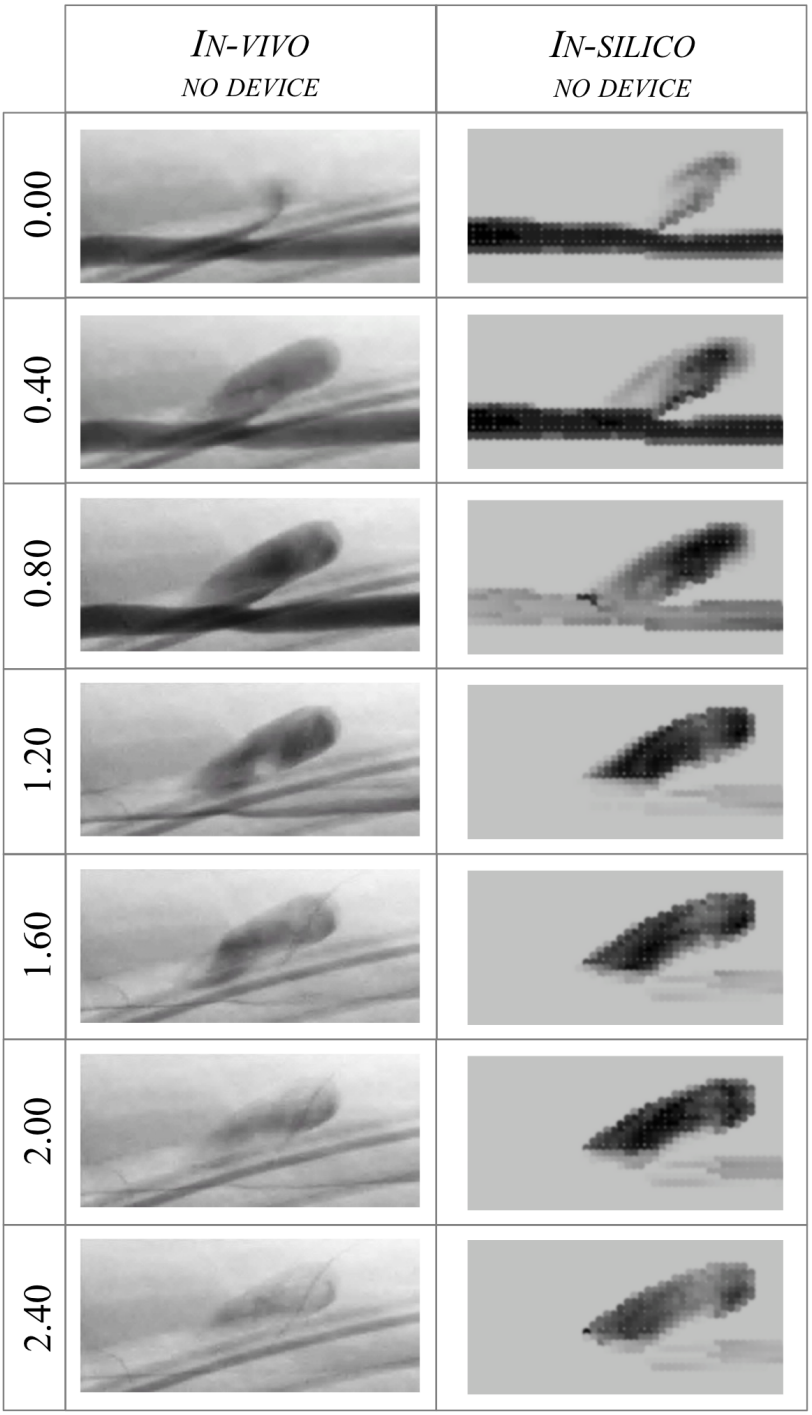

Figure 6.18: *Virtual and in-vivo angiography (images taken at 0.40 second intervals from peak contrast concentration) with no device deployed. Images are aligned to the peak aneurysm contrast concentration at 0.80 seconds*

for cerebral aneurysm imaging. Despite this, the most extreme range of properties are selected in order to quantify the maximum influence changes viscosity and density may have of the simulated contrast residence curve.

Table 6.1: *Contrast Properties*

CONTRAST	DENSITY	VISCOSITY
Omnipaque™ 180	1164 kg m^{-3}	0.0015 Pa s
Omnipaque™ 350	1410 kg m^{-3}	0.0204 Pa s

To avoid the complications of two-fluid simulations and to retain the simplified scalar approach, the simulations are run assuming that a perfect mixture of blood and contrast, in equal proportions, is flowing through the geometry at all times. Additionally, the same set of eight contrast pulses are propagated through the fluid as discussed in section 6.4.2. As such, the only change to the simulations compared to that of section 6.4.3 is a slight increase or decrease in fluid density and viscosity. Although this rationale of a perfect and perpetual mixture of contrast and blood is not realistic and will not capture any flow effects due to local viscosity and density gradients, the method does allow for the bracketing of the global influence of viscosity and density on the contrast decay rate.

Contrast, which typically has a higher density than blood, has been observed 'settling' under the effects of gravity in aneurysm domes. [155] This effect is often cited as a source of error in computational models of contrast transport. However, incorporating this effect into a virtual contrast model is highly problematic, requiring both a two-fluid model and knowledge of the direction gravitational forces, which vary considerably depending on whether a patient is lying down or standing upright. Additionally, all reports in the literature suggest that contrast settling would encourage contrast residence and lead to computational models *overestimating* the corresponding aneurysm contrast decay rate. This is the opposite of the error seen in the simulated contrast model of the previous section, which *underestimated* contrast decay rate. Consequently, error from localised contrast settling is considered insignificant in this study.

Table 6.2: *Summary of contrast mixture properties*

	DENSITY	VISCOSITY	MODIFIED RE
High Re (50:50 mix Blood & Omnipaque™ 180)	1080 kg m^{-3}	0.00275 Pa s	+70%
Low Re (50:50 mix Blood & Omnipaque™ 350)	1200 kg m^{-3}	0.0122 Pa s	-40%

The global density and viscosity of the two simulations modelling the presence of perfectly mixed blood and Omnipaque^{TM} 180 or Omnipaque^{TM} 350 contrast media are summarised in table 6.2. The corresponding effective change in simulation Reynolds number is an increase of 57% and

a decrease of 61% for the 'HighRe' and 'LowRe' simulations respectively. For perspective, the contrast agent used in the *in-vivo* experiment (Omnipaque^{TM} 240, ρ =1280 kg m^{-3}, μ= 0.0034 Pa s) would have the effect of increasing the simulation Reynolds number by 23% in a perfect 50:50 mixture.

6.6.2 Simulation Results

The simulations are repeated as detailed in section 6.4.3. No substantial changes in simulation time or the number of iterations to reach convergence are observed as a result of the Reynolds number changes.

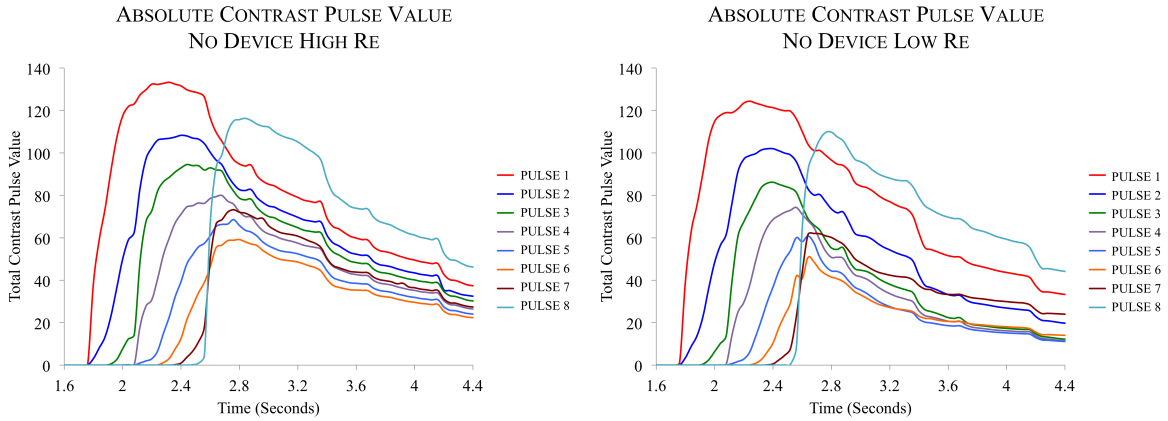

(a) *High Reynolds number simulation* **(b)** *Low Reynolds number simulation*

Figure 6.19: *Total contrast pulse value in the aneurysm domes for the 'High Re' and 'Low Re' simulations*

The variation in contrast pulse value for both 'High Re' and 'Low Re' simulations is depicted in figure 6.19. A pattern emerges in both simulations that is broadly similar to the result seen in the previous section: around twice the volume of a contrast pulse injected up to 0.3 seconds before peak systole infiltrates the aneurysms compared to a pulse injected around diastole. The volume of each pulse infiltrating the aneurysm (in arbitrary units) does not vary considerably between the two simulations, nor does it differ from the volumes observed in the initial simulation of section 6.4.

The relative contrast pulse residence curves for the 'High Re' and 'Low Re' simulations are plotted in figure 6.20. The rate of pulse infiltration appears broadly similar between the two

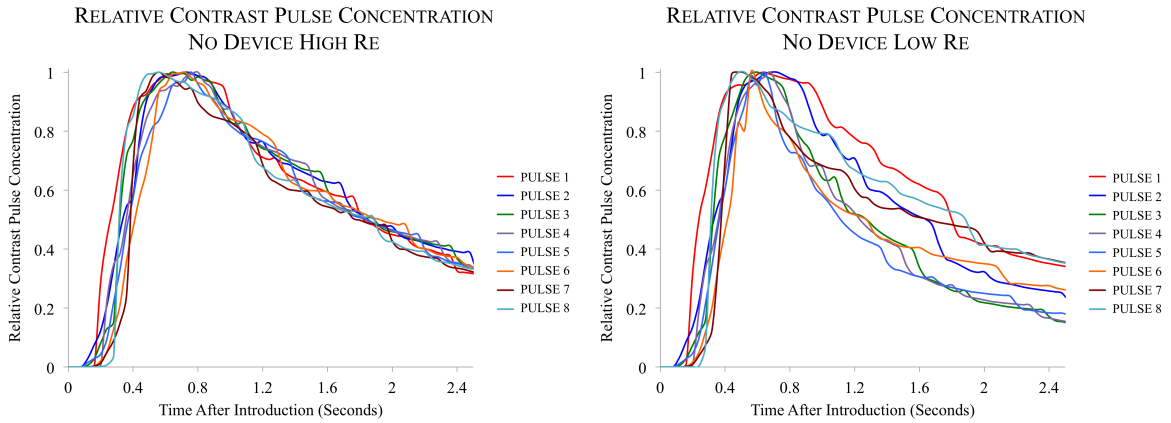

(a) *High Reynolds number simulation* **(b)** *Low Reynolds number simulation*

Figure 6.20: *Relative contrast pulse distributions for the 'High Re' and 'Low Re' simulations*

simulations and across the cardiac cycle: each contrast pulse reaches peak concentration in around 0.8 seconds. The overall shape of the plots is identical to the original 'No Device' simulation (figure 6.15) but with the 'Low Re' simulation showing faster decay of the contrast pulses and greater variation in the decay rate.

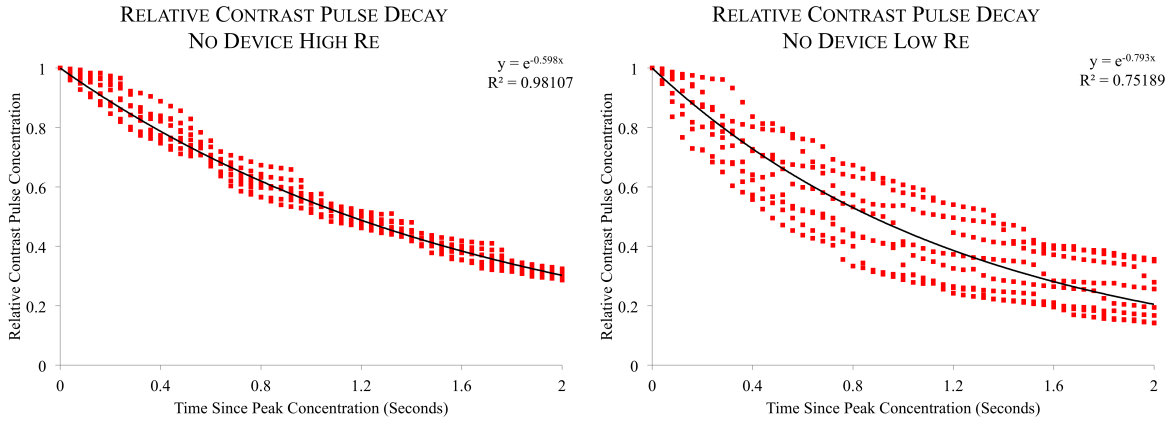

(a) *High Reynolds number simulation* **(b)** *Low Reynolds number simulation*

Figure 6.21: *Relative contrast pulse decay for the 'High Re' and 'Low Re' simulations*

The decay portions of both plots from figure 6.20 are shown in figure 6.21 with exponential trend lines fitted representing mean pulse decay rate and yielding decay constants of 0.598 s^{-1} and 0.793 s^{-1} for the 'High Re' and 'Low Re' simulations respectively. The 'Low Re' simulation shows greater variation in the contrast pulse decay rate (hence the lower R^2 value of 0.752) with between approximately 15% and 40% of each contrast pulse remaining in the aneurysm

dome after 2.0 seconds, depending on the cardiac position at the injection of the pulse. Such increased scatter suggests that in the 'Low Re' simulation, where flow can be considered more 'shear driven', the rate of contrast pulse decay varies considerably depending on the parent vessel velocity both instantaneously and at the time when a given contrast pulse entered into the aneurysm.

Finally, cycle-averaged contrast residence curves are created by the linear sum of the contrast pulse components, as previously described, and plotted for the 'High Re' and 'Low Re' simulations in figure 6.22 and figure 6.23 respectively. Similar behaviour is seen in the contrast plots as in the individual pulse residence curves: a contrast infiltration time of around 0.8 seconds and a greater rate of contrast decay in the 'Low Re' case.

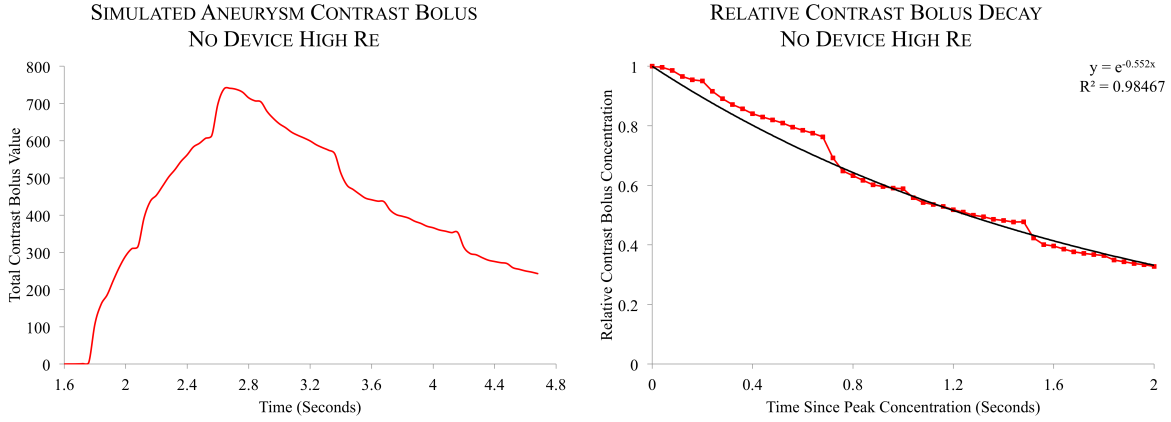

(a) *Contrast residence curve* **(b)** *Contrast decay*

Figure 6.22: *Cycle-averaged contrast bolus residence and decay for the High Reynolds number simulation*

The decay portions of the contrast curves are also plotted in figure 6.22 and figure 6.23 with exponential decay trend lines fitted and yielding decay constants of 0.552 s^{-1} and 0.677 s^{-1} for the 'High Re' and 'Low Re' cases respectively. The contrast decay rates are summarised in table 6.3 in addition to the corresponding contrast decay rate predicted in the 'No Device' simulation.

The contrast decay rate of the 'Low Re' simulation is markedly lower than the corresponding average contrast pulse decay rate seen in figure 6.21b (0.677 s^{-1} vs 0.793 s^{-1}). This suggests that the 'Low Re' contrast residence behaviour is dominated by the pulses with lower decay rates (Pulses 1, 2 and 8), which correspond to the fraction of contrast entering the aneurysm

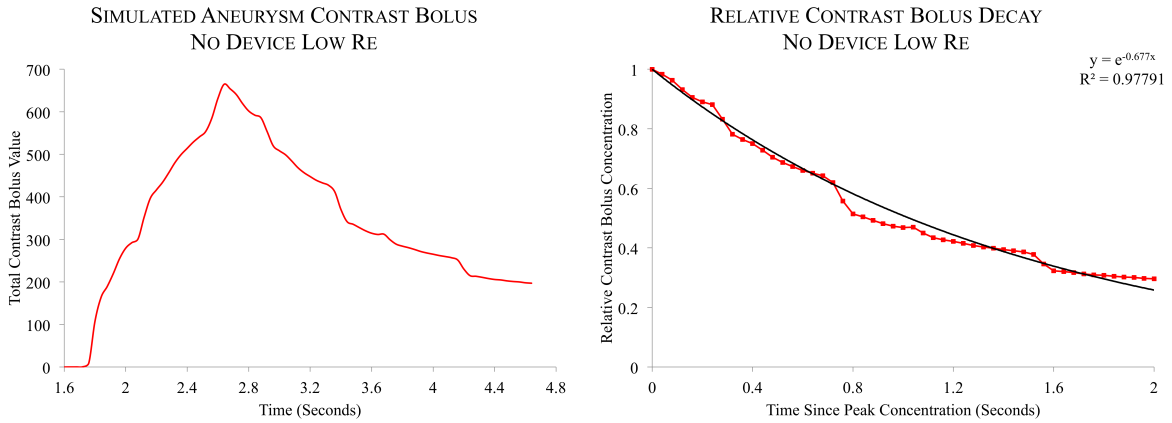

(a) *Contrast residence curve* **(b)** *Contrast decay*

Figure 6.23: *Cycle-averaged contrast bolus residence and decay for the Low Reynolds number simulation*

Table 6.3: *Exponential contrast decay constants for the 'High Re', 'Low Re', and initial 'No Device' simulations*

Simulation	Exponential Contrast Decay Constant
Initial	0.560 s^{-1}
High Re	0.522 s^{-1}
Low Re	0.677 s^{-1}

dome in the 0.3 seconds prior to peak systole. The dominance of contrast inflow in this portion of the cardiac cycle is reasonable given the relatively large volume of Pulses 1, 2 and 8 in the aneurysm dome, as shown in figure 6.19b. The degree of pulsatility in the residence traces of both simulations is similar, which supports the same assertion: despite the large range of instantaneous contrast washout seen in the 'Low Re' case, the overall contrast washout behaviour is dominated by contrast entering and exiting the aneurysm dome in the 0.3 seconds prior to peak systole.

The variation in aneurysm inflow rate for all three simulations is also plotted in figure 6.24 and summarised in table 6.4. It is interesting to note that despite the large difference in Reynolds number between the three simulations, the average aneurysm inflow rate is relatively unchanged at around 24-25 ml/min. The results of figure 6.24 also suggest that the variation seen in contrast decay rate (table 6.3) cannot be accounted for by variation in average aneurysm inflow alone. However, the larger range in instantaneous aneurysm inflow rate seen for the 'Low Re' simulation may explain why greater variation is seen in individual contrast pulse decay rates across the cardiac cycle in the 'Low Re' case (figure 6.21b.)

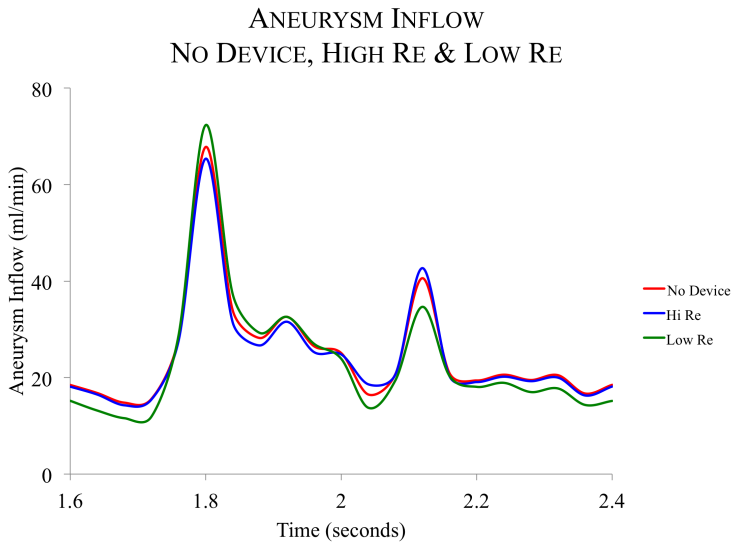

Figure 6.24: *Aneurysm inflow across the cardiac cycle for the initial, 'High Re', and 'Low Re' simulations*

Table 6.4: *Inflow summary for the 'High Re', 'Low Re', and initial 'No Device' simulations*

SIMULATION	MEAN INFLOW	INFLOW RANGE
Initial	25.2 ml/min	53.0 ml/min
High Re	24.7 ml/min	51.1 ml/min
Low Re	23.9 ml/min	60.8 ml/min

The mean and maximum velocity magnitude entering the aneurysm dome over the cardiac cycle are plotted in figure 6.25. From figure 6.25a it appears that the mean aneurysm inflow velocity varies very little over all three simulations; the plots are almost identical in the 'No Device' and 'High Re' cases, and in the 'Low Re' simulation, a slightly increased mean velocity is evident between diastole and systole. A clear pattern is seen in the plot of peak aneurysm inflow velocity magnitude shown in figure 6.25b; maximum velocity is consistently highest across the cardiac cycle in the 'High Re' case, followed by the 'No Device' case, and finally the 'Low Re' simulation, the latter showing a markedly reduced peak velocity across the entire cardiac cycle.

From the two plots of figure 6.25, it is clear that while the average aneurysm inflow rate does not differ significantly among all three simulations, the ratio of max:mean aneurysm inlet velocity is lower for the 'Low Re' case (4.77) compared to the same ratio for the 'High Re' and 'No Device' cases (7.76 and 7.23 respectively.)

This ratio of peak to mean inflow velocity can be considered as a measure of inflow jetting: a

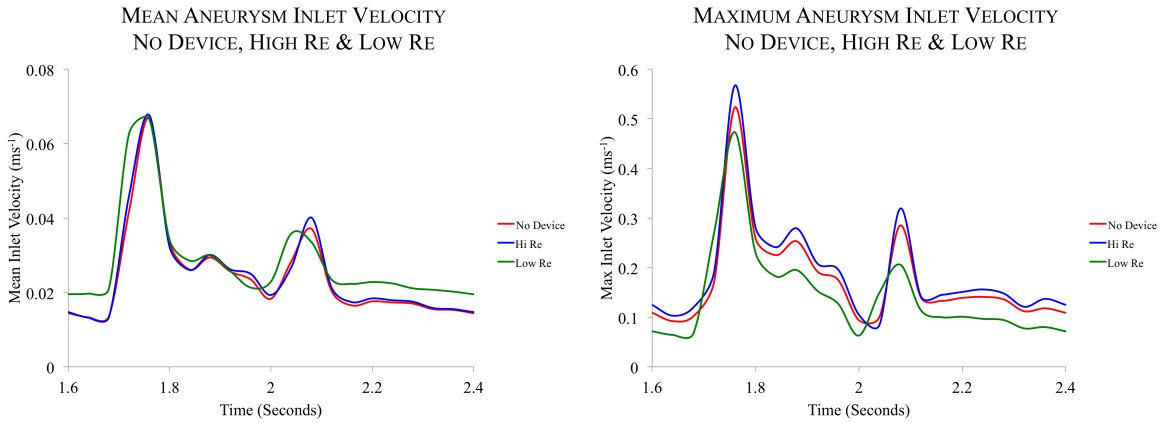

(a) *Mean velocity* **(b)** *Maximum velocity*

Figure 6.25: *Velocity magnitude at the aneurysm neck for the initial 'No Device', 'High Re', and 'Low Re' simulations*

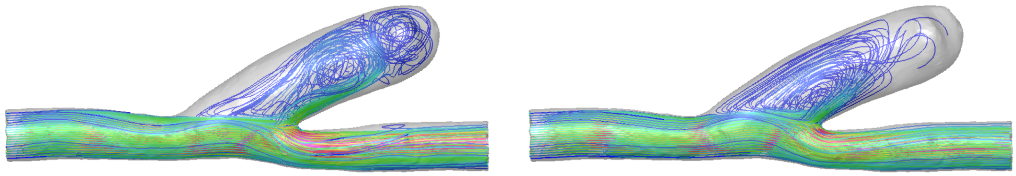

High Reynolds Number
(Average U_{max}:U_{mean}=7.76)

Low Reynolds Number
(Average U_{max}:U_{mean}=4.77)

Figure 6.26: *Different degrees of flow infiltration and vortex position in the 'High Re', and 'Low Re' simulations at mean parent vessel flow rate*

high ratio indicates a localised peak of inflow, whereas a low ratio implies a relatively diffuse plug of inflow. The lower ratio in the 'Low Re' case corresponds to less infiltration of the flow into the aneurysm sac, as shown in figure 6.26. Consequently, the contrast that enters the aneurysm in the 'Low Re' case is more confined to the lower half of the aneurysm, where it is quickly swept back out into the parent vessel, resulting in a faster rate of contrast decay. Conversely, in the 'High Re' case, flow carries contrast deeper into the aneurysm dome increasing the transport time of the contrast leaving the aneurysm, which results in a reduced rate of contrast decay.

Finally, the contrast decay curve predicted from each simulation is plotted relative to the experimental contrast decay in figure 6.27.

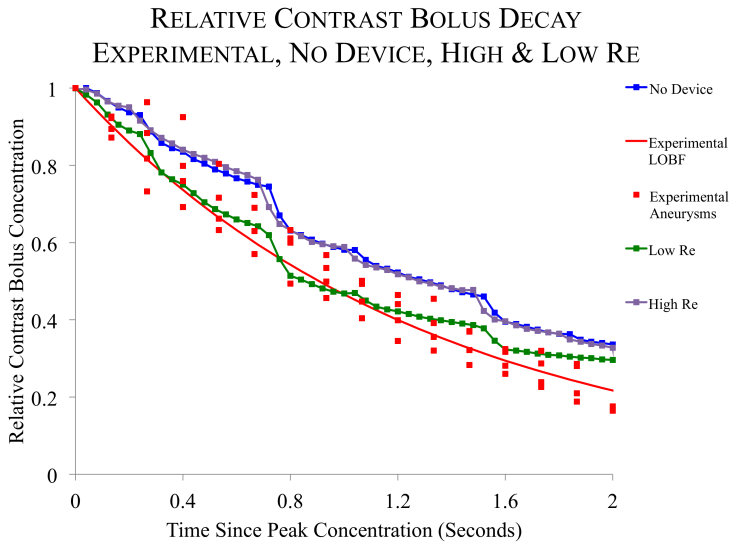

Figure 6.27: *Experimental and simulated contrast bolus concentration decay including 'High Re' and 'Low Re' simulations*

6.6.3 Summary: The Influence of Contrast Viscosity and Density

The relative difference between all three simulated contrast decay curves in figure 6.27 is small and falls within the scatter of the experimental data. The spread of the 'High Re' and 'Low Re' curves about the original simulation is highly asymmetric, with little variation seen between the original simulation and the 'High Re' case, despite a 57% increase in Reynolds number. Conversely, the difference between the 'Low Re' case and the original simulation is relatively large after similar sized (61%) decrease in Reynolds number. Given that the properties of the contrast used experimentally in section 6.3 would result in a 23% increase in Reynolds number if simulated, it is likely that the results of such a simulation would be almost identical to the decay curve of the original simulation.

From the decay rates of these three simulations, it appears that when substantial changes are present in the working fluid density and viscosity, and hence, in local Reynolds number, aneurysm inflow rate alone is not a good predictor of the volume or rate of contrast entering and exiting the aneurysm dome. In fact, at constant inflow rate, variation in contrast infiltration and decay is seen as a result of different aneurysm flow patterns and the degree of inflow jetting. Additionally, figure 6.26 suggests that significant differences between *in-silico* and *in-vivo* contrast properties could be identified by differences in aneurysm flow pattern alone.

Considering that the variation in contrast decay rate seen is representative of the most extreme variation in contrast properties commercially available, and that incorporating the experimental contrast properties into a simulation would not dramatically alter the original simulation decay rate, it must be concluded that the error associated with changes in fluid density and viscosity is negligible. As such, the error seen between the experimental and 'No Device' simulated contrast washout cannot be accounted for by density and viscosity changes.

6.7 Accounting for Parent Vessel Flow Rate

The simulations of the previous section are conducted assuming an inlet flow rate typical of the human ICA mean flow rate as calculated from a 1D arterial tree model. Other studies discussed in section 6.1.2 have shown the influence of parent vessel flow velocity on contrast washout rate, suggesting parent vessel flow rate may be a major source of inaccuracy in any virtual contrast model, especially if the flow rate used is not patient-specific. However, accurately obtaining such patient-specific flow rates is complicated, and often impossible.

One method to incorporate patient-specific flow rates into simulation boundary conditions is to infer arterial flow rate from angiographic contrast transport. [43] Although this method allows for accurate prediction of the flow conditions typical during the angiography, such conditions may be substantially underestimating the true vessel flow rate when the vessel lumen is not obstructed by the angiographic catheter. In one study, Ford et al. [47] saw substantial 'angiography-induced' changes in simulated local flow patterns that resulted from the velocity of the injected contrast bolus. As such, mean flow rates may actually be inherently more representative of 'typical' flow conditions (compared to flow rates calculated from angiography), as they are derived from computational models of the vasculature assuming an unobstructed lumen and are verified *in-vivo* with trans-cranial doppler probes that do not interrupt the vessel flow.

Given the importance of parent vessel flow rate alongside the lack of non-invasive methods for measuring patient-specific flows, it is prudent to attempt to quantify any errors in a virtual contrast model due to flow rate changes. In fact the clinical relevance of such a model would be substantially improved, as it would allow the relative impact of the dominant clinical measurement technique (angiography) on the aneurysm flow to be quantified. To this end, the effect of

parent vessel flow rate on virtual contrast washout is investigated.

6.7.1 The Effect of Placing a Catheter in a Vessel Lumen

Initially, any effect that the angiographic catheter used in the experimental studies may have had on the resultant aneurysm flow is quantified. The effect of the increased resistance of a catheter that is blocking a vessel lumen is two-fold: to reduce the flow rate in the vessel lumen due to the obstruction and to alter the cross-sectional velocity profile from the approximate parabola of the unobstructed lumen.

Each of these effects is briefly investigated and quantified with simple simulations. Initially, a model of a straight vessel lumen 30mm long and 4mm diameter is used to calculate *in-silico* the pressure gradient required to drive steady, parabolic flow at the mean and maximum human ICA flow rates (230 and 575ml/min respectively) in an unobstructed lumen.

The calculated pressure gradient (127Pa and 315Pa for the mean and maximum flow rates respectively) is then used as a boundary condition for repeated simulations with an angiographic catheter (size: 4Fr with a diameter of 1.33mm) that is aligned with the vessel centreline. For simplicity, the catheter is assumed to be coincident with the lumen centreline, although in reality, due to vessel curvature, the catheter will likely be angled, thereby blocking more of the lumen area and increasing the flow resistance. A cross-sectional view of the model is shown schematically in figure 6.28 (top).

Secondly, the effect of the catheter on the cross-sectional velocity profile further downstream is evaluated with the model shown in figure 6.28 (bottom). The cross-sectional velocity profiles calculated in the previous simulations are used as inlet velocity conditions, and the degree of mixing is observed five vessel-diameters downstream of the catheter tip (at the outlet of the geometry shown in figure 6.28 (bottom)). In all cases, angiographic contrast with a density and viscosity equal to blood is assumed to be flowing in the catheter at a constant rate of 2ml/s.

The geometries of figure 6.28 are meshed in CFD-VisCART as detailed in section 6.4.3. The vessel geometry with and without the catheter present have mesh sizes of 1,090,000 and 2,080,000 elements respectively. The geometry partially blocked by the 5mm length of catheter has a

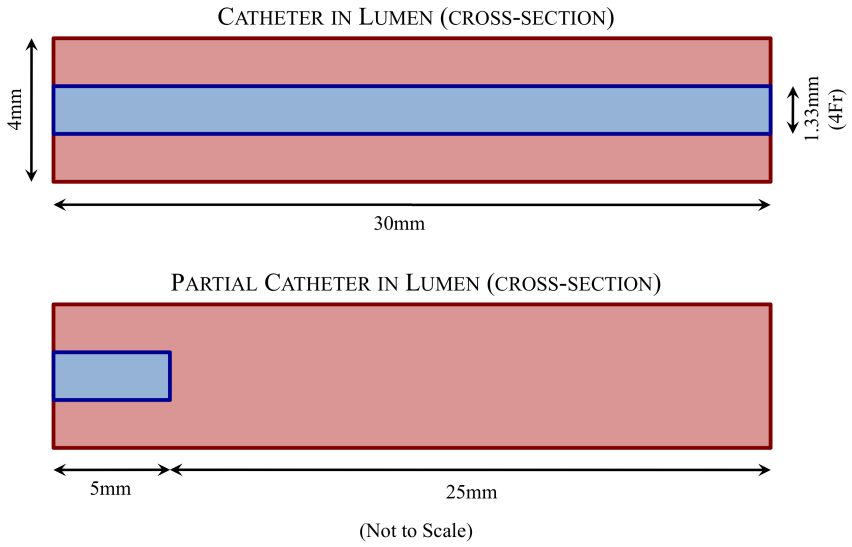

Figure 6.28: *Vessel (red) and catheter (blue) model cross-sections*

mesh size of 2,190,000 elements. Steady state simulations are run in CFD-ACE+ at mean and maximum ICA flow conditions with solver settings previously discussed in section 6.4.3. All results are post-processed in CFD-VIEW.

Results of the first set of simulations, calculating the reduced pressure-driven flow rate as a result of a catheter blocking the lumen, are shown in figure 6.29 and summarised in table 6.5. The corresponding velocity profiles in the obscured lumen are as expected (annular and parabolic). The net-effect of the catheter, at both mean and maximum ICA flow rates, is to reduce the blood flow rate and mean flow velocity to around 30% of that of the un-obscured lumen. Such a result suggests that the presence of the angiographic catheter in the vessel lumen has a substantial effect on the flow rate in the parent vessel. Even when the flow rate of the contrast in the catheter is considered in addition to the blood flowing in the lumen, the relative flow rates at maximum and mean ICA flow conditions are still only 50% and 80% of their unobstructed values respectively.

Table 6.5: *Flow reductions due to catheter occlusions*

	MEAN ICA PRESSURE (127PA)	PEAK ICA PRESSURE (315PA)
Unobstructed Flowrate	230 ml/min	575 ml/min
Obstructed Flowrate	67 ml/min (71% reduction)	165 ml/min (71% reduction)
Including Catheter Flowrate*	187 ml/min (19% reduction)	285 ml/min (50% reduction)

* Assuming a steady flow rate of 120 ml/min

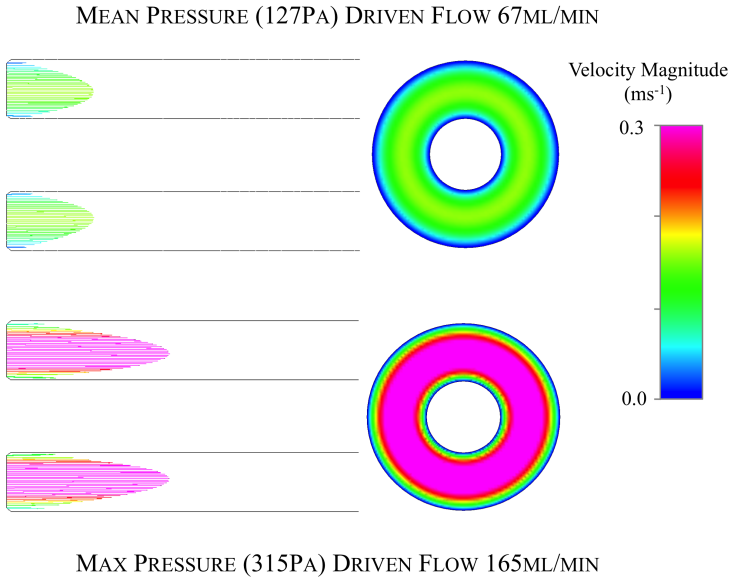

Figure 6.29: *Velocity profiles of pressure-driven flow in the blocked vessel lumen at mean and maximum ICA flow rates*

The results of the second set of simulations are shown in figure 6.30 and figure 6.31. From the figures, it appears that despite the large discrepancy between catheter and vessel flow velocities at the geometry inlet, at a distance of five vessel-diameters downstream from the catheter tip, sufficient mixing has occurred for the vessel flow velocity profile shape to be approximately parabolic. This effect is seen at both mean and maximum ICA flow rate conditions and suggests that the injection of contrast at a rate of 2ml/sec into typical flow conditions in the ICA does not dramatically effect the shape of the vessel velocity profile downstream. In reality, the curved nature of the cerebral vessels will increase the degree of mixing across the vessel lumen and negate this effect even faster.

From the results of this simple analysis, it can be concluded that the presence of a catheter in a vessel substantially alters the flow rate of blood in that vessel under the same pressure gradient as prior to the obstruction. Although in reality auto-regulation mechanisms such as increased arterial pressure gradient and the enlarging of the vessel lumen may counter this flow-reducing effect of the catheter, there is also a risk that vessel spasm will actually constrict the vessel and further reduce the blood flow rate. These simulations suggest that the parent vessel flow rate seen experimentally in section 6.3 may differ substantially from the mean ICA flow rate assumed for the subsequent *in-silico* simulations of the previous sections.

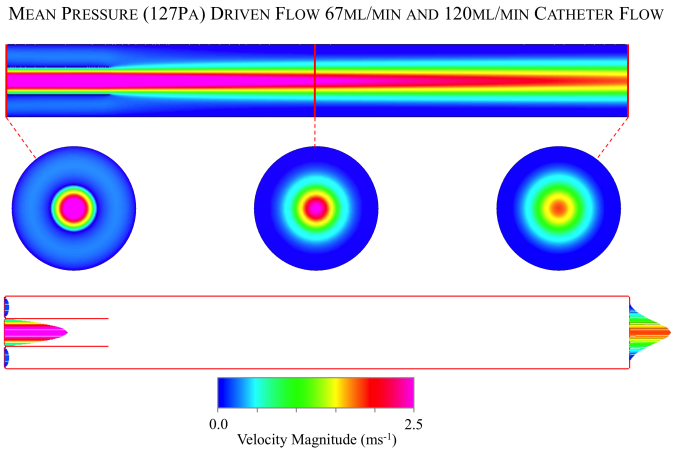

Figure 6.30: *Catheter and vessel flows mixing at mean ICA flow conditions*

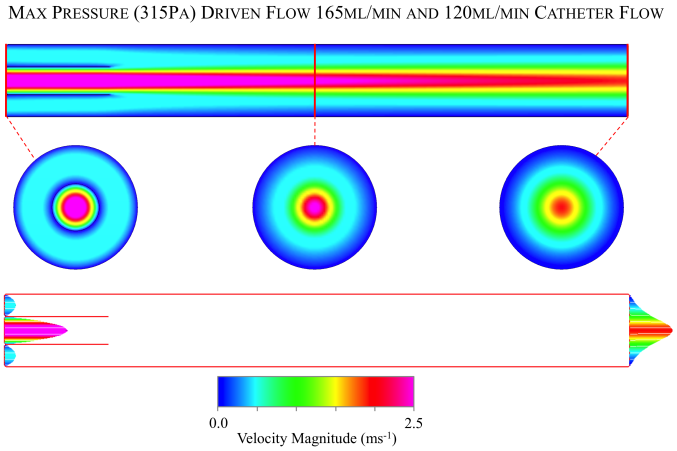

Figure 6.31: *Catheter and vessel flows mixing at maximum ICA flow conditions*

More broadly, flow conditions in a vessel observed and measured angiographically are unlikely to be representative of normal flow conditions in the vessel. This challenges the validity of angiographically derived patient-specific flow rates. However, it is apparent that the presence of the catheter in the vessel does not dramatically alter the velocity profile across the lumen at a reasonable distance downstream of the catheter tip (approximately five vessel-diameters).

6.7.2 Simulations Incorporating Variation in Parent Vessel Flow Rates

Given the results of the previous section (6.7.1), the *in-silico* virtual contrast simulations of the experimental porcine aneurysm are repeated with reduced parent vessel flow rate to quantify the effect that the angiographic catheter may have had on the contrast residence observed. The effect of previously assuming a parent vessel flow rate typical of the human ICA is also investigated by

running a further simulation with an increased parent vessel flow rate. As such, the simulation inlet velocities are chosen to bracket the extremes of flow rate that may be experienced in the experimental vessel. In one simulation, the parent flow rate is increased by 50% to a mean of 345ml/min, conditions similar to the human CCA. In a second simulation, the parent vessel flow rate is decreased by 50% to 115ml/min, which is more representative of a human ICA obstructed by a catheter. The resulting mean inlet Reynolds numbers for the simulations are 408 (maximum 1020) and 136 (maximum 340) for the higher and lower flow rates respectively, which confirms that flow remains confined to the laminar regime. All other simulation parameters remain the same as in section 6.4 with no changes in blood viscosity or density.

6.7.3 Simulation Results

Simulations are again run on 32 cores with a typical solution time of around 40 minutes per time step and reaching the convergence criterion of five orders of magnitude residual reduction is less than 100 iterations per time step.

As before, the eight independent contrast pulses are extracted at every fourth time step and projected into the same plane as the experimental angiography. The absolute value of each pulse in time is plotted in figure 6.32 for both the increased parent vessel flow rate simulation, 'High Q', and the reduced parent vessel simulation, 'Low Q'.

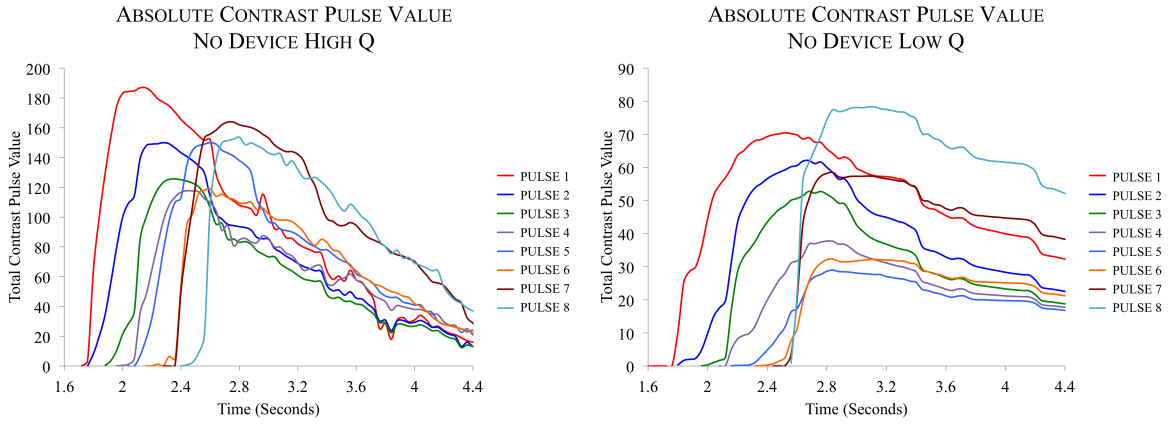

(a) *High flow rate simulation* **(b)** *Low flow rate simulation*

Figure 6.32: *Total absolute contrast pulse values for the 'High Q' and 'Low Q' simulations*

In the 'High Q' case, the relative volumes of each contrast pulse that are washed into the

aneurysm dome are similar to the previous simulations ('No Device', 'High Re' and 'Low Re') with the highest infiltration seen for Pulse 1. However, in the 'Low Q' simulation, the greatest infiltration is seen from Pulse 8, which is introduced 0.1 seconds earlier in the cardiac cycle than Pulse 1. This phenomena is indicative of the substantially reduced parent vessel flow rate for the 'Low Q' simulation. In all other simulations, the bulk flow rate has transported Pulse 1 from the geometry inlet to the aneurysm neck in a time roughly coincident with the increased aneurysm inflow corresponding to peak systole. In the 'Low Q' case, the bulk flow rate is sufficiently low that the transit time from the geometry inlet to the aneurysm neck is increased, and hence, Pulse 8, the contrast pulse injected 0.1 seconds prior to Pulse 1, is transported to the aneurysm neck coincident with the large inflow associated with peak systole.

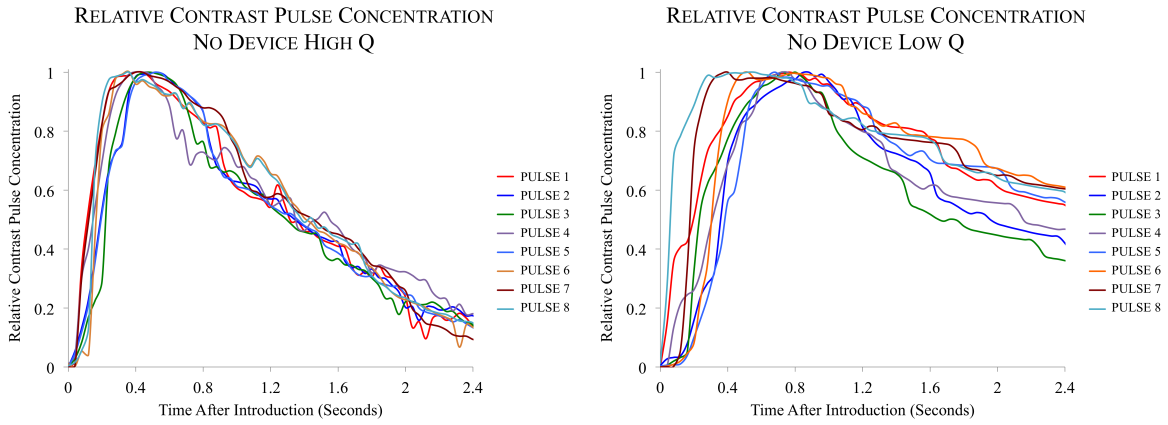

(a) *High flow rate simulation* **(b)** *Low flow rate simulation*

Figure 6.33: *Relative contrast pulse distributions for the 'High Q' and 'Low Q' simulations*

The relative contrast pulse concentration curves are plotted in figure 6.33 for both simulations. From the figure, it is immediately clear that the decay rate of all pulses in the 'High Q' simulation is much higher than in the 'Low Q' case. Additionally, the decay portions of the curves of the 'High Q' simulation appear more erratic, with sudden changes in contrast pulse value seen. The 'Low Q' plot (figure 6.33b) also shows considerable variation in contrast pulse infiltration time, with the time to reach peak concentration across the pulses varying between 0.3 and 1.0 seconds, which suggests that large ranges in instantaneous inflow rate are present in the 'Low Q' simulation. For comparison, peak contrast pulse concentration is reached in 0.30-0.60 seconds for the 'High Q' simulation.

The decay portions of the contrast pulse residence curves for both simulations are plotted in

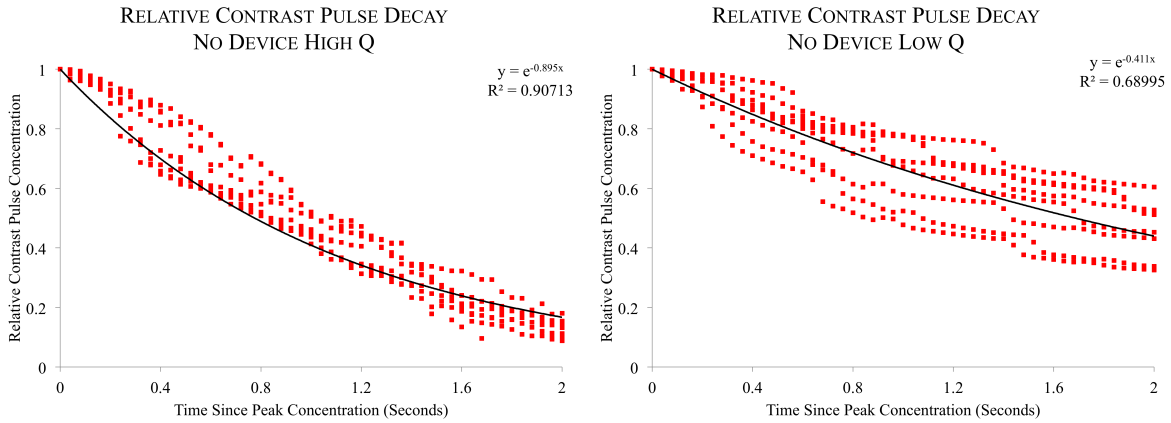

(a) *High flow rate simulation* **(b)** *Low flow rate simulation*

Figure 6.34: *Relative contrast pulse decay for the 'High Q' and 'Low Q' simulations*

figure 6.34. Exponential trend lines representing mean pulse decay rate are fitted to the simulation data with decay constants of 0.895 and 0.411 s^{-1} for the high and low flow rate simulations respectively. Substantial scatter is seen in the 'Low Q' simulation results, which reduces the significance of the trend line fitted to the data, and suggests that pulses entering the aneurysm dome at different points in the cardiac cycle experience very different decay times.

Finally, cycle-averaged contrast bolus residence and decay curves are created with linear combinations of the contrast pulse distributions and are plotted in figure 6.35 and figure 6.36. The corresponding decay constants of the exponential decay trend lines fitted to the contrast bolus concentration curves are summarised in table 6.6.

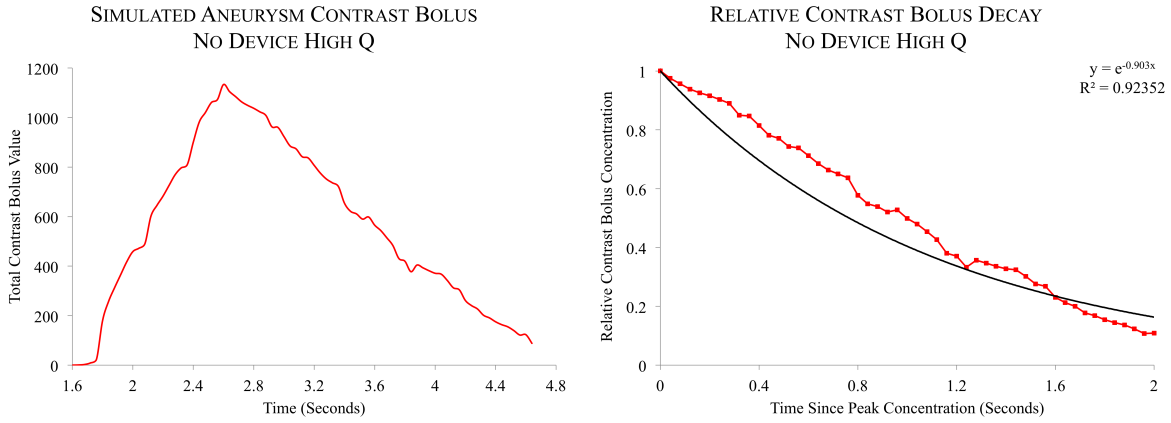

(a) *Contrast residence curve* **(b)** *Contrast decay*

Figure 6.35: *Cycle-averaged contrast bolus residence and decay for the high flow rate simulation*

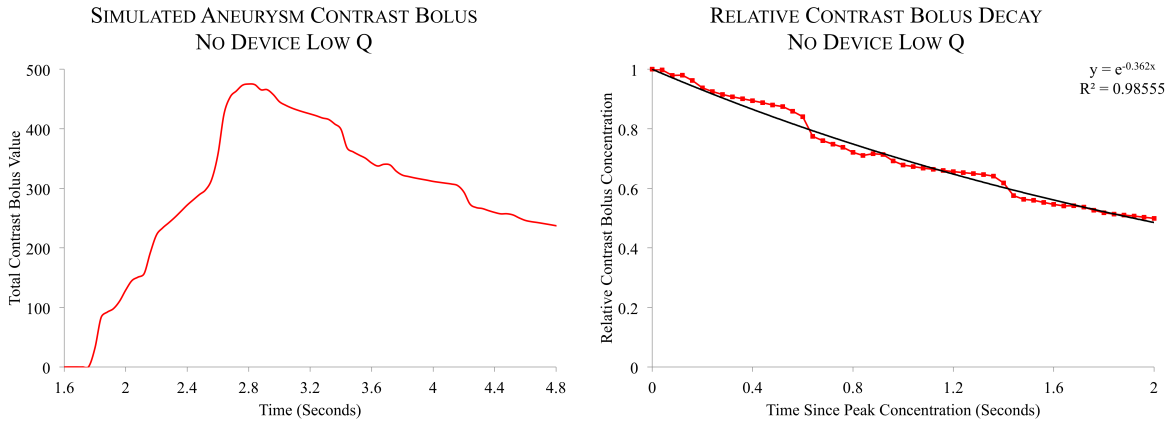

(a) *Contrast residence curve* **(b)** *Contrast decay*

Figure 6.36: *Cycle-averaged contrast bolus residence and decay for the low flow rate simulation*

Table 6.6: *Exponential decay time constants for the 'High Q', 'Low Q', and original simulations*

Simulation	Exponential Contrast Decay Constant
Initial	0.560 s^{-1}
High Q	0.903 s^{-1}
Low Q	0.362 s^{-1}

The contrast residence curve shapes seen in figure 6.35 and figure 6.36 are similar to the curves generated in previous simulations, with the exception of the decay portion of the 'High Q' case, which appears more linear than exponential. The contrast infiltration rate of the 'High Q' simulation is slightly higher than in previous simulations, taking approximately 0.7 seconds to reach peak contrast concentration. In the 'Low Q' case, peak concentration is reached in around 1.0 second. This variation is attributed to the dramatically different rates of parent vessel flow between the simulations, which leads to proportionally increased or decreased aneurysm inflow rates and hence, contrast inflow rates. As such, the decay rates of the two simulations also differ substantially due to the large difference in average aneurysm inflow.

Figure 6.37 and table 6.7 show the instantaneous aneurysm inflow rate across the cardiac cycle for the original, high flow rate, and low flow rate simulations. The average aneurysm inflow rate shows a 47.6% increase as a result of the 50% increase in parent vessel flow for the 'High Q' case and a 32.5% decrease as a result of the 50% decrease in parent vessel flow for the 'Low Q' case. The corresponding 61.3% increase and 35.4% decrease in simulated contrast decay constant would suggest that the average rate of contrast washout and the average aneurysm

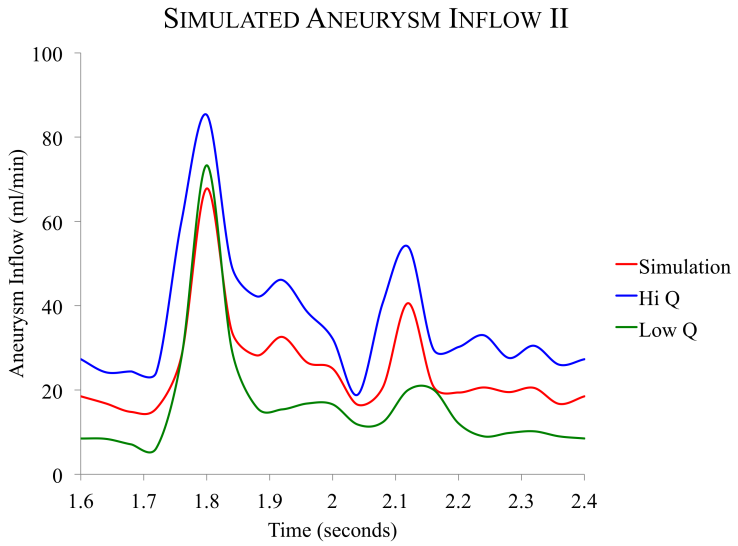

Figure 6.37: *Aneurysm inflow across the cardiac cycle for the original, high flow rate, and low flow rate simulations*

inflow are strongly linked. Additionally, the high range of instantaneous aneurysm inflow in the 'Low Q' case (approximately 4x the mean flow rate) is likely the cause of the large variation in contrast pulse decay rate with cardiac cycle position that is seen in figure 6.36b.

Table 6.7: *Mean and range of aneurysm inflow for the original, high and low inflow simulations*

SIMULATION	MEAN INFLOW	INFLOW RANGE
Initial	25.2 ml/min	53.0 ml/min
High Q	37.2 ml/min	66.4 ml/min
Low Q	17.0 ml/min	67.1 ml/min

The evolution of the maximum and mean aneurysm inflow velocities for both 'High Q' and 'Low Q' simulations are plotted in figure 6.38.

From figure 6.38, it is clear that with a small number of exceptions, both peak and mean inlet velocity scale with parent vessel flow rate: the largest values of mean and maximum velocity are seen in the 'High Q' simulation and the smallest values are seen for the 'Low Q' case.

Variation in aneurysm flow pattern is seen between the 'High Q' and 'Low Q' simulations. Figure 6.39 shows aneurysm flow at a high flow rate is dominated by a single vortex with a core of fast-moving flow penetrating deep into the aneurysm dome. In the low flow rate simulation, a dominant counterclockwise vortex occupies the main aneurysm dome, with a small clockwise-rotating vortex at the aneurysm tip. There appears to be a marked lack of flow circulation in

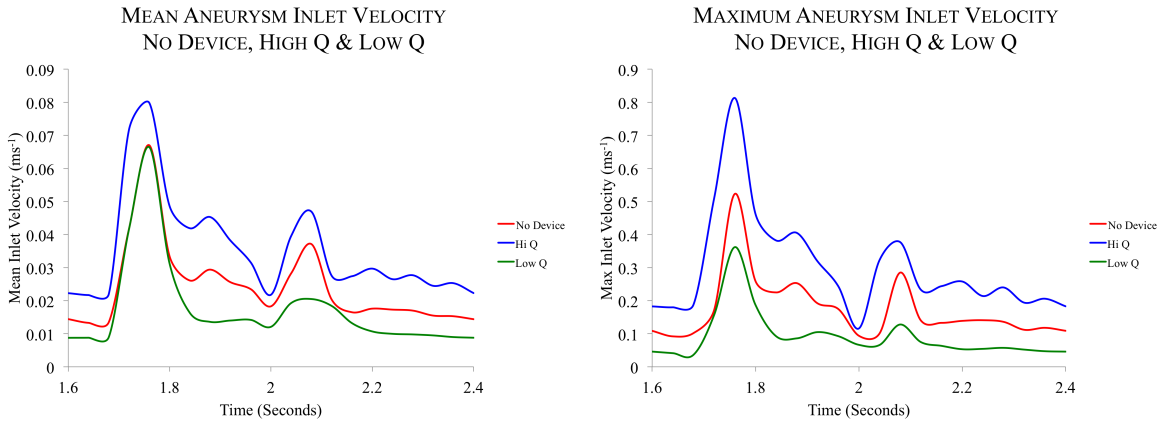

(a) *Mean velocity* **(b)** *Maximum velocity*

Figure 6.38: *Velocity magnitude at the aneurysm neck for the initial 'No Device', 'High Q', and 'Low Q' simulations*

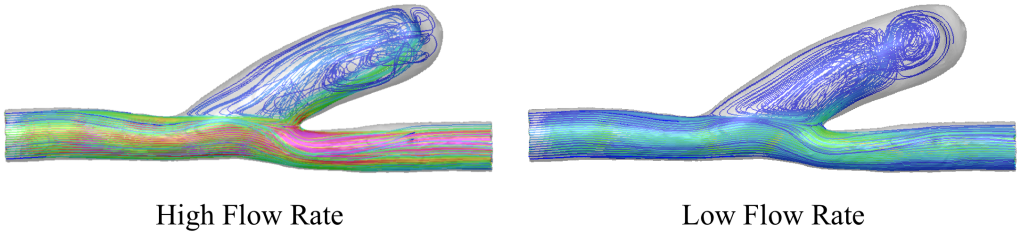

Figure 6.39: *Different degrees of flow infiltration and vortex position in the 'High Q', and 'Low Q' simulations at mean parent vessel flow rate*

the 'High Q' simulation: flow enters the aneurysm dome along the distal edge, there is an area of impingement at the aneurysm tip with some mixing, and flow quickly exits the aneurysm with very little recirculation. This lack of recirculation in the 'High Q' simulation may explain the rapid and relatively linear contrast decay seen in figure 6.35b.

6.7.4 Summary: The Influence of Parent Vessel Flow Rate

Finally, the contrast bolus decay curve predicted from each simulation is plotted relative to the experimental contrast decay in figure 6.40.

The relative difference between all three simulated contrast bolus decay curves in figure 6.40 is large, with a range of 10-50% contrast remaining in the aneurysm dome 2.0 seconds after peak concentration. The spread of the 'High Q' and 'Low Q' decay curves about the original simulation is relatively symmetric; a 50% increase in parent vessel flow rate results in a 61.3%

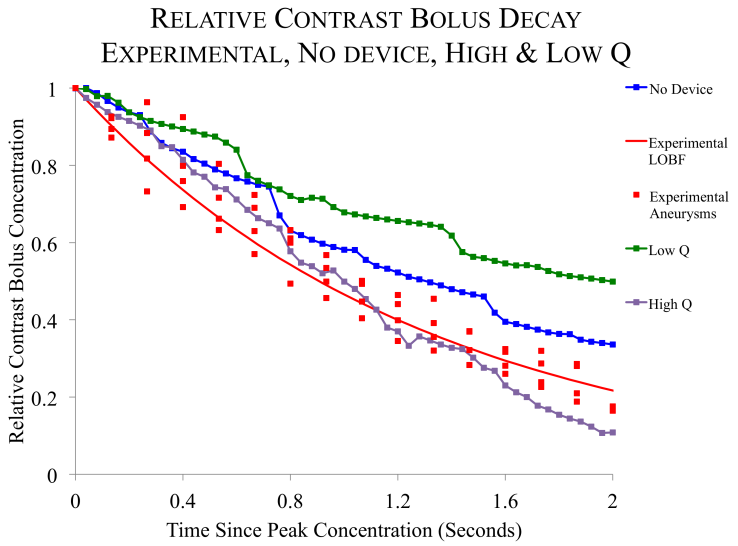

Figure 6.40: *Experimental and simulated contrast concentration decay, including 'High Q' and 'Low Q' simulations*

increase in contrast decay rate and a 50% decrease in parent vessel flow rate leads to a 35.4% decrease in contrast decay rate. Contrast decay rate and parent vessel flow rate are plotted in figure 6.41, and a linear trend line assuming the two measures are directly proportional is fitted with good accuracy.

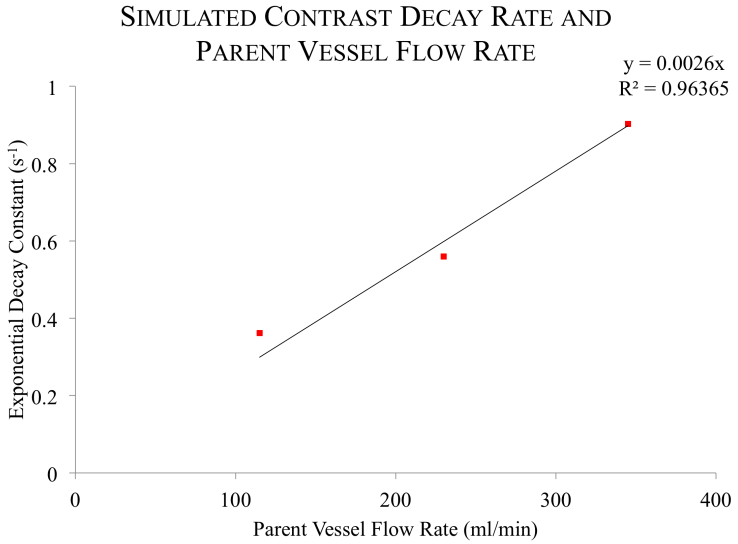

Figure 6.41: *Contrast decay rates for all three simulations ('No Device', 'High Q', and 'Low Q') conducted at different parent vessel flow rates*

From the decay curves in figure 6.40, it appears that a simulation adopting a parent vessel flow rate between the human ICA mean of the original simulation and the human CCA mean of the

'High Q' case would result in a contrast decay curve similar to that obtained experimentally. Thus, assuming the linear relationship described in figure 6.41 and a cardiac profile similar to the human ICA/CCA, a mean parent vessel flow rate of around 290ml/min would mimic the contrast decay rate of the *in-vivo* model (0.758 s^{-1}).

For comparison, the *in-vivo* experimental parent vessel flow rate may be approximated by tracking the movement of the injected contrast front through the vasculature. For all four experimental aneurysm cases the approximate velocity of contrast transport is estimated between consecutive angiographic images, which is repeated in two separate measurements for each geometry. This results in eight individual estimates of parent vessel flow velocity, from various points in the cardiac cycle, across the four experimental aneurysms. Assuming a poiseuille flow profile, these estimates of flow velocity correspond to a range of parent vessel flow rates of 202-516 ml/min and a mean flow rate of 296ml/min, values that give strong support to the simulated flow rate of 290 ml/min, which was predicted to result in a virtual contrast decay rate equal to that seen experimentally.

Given the relatively large range of contrast decay rate seen across simulations conducted with variable parent vessel flow rate, it is apparent that estimates of parent vessel flow rates are a substantial source of error in virtual contrast models. The difference between the experimental contrast decay rate observed *in-vivo* and the rate predicted by the *in-silico* model of section 6.4 is most likely due to such a modelling discrepancy, with the true parent vessel flow rate being underestimated *in-silico*.

6.8 Chapter Conclusions: Evaluating the Virtual Contrast Model

In this chapter, a virtual contrast model has been proposed and evaluated. The model is built on the principle of simplifying the presence of an angiographic contrast as a scalar quantity that is transported in the blood, in a similar manner to dye particles. Despite the potential errors of this assumption, the agreement between the experimental and simulated aneurysm contrast washout is good. Sources of modelling error discussed in the literature, such as the mismatch between blood and contrast viscosity and density, have been quantified, with their effect on predicted contrast decay rate shown in figure 6.42 and table 6.8. The sensitivity of the virtual contrast

decay rate to changes in parent vessel flow rate, a factor unrelated to the scalar assumption, was also investigated.

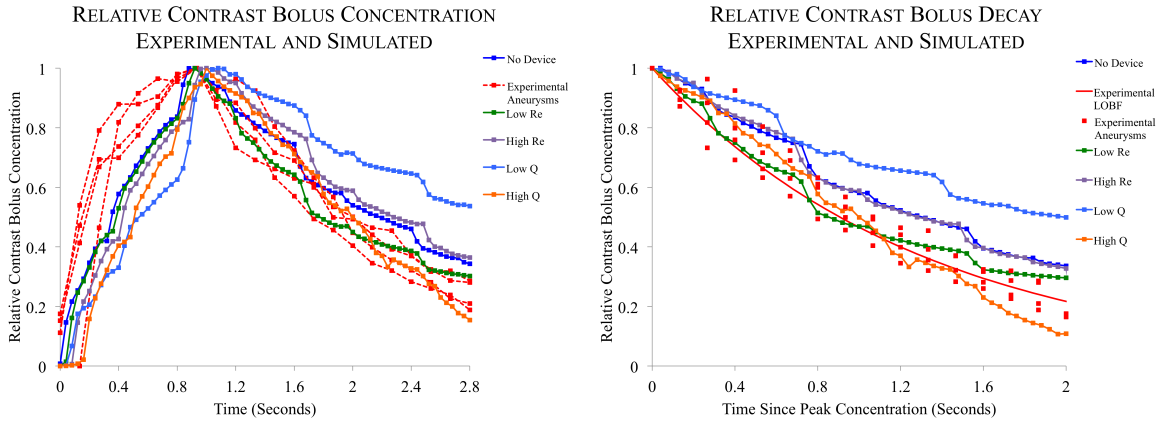

(a) *Contrast residence curve* **(b)** *Contrast decay*

Figure 6.42: *Contrast residence and decay curves for experimental and all cycle-averaged simulations*

Table 6.8: *Exponential decay constants: experimental and all cycle-averaged simulations*

	Exponential Contrast Decay Constant
in-vivo	0.758 s^{-1}
Initial Simulation	0.560 s^{-1}
High Re Simulation	0.552 s^{-1}
Low Re Simulation	0.677 s^{-1}
High Q Simulation	0.903 s^{-1}
Low Q Simulation	0.362 s^{-1}

Localised changes in blood-contrast mixture have been modelled with densities and viscosities typical of the range of angiographic contrast agents that are commercially available. These properties result in a range of changes in effective Reynolds number: a Reynolds number increase of 57% corresponds to a decrease in simulated contrast decay rate of 1.4%, and a 61% decrease in local Reynolds number results in a 21% increase in contrast decay rate. Such a range of decay rate is considered insignificant and within the scatter of the results obtained experimentally. Additionally, if the density and viscosity of the contrast agent used experimentally are incorporated into the simulation, no noticeable change in contrast decay rate is observed. However, density and viscosity mismatch effects, where local gradients of viscosity and density result in flow regime changes, have not been modelled and may still contribute significantly towards errors between real and virtual contrast models.

Discrepancies in fluid density and viscosity have been shown to result in significant differences in aneurysm flow pattern. Such differences may be observed visually from contrast infiltration and decay patterns. Flow entering the aneurysm dome with a pronounced jet (characterised by a high ratio of maximum to mean inlet velocity) has been shown to penetrate further into the aneurysm dome, increasing the contrast residence time, and decreasing the contrast decay rate for constant aneurysm inflow. However, even when no contrast density or viscosity properties are incorporated into the model, the visual correspondence is good between the contrast jetting and circulation seen *in-vivo* and in virtual angiograms generated from the model.

The effect of parent vessel flow rate on changes in contrast decay rate was also investigated. Simulations conducted with a 50% decrease in parent vessel flow rate resulted in 35.4% decrease in contrast decay rate, whereas a 50% increase in parent vessel flow rate was found to correspond to a 61.3% increase in contrast decay rate. These changes are attributed to higher rates of aneurysm inflow increasing flow velocities throughout the aneurysm dome and reducing the average residence times. Any changes in contrast residence time related to flow jetting or differences in aneurysm flow pattern appear insignificant when compared to the effect of parent vessel flow rate.

The presence of an angiographic catheter in a vessel lumen has been shown to significantly reduce the vessel flow rate, compared to the un-obstructed vessel. Consequently, angiographically obtained *in-vivo* aneurysm washout data may not be representative of typical flow conditions. This fundamentally challenges the validity of using angiography as a clinical gold-standard of 'typical' physiological flow conditions against which any virtual contrast model must be verified.

Finally, the predicted contrast decay rate of the 'No Device' simulation conducted in this chapter underestimates the experimentally observed rate by around 26%. This underestimate is attributed to incorrect estimation of the parent vessel flow rate alone. Linear interpolations of decay rate varying with parent vessel flow rate suggest that a simulated inflow of approximately 290 ml/min (an increase of around 26% from the 'No Device' simulation) would match the predicted decay rate to that seen experimentally. Angiographically measured estimates of experimental parent vessel flow rate suggest a mean *in-vivo* flow rate of 296 ml/min, which validates the linear interpolation of vessel flow rate and contrast decay constant.

Chapter 7

Applying the Virtual Contrast Model to Flow-Diverter Treatment in Animal Models

In this chapter, the virtual contrast model developed in chapter 6 is applied to an aneurysm geometry with a flow-diverter device deployed. A novel flow-diverter device is deployed in experimental swine aneurysms, and the resulting contrast residence curve is calculated in section 7.2. Virtual contrast residence is simulated for the post-deployment aneurysm geometry in section 7.3 with the calculation of the change in contrast decay rate after device deployment and the generation of virtual angiography. The effects of both parent vessel straightening and partial aneurysm thrombosis after device deployment are investigated in section 7.4. Finally, simulated contrast residence changes due to device deployment are compared to the in-vivo changes seen experimentally in section 7.5.

7.1 Introduction

Angiographic contrast may be employed clinically to immediately assess the success of an aneurysm treated with a flow-diverter. The aneurysm is first highlighted prior to device placement with a bolus of contrast. This imaging may then be compared to the equivalent bolus of

contrast injected after device deployment; greater reduction in contrast infiltration and in the rate of contrast decay is associated with more effective aneurysm occlusion.

Thus, the advantage of accurately simulating contrast washout changes due to the placement of a device is clear. Simulated treatment may be validated with *in-vivo* angiography of a previous procedure with a current flow-diverter design, and many novel device designs may be used to virtually treat an aneurysm to ascertain whether alternative treatment options could be more successful. To this end, the virtual contrast model developed in the previous chapter is integrated into a model of an aneurysm after treatment with a flow-diverter.

7.2 *In-vivo* Flow-Diverter Deployment

7.2.1 Experimental Protocol

Two of the created aneurysms discussed in the previous chapter (experimental aneurysms 2 and 4) are subsequently implanted with a novel flow-diverter device. Both devices used are identical to 'Stent III' in chapter 3 and placed with the mesh in a 'diverging' orientation to the flow direction using the same experimental protocol discussed in chapter 6. Within a few minutes of device placement, 3D rotational angiography is performed on one aneurysm. The 3D imaging is segmented in Osirix. The resulting 3D reconstruction is shown in figure 7.1 and compared to the same geometry prior to device deployment. From the figure, it is clear that a fraction of the aneurysm dome has already thrombosed in the few minutes between device deployment and 3D scan acquisition. Clear vessel straightening after device deployment is also visible between the two 3D geometries.

Conventional 2D DSA is also performed on each of the two treated aneurysms to assess the degree of aneurysm thrombosis approximately 10 minutes after device deployment. Substantial reduction in contrast infiltration is seen in both geometries, compared to the same geometries with no device deployed, as shown in figure 7.2.

The lack of contrast infiltration along the upper edge of both aneurysm domes supports the possible partial thrombosis seen in the 3D reconstruction of figure 7.1.

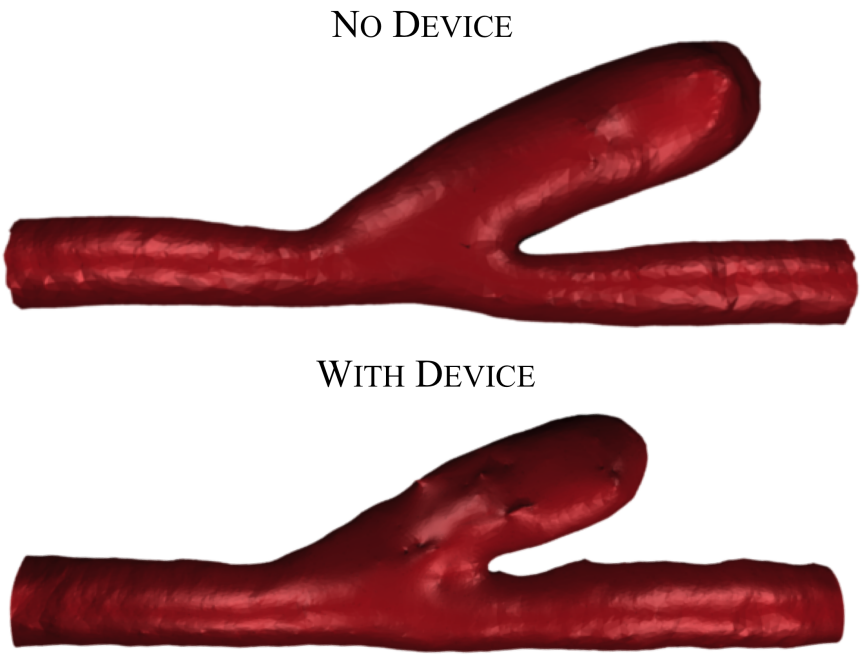

Figure 7.1: *Reconstructions based on 3D angiography before and after flow-diverter deployment*

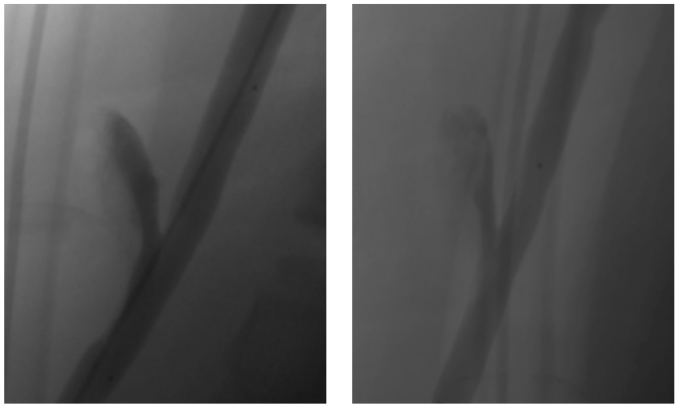

Figure 7.2: *Reduced contrast infiltration is seen in both aneurysms after flow-diverter device deployment*

7.2.2 Contrast Decay

The corresponding contrast decay after device deployment for aneurysm 2 is shown in figure 7.3, with almost identical behaviour seen for aneurysm 4. Consistently in both cases, no contrast infiltration is seen along the upper edge of the aneurysm.

The relative contrast concentration within the aneurysm dome of both treated aneurysms is calculated, as previously detailed in section 6.3 of chapter 6. Experimental contrast residence

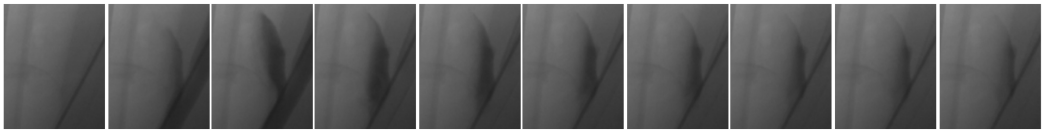

Figure 7.3: *Contrast infiltration and decay after device deployment. Images are separated by 0.4 seconds.*

curves following device deployment are plotted in figure 7.4. The decay portion of both curves is plotted in figure 7.5.

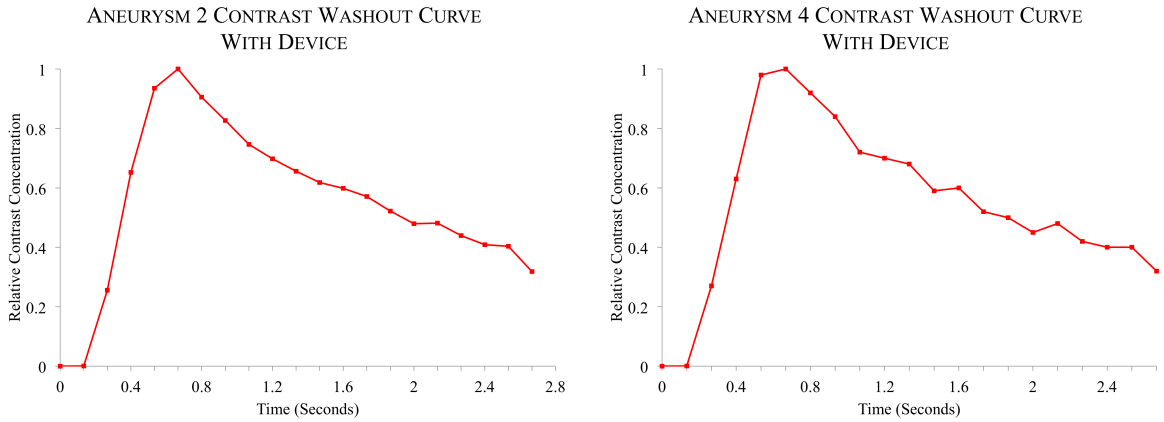

(a) *Experimental aneurysm 1* **(b)** *Experimental aneurysm 2*

Figure 7.4: *Contrast washout curves for both experimental aneurysms implanted with a flow-diverter*

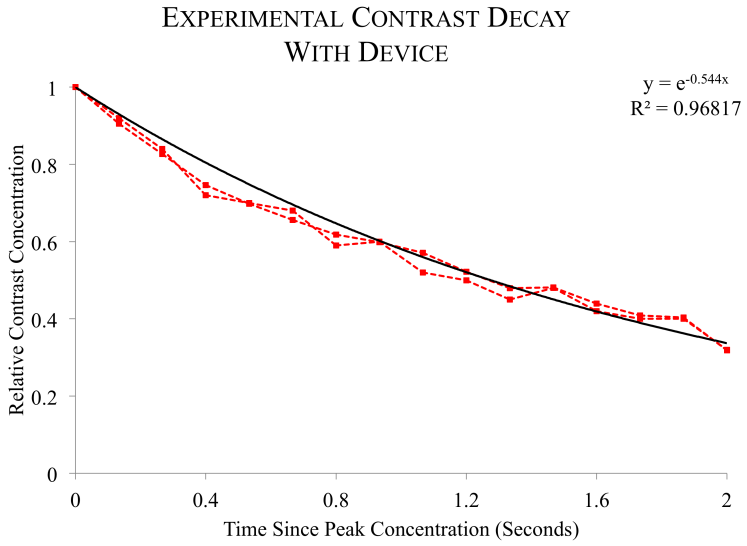

Figure 7.5: *Decay portions of the experimental contrast residence curves with an exponential decay trend line fitted*

Despite substantial visual differences between the degree of contrast infiltration before and after the device placement, figure 7.5 indicates that the actual rate of contrast decay decreases

only slightly after device deployment; the exponential decay constant decreases from 0.764 s^{-1} (calculated in section 6.3) to 0.544 s^{-1} after device deployment.

7.3 *In-silico* Flow-Diverter Deployment and Contrast Modelling

7.3.1 Simulation Setup

The post-deployment 3D geometry shown in figure 7.1 is virtually implanted with a flow-diverter model identical to that used experimentally and shown in figure 7.6 below. The device is manually expanded into the aneurysm geometry with a final orientation consistent with post-mortem resections of the experimental aneurysm geometries. To reduce mesh size and improve computational efficiency, the device is trimmed longitudinally once positioned so as to only occupy an area of the vasculature in the region of the aneurysm neck.

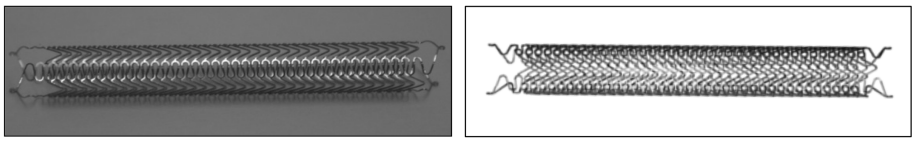

Figure 7.6: *Flow-diverter device used experimentally (a) and the same device modelled virtually (b)*

Good visual and quantitative similarity is seen in contrast residence between both experimental aneurysm geometries implanted with the flow-diverter device. As such, only one representative geometry is used for computational simulations, which increases computational efficiency and matches the rationale used in the previous chapter for the modelling of the 'No Device' experimental aneurysms.

The representative geometry with the flow-diverter device deployed is meshed with identical parameters to those detailed in section 6.4 of the previous chapter. This yields a computational model with a mesh size of 4,370,000 elements. Transient flow simulations are performed with the same boundary conditions and solver parameters as previous 'No Device' simulations in section 6.4. An inlet velocity condition typical of the human ICA is again prescribed, and the same arrangement of eight independent contrast pulses is applied at the geometry inlet after two full cardiac cycles. Convergence is achieved in approximately 40 minutes per time step and

typically in under 100 iterations.

7.3.2 Simulation Results

Simulated flow streamlines at mean parent vessel flow rate for the 'With Device' geometry are shown in figure 7.7. It is clear that the flow-diverter placement dramatically changes the flow pattern within the aneurysm dome; the elongated vortex present in the 'No Device' case is eliminated and replaced with a smaller, slower and less-coherent vortex positioned closer to the aneurysm neck.

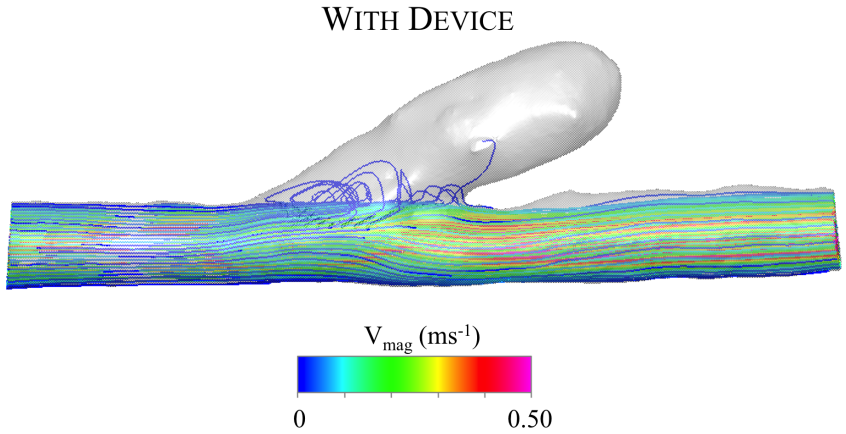

Figure 7.7: *Simulated flow streamlines in the 'With Device' case at mean parent vessel flow rate*

Flow appears to enter into the 'With Device' aneurysm dome with a relatively uniform distribution and velocity, and does not exhibit the concentrated distal jet visible in the 'No Device' case. Most of the blood entering the aneurysm appears to do so in the middle-portion of the neck and leaves in the distal portion; some circulation can be seen in the distal area of the neck and towards the centre of the aneurysm dome. The flow-diverter device results in a mean aneurysm inflow reduction of 73.8% and a range over the cardiac cycle of 41.4-76.9%. It is apparent that the vessel-straightening effect of the device also contributes to reduced aneurysm inflow by reducing the non-longitudinal velocity components at the aneurysm entrance.

The value of each of the eight independent contrast pulses is exported for every fourth time step and plotted in figure 7.8. The overall pattern of the contrast residence differs substantially from that seen across all five variations of the 'No Device' simulation in the previous chapter; a secondary peak in contrast value is present in the three pulses released in the second half of the

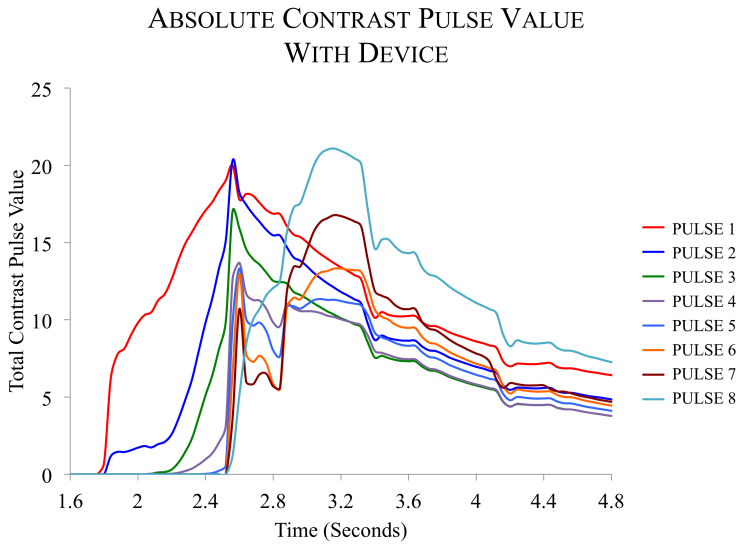

Figure 7.8: *Absolute value for all eight contrast pulses in the With Device geometry*

cardiac cycle (Pulses 5-7). This effect appears to be the result of contrast that is 'trapped' in the low flow-speed region at the proximal end of the aneurysm neck and retained by the flow-diverter mesh as shown in figure 7.9. The contrast is progressively drawn out of and into the aneurysm dome by the sudden changes in parent vessel flow rate from systole to diastole.

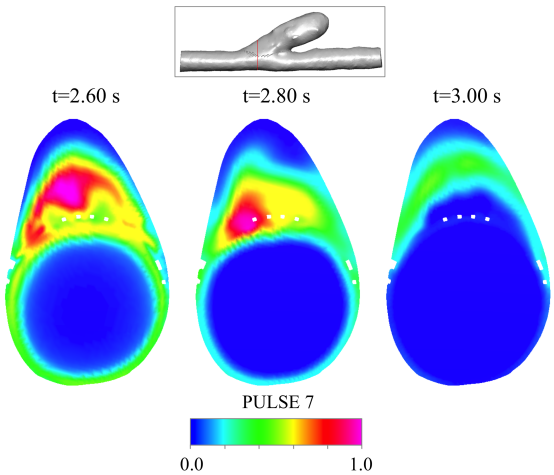

Figure 7.9: *Evolution of Pulse 7 for the 'With Device' simulation in the proximal region of the aneurysm neck. The contrast pulse concentration is shown at times 2.60 seconds (systole), 2.80 seconds (diastole), and 3.00 seconds*

The contrast residence curves of all eight contrast pulses are plotted in figure 7.10a. Considerable variation can be seen in the inflow portion of the curves, especially when compared to the same pulse distributions with 'No Device'. Due to the position of Pulse 1 (and a lesser degree Pulses

2 and 3) in the cardiac cycle almost all of the contrast enters the aneurysm dome quickly during the fast and accelerating flow of peak systole; the contrast is washed into the aneurysm in one coherent volume, similar to the action of the 'No Device' case. All other contrast pulses occur at points in the cardiac cycle with regions of slow or decelerating flow and as such contrast enters the aneurysm dome in a more varied fashion, and with more viscosity-dominated creeping flow, leading to a dramatically different infiltration profile. The double-peak variation seen for some pulses is likely the result of a portion of the contrast quantity leaving and re-entering the aneurysm dome by the mechanism shown in figure 7.9. The characteristic waveform of peak systole is evident in much of the variation seen. This confirms that sudden increases in contrast concentration are occurring at peak flow rate, which suggests that what little contrast does enter the aneurysm does so under the higher flow rate of peak systole.

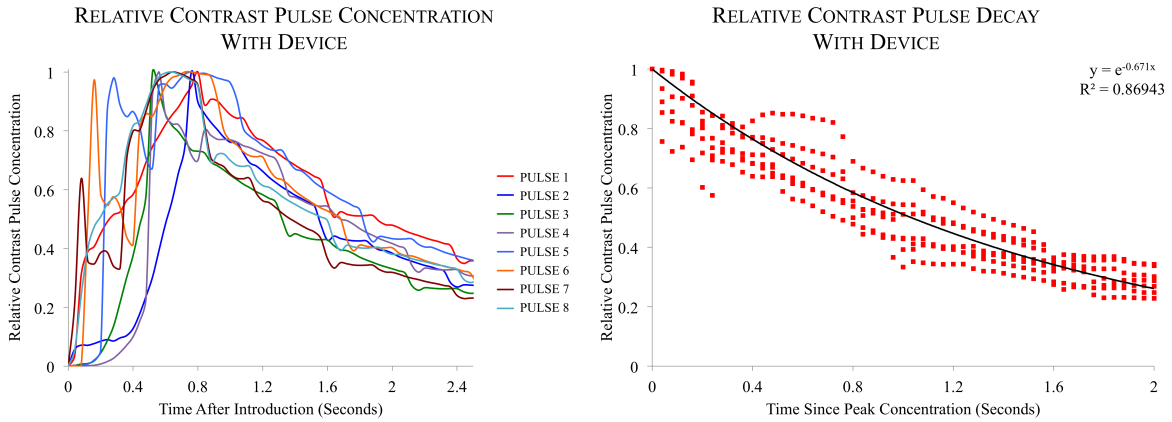

(a) *Relative contrast pulse concentration* **(b)** *Relative contrast pulse decay*

Figure 7.10: *Relative contrast residence and decay for all eight contrast pulses in the 'With Device' geometry*

The decay portion of the contrast pulse residence curves is plotted in figure 7.10b with a fitted exponential decay curve yielding a decay constant of 0.671s^{-1}. The large degree of scatter about the mean pulse decay rate, especially in the early portion of the decay, is due to the contrast re-entry behaviour seen.

A cycle-averaged contrast bolus residence curve is generated from a linear combination of the contrast pulse residence traces and is plotted in figure 7.11a. The decay portion of the curve is also plotted in figure 7.10b, where an exponential decay trend line is fitted. Contrast re-entry behaviour similar to that seen in figure 7.8 and figure 7.9 is apparent in the first 0.8 seconds

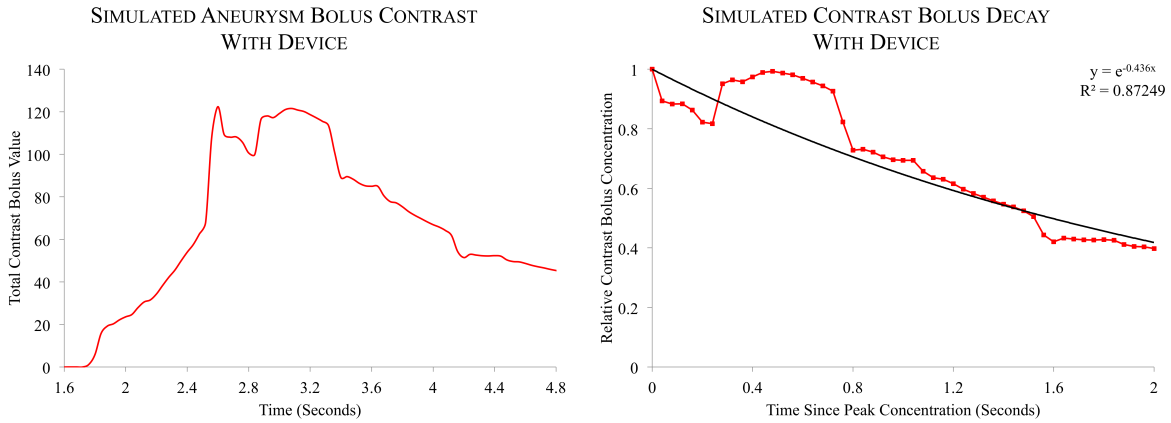

(a) *Contrast concentration* **(b)** *Relative contrast decay*

Figure 7.11: *Cycle-average contrast bolus residence and decay in the 'With Device' geometry*

of the simulated contrast decay trace. Initially, contrast moves out of the aneurysm dome for the first 0.3 seconds of the decay curve (systole to diastole), but the contrast is retained in the low-flow area below the aneurysm entry plane and adjacent to the flow-diverter. This contrast, in addition to the contrast already residing in the low-flow region, is then washed back into the aneurysm dome between approximately 0.3 and 0.5 seconds of the decay trace before once more washing out of the aneurysm dome.

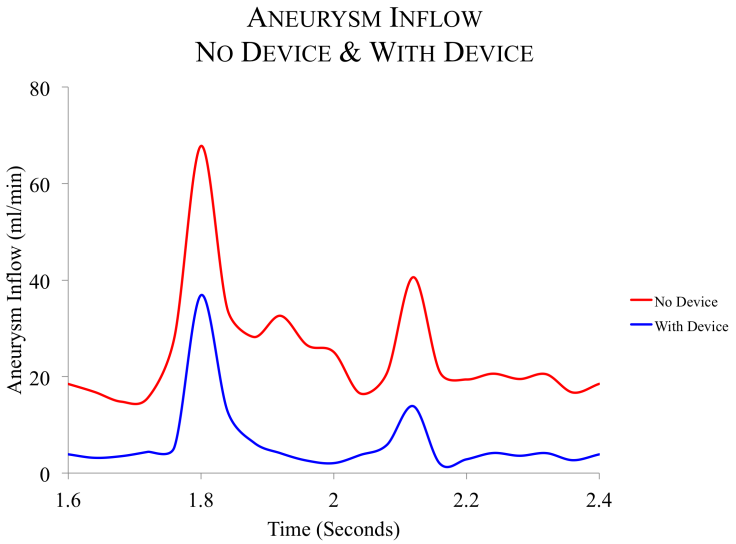

Figure 7.12: *Simulated instantaneous aneurysm inflow with and without a flow-diverter device deployed*

The instantaneous aneurysm inflow rate for the 'With Device' simulation is plotted in figure 7.12 alongside the corresponding inflow when no flow-diverter device is present. The average and

Table 7.1: *Aneurysm Inflow With and Without a Flow-Diverter Deployed*

Simulation	Mean Inflow	Inflow Range
No Device	25.2 ml/min	53.0 ml/min
With Device	6.39 ml/min	34.8 ml/min

range of inflow experienced is summarised in table 7.1. It is apparent that the flow-diverter device consistently reduces the instantaneous inflow by a around 80% for the majority of the cardiac cycle but that this flow reduction drops to around 45% at peak systole.

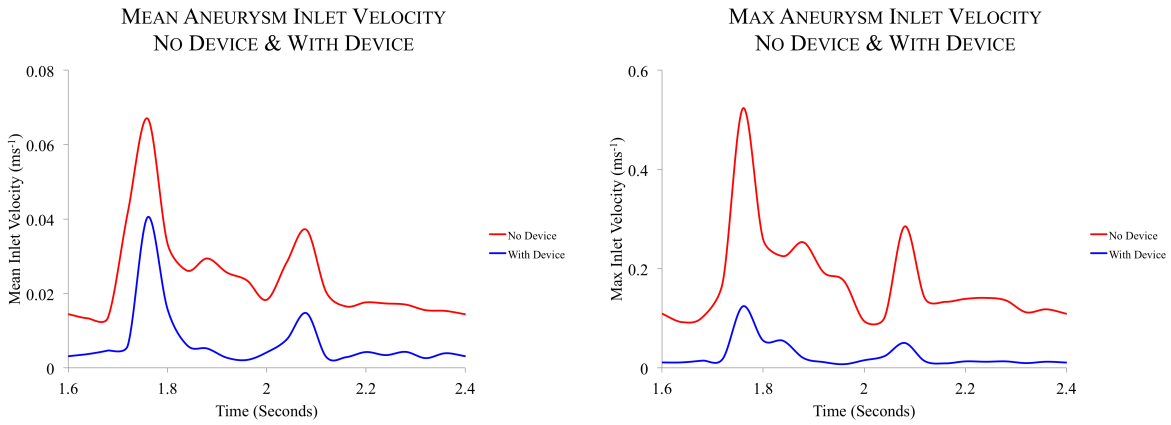

(a) *Mean Aneurysm Inlet Velocity* **(b)** *Maximum Aneurysm Inlet Velocity*

Figure 7.13: *Maximum and mean aneurysm inlet velocity with and without device (in-silico)*

The mean and maximum aneurysm inlet velocity distributions over one cardiac cycle both before and after device placement are plotted in figure 7.13. From the figure, it appears that the action of the device is both to reduce the mean inlet velocity by around 50-75% consistently over the cardiac cycle and also to substantially reduce peak velocities, thereby creating a more diffuse inflow jet—reinforced by the diffuse velocity distribution seen in figure 7.7. This effect is confirmed by the substantially lower ratio of maximum to mean aneurysm inlet velocity for the 'With Device' geometry (3.68) compared to the 'No Device' geometry (7.23).

Finally, the absolute quantity of simulated contrast that infiltrates the aneurysm dome with and without a device deployed is summarised in figure 7.14. The peak contrast volume in the aneurysm is reduced by around 85% following device deployment, which suggests an almost direct correspondence between average aneurysm inflow reduction and peak aneurysm concentration reduction. From figure 7.14 it is also clear that while relative contrast decay rate decreases after

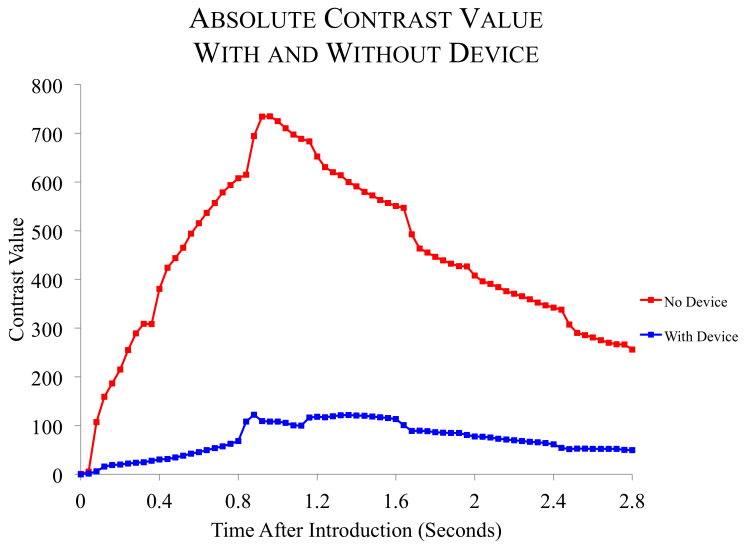

Figure 7.14: *Total contrast volume in the aneurysm dome with and without a device deployed*

device deployment, changes in the rate of contrast infiltration are not detected, with a similar time to peak contrast infiltration of around 0.8 seconds in both cases.

7.4 Accounting for Partial Thrombosis of the Aneurysm

Both the simulated and experimental contrast decay rates seen in the previous section represent a scenario where substantial aneurysm thrombosis has already occurred, as is evident from the dramatic change in aneurysm volume visible in figure 7.1. In order to quantify the effect of flow-diverter placement in the absence of any subsequent remodelling of the aneurysm dome, the 'With Device' simulation is repeated, but with the flow-diverter device placed in the original 'No Device' aneurysm geometry. Thus, an approximation to the instant after the flow-diverter device is deployed and before any thrombosis has initiated may be made to investigate the changes in hemodynamic environment due to the device presence alone.

In the absence of a distensible vessel wall model, which would capture the vessel-straightening seen following device deployment, the flow-diverter device is deployed into the 'No Device' aneurysm geometry assuming a perfectly rigid vessel wall. As such, the flow-diverting effect of the device is likely to be underestimated, as discussed in section 7.3.2.

The geometry with the flow-diverter device deployed is trimmed and meshed as previously

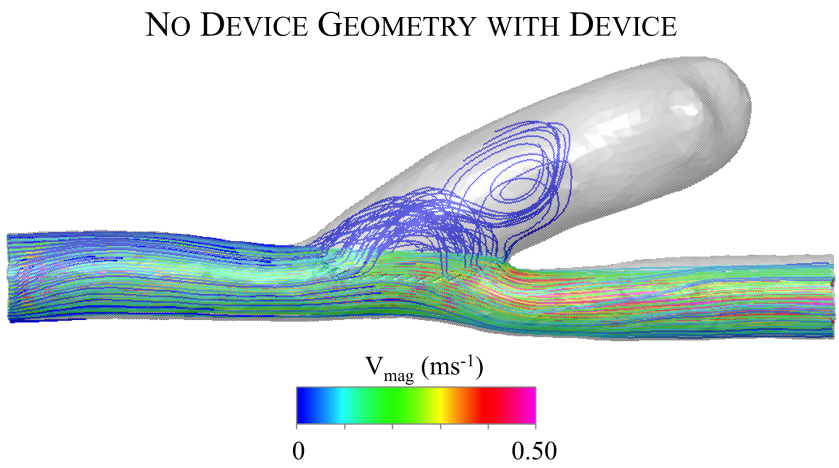

Figure 7.15: *Flow streamlines at mean flow for the 'No Device' geometry with a flow-diverter deployed*

detailed, resulting in a mesh size of 4,980,000 cells. Convergence is reached in approximately 45 minutes per time step and in less than 100 iterations. The corresponding flow streamlines at mean parent vessel flow rate are shown in figure 7.15. The flow pattern within the aneurysm dome is broadly similar to the 'With Device' geometry, but a stronger secondary vortex is visible in this case around the centre of the aneurysm dome. As in the 'With Device' geometry (figure 7.7), the majority of the flow entering the aneurysm dome does so at the proximal portion of the aneurysm neck before leaving in the distal portion. Although a small number of flow streamlines can be seen entering the aneurysm distally and forming the secondary vortex, most of the flow in the secondary vortex results from flow entering proximally and moving distally to form a weak jet at the distal aneurysm wall. The placement of the flow-diverter device results in a mean flow reduction of 35.6% with a range over the cardiac cycle of 11.5-62.0%, which is substantially lower than the corresponding flow reduction predicted using the straightened and partially thrombosed 'With Device' geometry.

The absolute value of each contrast pulses is extracted at every fourth time step and plotted in figure 7.16. The pattern on of contrast infiltration and decay seen in the figure more closely resembles the traces seen in previous 'No Device' simulations than the equivalent plot for the partially thrombosed geometry with a flow-diverter deployed. No 'double-peak' behaviour like that of figure 7.8 is seen in this geometry and device combination, which suggests the previously discussed phenomena of contrast entering, exiting and re-entering the aneurysm dome in the region of the flow-diverter device is not evident in this case.

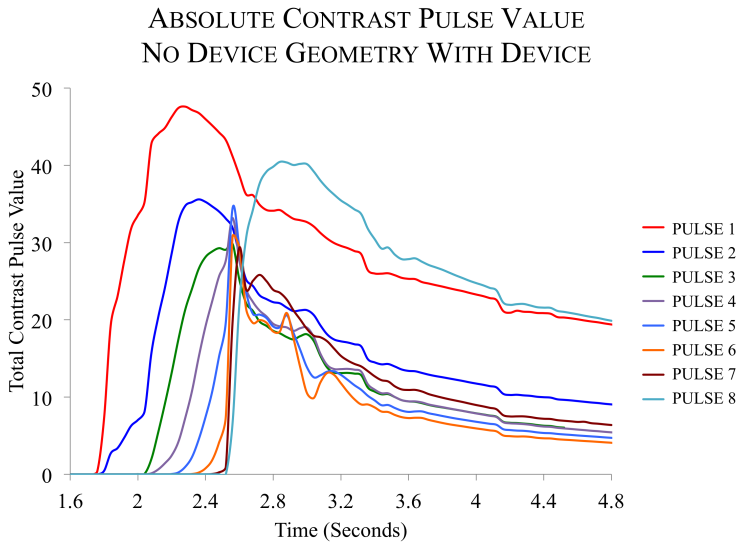

Figure 7.16: *Total absolute value for all eight contrast pulses in the 'No Device' geometry with a flow-diverter deployed*

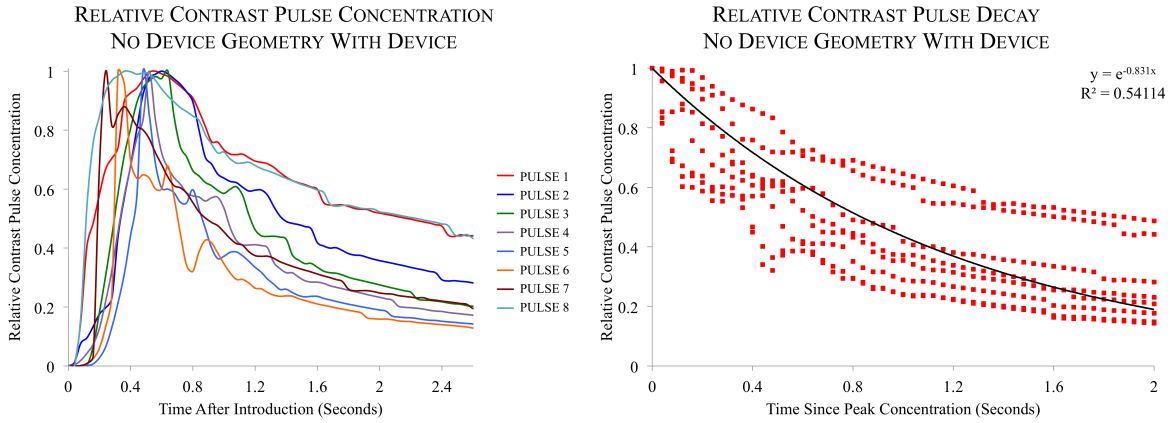

(a) *Relative contrast pulse concentration* **(b)** *Relative contrast pulse decay*

Figure 7.17: *Relative residence and decay for all eight contrast pulses in the 'No Device' geometry with a flow-diverter deployed*

The relative contrast pulse residence curves are plotted in figure 7.17a, and the corresponding decay portions of the curves are plotted in figure 7.17b with an exponential trend line fitted and a corresponding exponential decay constant of 0.831 s^{-1}.

Once again, considerable variation is seen in contrast pulse infiltration rate, with a time to peak contrast concentration of 0.2-0.6 seconds. The scatter of the contrast decay about the mean decay trend line is also considerable. The decay traces in figure 7.17b appear to divide into two distinct groups: Pulses 2-7 all show a decay constant similar to the mean trend line value, but

Pulses 1 and 8, which both exhibit the greatest volume of contrast infiltration, show a much slower rate of decay. The split of the pulses into these two groups with different approximate rates of decay results in the poor coefficient of determination (R^2=0.541) for the trend line fitted to the contrast pulse decay. This suggests a flow pattern previously discussed, whereby the contrast pulses that are washed into the aneurysm dome around peak systole (Pulses 1 and 8) are forced deeper into the aneurysm with a longer residence time and hence, slower decay rate.

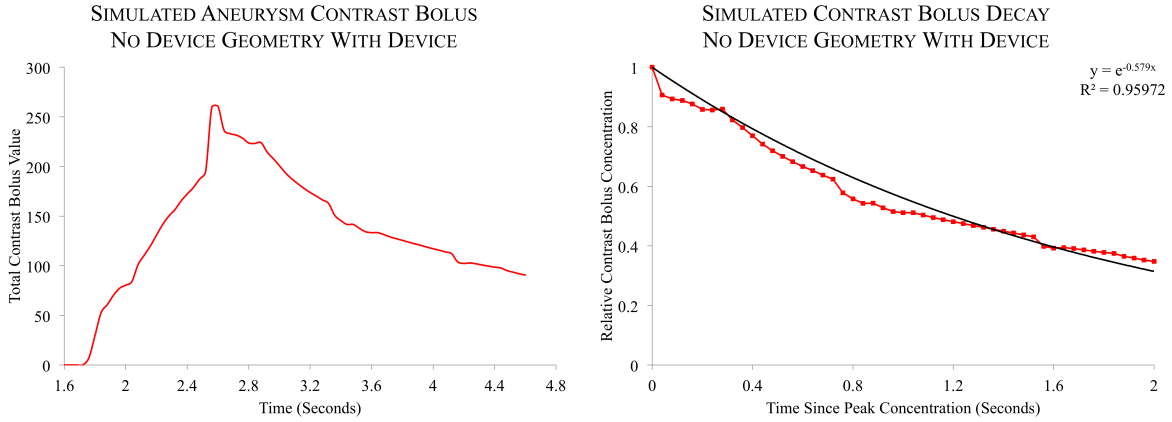

(a) *Contrast concentration* **(b)** *Relative contrast decay*

Figure 7.18: *Contrast bolus residence and decay in the 'No Device' geometry with a flow-diverter deployed*

Cycle-averaged contrast bolus residence and decay curves are constructed from the contrast pulse traces, as previously discussed, and plotted in figure 7.18. An exponential decay curve is fitted to the contrast decay and yields a decay constant of 0.579 s^{-1}. Such a decay constant is considerably lower than the corresponding average contrast pulse decay constant (plotted in figure 7.17b), which confirms that the contrast decay behaviour is dominated by contrast washed into the aneurysm dome around peak systole with a correspondingly lower decay rate. It is interesting to note that this contrast decay rate is higher than the corresponding 'No Device' contrast decay rate (0.560 s^{-1}) despite the average aneurysm inflow being reduced by 35.6% after the flow-diverter is deployed.

Instantaneous aneurysm inflow rate for the 'No Device' geometry implanted with a flow-diverter is plotted in figure 7.19 in addition to the flow rates for the 'No Device' and 'With Device' simulations. The graph shows that the aneurysm inflow for the 'No Device' geometry implanted

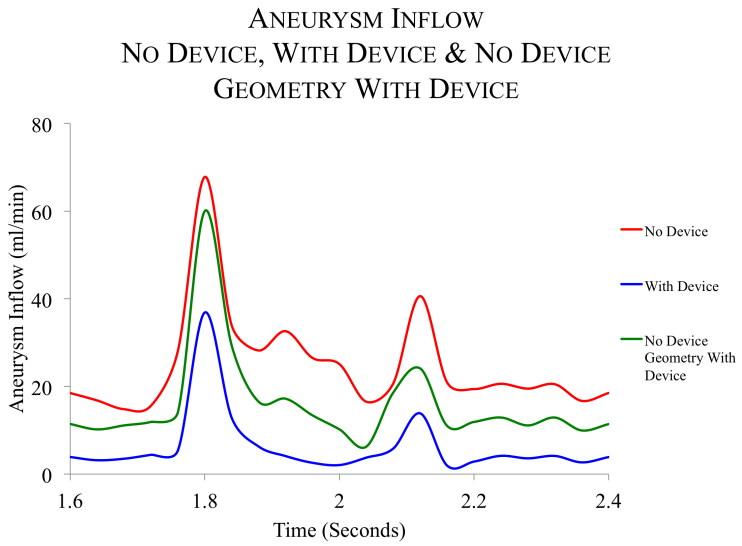

Figure 7.19: *Simulated instantaneous aneurysm inflow with and without a flow-diverter device deployed in both the with and without device geometries*

with a flow-diverter falls approximately between the 'No Device' and 'With Device' cases except at peak systole. At peak systole, the instantaneous aneurysm inflow for the 'No Device' geometry implanted with the flow-diverter is around 90% of the inflow seen for the 'No Device' geometry. Given the similarity between these inflow rates alongside the vast difference in the degree of flow penetration into the aneurysm at peak systole for both simulations (figure 7.20), it becomes clear why the contrast residence time may actually be shorter after the device is placed.

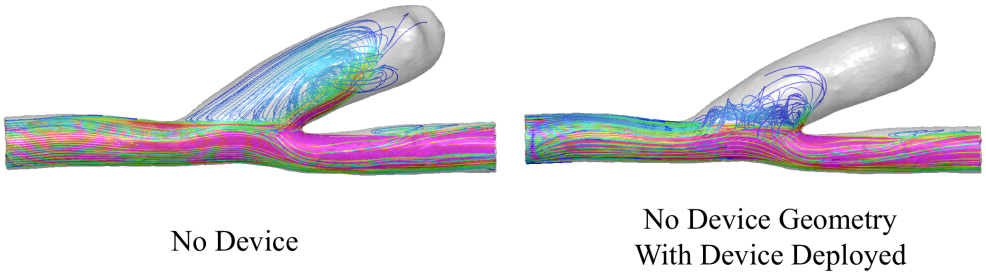

Figure 7.20: *Flow pattern at peak systole for the 'No Device' simulation and the No Device geometry implanted with a flow-diverter device*

The corresponding mean and maximum aneurysm inlet velocity is plotted in figure 7.21 alongside the distributions for the 'No Device' and 'With Device' simulations. A similar pattern to the inflow graph of figure 7.19 emerges: implanting a flow-diverter in the 'No Device' geometry significantly reduces both mean and maximum aneurysm inflow velocities over the cardiac cycle except at peak systole where the device has almost no effect. The average ratio of maximum to

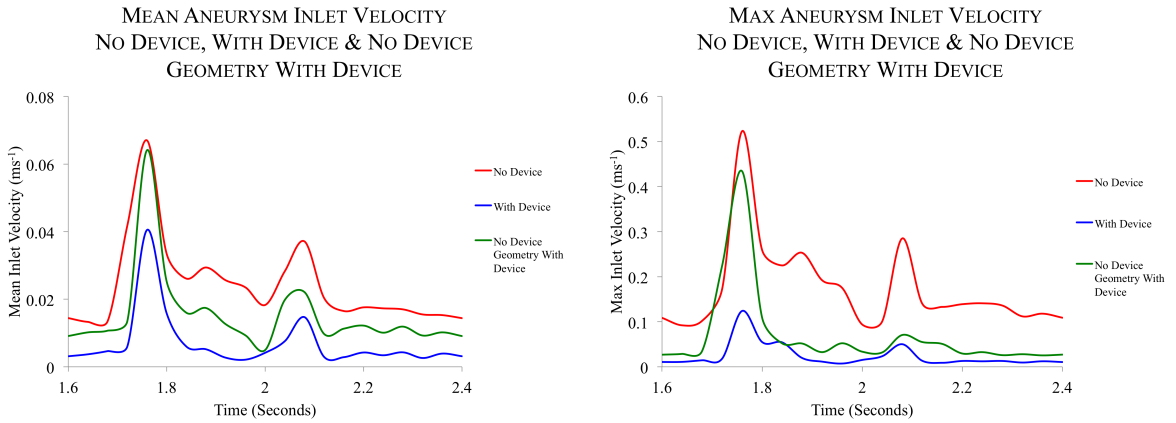

(a) *Mean Aneurysm Inlet Velocity* **(b)** *Maximum Aneurysm Inlet Velocity*

Figure 7.21: *Maximum and mean aneurysm inlet velocity with and without a flow-diverter device deployed in both the with and without device geometries*

mean inlet velocity for the 'No Device' geometry with a flow-diverter deployed is 4.25, similar to the 3.68 seen in the 'With Device' simulation and markedly lower than the 7.23 recorded in the 'No Device' simulation.

7.5 Comparing the Effect of Device Deployment: *in-silico* and *in-vivo*

7.5.1 The 'No Device' and 'With Device' Cases

The changes seen between the 'No Device' and 'With Device' simulations may be compared to the corresponding experimental imaging of the aneurysm with and without a flow-diverter deployed. Both the experimental and simulated contrast decay curves for the aneurysm geometry with and without a flow-diverter deployed are plotted in figure 7.22. The corresponding decay constants of the exponential trend lines fitted to each decay curve are summarised in table 7.2.

Table 7.2: *Experimental and simulated contrast decay rates*

Exponential Contrast Decay Constant	No Device	With Device	Reduction
Experimental	0.758 s^{-1}	0.544 s^{-1}	28.2%
Simulated	0.560 s^{-1}	0.436 s^{-1}	22.1%

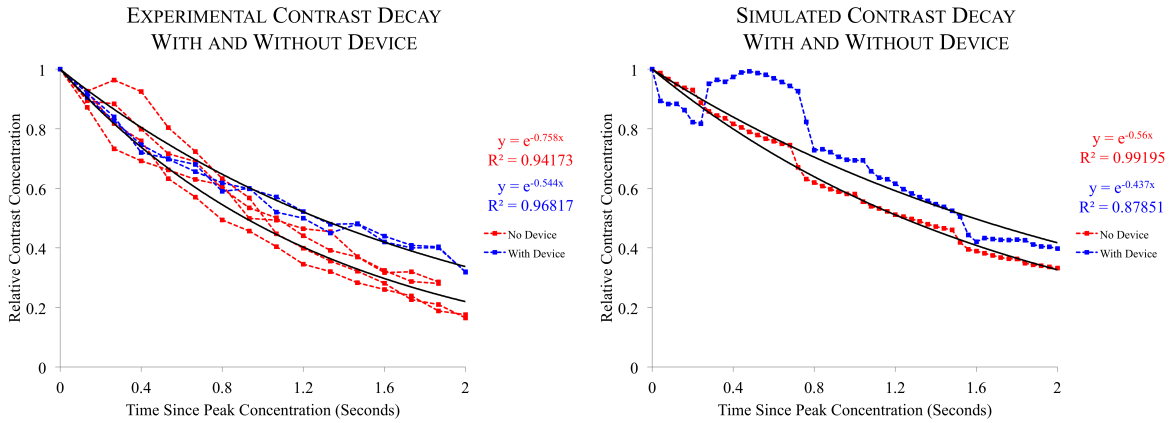

(a) *Experimental contrast decay* **(b)** *Simulated contrast decay*

Figure 7.22: *Comparing experimental and simulated contrast decay with and without device*

From figure 7.22, it is clear that for the 'No Device' and 'With Device' cases the simulated contrast washout underestimates the experimental contrast decay rate by around 20-25% in both cases. With no device deployed, approximately 22% and 33% of peak contrast remain after 2.0 seconds in the experimental and simulated models respectively. Once the device is deployed, around 34% and 42% of the peak contrast concentrations remain after 2.0 seconds for the experimental and simulated cases respectively. As discussed in the previous chapter, the general underestimation of contrast decay in the simulated aneurysm geometry is likely attributed to an underestimate of the mean parent vessel flow rate (chosen to equal the human ICA) compared to the actual rate experienced in the experimental porcine CCA. The relative reduction in contrast decay rate due to device deployment seen experimentally is also underestimated by around 20% (22.1% vs. 28.2%) for the simulated contrast model.

The simulated and experimental contrast infiltration and decay after a flow-diverter device has been deployed is visualised with virtual angiography in figure 7.23. For comparison, the corresponding real and virtual angiography for the aneurysm geometry with no device deployed are also repeated from chapter 6 in figure 7.24.

From figure 7.23, it is clear that the pattern of aneurysm contrast infiltration differs between the experimental and simulated geometries. Contrast entering the simulated geometry appears to do so as both a relatively uniform bolus across the whole aneurysm neck and as a small jet at the extreme distal point of the aneurysm neck. However, in the experimental case, also shown in

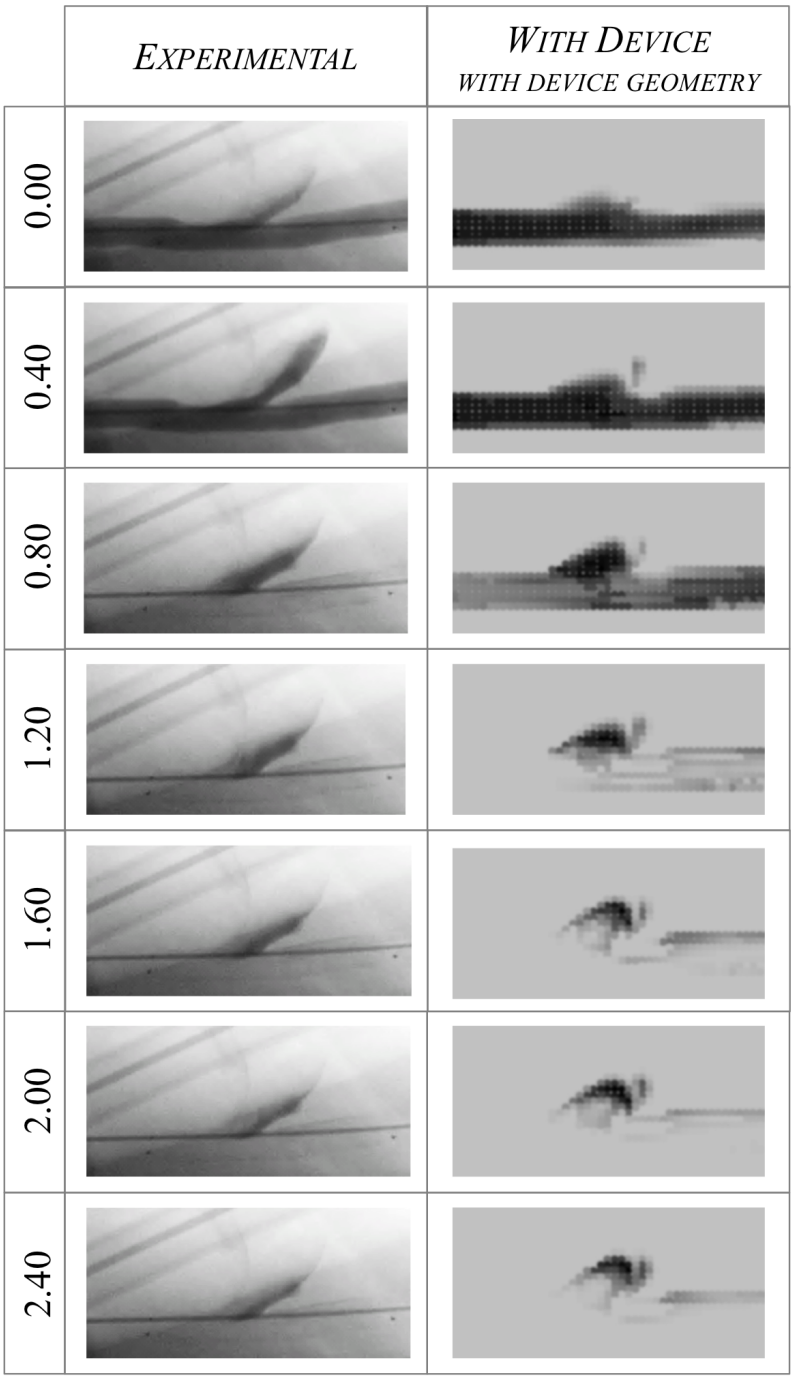

Figure 7.23: *Virtual and in-vivo angiography (images taken at 0.40 second intervals from peak contrast concentration) with a flow-diverter device deployed. Images are aligned to the peak aneurysm contrast concentration at 0.80 seconds*

figure 7.23, aneurysm contrast infiltration after device placement is dominated by the jet entering at the distal end of the aneurysm neck. But a small degree of contrast infiltration can be seen in the proximal portion of the experimental aneurysm neck at a time of 0.40 seconds. Contrast

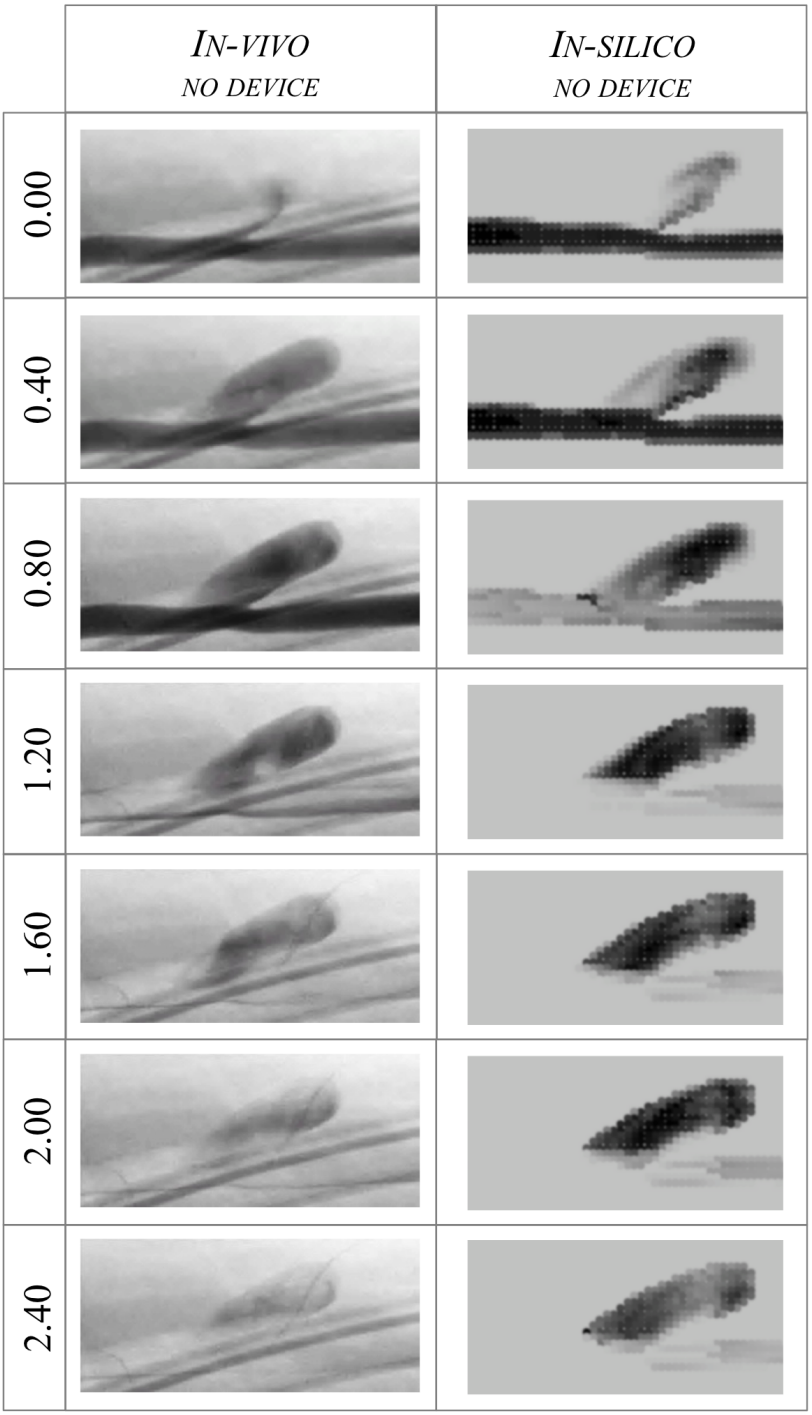

Figure 7.24: *Virtual and in-vivo angiography (images taken at 0.40 second intervals from peak contrast concentration) with no device deployed. Images are aligned to the peak aneurysm contrast concentration at 0.80 seconds*

infiltrates almost the full length of the experimental aneurysm, but no significant flow circulation behaviour is visible unlike the experimental geometry with no device deployed (figure 7.24). In the simulated 'With Device' case, however, contrast only infiltrates approximately $1/3^{rd}$ of the

way into the aneurysm dome.

The mechanism of contrast washout seen in figure 7.23 is complex in both the experimental and simulated cases. The rate of experimental contrast decay in the aneurysm is greatest at the aneurysm tip and in the proximal portion of the aneurysm neck. This decay behaviour is the reverse of that seen in the experimental 'No Device' contrast washout (figure 7.24), where decay is driven from a concentrated jet in the distal portion of the aneurysm dome—the region that is slowest to clear once the device has been deployed. The simulated contrast decay seen in figure 7.23 appears to be driven by relatively uniform flow entering around the mid-portion of the aneurysm neck as well as by a small jet of flow entering at the distal edge of the aneurysm neck. This leads to contrast being ejected from the aneurysm dome in the area between these two inflow regions, clearly visible at a time of 2.40 seconds in figure 7.23.

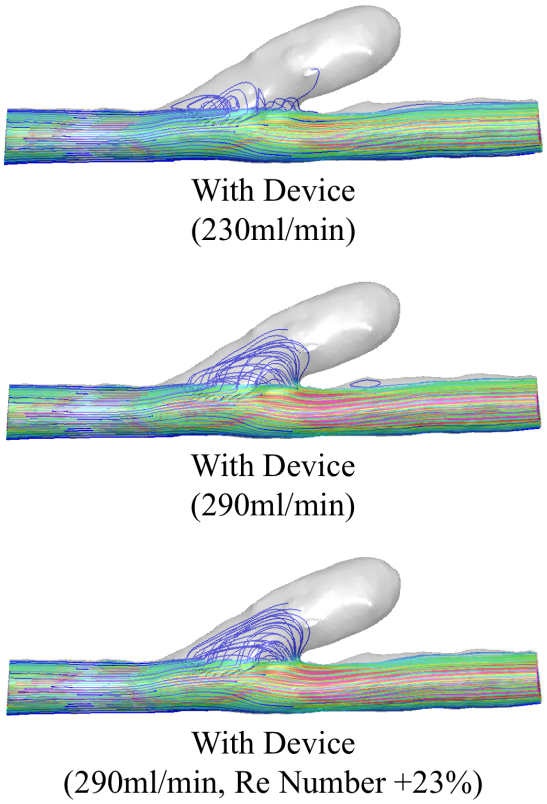

Figure 7.25: *Effect of increased mean parent vessel flow rate and Reynolds number (consistent with a 50% concentration of Omnipaque 240) on aneurysm flow pattern*

Despite the large visual differences in contrast distribution resulting from both experiment and simulation seen in figure 7.23, it is interesting to note that both cases show a high rate of

contrast infiltration at the distal neck area of the aneurysm dome but a very low rate of contrast decay in the same region. This effect is unlikely to be due to the difference in experimental contrast and blood viscosity, which only amounts to a discrepancy of around 10%. Instead, as previously discussed in chapter 6, it is likely that the the parent vessel flow rate assumed in the 'With Device' simulation underestimates the flow rate seen *in-vivo* by around 20%. Given the relatively large changes in aneurysm flow pattern due to variation in parent vessel flow rate, which were previously shown in figure 6.39, it is likely that the variation between simulated and experimental contrast distribution seen in figure 7.23 is also attributed to differences in flow rate.

The relative influence of both parent vessel flow rate and localised viscosity and density changes on the 'With Device' simulation are shown in figure 7.25. In the figure, results are shown for steady state simulations at the increased parent vessel flow rate of 290 ml/min (previously discussed as being more representative of *in-vivo* conditions) and with increased local Reynolds number due to experimental contrast properties. These cases are shown alongside the flow pattern experienced by the same geometry at the original simulated mean flow rate of 230ml/min. From the figure, it is clear that increases in parent vessel flow rate have a substantially greater effect on aneurysm flow patterns when compared to similar sized increases in local Reynolds number attributed to contrast properties.

7.5.2 The 'With Device' and 'No Device Geometry With Device' Cases

Virtual deployment of the flow-diverter device in a rigid geometry derived from experimental imaging prior to flow-diverter deployment results in a 3.4% *increase* in contrast decay rate, as shown in figure 7.26.

Virtual angiography for the 'No Device Geometry With Device' case is generated, as previously detailed, and is shown in figure 7.27 alongside *in-vivo* angiography of the experimental angiography after device deployment. The action of the simulated contrast infiltration appears similar to the 'With Device' case (figure 7.23) whereby contrast enters the aneurysm dome both relatively uniformly across the central portion of the aneurysm neck and as a concentrated jet at the distal extreme of the aneurysm neck. The fraction of contrast entering the aneurysm via this concen-

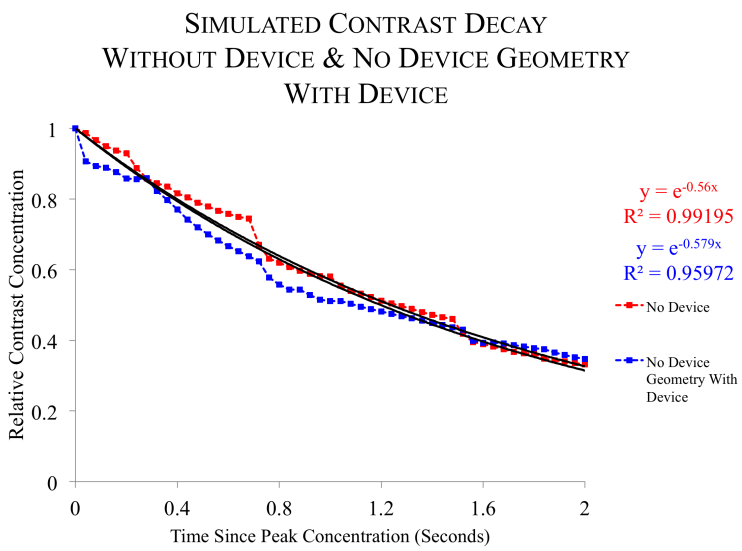

Figure 7.26: *Comparing experimental and simulated contrast decay with and without device*

trated jet appears greater in this case than in the 'With Device' simulation, which results in simulated contrast penetrating deeper into the aneurysm dome. This deeper contrast penetration is focused along the distal wall of the aneurysm and results in a virtual contrast distribution more similar to that seen experimentally. Simulated contrast washout again occurs by the same mechanism of a broad inflow at the centre of the aneurysm neck and a concentrated distal jet, which leads to a pattern of contrast ejection similar to the 'With Device' simulation.

The respective flow pattern streamlines at mean and maximum parent vessel flow are indicated for both the 'With Device' and 'No Device Geometry With Device' cases in figure 7.28. The difference between the flow patterns seen in the figure is substantial: flow penetrates much further into the aneurysm dome for the 'No Device Geometry With Device' simulation, especially at mean flow rate. This additional flow penetration is likely to be the driver behind the higher degree of contrast penetration seen in figure 7.26. Interestingly, at peak flow rate, the two simulated flow patterns become more similar and are characterised by more chaotic flow close to the aneurysm neck and limited flow penetration deeper into the aneurysm dome.

The increased flow penetration seen for the 'No Device Geometry With Device' simulation correlates with a simulated rate of aneurysm inflow approximately halfway between the 'With Device' and 'No Device' cases. A significant portion of this increased inflow is attributed to the lack of parent vessel straightening in the 'No Device Geometry With Device' geometry,

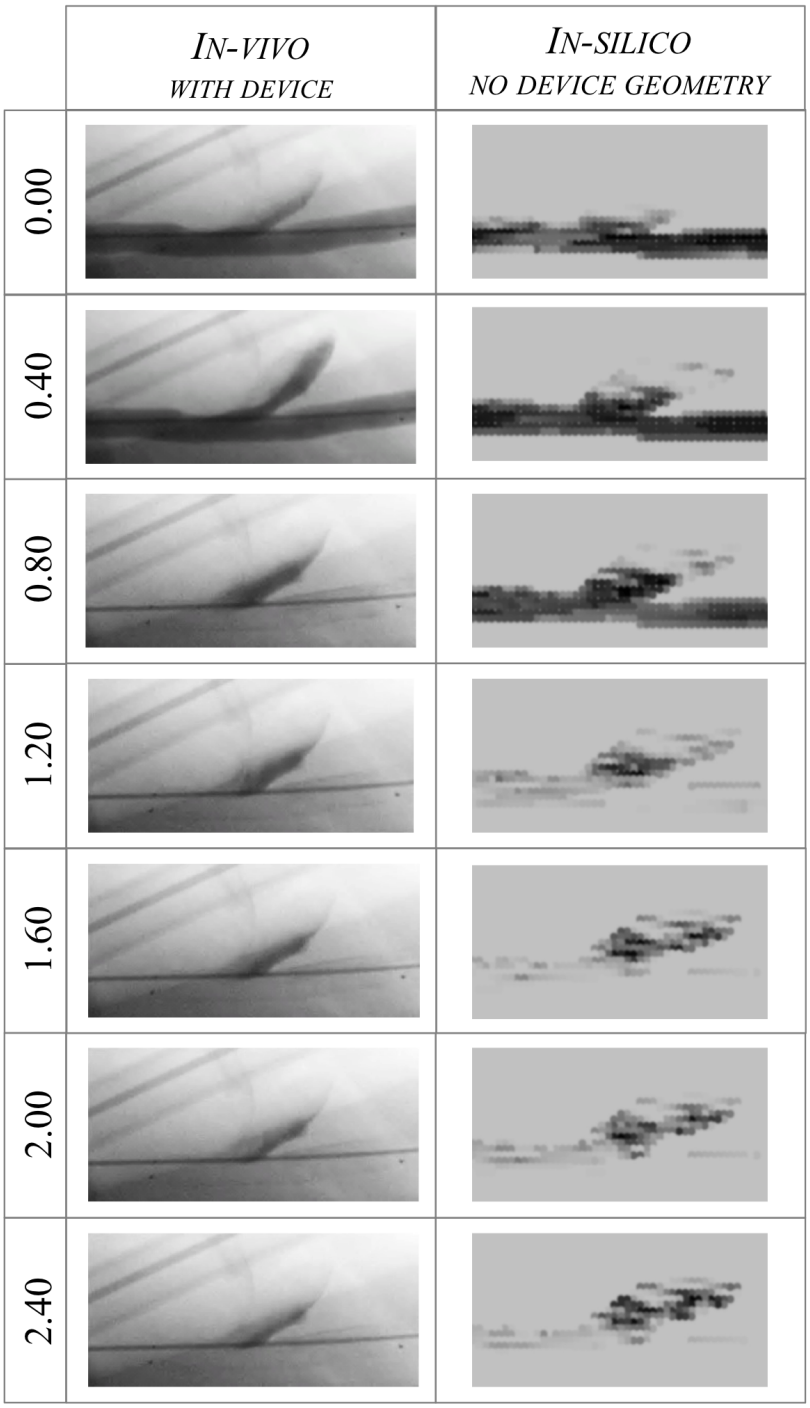

Figure 7.27: *Virtual and in-vivo angiography (images taken at 0.40 second intervals from peak contrast concentration) with a flow-diverter device deployed in the 'No Device' geometry compared to the experimental case after device deployment. Images are aligned to the peak aneurysm contrast concentration at 0.80 seconds*

whereby the localised narrowing of the undeformed geometry parent vessel at the aneurysm neck deflects flow distally into the aneurysm in a similar fashion to that seen in the 'No Device' simulation. Despite this, it is noteworthy that the degree of flow penetration seen for the 'No

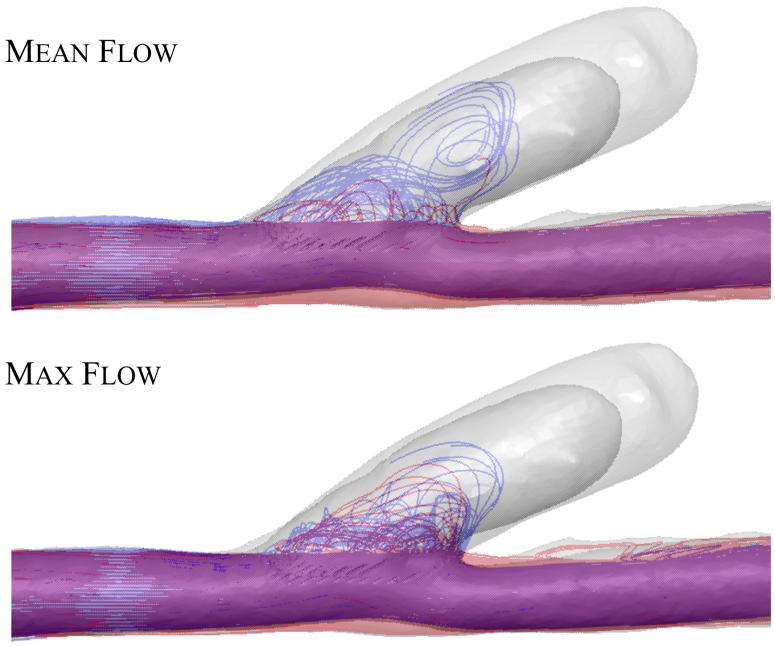

Figure 7.28: *Overlapped flow patterns within the aneurysm dome with a flow-diverter deployed for the 'no device' geometry (blue) and the 'with device' geometry (red) at mean and maximum flow rate*

Device Geometry With Device' case in figure 7.28 is approximately confined to the partially thrombosed aneurysm dome. Thus, the approximate effect of device deployment, exclusive of vessel-straightening effects, on initial aneurysm thrombosis could be predicted from the flow pattern seen in the simulated 'No Device Geometry With Device' geometry.

However, in the absence of any validated model of aneurysm thrombosis, this observation is purely casual. Substantially more robust investigation is needed to ascertain whether the partial aneurysm thrombosis seen between the 'No Device' and 'With Device' geometries could be accurately predicted *a priori* from a simulation of the 'No Device' vessel virtually implanted with a device alone.

7.6 Conclusions

In this final chapter, the virtual contrast model previously discussed in chapter 6 has been integrated into a number of CFD simulations to describe the changes seen a matter of minutes after a flow-diverter device is deployed to treat a sidewall aneurysm. It is clear that this behaviour is both complex and highly dynamic.

The simulated rate of contrast decay after device deployment underestimates the rate of decay seen experimentally by around 20%, with the corresponding relative reduction in contrast decay rate due to device deployment also underestimated by approximately 22% in the simulated case. These underestimates are attributed to the simulated parent vessel flow rate underestimating that seen experimentally by a similar percentage. Specifically, the flow pattern within the aneurysm dome after device deployment appears more sensitive to parent vessel flow rate than in the same geometry with no device deployed, at least in the range of flow rates considered in this study. As such, the visual correspondence between simulated and experimental contrast washout was reduced compared to the 'No Device' case in the previous chapter. This reinforces a major conclusion from the previous chapter, which asserts that accurate measurement of *in-vivo* parent vessel flow rate is vital for accurate simulation and verification of contrast residence behaviour.

Substantial changes in aneurysm and parent vessel geometry were observed after device deployment *in-vivo*; such changes present significant challenges to accurately predicting contrast residence after device placement *a priori*. Significant variation in aneurysm inflow reduction ($\approx$ 40%) was observed in simulated geometries and was entirely attributed to the degree of parent vessel straightening induced by the device.

Chapter 8

Conclusions and Future Work

This final chapter includes detailed summaries of each aspect of this study, the specifics of the contribution made to the field, and finally, suggestions of future work.

8.1 Summary

After almost 10 years of clinical use, the basic design of cerebral flow-diverters has remained entirely unchanged, and the precise mechanisms of successful treatment by flow-diverter are still unclear. The purpose of this study was to interrogate the effect of cerebral flow-diverter design on aneurysm flow patterns. Both abstract flow-diverter concepts and specific flow-diverter mesh designs have been investigated by means of virtual device deployment in patient-specific aneurysm geometries and subsequent blood flow predicted with CFD methods. Overall, the subtle complexity of the aneurysm hemodynamic environment is emphasised, with the specific findings from each of the preceding chapters summarised below.

Chapter 1 set the trajectory of flow-diverter development in the context of the evolution of endovascular treatment for cerebral aneurysms. Flow-diverter development was summarised, and the hemodynamically-driven biochemical environment of the cerebral aneurysm was introduced. Motivation for the study was established with a brief survey of the limited scope of current clinically used flow-diverter designs, and discussion of the link between complex aneurysm flow patterns and successful aneurysm isolation by thrombosis was presented.

A summary of the numerical methods utilised to virtually model the effects of flow-diverter treatment was given in chapter 2. Initially, the chapter focussed on CFD and specifically the finite volume method for the solution of blood flow in 3D. Discretisation mesh quality and the important underlying flow regime features typical of blood flow in the cerebral circulation were also discussed. The application of pressure and velocity boundary conditions models to patient-specific aneurysm geometries was introduced and their subsequent application in the study was clarified. Finally, methods of virtual device deployment were detailed with the introduction of the fast deployment algorithm, which was subsequently used throughout the study.

In chapter 3, the role of mesh topology in (conventional) cylindrical flow-diverter design was explored by specifically focusing on the large-scale flow effects introduced by the mesh. Flow-diverter designs were deployed in idealised and patient-specific aneurysm geometries with flow reduction and changes in aneurysm flow pattern observed. In idealised geometries, major differences were observed in the action of woven mesh designs with small, closed pores and laser-cut meshes with strongly-directional pore shapes. Woven flow-diverter mesh designs were found to significantly reduce secondary flow features and the vorticity of flow passing through the device, whereas the orientation of mesh pores in novel device designs was seen to introduce secondary features into the flow.

When novel and conventional flow-diverter designs were compared in patient-specific aneurysm geometries, differences in flow reduction and aneurysm flow pattern were observed. Consistently, over the three aneurysm geometries investigated, variability attributed to flow-diverter mesh design was seen in aneurysm inflow reduction. Typically this variation in flow-reduction was of the order of 10%, but in one geometry, MCA, a range of around 35% in aneurysm inflow reduction was observed due to device mesh design alone. In one aneurysm geometry, device design was shown to have a more significant effect than mesh porosity on aneurysm inflow reduction. Substantial differences in aneurysm flow pattern after device deployment, including secondary flow effects, were also observed across the device designs for this geometry. A large range in mean aneurysm inflow reduction ($\approx$25-80%) was seen across different aneurysm geometries. Wall shear stress patterns in the aneurysm dome were shown to remain approximately unchanged after device deployment, regardless of device design or porosity; the magnitude of WSS within the aneurysm dome scaled approximately with average aneurysm inflow, with reductions around 30-

60% seen in spatially-averaged aneurysm WSS following device deployment. Overall in chapter 3, flow-diverter mesh design was shown to have a significant effect on aneurysm inflow rate and aneurysm flow pattern.

The concept of a non-cylindrical flow-diverter device for the dedicated treatment of bifurcation aneurysms was introduced in chapter 4. Initially devices were modelled in an idealised bifurcation aneurysm geometry. When later compared to six patient-specific bifurcation aneurysm geometries, the idealised geometry was found to be a poor representation of the flow conditions typically seen in a bifurcation aneurysm. Simulations of the novel device, known as the 'Sphere', deployed in six bifurcation aneurysms in both the ICA and BA suggested the mean aneurysm inflow reduction achieved by the device fell in the range of approximately 30-70%. The 'Sphere' device was shown to substantially alter both the magnitude and distribution of WSS within the aneurysm dome after deployment. In particular, areas of elevated WSS due to flow jet impingement were markedly reduced by the device.

Later in the same chapter, the performance of the novel 'Sphere' device was compared to the flow reduction achieved by virtually deploying a conventional flow-diverter design in the same six aneurysm geometries and jailing one or more daughter vessels. A conventional device was shown to equal the flow reduction achieved by the 'Sphere' in half of the simulated geometries and outperform the 'Sphere' in the remaining cases. Despite large anatomical variation in the aneurysm geometries investigated, the conventional device produced a relatively constant mean flow reduction of 50-70% in all cases. Substantial reductions in aneurysm WSS were seen after conventional device deployment and areas of elevated WSS due to flow jetting were almost entirely eliminated.

Simulations were conducted with equal, fixed outlet pressure boundary conditions applied to all bifurcation daughter vessels, whether they remained patent or jailed, following virtual deployment of the conventional flow-diverter device. No significant changes were observed in the relative proportions of flow exiting each of the respective daughter vessels after device deployment, suggesting that there is little risk of jailed vessel occlusion immediately following device deployment. The long-term patency of daughter vessels jailed by conventional flow-diverters remains unknown. Changes in aneurysm pressure due to deployment of either a novel or conventional flow-diverter device were found to be insignificant.

In response to a number of flow phenomena observed in the previous two chapters, flow instability within the cerebral aneurysm dome was investigated in chapter 5. In two aneurysm geometries the lack of convergence in steady state at mean parent vessel flow was investigated. One geometry showed trivial oscillations that dissipated after around 3000 iterations at steady state, whereas the second aneurysm geometry exhibited consistent oscillatory behaviour. The jet of flow entering the aneurysm dome was shown to oscillate at approximately 10Hz under stationary inlet and outlet boundary conditions.

In the second half of the chapter radically different flow regimes were observed in steady state and transient simulations under identical inlet boundary conditions. The presence of two equilibrium flow regimes within an aneurysm dome was detected; one regime was shown to be unstable and associated with reduced flow momentum in one half of the aneurysm dome whereas the second stable regime was associated with higher flow momentum. The discrepancy observed between steady state and transient studies was found to result from the unstable equilibrium solution meeting the solution convergence criterion, despite the presence of underlying instability.

The unusual flow phenomena observed in chapter 5 reinforce the cautious warning issued by a growing number of authors in the field: that previous CFD studies of aneurysm flow in the literature may be under-resolved and that the omission of important but subtle non-linear flow effects, might have entirely unknown consequences.

In an extension of the analysis of previous chapters, the issue of *in-silico* flow verification was interrogated with the development of a virtual contrast model in chapter 6. A virtual contrast model based on the transport of an independent scalar was implemented and used to calculate the exponential rate of contrast decay within an aneurysm, and to project simulated contrast concentrations into virtual angiography. The virtual model was compared to the results of an experimental study in which four identical sidewall aneurysms were created in a swine model. The influence of the viscosity and density of the contrast agents used *in-vivo* on the subsequent aneurysm flow patterns and contrast decay rate were investigated with the extremes of contrast properties available commercially. Assuming a simplified model of perfectly mixed contrast agent, the full range of commercially available contrast properties was shown to have a negligible effect on the rate of aneurysm contrast decay.

The influence of parent vessel flow rate on aneurysm contrast decay was also investigated in the second half of the chapter. Variation in flow rate attributed to both a 50% increase and decrease in flow was considered with substantial differences in aneurysm contrast washout rate observed. Additionally, the presence of the angiographic catheter in the aneurysm parent vessel lumen, which is used to deliver contrast *in-vivo*, was shown to substantially reduce the parent vessel flow rate by around 50%. Such a phenomenon challenges the validity of clinically derived angiography as the 'gold-standard' for normal aneurysm flow conditions.

Good visual correspondence between *in-vivo* and virtual angiography was observed, suggesting good correspondence between the flow patterns seen experimentally and those predicted by simulation. Deviation between the aneurysm contrast washout rate predicted from simulations and that seen experimentally was attributed to an underestimation of the physiologically correct parent vessel flow rate used in the simulation.

Finally, in chapter 7, the virtual contrast model developed in chapter 6 was applied to the real and virtual treatment of an animal model aneurysm with a novel flow-diverter device. Two of the swine model aneurysms discussed in chapter 6 were implanted with a device from chapter 3. Both experimental and simulated contrast decay curves were generated for the aneurysm geometry before and after device placement. Simulated aneurysm geometries were constructed from *in-vivo* imaging acquired before and after device deployment with the imaging after deployment, showing almost immediate partial-thrombosis of the aneurysm dome. The experimental aneurysm contrast decay rate is underestimated by the simulations for the aneurysm geometry both with and without a device deployed. The 28.2% relative reduction in contrast decay rate seen experimentally following flow-diverter deployment is also underestimated virtually with a relative reduction in contrast decay of only 22.1%. This error was attributed to the same error discussed in chapter 6, namely an underestimate of the parent vessel flow rate in the simulated case. Visually, the pattern of contrast infiltration and decay following device deployment differs substantially between the experimental and simulated angiography. A brief investigation revealed high sensitivity of aneurysm flow pattern to changes in parent vessel flow rate.

The immediate effect of flow-diverter placement was also modelled in chapter 7, with the virtual placement of the flow-diverter device into the geometry acquired from *in-vivo* imaging prior to device placement. Hence, this geometry had a device deployed but no thrombosis had initiated.

The influence of the absence of device-induced vessel-straightening was clear, resulting in a substantially increased aneurysm inflow rate compared to the virtual geometry extracted from *in-vivo* imaging after device deployment. Although the contrast infiltration and decay pattern seen in this simulated geometry bore close visual similarity to that seen experimentally, the predicted reduction in simulated contrast decay rate was actually negative and corresponded to a 3% increase in contrast washout rate after device placement. Such a phenomenon was observed to correlate with reduced overall infiltration of contrast after device placement, thereby substantially reducing contrast residence time.

Both of the geometries virtually implanted with flow-diverters in chapter 7 illustrated the importance of subtle changes in aneurysm flow pattern and the sensitivity of this flow regime to parent vessel conditions. Accurately incorporating these factors into *in-silico* simulations of aneurysm treatment by flow-diverter remains *very* challenging. Substantial changes in aneurysm inflow reduction and contrast decay rate were observed in simulated sidewall aneurysm geometries due to parent vessel straightening effect alone. This may have significant consequences for the accuracy of findings resulting from simulations in the literature that model flow-diverter deployment assuming a rigid vessel wall.

8.2 Specific Contributions to the Field

A number of observations related to flow-diverter devices and large scale flow effects have been made over the course of this study. These observations are summarised below and, to the best of the author's knowledge, are unreported in the literature.

- Cerebral flow-diverter mesh design has been shown to have a significant effect on simulated aneurysm inflow reduction, flow pattern, and the entire hemodynamic environment of the aneurysm dome. Current woven designs of flow-diverter device cannot exploit variation in mesh design and, as a result, may not be fully optimised for aneurysm treatment.

- Specifically in this study, a flow-diverter mesh design with 'Diverging' shaped struts was found to more effectively reduce aneurysm inflow than other mesh designs of the same porosity. The 'Diverging' mesh design achieved this result by a dual action of frictional resistance to flow

passing through the mesh and by imparting vorticity into the flow to direct it out of the aneurysm dome.

- Flow instability was observed in a number of simulated aneurysm geometries. Non-stationary behaviour was observed under stationary boundary conditions, consistent with the findings of other authors. In one case, the emergence of both unstable and stable stationary solutions were noted in the same geometry, which lead to inconsistent transient and steady state simulation results.

- The influence of angiographic contrast medium density and viscosity in simulated models of contrast transport was investigated. In the side wall aneurysm geometry investigated, the effect of both contrast density and viscosity were found to be insignificant when compared to the effects of relatively small variation in parent vessel flow rate. As such, the validity of using angiography as a clinical 'gold standard' that represents typical aneurysm flow conditions is also challenged.

- A simplified virtual contrast model has been shown to accurately capture the flow characteristics seen experimentally in an animal aneurysm model. In the sidewall aneurysm investigated, variation in contrast decay rate scaled proportionally with parent vessel flow rate, when aneurysm flow patterns were observed to remain approximately constant over such flow rates.

- A virtual contrast model was applied to the simulated treatment of a side-wall aneurysm by flow-diverter, with changes in contrast washout rate predicted. Significant variation in contrast infiltration pattern was seen between experimental and simulated geometries, attributed to difference in parent vessel flow rate.

- Both the highly dynamic (but variable) nature of aneurysm thrombosis formation and the complex mechanical response of a vessel implanted with a flow-diverter present substantial challenges to the development of accurate and well-verified models that are capable of *a priori* prediction of device-induced aneurysm occlusion.

8.3 Future Work

Results from this study suggest that flow-diverter mesh design may have as significant an effect on aneurysm inflow reduction as mesh porosity. Such a hypothesis needs further investigation, as the resulting clinical implications may be substantial. Rigorous further testing in multiple aneurysm geometries is required, in addition to a full parametric study of device mesh designs, before a generalisable result can be confidently drawn.

The aneurysm instabilities seen in chapter 5 warrant substantial further investigation. Again, generalisability must be investigated fully in order to ascertain whether the phenomena observed are the result of obscure parameters that are unique to the geometries discussed, or whether the behaviour seen has greater implications for past and future CFD studies of aneurysm flow. In particular the phenomena seen in chapter 5 should be independently verified to be physical, and not the result of numerical instability, with 3D *in-vitro* models and detailed PIV analysis.

Finally, the virtual contrast model introduced in this study has given only a very brief glimpse into the myriad complexities associated with accurate *in-vivo* verification of simulated aneurysm flows. A major weakness in current patient-specific simulations lies in a lack of accurate patient-specific flow conditions, from which significantly more representative simulations could be conducted and verified. However, given the brief investigation conducted in this study on the effect of an angiographic catheter on vessel flow rate, the fundamental validity of using contrast to quantify 'normal' flow conditions *in-vivo* must be investigated further.

Sophisticated virtual treatment planning that trials current and novel devices on a patient-specific basis in near real-time remains the primary goal of research in the field. Although advances in computational power may move this prospect incrementally closer year by year, it is clear that revolutionary leaps in understanding combined with well-verified models of *in-vivo* mechanisms are vital if such a goal is to ever become a reality.

List of Software Utilised in this Study

Software	Use in this Study
OsiriX v. 6.5 (Freeware) Pixmeo, Bernex, Switzerland http://www.osirix-viewer.com/Downloads.html	Segmentation of imaging DICOMs and generation of 3D surface meshes in .STL format
MeshLab v. 1.3.0 (Freeware) Visual Computing Lab, CNR-ISTI, Pisa, Italy http://meshlab.sourceforge.net	Smoothing, repairing and editing .STL meshes
Blender v.2.70 (Freeware) Stichting Blender Foundation, Amsterdam, The Netherlands http://www.blender.org/download/	Generation and editing of .STL meshes for patient-specific and idealised aneurysm geometries, and different device designs
CFD-VisCART v. 2010.0 ESI Group, Paris, France	Volumetric meshing in .DTF format of .STL surface mesh files for CFD-ACE solver
CFD-ACE v. 2013.0 ESI Group, Paris, France	Finite-volume CFD solver for .DTF meshes
Matlab v. 2014a MathWorks, Natick, MA, USA	i. Virtual deployment of flow-diverter devices ii. Post-processing of alphanumeric output from CFD-ACE solver
CFD-VIEW v. 2013.0 ESI Group, Paris, France	Postprocessor and GUI for solved .DTF meshes

List of Publications and Presentations

Peer-Reviewed Journal Articles

Personalizing Flow-Diverter Intervention for Cerebral Aneurysms: from Computational Hemodynamics to Biochemical Modeling, T. W. Peach, M. Ngoepe, K. Spranger, Y. Ventikos and D. Zajarias-Fainsod, International Journal for Numerical Methods in Biomedical Engineering, Volume 30, Issue 11, pages 1387-1407, 2014, DOI: 10.1002/cnm.2663

The Sphere – A Dedicated Bifurcation Aneurysm Flow-Diverter Device, T. W. Peach, J.F Cornhill, A. Nguyen, H.A Riina and Y. Ventikos, Cardiovascular Engineering and Technology, Volume 5, Issue 4, 2014, Page 334-347, DOI: 10.1007/s13239-014-0188-4

The Effect of Patient-Specific Flow-Diverter Deployment on Intervention Outcomes for Bifurcation Aneurysms: From Implantation Rehearsal to Virtual Angiograms, T. W. Peach, K. Spranger and Y. Ventikos, Annals of Biomedical Engineering, (under review)

Stable, Unstable and Pseudo-Stable Aneurysm Flow Regimes in Steady State and Transient Simulations, T. W. Peach and Y, Ventikos, (in preparation)

In-vivo Validation of a CFD Virtual Contrast Model, T. W. Peach, J. Ma, Z. You, J. Byrne, R. Rizkallah and Y.Ventikos, (in preparation)

Peer-Reviewed Conference Proceedings

A Novel Flow-Diverter for Direct Treatment of Cerebral Aneurysms J. Ma, T.W. Peach, Z. You, R. R. Rizkallah and J. Byrne, ASME 7th Frontiers in Biomedical Devices, Buffalo NY, USA 17-20 August 2014, DETC2014-35699

Book Chapters

Treating Intracranial Aneurysms – A Review of Existing and Emerging Methods, Z. You, J. Ma, T. W. Peach and X. Zhou, Reference Module in Biomedical Science, Volume 5: Medical Biotechnology and Healthcare, Elsevier, (Forthcoming)

Conference Presentations

A Virtual Contrast CFD Model Verified in Swine Sidewall Aneurysms, T. W. Peach, J. Byrne, J. Ma, R. Rizkallah, Y. Ventikos and Z. You, Interdisciplinary Cerebrovascular Symposium, Zurich, 2014

Personalising Flow-Diverter Intervention for Cerebral Aneurysms, T.W. Peach, Y. Ventikos, et al., CLMS Medical Imaging and Simulation Workshop, University College, London, 2013

The Balance Between Speed and Accuracy in Blood Flow Simulations in the Clinical Setting, T.W. Peach, Y. Ventikos and Z. You, Meeting of the Wellcome Trust Board of Executives and Governors, Oxford, 2013

Effects of Intracranial Flow-Diverter Design on Aneurysm Flow, T. W. Peach and Y. Ventikos , EPFDC, Imperial College, London, 2012

Going with the Flow: Effects of Stent Design on Parent Vessel Branch Perfusion After Aneurysm Treatment with Flow Diverters, T. W. Peach, Y. Ventikos et al., ABC-WIN Interventional Neurology Conference, Val DÕIsere, 2012

Conference Contributions

Can Multi-scale Modeling of Thrombus Formation Add Value to Implant Design and Patient Management? Y. Ventikos, M. Ngoepe, T. W. Peach, K. Spranger and D. Zajarias-Fainsod, International Intracranial Stent Meeting, Madison WI, USA, 2012

Hemodynamics of Cerebral Aneurysms with Implanted Flow-Diverters, Y. Ventikos, T. W. Peach, and D. Zajarias-Fainsod, ECCOMAS 2012, Vienna, 2012

Modelling Intracranial Aneurysms Treated with Flow-Diverters: Correlation of Intra-aneurysm Sac Flow Dynamics with Thrombus Evolution, D. Zajarias-Fainsod, K. Spranger, et al. ESMC2012, London, 2012

Transport Phenomena, Fluid Mechanics and Multiscale Modelling Techniques for Clinical Decision Support, E. C. Holland, T. W. Peach, et al., ICFD2011, Paris, 2011

Bibliography

[1] Mohamed Abdihalim, Masaki Watanabe, Saqib a Chaudhry, Bharati Jagadeesan, M Fareed K Suri, and Adnan I Qureshi. Are Coil Compaction and Aneurysmal Growth Two Distinct Etiologies Leading to Recurrence Following Endovascular Treatment of Intracranial Aneurysm? *Journal of neuroimaging : official journal of the American Society of Neuroimaging*, pages 1–5, January 2013.

[2] Yazan J. Alderazi, Darshan Shastri, Tareq Kass-Hout, Charles J. Prestigiacomo, and Chirag D. Gandhi. Flow diverters for intracranial aneurysms. *Stroke Research and Treatment*, 2014, 2014.

[3] Tomohiro Aoki and M Nishimura. Targeting chronic inflammation in cerebral aneurysms: focusing on NF-kappaB as a putative target of medical therapy. *Expert opinion on therapeutic targets*, 14:265–273, 2010.

[4] S Appanaboyina, F Mut, C M Putman, R Lohner, and J R Cebral. Computational Fluid Dynamics of Stented Intracranial Aneurysms Using Adaptive Embedded Unstructured Grids. *International Journal for Numerical Methods in Fluids*, 57:475–493, 2008.

[5] Sunil Appanaboyina, Fernando Mut, Rainald Löhner, Christopher Putman, and Juan Cebral. Simulation of intracranial aneurysm stenting: Techniques and challenges. *Computer Methods in Applied Mechanics and Engineering*, 198(45-46):3567–3582, September 2009.

[6] Luca Augsburger, Mohamed Farhat, Philippe Reymond, Edouard Fonck, Zsolt Kulcsar, Nikos Stergiopulos, and Daniel a Rüfenacht. Effect of flow diverter porosity on intraaneurysmal blood flow. *Klinische Neuroradiologie*, 19(3):204–14, August 2009.

[7] H Baek, M V Jayaraman, P D Richardson, and G E Karniadakis. Flow Instability and Wall Shear Stress Variation in Intracranial Aneurysms. *Journal of the Royal Society, Interface / the Royal Society*, 7(47):967–88, June 2010.

[8] J B Bederson, I a Awad, D O Wiebers, D Piepgras, E C Haley, T Brott, G Hademenos, D Chyatte, R Rosenwasser, and C Caroselli. Recommendations for the management of patients with unruptured intracranial aneurysms: A Statement for healthcare professionals from the Stroke Council of the American Heart Association. *Stroke; a journal of cerebral circulation*, 31:2742–2750, 2000.

[9] a. Bernardini, I. Larrabide, H. G. Morales, G. Pennati, L. Petrini, S. Cito, and a. F. Frangi. Influence of different computational approaches for stent deployment on cerebral aneurysm haemodynamics. *Interface Focus*, 1(3):338–348, March 2011.

[10] Frederic J Blom. Considerations on the Spring Analogy. *International Journal for Numerical Methods in Fluids*, 32:647–668, 2000.

[11] T. J. Bowker, P. N. Watton, P. E. Summers, J. V. Byrne, and Y. Ventikos. Rest versus exercise hemodynamics for middle cerebral artery aneurysms: A computational study. *American Journal of Neuroradiology*, 31:317–323, 2010.

[12] Jonathan L Brisman, Joon K Song, and David W Newell. Cerebral aneurysms. *The New England Journal of Medicine*, 355(9):928–39, August 2006.

[13] A. C. Burleson and V. T. Turitto. Identification of quantifiable hemodynamic factors in the assessment of cerebral aneurysm behavior . On behalf of the Subcommittee on Biorheology of the Scientific and Standardization Committee of the ISTH . *Thromb Haemost.*, 76(1):118–23, 1996.

[14] Joseph D. Burns, John Huston, Kennith F. Layton, David G. Piepgras, and Robert D. Brown. Intracranial aneurysm enlargement on serial magnetic resonance angiography: Frequency and risk factors. *Stroke*, 40:406–411, 2009.

[15] V D Butty, K Gudjonsson, P Buchel, V B Makhijani, Y Ventikos, and D Poulikakos. Residence times and basins of attraction for a realistic right internal carotid artery with two aneurysms. *Biorheology*, 39(3-4):387–93, January 2002.

[16] James V Byrne, Radu Beltechi, Julia a Yarnold, Jacqueline Birks, and Mudassar Kamran. Early experience in the treatment of intra-cranial aneurysms by endovascular flow diversion: a multicentre prospective study. *PloS one*, 5(9), January 2010.

[17] James V Byrne and I Szikora. Flow Diverters in the Management of Intracranial Aneurysms : A Review. *EJMINT*, 2012.

[18] Adriana Campi, Najib Ramzi, Andrew J Molyneux, Paul E Summers, Richard S C Kerr, Mary Sneade, Julia a Yarnold, Joan Rischmiller, and James V Byrne. Retreatment of ruptured cerebral aneurysms in patients randomized by coiling or clipping in the International Subarachnoid Aneurysm Trial (ISAT). *Stroke*, 38(5):1538–44, May 2007.

[19] Marcelo Castro, Christopher Putman, Alessandro Radaelli, Alejandro Frangi, and Juan Cebral. Hemodynamics and Rupture of Terminal Cerebral Aneurysms. *Academic Radiology*, 16:1201–1207, 2009.

[20] J R Cebral, F Mut, M Raschi, E Scrivano, R Ceratto, P Lylyk, and C M Putman. Aneurysm Rupture Following Treatment with Flow-diverting Stents: Computational Hemodynamics Analysis of Treatment. *AJNR*, 32(1):27–33, January 2011.

[21] Juan R Cebral and Rainald Löhner. Efficient simulation of blood flow past complex endovascular devices using an adaptive embedding technique. *IEEE Transactions on Medical Imaging*, 24(4):468–76, April 2005.

[22] Juan R Cebral, Richard S Pergolizzi, and Christopher M Putman. Computational fluid dynamics modeling of intracranial aneurysms: qualitative comparison with cerebral angiography. *Academic radiology*, 14(7):804–13, July 2007.

[23] Juan R Cebral and Marcelo Raschi. Suggested Connections Between Risk Factors of Intracranial Aneurysms: A Review. *Annals of Biomedical Engineering*, December 2012.

[24] I. Chatziprodromou, D. Poulikakos, and Y. Ventikos. On the influence of variation in haemodynamic conditions on the generation and growth of cerebral aneurysms and atherogenesis: A computational model. *Journal of Biomechanics*, 40:3626–3640, 2007.

[25] I. Chatziprodromou, a. Tricoli, D. Poulikakos, and Y. Ventikos. Haemodynamics and wall remodelling of a growing cerebral aneurysm: A computational model. *Journal of Biomechanics*, 40:412–426, 2007.

[26] Iordanis Chatziprodromou, Vincent D Butty, and Yiannis Ventikos. Pulsatile Blood Flow in Anatomically Accurate Vessels with Multiple Aneurysms : A Medical Intervention Planning Application of Computational Haemodynamics. *Flow, Turbulence and Combustion*, 71:333–346, 2003.

[27] Haoyu Chen, Alisa Selimovic, Harry Thompson, Alessandro Chiarini, Justin Penrose, Yiannis Ventikos, and Paul N Watton. Investigating the Influence of Haemodynamic Stimuli on Intracranial Aneurysm Inception. *Annals of Biomedical Engineering*, 41(7):1492–504, July 2013.

[28] S. Cito, a. J. Geers, M. P. Arroyo, V. R. Palero, J. Pallarés, a. Vernet, J. Blasco, L. San Román, W. Fu, a. Qiao, G. Janiga, Y. Miura, M. Ohta, M. Mendina, G. Usera, and a. F. Frangi. Accuracy and Reproducibility of Patient-Specific Hemodynamic Models of Stented Intracranial Aneurysms: Report on the Virtual Intracranial Stenting Challenge 2011. *Annals of Biomedical Engineering*, 43(1):154–167, 2014.

[29] E Sander Connolly, Alejandro a Rabinstein, J Ricardo Carhuapoma, Colin P Derdeyn, Jacques Dion, Randall T Higashida, Brian L Hoh, Catherine J Kirkness, Andrew M Naidech, Christopher S Ogilvy, Aman B Patel, B Gregory Thompson, and Paul Vespa. Guidelines for the Management of Aneurysmal Subarachnoid Hemorrhage: A Guideline for Healthcare Professionals From the American Heart Association/American Stroke Association. *Stroke*, 43(6):1711–1737, June 2012.

[30] A N Cookson, D J Doorly, and S J Sherwin. Mixing through stirring of steady flow in small amplitude helical tubes. *Annals of biomedical engineering*, 37(4):710–21, April 2009.

[31] M. Crompton. Mechanism of Growth and Rupture in Cerebral Berry Aneurysms. *British Medical Journal*, 1:1138–1142, 1966.

[32] Lishan Cui, Qiang Peng, Wenbo Ha, Dexiang Zhou, and Yang Xu. Parent artery occlusion for intracranial aneurysms. *Interventional neuroradiology : journal of peritherapeutic*

neuroradiology, surgical procedures and related neurosciences, 15:309–315, 2009.

[33] Walter E Dandy. Intracranial Aneurysm of the Internal Carotid Artery. *Annals of Surgery*, 107(5):654–659, 1938.

[34] B Davis, K Royalty, M Kowarschik, C Rohkohl, E Oberstar, B Aagaard-Kienitz, D Niemann, O Ozkan, C Strother, and C Mistretta. 4D digital subtraction angiography: implementation and demonstration of feasibility. *AJNR. American journal of neuroradiology*, 34(10):1914–21, October 2013.

[35] S De Bock, F Iannaccone, G De Santis, M De Beule, P Mortier, B Verhegghe, and P Segers. Our capricious vessels: The influence of stent design and vessel geometry on the mechanics of intracranial aneurysm stent deployment. *Journal of biomechanics*, 45(8):1353–9, May 2012.

[36] Nicolien K. De Rooij, Birgitta K. Velthuis, Ale Algra, and G. J E Rinkel. Configuration of the circle of Willis, direction of flow, and shape of the aneurysm as risk factors for rupture of intracranial aneurysms. *Journal of Neurology*, 256:45–50, 2009.

[37] W.R. Dean. Dean Flow. *The London, Edinburgh, and Dublin Philosophical Magazine and Journal of Science*, 5:402–420, 1928.

[38] W.R. Dean. The stream-line motion of fluid in a curved pipe. *The London, Edinburgh, and Dublin Philosophical Magazine and Journal of Science*, 5(30):673–695, April 1928.

[39] Laura Dempere-Marco, Estanislao Oubel, Marcelo Castro, Christopher Putman, Alejandro Frangi, and Juan Cebral. CFD Analysis Incorporating the Influence of Wall Motion: Application to Intracranial Aneurysms. *MICCAI 2006*, pages 438–45, January 2006.

[40] S. Dhar, M. Tremmel, J. Mocco, M. Kim, and J. Yamamoto. Morphology Parameters for Intracranial Aneurysm Rupture Risk Assessment. *Neurosurgery*, 63(2):185–197, 2008.

[41] J P Van Doormaal and G D Raithby. Enhancements of the Simple Method for Predicting Incompressible Fluid Flows. *Numerical Heat Transfer*, 7:147–163, 1984.

[42] Pietro I D'Urso, Giuseppe Lanzino, Harry J Cloft, and David F Kallmes. Flow Diversion for Intracranial Aneurysms: a Review. *Stroke*, 42:2363–8, August 2011.

[43] Jürgen Endres, Markus Kowarschik, Thomas Redel, Puneet Sharma, Viorel Mihalef, Joachim Hornegger, and Arnd Dörfler. A workflow for patient-individualized virtual angiogram generation based on CFD simulation. *Computational and mathematical methods in medicine*, 2012:306765, January 2012.

[44] C Farhat. Torsional Springs for Two-Dimensional Dynamic Unstructured Fluid Meshes. *Computer Methods in Applied Mechanics and Engineering*, 25(98), 1998.

[45] Hector Fernandez, Juan M. Macho, Jordi Blasco, Luis San Roman, Werner Mailaender, Luis Serra, and Ignacio Larrabide. Computation of the change in length of a braided device when deployed in realistic vessel models. *International Journal of Computer Assisted Radiology and Surgery*, 2015.

[46] J. H. Ferzinger and M. Peric. *Computational methods for fluid dynamics*. Springer, 2003.

[47] Matthew D Ford, Gordan R Stuhne, Hristo N Nikolov, Damiaan F Habets, Stephen P Lownie, David W Holdsworth, and David Steinman. Virtual angiography for visualization and validation of computational models of aneurysm hemodynamics. *IEEE transactions on medical imaging*, 24(12):1586–92, December 2005.

[48] Juhana Frösen, Anna Piippo, Anders Paetau, Marko Kangasniemi, Mika Niemelä, Juha Hernesniemi, and Juha Jääskeläinen. Remodeling of saccular cerebral artery aneurysm wall is associated with rupture: Histological analysis of 24 unruptured and 42 ruptured cases. *Stroke*, 35:2287–2293, 2004.

[49] D L Fry. Certain histological and chemical responses of the vascular interface to acutely induced mechanical stress in the aorta of the dog. *Circulation research*, 24(1):93–108, 1969.

[50] Wenyu Fu, Zhaoyong Gu, Xianlong Meng, Bo Chu, and Aike Qiao. Numerical Simulation of Hemodynamics in Stented Internal Carotid Aneurysm Based on Patient-specific Model. *Journal of Biomechanics*, 43:1337–42, May 2010.

[51] Bruce Furie and Barbara C Furie. Thrombus formation in vivo. *Journal of Clinical Investigation*, 115(12):3355–3362, 2005.

[52] Bruce Furie and Barbara C Furie. Mechanisms of thrombus formation. *The New England journal of medicine*, 359(9):938–49, August 2008.

[53] Jan Van Gijn, Richard S Kerr, and Gabriel J E Rinkel. Subarachnoid haemorrhage. *Lancet*, 369:306–318, 2007.

[54] T M Griffith. Modulation of Blood Flow and Tissue Perfusion by Endothelium-Derived Relaxing Factor. *Experimental Physiology*, 79:873–913, 1994.

[55] G Guglielmi, F Vinuela, I Sepetka, and V Macellari. Electrothrombosis of saccular aneurysms via endovascular approach. *Neurosurgery*, pages 1–7, 1991.

[56] B Y J F Hale, D A Mcdonald, and J R Womersley. Velocity Profiles of Oscillating Arterial Flow, with some Calculations of Viscous Drag and the Reynolds Number. *Physiology*, 128:629–640, 1955.

[57] W. Harvey. *Exercitatio Anatomica do Motu Cordis et Sanguinis in Animalibus (trans: An Anatomical Exercise on the Motion of the Heart and Blood in Living Beings)*. 1628.

[58] M. Hennerici, W Rautenberg, G Sitzer, and A Schwartz. Transcranial Doppler Ultrasound for the Assessment of Intracranial Arterial Flow Velocity–Part1. *Surg. Neurol.*, 27:439–48, 1987.

[59] B.L. Hoh, C.L. Sistrom, C.S. Firment, G.L. Fautheree, G.J. Velat, J.H. Whiting, J.F. Reavey-Cantwell, and S.B. Lewis. Bottleneck factor and height-width ratio: association with ruptured aneurysms in patients with multiple cerebral aneurysms. *Neurosurgery*, 61(4):716–723, 2007.

[60] G a Holzapfel, T C Gasser, and R W Ogden. A new constitutive framework for arterial wall mechanics and a comperative study of material models. *J. Elasticity*, 61:1–48, 2000.

[61] J. D. Humphrey and P. B. Canham. Structure, mechanical properties, and mechanics of intracranial saccular aneurysms. *Journal of Elasticity*, 61:49–81, 2000.

[62] S. Iqbal. A Comprehensive Study of the Anatomical Variations of the Circle of Willis in Adult Human Brains. *Journal of Clinical and Diagnostic Research*, 2013.

[63] G Janiga, P Berg, S Sugiyama, K Kono, and D A Steinman. The Computational Fluid Dynamics Rupture Challenge 2013 â Phase I : Prediction of Rupture Status in Intracranial Aneurysms. *AJNR*, 2015.

[64] Gábor Janiga, Christian Rössl, Martin Skalej, and Dominique Thévenin. Realistic Virtual Intracranial Stenting and Computational Fluid Dynamics for Treatment Analysis. *Biomechanics*, 46(1):7–12, October 2013.

[65] Andrew K Johnson, Daniel M Heiferman, and Demetrius K Lopes. Stent-assisted embolization of 100 middle cerebral artery aneurysms. *Journal of neurosurgery*, pages 1–6, February 2013.

[66] S C Johnston, R a Dudley, D R Gress, and L Ono. Surgical and endovascular treatment of unruptured cerebral aneurysms at university hospitals. *Neurology*, 52:1799–1805, 1999.

[67] S C Johnston, S Selvin, and D R Gress. The burden, trends, and demographics of mortality from subarachnoid hemorrhage. *Neurology*, 50(5):1413–1418, 1998.

[68] L-D Jou and M E Mawad. Analysis of intra-aneurysmal flow for cerebral aneurysms with cerebral angiography. *AJNR. American journal of neuroradiology*, 33(9):1679–84, October 2012.

[69] Liang-Der Jou and Michel E Mawad. Hemodynamic Effect of Neuroform Stent on Intimal Hyperplasia and Thrombus Formation in a Carotid Aneurysm. *Medical Engineering & Physics*, 33:573–80, June 2011.

[70] Yutaka Kai, Jun-ichiro Hamada, Motohiro Morioka, Shigetoshi Yano, and Jun-ichi Kuratsu. Evaluation of the Stability of Small Ruptured Aneurysms with a Small Neck after Embolization with Guglielmi Detachable Coils: Correlation between Coil Packing Ratio and Coil Compaction. *Neurosurgery*, 56(4):785–792, April 2005.

[71] Alexey V Kamenskiy, Yuris a Dzenis, Jason N Mactaggart, Anastasia S Desyatova, and Iraklis I Pipinos. In Vivo Three-dimensional Blood Velocity Profile Shapes in the Human Common, Internal, and External Carotid Arteries. *Vascular Surgery*, 54:1011–20, October 2011.

[72] M. Kim, D. Taulbee, M. Tremmel, and H Meng. Comparison of Two Stents in Modifying Cerebral Aneurysm Hemodynamics. *Annals of Biomedical Engineering*, 36(5):726–741, 2009.

[73] Minsuok Kim, E Levy, H Meng, and L Nelson Hopkins. Quantification of Hemodynamic Changes Induced by Virtual Placement of Multiple Stents Across a Wide-necked Basilar Trunk Aneurysm. *Neurosurgery*, 61:1305–1313, 2007.

[74] Joachim Klisch, Vojtech Sychra, Christoph Strasilla, Thomas Liebig, and David Fiorella. The Woven EndoBridge Cerebral Aneurysm Embolization Device (WEB II): Initial Clinical Experience. *Neuroradiology*, 53:599–607, August 2011.

[75] D Krex, H K Schackert, and G Schackert. Genesis of cerebral aneurysms–an update. *Acta neurochirurgica*, 143(5):429–448, 2001.

[76] David N. Ku. Blood Flow in Arteries. *Annual Review of Fluid Mechanics*, 29(1):399–434, January 1997.

[77] Z. Kulcsár, E. Houdart, a. Bonafé, G. Parker, J. Millar, a. J P Goddard, S. Renowden, G. Gál, B. Turowski, K. Mitchell, F. Gray, M. Rodriguez, R. Van Den Berg, a. Gruber, H. Desal, I. Wanke, and D. a. Rüfenacht. Intra-aneurysmal thrombosis as a possible cause of delayed aneurysm rupture after flow-diversion treatment. *American Journal of Neuroradiology*, 32(7):20–25, 2011.

[78] Zsolt Kulcsár, Ulrike Ernemann, Stephan G Wetzel, Alexander Bock, Sophia Goericke, Vasilis Panagiotopoulos, Michael Forsting, Daniel a Ruefenacht, and Isabel Wanke. High-profile Flow Diverter (Silk) Implantation in the Basilar Artery. *Stroke*, 41(8):1690–6, August 2010.

[79] Zsolt Kulcsár, Stephan G Wetzel, Luca Augsburger, Andreas Gruber, Isabel Wanke, and Daniel Andre Rüfenacht. Effect of Flow Diversion Treatment on Very Small Ruptured Aneurysms. *Neurosurgery*, 67(3):789–93, September 2010.

[80] S. C. Kwon, Y. H. Ding, D. Dai, R. Kadirvel, D. A. Lewis, and David F. Kallmes. Preliminary results of the luna aneurysm embolization system in a rabbit model: A new intrasaccular aneurysm occlusion device. *American Journal of Neuroradiology*, 32(3):602–606, 2011.

[81] Rohan R Lall, Christopher S Eddleman, Bernard R Bendok, and H Hunt Batjer. Unruptured intracranial aneurysms and the assessment of rupture risk based on anatomical and

morphological factors: sifting through the sands of data. *Neurosurgical focus*, 26(May), 2009.

[82] Ignacio Larrabide, Minsuok Kim, Luca Augsburger, Maria Cruz Villa-Uriol, Daniel Rüfenacht, and Alejandro F. Frangi. Fast virtual deployment of self-expandable stents: Method and in vitro evaluation for intracranial aneurysmal stenting. *Medical Image Analysis*, 16(3):721–730, 2012.

[83] Ignacio Larrabide, Maria-Cruz Villa-Uriol, Rubén Cárdenes, Valeria Barbarito, Luigi Carotenuto, Arjan J Geers, Hernán G Morales, José M Pozo, Marco D Mazzeo, Hrvoje Bogunović, Pedro Omedas, Chiara Riccobene, Juan M Macho, and Alejandro F Frangi. AngioLab-A software tool for morphological analysis and endovascular treatment planning of intracranial aneurysms. *Computer methods and programs in biomedicine*, 108(2):806–19, November 2012.

[84] Baruch B. Lieber, Veronica Livescu, L. N. Hopkins, and Ajay K. Wakhloo. Particle Image Velocimetry Assessment of Stent Design Influence on Intra-Aneurysmal Flow. *Annals of Biomedical Engineering*, 30(6):768–777, June 2002.

[85] Tong-Miin Liou, Yi-Chen Li, and Wei-Cheng Juan. Numerical and Experimental Studies on Pulsatile Flow in Aneurysms Arising Laterally from a Curved Parent Vessel at Various Angles. *Biomechanics*, 40(6):1268–75, January 2007.

[86] Tong-Miin Liou, Shun-Nan Liou, and Kai-Lung Chu. Intra-Aneurysmal Flow With Helix and Mesh Stent Placement Across Side-Wall Aneurysm Pore of a Straight Parent Vessel. *Journal of Biomechanical Engineering*, 126(1):36, 2004.

[87] Boris Lubicz, Laurent Collignon, Gaï Raphaeli, and Olivier De Witte. Pipeline flow-diverter stent for endovascular treatment of intracranial aneurysms: preliminary experience in 20 patients with 27 aneurysms. *World neurosurgery*, 76(1-2):114–9, 2011.

[88] Pedro Lylyk, Carlos Miranda, Rosana Ceratto, Angel Ferrario, Esteban Scrivano, Hugh Ramirez Luna, Aaron L. Berez, Quang Tran, Peter K. Nelson, and David Fiorella. Curative Endovascular Reconstruction of Cerebral Aneurysms With the Pipeline Embolization Device. *Neurosurgery*, 64(4):632–643, April 2009.

[89] Ding Ma, Gary F Dargush, Sabareesh K Natarajan, Elad I Levy, Adnan H Siddiqui, and Hui Meng. Computer modeling of deployment and mechanical expansion of neurovascular flow diverter in patient-specific intracranial aneurysms. *Journal of biomechanics*, 45(13):2256–63, August 2012.

[90] Jiayao Ma, Zhong You, James Byrne, and Rafik R Rizkallah. Design and mechanical properties of a novel cerebral flow diverter stent. *Annals of Biomedical Engineering*, 42(5):960–70, May 2014.

[91] Shimon Maimon, Lior Gonen, Erez Nossek, Ido Strauss, Ronen Levite, and Zvi Ram. Treatment of Intra-cranial Aneurysms with the SILK Flow Diverter: 2 Years' Experience with 28 Patients at a Single Center. *Acta neurochirurgica*, 154(6):979–87, March 2012.

[92] Adel M Malek, Seth L Alper, and Seigo Izumo. Hemodynamic Shear Stress and Its Role in Atherosclerosis. *The Journal of the American Medical Association*, 282(21):2035–2042, 1999.

[93] Colin D. Mathers and Dejan Loncar. Projections of global mortality and burden of disease from 2002 to 2030. *PLoS Medicine*, 3(11):2011–2030, 2006.

[94] Marc R Mayberg, H Hunt Batjer, Ralph Dacey, Michael Diringer, E Clarke Haley, Roberto C Heros, Linda L Sternau, James Torner, Harold P Adams, William Feinberg, William Thies, and Ex Officio Members. Guidelines for the Management of Aneurysmal Subarachnoid Hemorrhage A Statement for Healthcare Professionals From a Special Writing Group of the Stroke Council , American Heart Association. *Circulation*, 90(5):2592–2605, 1994.

[95] H. Meng, V. M. Tutino, J. Xiang, and a. Siddiqui. High WSS or Low WSS? Complex interactions of hemodynamics with intracranial aneurysm initiation, growth, and rupture: Toward a unifying hypothesis. *American Journal of Neuroradiology*, 35(7):1254–1262, 2014.

[96] H Meng, Z Wang, M Kim, R D Ecker, and L N Hopkins. Saccular aneurysms on straight and curved vessels are subject to different hemodynamics: implications of intravascular stenting. *AJNR. American journal of neuroradiology*, 27(9):1861–5, October 2006.

[97] R D Millán, J M Pozo, J R Cebral, A F Frangi, and Senior Member. Morphological Characterization of Intracranial Aneurysms Using 3-D Moment Invariants. *IEEE transactions on medical imaging*, 26(9):1270–1282, 2007.

[98] L. M. Milne-Thomson. *Theoretical Aerodynamics*. Macmillan, London, 1948.

[99] Andrew Molyneux, Richard Kerr, Irene Stratton, Peter Sandercock, Mike Clarke, Julia Shrimpton, and Rury Holman. International Subarachnoid Aneurysm Trial (ISAT) of neurosurgical clipping versus endovascular coiling in 2143 patients with ruptured intracranial aneurysms: a randomised trial. *Lancet*, 360(9342):1267–74, October 2002.

[100] Andrew J Molyneux, Saruhan Cekirge, Isil Saatci, and Gyula Ga. Cerebral Aneurysm Multicenter European Onyx (CAMEO) Trial : Results of a Prospective Observational Study in 20 European Centers. *AJNR*, 25:39–51, 2004.

[101] Hernán G. Morales, Ignacio Larrabide, Arjan J. Geers, Martha L. Aguilar, and Alejandro F. Frangi. Newtonian and non-Newtonian blood flow in coiled cerebral aneurysms. *Journal of Biomechanics*, 46(13):2158–2164, 2013.

[102] H.G Morales, M Kim, E E Vivas, M-C Villa-Uriol, I Larrabide, T Sola, L Guimaraens, and A F Frangi. How Do Coil Configuration and Packing Density. *AJNR*, pages 1935–1941, 2011.

[103] H Nakatani, N Hashimoto, Y Kang, N Yamazoe, H Kikuchi, S Yamaguchi, and H Niimi. Cerebral blood flow patterns at major vessel bifurcations and aneurysms in rats. *Journal of neurosurgery*, 74(2):258–62, February 1991.

[104] P K Nelson, P Lylyk, I Szikora, S G Wetzel, I Wanke, and D Fiorella. The Pipeline Embolization Device for the Intracranial Treatment of Aneurysms Trial. *AJNR*, 32(1):34–40, January 2011.

[105] Ming-jiu Ni and Mohamed A Abdou. A Bridge Between Projection Methods and SIMPLE Type Methods for Incompressible Navier â Stokes Equations. *IJNMBE*, 72:1490–1512, 2007.

[106] M Ohta, M. Hirabayashi, S G Wetzel, P Lylyk, H. Wata, S. Tsutsumi, and D. A. Rufenacht. Impact of Stent Design on Intra-Aneurysmal Flow. *Interventional Neuroradiology*, 10:85–94, 2004.

[107] R. Ouared, B. Chopard, B. Stahl, D.a. Rüfenacht, H. Yilmaz, and G. Courbebaisse. Thrombosis modeling in intracranial aneurysms: a lattice Boltzmann numerical algorithm. *Computer Physics Communications*, 179(1-3):128–131, July 2008.

[108] S V Patankar. *Numerical heat transfer and fluid flow*. McGraw-Hill, New York, 1980.

[109] T W Peach, M Ngoepe, K Spranger, D Zajarias-Fainsod, and Y Ventikos. Personalizing flow-diverter intervention for cerebral aneurysms: from computational hemodynamics to biochemical modeling. *International journal for numerical methods in biomedical engineering*, 30(11):1387–1407, November 2014.

[110] Thomas Peach, J. Frederick Cornhill, Anh Nguyen, Howard Riina, and Yiannis Ventikos. The âSphereâ: A Dedicated Bifurcation Aneurysm Flow-Diverter Device. *Cardiovascular Engineering and Technology*, 5(4):334–347, August 2014.

[111] K Perktold, M Resch, and H Florian. Pulsatile Non-Newtonian Flow Characteristics in a Three-dimensional Human Carotid Bifurcation Model. *Biomechanical Engineering*, 113(4):464–75, November 1991.

[112] Laurent Pierot. Flow Diverter Stents in the Treatment of Intracranial Aneurysms: Where are we? *Neuroradiology*, 38(1):40–6, March 2011.

[113] Laurent Pierot, Joachim Klisch, Christophe Cognard, Istvan Szikora, Benjamin Mine, Krzysztof Kadziolka, Vojtech Sychra, Istvan Gubucz, Anne-Christine Januel, and Boris Lubicz. Endovascular WEB flow disruption in middle cerebral artery aneurysms: preliminary feasibility, clinical, and anatomical results in a multicenter study. *Neurosurgery*, 73(1):27–34; discussion 34–5, July 2013.

[114] M Piotin, N Sourour, A Biondi, C Mounayer, and R Blanc. The Luna Aneurysm Embolization System for Treatment of Intracranial Aneurysms. *Journal of NeuroInterventional Surgery*, 4:A16, 2012.

[115] Christian Poelma, Paul N Watton, and Yiannis Ventikos. Transitional flow in aneurysms and the computation of haemodynamic parameters. *Interface Focus*, 2015.

[116] Wojciech Poncyljusz, Leszek Sagan, Krzysztof Safranow, and Monika Rac. Initial experience with implantation of novel dual layer flow-diverter device FRED. *Videosurgery and Other Miniinvasive Techniques*, 3:258–264, 2013.

[117] Raffaele Ponzini, Christian Vergara, Giovanna Rizzo, Alessandro Veneziani, Alberto Roghi, Angelo Vanzulli, Oberdan Parodi, and Alberto Redaelli. Womersley Number-Based Estimates of Blood Flow Rate in Doppler Analysis : In Vivo Validation by. *IEEE Transactions on Biomedical Engineering*, 57(7):1807–1815, 2010.

[118] Wouter V Potters, Pim van Ooij, Henk Marquering, Ed Vanbavel, and Aart J Nederveen. Volumetric arterial wall shear stress calculation based on cine phase contrast MRI. *Journal of magnetic resonance imaging*, pages 1–12, January 2014.

[119] A G Radaelli, L Augsburger, J R Cebral, M Ohta, D a Rüfenacht, R Balossino, G Benndorf, D R Hose, A Marzo, R Metcalfe, P Mortier, F Mut, P Reymond, L Socci, B Verhegghe, and a F Frangi. Reproducibility of Haemodynamical Simulations in a Subject-specific Stented Aneurysm Model–a Report on the Virtual Intracranial Stenting Challenge 2007. *Biomechanics*, 41(10):2069–81, July 2008.

[120] Ransokoff. Moore's Treatment of Aneurysm, 1886.

[121] Robert S. Reneman, Theo Arts, and Arnold P G Hoeks. Wall shear stress - An important determinant of endothelial cell function and structure - In the arterial system in vivo: Discrepancies with theory. *Journal of Vascular Research*, 43:251–269, 2006.

[122] Nitzan Resnick, Hava Yahav, and a Shay-Salit. Fluid shear stress and the vascular endothelium: for better and for worse. *Progress in biophysics ...*, 81:177–199, 2003.

[123] Philippe Reymond, Fabrice Merenda, Fabienne Perren, and Daniel Ru. Validation of a One-Dimensional Model of the Systemic Arterial Tree. *American Journal of Physiology - Heart and Circulatory Physiology*, 297:208–222, 2009.

[124] Philippe Reymond, Orestis Vardoulis, and Nikos Stergiopulos. Generic and patient-specific models of the arterial tree. *Journal of Clinical Monitoring and Computing*, 26(5):375–82, October 2012.

[125] Kyehan Rhee, Moon Hee Han, and Sang Hoon Cha. Changes of Flow Characteristics by Stenting in Aneurysm Models: Influence of Aneurysm Geometry and Stent Porosity. *Annals of Biomedical Engineering*, 30(7):894–904, July 2002.

[126] E. Ringelstein, B. Kahlscheuer, E. Niggemeyer, and S. Otis. Transcranial Doppler Sonography: Anatomical Landmarks and Normal Velocity Values. *Ultrasound in Med. & Biol.*, 16(8):745–761, 1990.

[127] M R Roach, S Scott, and G G Ferguson. The hemodynamic importance of the geometry of bifurcations in the circle of Willis (glass model studies). *Stroke; a journal of cerebral circulation*, 3(1):255–267, 1972.

[128] Breigh N Roszelle, Priya Nair, L Fernando Gonzalez, M Haithem Babiker, Justin Ryan, and David Frakes. Comparison Among Different High Porosity Stent Configurations: Hemodynamic Effects of Treatment in a Large Cerebral Aneurysm. *Journal of biomechanical engineering*, 136(February):1–9, December 2013.

[129] Maryam Saadatmand, Takuji Ishikawa, Noriaki Matsuki, Mohammad Jafar Abdekhodaie, Yohsuke Imai, Hironori Ueno, and Takami Yamaguchi. Fluid particle diffusion through high-hematocrit blood flow within a capillary tube. *Journal of biomechanics*, 44(1):170–5, January 2011.

[130] I. Saatchi, K. Yavuz, C. Ozer, S. Geyik, and H.S. Cekirge. Treatment of Intracranial Aneurysms Using the Pipeline Flow-Diverter Embolization Device: A Single-Center Experience with Long-Term Follow- Up Results. *AJNR*, 33, 2012.

[131] Chander Sadasivan, Liliana Cesar, Jaehoon Seong, Audrey Rakian, Qing Hao, Fermin O Tio, Ajay K Wakhloo, and Baruch B Lieber. An original flow diversion device for the treatment of intracranial aneurysms: evaluation in the rabbit elastase-induced model. *Stroke; a journal of cerebral circulation*, 40(3):952–8, March 2009.

[132] Chander Sadasivan, Baruch B Lieber, Matthew J Gounis, Demetrius K Lopes, and L N Hopkins. Angiographic quantification of contrast medium washout from cerebral aneurysms after stent placement. *AJNR. American journal of neuroradiology*, 23(7):1214–21, August 2002.

[133] M. Scanarini, S. Mingrino, R. Giordano, and a. Baroni. Histological and ultrastructural study of intracranial saccular aneurysmal wall. *Acta Neurochirurgica*, 43:171–182, 1978.

[134] Santhosh Seshadhri, GaÌbor Janiga, Oliver Beuing, Martin Skalej, and Dominique TheÌvenin. Impact of Stents and Flow Diverters on Hemodynamics in Idealized Aneurysm Models. *Journal of Biomechanical Engineering*, 133(7):071005, 2011.

[135] Daniel M Sforza, Christopher M Putman, and Juan Raul Cebral. Hemodynamics of Cerebral Aneurysms. *Annu. Rev. Fluid Mech.*, 41:91–107, 2009.

[136] Masaaki Shojima, Marie Oshima, Kiyoshi Takagi, Ryo Torii, Motoharu Hayakawa, Kazuhiro Katada, Akio Morita, and Takaaki Kirino. Magnitude and role of wall shear stress on cerebral aneurysm: computational fluid dynamic study of 20 middle cerebral artery aneurysms. *Stroke; a journal of cerebral circulation*, 35(11):2500–5, November 2004.

[137] D Songsaeng, S Geibprasert, R Willinsky, M Tymianski, K G TerBrugge, and T Krings. Impact of anatomical variations of the circle of Willis on the incidence of aneurysms and their recurrence rate following endovascular treatment. *Clinical radiology*, 65(11):895–901, November 2010.

[138] F. Sotiropoulos, Y. Ventikos, and T. Lackey. Chaotic Advection in Three-Dimensional Stationary Vortex-Breakdown Bubbles. *Fluid Mechanics*, 444:257–297, 2001.

[139] K. Spranger, C. Capelli, G. Bosi, S. Schievano, and Y Ventikos. Comparison and Calibration of a Real-time Virtual Stenting Algorithm Using Finite Element Analysis and Genetic Algorithms. *Computer Methods in Applied Mechanics and Engineering*, 293:462–480, 2015.

[140] Katerina Spranger and Yiannis Ventikos. Which spring is the best? Comparison of methods for virtual stenting. *IEEE transactions on bio-medical engineering*, 61(7):1998–2010, July 2014.

[141] David a Steinman, Yiemeng Hoi, Paul Fahy, Liam Morris, Michael T Walsh, Nicolas Aristokleous, Andreas S Anayiotos, Yannis Papaharilaou, Amirhossein Arzani, Shawn C Shadden, Philipp Berg, Gábor Janiga, Joris Bols, Patrick Segers, Neil W Bressloff, Merih Cibis, Frank H Gijsen, Salvatore Cito, Jordi Pallarés, Leonard D Browne, Jennifer a Costelloe, Adrian G Lynch, Joris Degroote, Jan Vierendeels, Wenyu Fu, Aike Qiao, Simona Hodis, David F Kallmes, Hardeep Kalsi, Quan Long, Vitaly O Kheyfets, Ender a Finol, Kenichi Kono, Adel M Malek, Alexandra Lauric, Prahlad G Menon, Kerem Pekkan, Mahdi Esmaily Moghadam, Alison L Marsden, Marie Oshima, Kengo Katagiri, Véronique Peiffer, Yumnah Mohamied, Spencer J Sherwin, Jens Schaller, Leonid Goubergrits, Gabriel Usera, Mariana Mendina, Kristian Valen-Sendstad, Damiaan F Habets, Jianping Xiang, Hui Meng, Yue Yu, George E Karniadakis, Nicholas Shaffer, and Francis Loth. Variability of computational fluid dynamics solutions for pressure and flow in a giant aneurysm: the ASME 2012 Summer Bioengineering Conference CFD Challenge. *Journal of biomechanical engineering*, 135(2):021016, 2013.

[142] Gordan R. Stuhne and David A. Steinman. Finite-Element Modeling of the Hemodynamics of Stented Aneurysms. *Biomechanical Engineering*, 126:382–7, 2004.

[143] Jiro Suzuki and H. Ohara. Clinicopathological Study of Cerebral Aneurysms. *Neurosurgery*, 48:505–514, 1978.

[144] A. Trager, C. Sadasivan, and B B Lieber. Comparison of the In Vitro Hemodynamic Performance of New Flow Diverters for Bypass of Brain Aneurysms. *Journal of Biomechanical Engineering*, 134(8):1–15, 2012.

[145] M. Tremmel, S. Dhar, E. Levy, J. Mocco, and H Meng. Influence of Intracranial Aneurysm-to-Parent Vessel Size Ratio on Hemodynamics and Implication for Rupture: Results from a Virtual Experimental Study. *Neurosurgery*, 64(4):622–631, 2010.

[146] H Ujiie, Y Tamano, K Sasaki, and T Hori. Is the Aspect Ratio a Reliable Index for Predicting the Rupture of a Saccular Aneurysm? *Neurosurgery*, 48(3):495–502, March 2001.

[147] K Valen-Sendstad and D Steinman. Mind the Gap: Impact of Computational Fluid Dynamics Solution Strategy on Prediction of Intracranial Aneurysm Hemodynamics and

Rupture Status Indicators. *AJNR*, pages 1–8, November 2013.

[148] Kristian Valen-Sendstad, Kent-André Mardal, Mikael Mortensen, Bjørn Anders Pettersson Reif, and Hans Petter Langtangen. Direct numerical simulation of transitional flow in a patient-specific intracranial aneurysm. *Journal of biomechanics*, 44(16):2826–32, November 2011.

[149] Kristian Valen-Sendstad, Kent-André Mardal, and David Steinman. High-resolution Computational Fluid Dynamics Detects High-frequency Velocity Fluctuations in Bifurcation, but not Sidewall, Aneurysms of the Middle Cerebral Artery. *Journal of Biomechanics*, 46(2):402–7, November 2012.

[150] Kristian Valen-Sendstad, Kent-André Mardal, and David Steinman. High-Resolution CFD Detects High-Frequency Velocity Fluctuations in Bifurcation, but not Sidewall, Aneurysms. *Journal of Biomechanics*, 46(2):402–7, January 2013.

[151] Charles Vega, Jeremiah V Kwoon, and Sea D Lavine. Intracranial aneurysms: current evidence and clinical practice. *American family physician*, 66:601–608, 2002.

[152] Y Ventikos. Resolving the Issue of Resolution. *AJNR*, 35:544–545, 2014.

[153] Meike W Vernooij, M Arfan Ikram, Hervé L Tanghe, Arnaud J P E Vincent, Albert Hofman, Gabriel P Krestin, Wiro J Niessen, Monique M B Breteler, and Aad van der Lugt. Incidental Findings on Brain MRI in the General Population. *The New England Journal of Medicine*, 357(18):1821–8, November 2007.

[154] HK Versteeg and W Malalasekera. *An introduction to computational fluid dynamics: the finite volume method*. Longman, Harlow, 2007.

[155] Zhi-Jie Wang, Kenneth R Hoffmann, Zhou Wang, Stephen Rudin, Lee R Guterman, and Hui Meng. Contrast settling in cerebral aneurysm angiography. *Physics in medicine and biology*, 50(13):3171–81, July 2005.

[156] N. P. Waterson and H. Deconinck. Design principles for bounded higher-order convection schemes - a unified approach. *Journal of Computational Physics*, 224(1):182–207, 2007.

[157] Paul N Watton, Yiannis Ventikos, and Gerhard a Holzapfel. Modelling the growth and stabilization of cerebral aneurysms. *Mathematical medicine and biology : a journal of the IMA*, 26(2):133–64, June 2009.

[158] R Webster. An Algebraic Multigrid Solver for Navier-Stokes Problems. *International Journal for Numerical Methods in Fluids*, 18:761–780, 1994.

[159] Marieke J H Wermer, Irene C. Van Der Schaaf, Ale Algra, and Gabriël J E Rinkel. Risk of rupture of unruptured intracranial aneurysms in relation to patient and aneurysm characteristics: An updated meta-analysis. *Stroke*, 38:1404–1410, 2007.

[160] F. White. *Fluid Mechanics*. McGraw-Hill, New York, 1999.

[161] J R Womersley. Method for the Calculation of Velocity, Rate of Flow and Viscous Drag in Arteries when the Pressure Gradient is Known. *J.Physiol.*, 127:553–563, 1955.

[162] M Zhao, S Amin-Hanjani, S Ruland, a P Curcio, L Ostergren, and F T Charbel. Regional cerebral blood flow using quantitative MR angiography. *AJNR. American journal of neuroradiology*, 28(8):1470–3, September 2007.

[163] Y. Zhou, P-F. Yang, Y-B. Fang, Y. Xu, B. Hong, W-Y. Zhao, Q. Li, R. Zhao, Q-H. Huang, and J-M. Liu. A Novel Flow-Diverting Device (Tubridge) for the Treatment of. *AJNR*, pages 1–8, 2014.